CRACK INITIATION BEHAVIOR OF OPTICAL GLASSES FROM VICKERS INDENTATION

BY

TREVOR WILANTEWICZ

A THESIS
SUBMITTED TO THE FACULTY OF

ALFRED UNIVERSITY

IN PARTIAL FULFILLMENT OF THE REQUIREMENTS
FOR THE DEGREE OF

DOCTOR OF PHILOSOPHY

IN

CERAMICS

ALFRED, NEW YORK

NOVEMBER, 2005

CRACK INITIATION BEHAVIOR OF OPTICAL GLASSES
FROM VICKERS INDENTATION

BY

TREVOR WILANTEWICZ

B.S. ALFRED UNIVERSITY (1996)

M.S. ALFRED UNIVERSITY (1998)

SIGNATURE OF AUTHOR_____ (Signature on file)_____

APPROVED BY_____ (Signature on file)_____
JAMES R. VARNER, ADVISOR

_____ (Signature on file)_____
WILLIAM C. LaCOURSE, ADVISORY COMMITTEE

_____ (Signature on file)_____
WILLIAM M. CARTY, ADVISORY COMMITTEE

_____ (Signature on file)_____
ARUN K. VARSHNEYA, ADVISORY COMMITTEE

_____ (Signature on file)_____
DOREEN EDWARDS, CHAIR, ORAL THESIS DEFENSE

ACCEPTED BY_____ (Signature on file)_____
ALASTAIR N. CORMACK,
DEAN, SCHOOL OF ENGINEERING

ACCEPTED BY_____ (Signature on file)_____
ALASTAIR N. CORMACK, DIRECTOR OF
THE GRADUATE SCHOOL, ALFRED UNIVERSITY

Acknowledgements

First, I would like to thank Dr. Varner for giving me the opportunity to work on such a wonderful topic and for providing helpful guidance and suggestions throughout. Thank you for having the patience to see this project to a completion, and for always helping me see the positive sides and outcomes of my work, even when experiments weren't going as planned. It was a privilege to work with such an excellent mentor, and a good friend as well.

I wish to thank all my thesis committee members for their helpful comments and suggestions, all of which made this thesis better. I would also like to sincerely thank Mr. George Quinn for thoroughly reading the entire first draft of the manuscript, and for providing invaluable comments and suggestions. I would also like to thank Prof. W. Roger Cannon at Rutgers University for allowing me time to finish writing this thesis while working there.

I would also like to sincerely thank Mr. Jim Thiebaud for his patient help in programming the test instrument used in this study. The many hours you dedicated to writing the program to function the way I needed it, for fixing things when they broke, and for answering all my questions about the instrumentation, has not been forgotten.

Finally, I would like to thank my entire family for their support throughout the writing of this manuscript. I would like to dedicate this thesis to my parents, who have supported me throughout this long period of time. Mom and Dad, thank you for all your encouragement and support when I needed it, and for keeping me on track to finish my work.

Table of Contents

List of Tables

List of Figures

Abstract

The crack initiation behavior of nine optical glass compositions was investigated in the current work. A recording microindenter equipped with optical observation and an acoustic emission detection system were used to monitor the crack initiation behavior in-situ from contact with a Vickers diamond.

Seven of the optical glasses had a deformation response that was shear-'flow' controlled, i.e., 'normal.' However, median-radial cracks formed readily on indenter loading. Thus, the popular notion that 'normal' glasses crack only on unloading, for relatively small loads, does not apply to these glasses. The two remaining optical glasses behaved 'anomalous' in the sense that compaction was the main indentation response, with accompanying ring-cone cracks, particularly at higher loads.

The quantities G/K (shear modulus/bulk modulus), E/H_V (Young's modulus/Vickers hardness), and RO_2 (RO_2 = moles RO_2/moles $RO+R_2O$) were found to govern the overall cracking behavior of the glasses examined. The ratio G/K was found to characterize a glass's relative tendency to undergo shear-'flow' vs. volume compaction (densification), and hence 'normal' or 'anomalous' behavior, respectively. The ratio E/H_V correlated with the relative plastic zone sizes and crack driving force around the indentations. In general, higher amounts of RO_2 were correlated with increased resistance to median-radial cracking. Glasses with G/K less than ≈ 0.6, E/H_V greater than ≈ 14, and RO_2 less than ≈ 2.0, tended to form median-radial cracks readily on indenter loading, while glasses with the opposite characteristics tended to form median-radial cracks primarily on unloading. Glasses with either tightly packed structures, characterized by relatively high density, little interstitial free volume, low G/K, and high E/H_V, or weak, loosely held structures, sheared readily beneath the indenter, generating large strains and stresses, and consequently median-radial cracked at low loads on indenter loading. Both glass types had low RO_2 and lacked a true three-dimensional network structure. For tightly packed structures the lack of open space, even in glasses with strong intrinsic bonds, resulted in shear-'flow' as the only means to accommodate the indenter. Weak, loosely held structures, even those with relatively low density, preferred to shear, since this offered the least resistance to deformation.

1.   INTRODUCTION

1.1   Significance of Work

As demonstrated by Griffith[1], the presence of small flaws on the surface of glass significantly degrades its strength. Other workers have since verified Griffith's original findings concerning surface flaws and glass strength.[2-4] On the contrary, processes such as glass lapping and grinding benefit from the removal of material associated with contact damage from sharp particles.[5-6] Understanding the mechanisms surrounding contact damage of glass, and the influence that glass composition, structure, and contact parameters have, is thus desirable. In addition, understanding contact damage of glass in relation to other mechanical properties and characteristics would be useful as well. Perhaps new and useful glass compositions, applications, or more efficient processing procedures can be realized from such studies.

1.2   Review

Past work has shown that deformation and crack initiation behavior of glass are strongly related to the glass composition.[7-12] These studies have mostly examined the deformation and cracking behavior associated with the penetration of a 'sharp' indenter into the material. Recently, Wagner[9] was able to identify changes in crack initiation behavior using a Vickers diamond

with changes in glass composition, for three commercially important glass systems: soda-lime-silicate, sodium-borosilicate, and sodium-aluminosilicate. A transition in deformation and crack initiation behavior from 'normal' to 'anomalous' was observed with changing glass composition for each series of glasses investigated. Wagner's study was the first to systematically investigate the dependence for several series of glasses and identify, though only approximately, a transition in deformation and cracking behavior.[9]

More recently, Canfield[10] has shown that crack initiation loads in 'normal' behaving silicate glasses, determined by recording microindentation, are strongly dependent on the glass 'brittleness' index, given by the ratio of hardness to fracture toughness, after Lawn and Marshall.[13] Several mixed-alkali and mixed-alkali/mixed-alkaline-earth glass series were studied by Canfield[10].

Regarding glass 'brittleness,' Sehgal and Ito[14] have developed what they term a 'less-brittle' glass in the soda-lime-silica system. Their work brings to light the topic of glass 'brittleness,' how it is defined and measured, and to what extent it can be correlated to other glass characteristics, such as crack initiation. The low 'brittleness index' was correlated with an increased resistance to crack formation from Vickers indentation testing, as well as to damage from scratch testing, compared to 'standard' soda-lime-silica compositions, including commercial soda-lime-silica glass. A closer

examination of the meaning of brittleness, and how it relates to crack initiation behavior of other glass compositions thus seems necessary.

In Wagner's work the transition from 'normal' to 'anomalous' cracking behavior was also dependent on the maximum indentation load used, for all three glass series investigated.[9] In addition, the transition was thought to be affected by the loading rate for one of the borosilicate glasses. The current work investigates crack initiation behavior of glass compositions not previously studied, and tries to relate this behavior to glass composition, structure, and important glass properties and characteristics such as hardness, fracture toughness, and elastic modulus. With regards to glass 'brittleness,' one of the challenges which remains is how to define and measure it, and determine what other characteristics of glass it relates to.

1.3   Experimental Approach

Past research into crack initiation of glass, which was briefly summarized, has pointed to the need for further study. In the current work, knowledge of the effects of glass composition and structure on crack initiation is greatly enhanced. This is done by examining thoroughly the past work, and by testing new glass compositions.

In the current work crack initiation testing was carried out using a Vickers diamond indenter. The geometry of this indenter lends itself to the formation

of cracks at relatively low forces, and the resulting fracture patterns are typical of those observed from particle impact with glass surfaces.[15-17]

The central theme of investigating a composition-structure relationship with crack initiation behavior of glass, and correlating this relationship with important glass properties, characteristics, and testing conditions, is the purpose of this work. To summarize, the main objectives of the current work are:

1. To further investigate the effect of glass composition and structure on crack initiation behavior of glass.
2. To further investigate possible relationships between mechanical properties and characteristics of glass, and crack initiation behavior.
3. Develop a model to explain crack initiation behavior in glass.

2.   REVIEW AND THEORY

2.1   The Elastic-Plastic Stress Field

When a Vickers diamond is pressed into glass, elastic (reversible) and plastic (irreversible or permanent) deformation ensue immediately.[18] The term 'plastic' is not being used to indicate the manner in which the deformation was created, i.e., by movement (slip) of dislocations, but is frequently used when discussing indentations in glass. Since glasses lack dislocations, plastic flow, i.e., dislocation motion, is not possible.

The complex elastic-plastic stress field that develops when a sharp indenter contacts glass has been studied by Johnson[19], Lawn et al.[20], Lawn and Evans[21], Evans[22], Perrot[23], Chiang et al.[24], Yoffe[25], and Cook and Pharr[11], to name a few exceptional studies. The resulting stress field under indenter loading is a composite consisting of both elastic and plastic (residual) contributions.[21,26] Although there are differences between the models, a general picture emerges in the analyses.

Upon pressing a sharp indenter into glass a roughly hemispherical zone of irreversible deformation forms beneath the contact site. The size of this plastic zone scales with the contact dimension, a. Experimental results confirm the general shape of the deformed zone in glass is approximately a hemisphere.[7-8] A schematic illustrating the general features is shown in Figure 1, using the model of Lawn et al.[20] At full loading, Figure 1a, the

(a) Full Loading
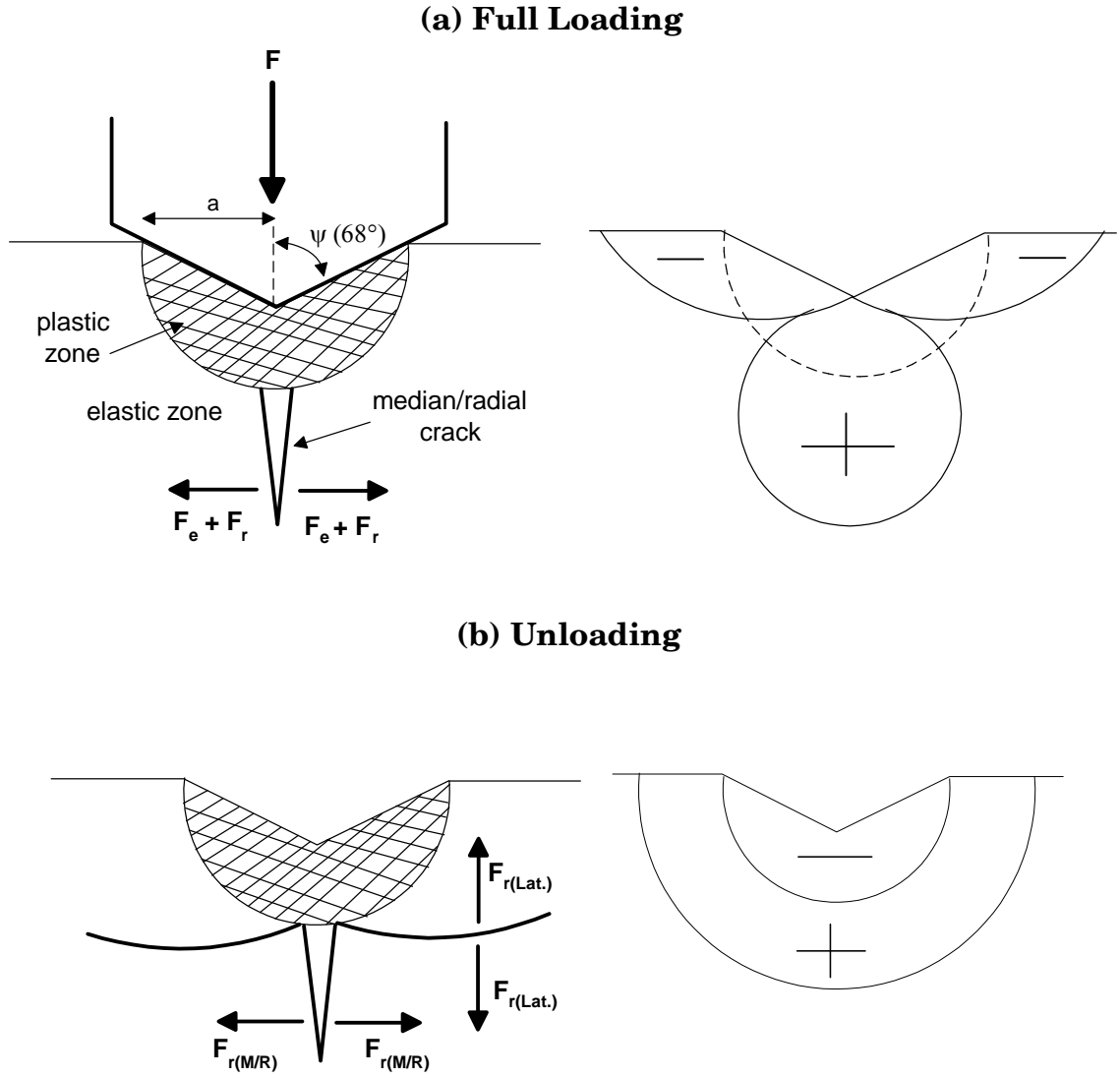
(b) Unloading

Figure 1. *Schematic illustrating the composite elastic-plastic field under full indenter loading (a) and after complete unloading (b). Negative signs designate compression, and positive signs tension. F_r is the wedge-opening force due to the residual stress field, and wedges open the lateral and median-radial (M/R) cracks, particularly on unloading. F_e is the elastic force which also wedges open median-radial cracks on loading. After Lawn et al.[20]*

stress field is a composite consisting of *elastic (reversible)* and *plastic (irreversible)* contributions. The elastic field is taken to operate outside the plastic zone. Near the surface the principal normal stresses are compressive, while beneath the surface they are tensile. The indenter half-angle of 68° (between *opposite* faces of diamond) represents a Vickers diamond.

The residual stress component is tensile at the surface, but the elastic stresses are compressive and dominate, hence the net stress at the surface is compressive on loading.[26] The residual stress field develops because of strain incompatibility between the elastic and plastically deformed regions, and remains near maximum intensity after complete load removal.[26] If loads are sufficiently high, a median-radial crack may initiate on loading somewhere beneath the surface in the tensile region along the elastic-plastic boundary, however remaining constrained by the surface compressive stresses. Lawn and Evans[21] believe this occurs near the bottom of the plastic zone, where the tension is presumed highest.

On unloading the indenter the compressive stresses at the surface diminish, causing the net tensile stress from the residual field to increase. Any median-radial cracks which formed on loading may close slightly beneath the surface as the load is removed, while simultaneously 'breaking-through' to the free surface which is now under increasing tensile stress. If no median-radial cracks form on loading, the residual stress may be intense enough to initiate median-radial cracks on unloading. Lateral cracks are also

observed to form at the base of the elastic-plastic boundary near complete unloading.[20]

The initiation and propagation of indentation cracks after indenter removal is due to the residual stress field, while crack initiation and propagation on loading occurs from the stress field made up of elastic plus plastic contributions, i.e., the superposed stress field.[18] During unloading, the residual field is responsible for the initiation and propagation of cracks, since the elastic field continually decreases as load removal progresses. The residual stress component remains at near maximum intensity after complete unloading, while the elastic component decreases to zero.[20]

The sequence of cracking events just described pertains mainly to 'normal' glasses. There are also 'anomalous' glasses, whose crack initiation behavior is different. The deformation and fracture behavior of both types of glasses will be described in more detail shortly. The intensity of the residual stress field, like the elastic stress field, presumably scales directly with the material hardness (mean contact pressure), and thus for Vickers indentation, where in principal the hardness should be independent of the applied load (geometric similarity), the intensity of the residual stress should also be independent of the applied load.[21] As seen in Figure 1 (b), the plastic zone is in compression after complete load removal, while the surrounding material remains in tension, propagating any median-radial and/or lateral cracks which may have initiated.

2.2   Deformation of 'Normal' and 'Anomalous' Glasses

2.2.1   'Normal' Glasses

In indentation testing, 'normal' glasses are defined as those whose main mode of permanent deformation is an inhomogeneous shear-induced faulting ('flow') of material.[7] The term 'normal' was originally used to describe glasses with high thermal expansion coefficient, a negative dependency of bulk modulus on temperature, and a positive dependency of bulk modulus on pressure, since most glasses exhibit this behavior.[27] Wiederhorn et al.[27] found that 'normal' glasses exhibited slow crack growth prior to catastrophic failure in controlled-crack-growth experiments, unlike 'anomalous' glasses, which just failed abruptly.

As shown by Arora et al.[7] and Peter[12], a minimum amount of network modifier ions is needed to cause this mode of deformation. That is, the composition of a glass determines to a large extent whether a glass behaves 'normal' or 'anomalous.' The deformation of 'normal' glasses is assumed to occur at constant volume, and to be reconstructive, i.e., bonds are continuously being broken and reformed.[7] The shape of the deformed zone beneath Vickers indentations shows that the indentation volume is formed by radial movement of material outwards, giving rise to the hemispherical shape of the deformed zone (see Figure 1).

Doremus[28] lists five different types of deformations that can occur in materials. They are elastic, anelastic, viscous, plastic, and faulting. According to Doremus, densification in indentation testing of glass is anelastic deformation, in which part or all of the densification can be removed by heating, but that network bonds are not broken.[28] Since the viscosity of glass at room temperature is greater than 10^{59} P, Doremus dismisses viscous flow as a possible deformation mechanism in indentation of glass at room temperature.[28] Since glass lacks dislocations, plasticity can not operate either. Doremus[28] believes the permanent impressions in 'normal' glasses are due to 'faulting' of the material, after the work of Hagan.[29] Faulting is a type of deformation that is non-recoverable and non-uniform. The 'flow' in normal glasses can thus be described as 'faulting,' since it resembles geologic faulting.[28] The fact that fault lines follow high shear stress trajectories suggests the high shear stresses associated with sharp indentation cause the faulting.[18]

Hagan[29] has shown that a series of lines, which he termed 'flow' lines, occurs beneath indentations in 'normal' glasses. The lines intersect one another at ~ 110°, not at 90°, as observed in materials undergoing pure plastic flow.[29] According to Hagan, this is evidence the 'flow' is not like that occurring in metals, possibly due to the effects of densification. Further, he believed the 'flow' lines were caused by genuine shear displacements, and were not cracks, judging by the small width of the lines, ~ 2 µm. Doremus[28]

points out the fault planes are distorted regions of the structure, and that not all bonds may reform back into the original structure. Evidence of these faults also appears on the surfaces of indentations, where they are observed to lie parallel to the indentation sides, and are the continuations of the sub-surface faults.[7,30]

As noted by Ernsberger[31], the nature of the actual deformation in 'normal' glasses is still a matter of controversy. Plasticity at room-temperature, such as can occur in metals, is due to the motion of dislocations. Thus movement by plasticity in glasses, which lack dislocations, is not possible. In addition, Neely[32] has shown that viscous flow is unlikely to occur during room-temperature indentation of silicate glass, since the glass viscosity is too high in spite of the large shear stresses present. Nonetheless, network modifiers and associated non-bridging oxygen's (NBO's) facilitate shear movement due to the weakness they introduce into the structure, providing easy 'slip' paths, since in vitreous silica few faults are observed.[7] Peter[12] has shown convincing evidence of material 'pile-up' around indentation edges of 'normal' glass indented with a sharp indenter. It is hard to imagine shear faulting causing this behavior, with the only other possible mechanism being viscous flow.

Although the deformation in normal glasses is assumed to occur at constant volume, i.e., be volume conserving, Ernsberger[31] has shown that densification does occur beneath Vickers indentations in soda-lime-silica

glass, and in borosilicate and vitreous silica glasses as well. In high-pressure experiments, Bridgman and Simon[33] found that additions of Na_2O, up to 33 mol % in vitreous silica, still resulted in densification of the glass. Increasing the molar amount of Na_2O from 10 to 23 to 31% caused the percent increase in density to decrease from 8.7% to 3.5% to 0.7%, respectively, for a pressure of ~ 110,000 atmospheres (~ 11.1 GPa). In comparison, the densification of vitreous silica at 100,000 atmospheres was about 0.1%, much less than for the 10% Na_2O glass, where the threshold pressure for densification was about 40,000 atmospheres (~ 4.1 GPa). Mackenzie[34] showed that the amount of shear deformation taking place in glass strongly affects the amount of densification achievable. Increasing shear results in increasing densification. This may help explain why the addition of 10% Na_2O increases the percent densification relative to vitreous silica, i.e., the Na^+ ions facilitate the shear taking place. However, further additions of Na^+ ions take up interstitial space which would otherwise compact (densify), and occurs to the extent that it dominates the shear effect, with the result that percent densification begins to decrease. Bridgman and Simon[33] also found that increasing the cation radius decreased the percent densification achievable, likely because of the greater reduction in interstitial space with the larger cations. For 23 mol % additions of Li_2O, Na_2O, and K_2O to vitreous silica, the percent densification was 6.9%, 3.5%, and 1.2% , respectively.[33]

2.2.2 'Anomalous' Glasses

'Anomalous' glasses in indentation testing are those whose main mode of permanent deformation is a pressure-induced densification (compaction) of a relatively open network.[7] The term 'anomalous' was first used to describe glasses having a low coefficient of thermal expansion, a negative dependence of bulk modulus on pressure (for pressures up to ~ 40 Kbar for vitreous silica (v-SiO_2), after which normal behavior occurs), and a positive dependence of bulk modulus on temperature (between 0 and 60 K for v-SiO_2).[27,35] The structural change can be described as a displacement transformation in which individual structural units, e.g., SiO_4 tetrahedra, become closer.[7] Spatial rearrangement of the structural units occurs, but few bonds are broken. Vitreous silica is the prototypical 'anomalous' glass. 'Anomalous' glasses tend to have open network structures. For v-SiO_2, it is believed the transverse bending vibrational modes of the Si-O-Si linkages between SiO_4 tetrahedra are primarily responsible for its 'anomalous' behavior[7]. Ernsberger[31] and Arora et al.[7] have observed densification in vitreous silica around Vickers indentations. Other glasses that behave 'anomalous' include v-GeO_2, v-BeF_2, and v-$Zn(PO_3)_2$.[7]

Bridgman and Simon[33] have found that vitreous silica begins to densify starting at pressures around 100,000 atmospheres (~ 10.1 GPa). The percent densification rose rapidly to about 7% at 200,000 atmospheres. According to Neely[32] the Vickers hardness of vitreous silica is around 6.2 GPa (200 g

indentation load); thus, based on the threshold pressure for densification from Bridgman and Simon[33] densification would not be expected to occur under Vickers indentation. However, Mackenzie[34] has shown that increasing the amount of shear stress present facilitates the densification process, making higher densities achievable. Thus, the high shear stresses present in indentation testing must lower the threshold for densification.

2.3   Fracture Geometry of 'Normal' and 'Anomalous' Glasses

Several different crack geometries can be distinguished in indentation testing of 'normal' and 'anomalous' glasses with a Vickers diamond indenter.[11] Other crack morphologies may form that do not fit into any of the classifications listed below, but are cracks nonetheless. The ring-cone crack usually forms in 'anomalous' glasses, and is characterized by a surface ring crack which flares out into a cone-shaped crack below the surface. The system is referred to as the ring-cone crack system. The median-radial crack can form either on indenter loading or unloading. When forming on loading, the initial shape of the crack resembles a full-penny, but the crack eventually breaks through to the specimen surface, in which the geometry changes to that of a half-penny. If a median-radial crack forms on indenter unloading, the initial shape may more resemble that of a half-penny. In either case, the final geometry is almost always half-penny.[11] Two mutually orthogonal sets of median-radial cracks usually form. Lateral cracks form at the base of the

plastic zone and spread out sideways, remaining mostly parallel to the free surface, but show some slight upward curvature at their ends. Shallow lateral cracks form closer to the specimen free surface than ordinary lateral cracks and frequently chip away material, leaving behind a scalloped-out impression. To summarize, the most prevalent crack systems observed in glass are:

1. Ring-Cone
2. Median-Radial
3. Lateral
4. Shallow Lateral

Palmqvist cracks, also known as *radial cracks*, are usually found in tougher crystalline ceramic materials, such as cemented carbides.[36] These cracks are distinguished from median-radial cracks by their shallow depth, which does not exceed the plastic zone depth. In this work, the term 'radial' in 'median-radial crack' is used to emphasize that these cracks radiate out from the indentation. The dominant cracks found in 'normal' glasses are the median-radial and lateral types. In 'anomalous' glasses the dominant crack system is usually the ring-cone, but median-radial and lateral cracks also initiate. The tendency for shallow lateral cracking and surface chipping of material is high in 'anomalous' glasses as well. Figure 2 schematically illustrates the dominant crack systems found around sharp indentations in glass.

A) Ring-Cone

B) Median-Radial

plastic
zone
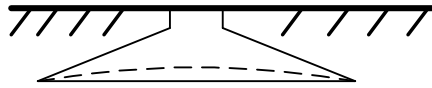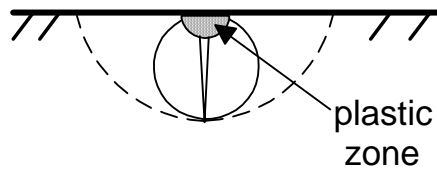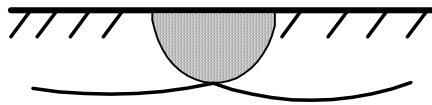
C) Lateral

Figure 2. *Schematic drawings showing the cross-sections of three major crack systems which develop in sharp indentation testing of 'normal' and 'anomalous' glasses: A) Ring-Cone, B) Median-Radial, and C) Lateral. Shallow lateral crack system not shown.*

2.4 Crack Initiation Sequence of 'Normal' and 'Anomalous' Glasses

The crack initiation sequence in 'normal' and 'anomalous' glasses indented with a Vickers diamond is well documented.[7,9,11,18] A summary of the important features are described below.

2.4.1 'Normal' Glasses

<u>Loading Cycle</u>

(i) Elastic-plastic deformation ensues upon contact of the Vickers indenter.

(ii) The size of the indentation and plastic zone grow with increasing load.

<u>Unloading Cycle</u>

(iii) At a critical point in the unloading cycle, median-radial cracks initiate (pop-in) and continue to extend with decreasing force.

(iv) At or near complete unloading, lateral cracks initiate near the base of the plastic zone and grow outwards, mostly parallel to the surface, but turning upwards slightly.

There are several exceptions to this sequence. Most notable is the formation of median-radial cracks on the *loading* cycle when indentation loads are sufficiently high. Arora et al.[7] and Lawn and Swain[37] found median-radial cracks initiated on loading in soda-lime-silica glass for high-enough loads. The median-radial cracks initiate somewhere below the surface along the elastic-plastic boundary, and continue to grow below the surface with increasing contact force. On unloading the median-radial cracks may show some closure, followed by breakthrough to the free surface, and growth along

the surface, resulting in a final half-penny geometry. For soda-lime-silica glass Arora et al.[7] found the critical pop-in load to be about 40 N (4.1 Kg). Still another variation in the sequence of initiation is when median-radial cracks break through to the surface on loading. Lawn and Swain[37] observed a median-radial crack to break through on indenter loading at around 500 N (51 Kg) force in soda-lime-silica glass.

2.4.2 'Anomalous' Glasses

Loading Cycle

(i) Elastic-plastic deformation ensues upon contact of the Vickers diamond.

(ii) At a critical force a ring-cone crack pops-in around the contact perimeter, and the cone crack grows downward with increasing force.

(iii) As loading continues multiple ring-cone cracks initiate and grow, with earlier ring-cone cracks being engulfed by the expanding impression and ceasing in their growth. A dominant ring-cone crack usually emerges and grows the most.

(iv) Median-radial cracks initiate and grow if loads are high enough.

Unloading Cycle

(v) One or more cone cracks begin to close and possibly heal slightly. A portion of the cone below the surface detaches from the rest of the cone.

(vi) Lateral and shallow lateral cracks initiate and grow.

(vii) Any median-radial cracks that formed on loading may close slightly, and additional median-radial cracks may initiate.

The above sequence was based on observations of crack initiation in vitreous silica by Cook and Pharr[11] and Arora et al.[7] Cook and Pharr noted

the formation of shallow laterals on unloading, while Arora et al. didn't. Cook and Pharr also pointed out that lateral crack initiation took place at higher loads on unloading in vitreous silica compared to soda-lime-silica glass (~ 33% of P_{max} compare to ~ 2% P_{max}, respectively). In addition, Cook and Pharr saw another set of smaller cracks, secondary radial cracks, initiate just after the shallow lateral cracks, though Arora et al. didn't observe this. Wagner[9] observed that when median-radial cracks initiated on unloading in vitreous silica, they did so accompanying partial closure of the cone crack. Arora et al.[7] suggest that in 'normal' glasses crack nuclei are formed along shear planes in the deformation zone beneath the contact site, and are responsible for median-radial crack initiation. However, in 'anomalous' glasses the densification (compaction) must generate enhanced elastic tensile stresses at the surface, which favors ring-cone crack initiation. It is apparent that glass composition and structure significantly influence the dominant deformation mechanism, and in turn the crack initiation behavior. However, indentation with a blunt indenter, so called Hertzian indentation, in which the contact is mainly elastic, produces ring-cone cracks in both 'normal' and 'anomalous' glasses, showing that indenter geometry is equally important in determining the deformation and fracture response of glass.[18]

2.5   Crack Initiation Models

A number of models have been put forth to describe how crack initiation occurs in brittle materials contacted with a sharp indenter. Several of the most notable models are described below. The initiation of cracks in glass involves two variables: flaws (crack nuclei) and stress. When a certain critical level of stress is reached at the tip of a flaw, a crack will initiate. Thus, the stress intensification of flaws to a critical level, close to the intrinsic cohesive strength of the material, results in crack initiation. In general two classes of models exist, those based on initiation from pre-existing flaws in the material, and those based on initiation from flaws generated by the contact process itself. The latter models seem to best describe crack initiation in glass from sharp indenters, where experimental evidence suggests the flaw population giving rise to cracks is created by the contact process itself.[30,38]

2.5.1   Pre-Existent Flaw Model

This model was proposed by Lawn and Evans.[21] It is based on the initiation of median-radial cracks beneath the surface, along the elastic-plastic boundary, from *pre-existing* flaws (crack nuclei) in the bulk of the specimen. Lawn and Evans assumed that crack initiation occurs when the stress intensity factor on a flaw reaches the critical stress intensity factor,

i.e., the fracture toughness (K_C), of the material. Since the principal normal tensile stress would be highest along planes containing the loading axis, and along an indentation diagonal, cracks would initiate collinear with the indentation diagonals, a prediction born out by direct experimental observation of the indentation process.[7,11,18,38] It is assumed that the indentation diagonals locally elevate the tensile stress because of their sharpness. By taking into account the spatial extent of the tensile field with indentation force, and using the stress intensity expression valid for an elliptic flaw being wedged open by a point force concentrated at the center of indentation, expressions for the critical force and flaw size for median-radial crack initiation were derived by Lawn and Evans:[21]

$$F_C = \left(\frac{54.47\alpha}{\eta^2 k^4} \right) \left(\frac{K_C}{H} \right)^3 K_C \tag{1}$$

$$c^* = \left(\frac{1.767}{k^2} \right) \left(\frac{K_C}{H} \right)^2 \tag{2}$$

where,

F_C = critical initiation force

α = const. (= 2 for Vickers diamond)

k = const. (= 0.2 for Vickers diamond)

η = const. (= 1 for Vickers diamond)

c^* = critical flaw size

K_C = critical stress intensity factor

H = Hardness

According to this model, the ratio (K_C/H) emerges as a controlling factor in determining the critical conditions. Materials with high fracture toughness and low hardness are predicted to have high crack initiation resistance; however, Lawn and Evans did not make actual measurements of the critical forces on materials. Lawn and Evans[21] showed that, for very small flaws, initiation would never take place no matter the contact force, simply because the stress intensity would never build to the critical level. For intermediate-sized flaws, spontaneous unstable crack development ('pop-in') would occur. For large flaws, a median-radial crack would initiate stably, i.e., no abrupt 'pop-in' event would be detected. In addition, no flaws regardless of their size were predicted to propagate for contact forces below F_C.

2.5.2 Intersecting Fault Line Model

Hagan[29] believes that crack initiation in Vickers indentation of glass is caused by the need to accommodate plastic strains at intersecting shear fault lines. He shows evidence in soda-lime-silica glass for initiation along and at the intersection of fault lines, where kinks and voids can form causing local stress intensification. The intersections of fault lines can result in no kinking, a kink in one line, or a kink in both lines. The last two processes can lead to void (crack nuclei) formation. The actual mechanisms generating these lines remains obscure, but Hagan suggests that local variations in density or chemical composition may be nucleation sites. Network modifying

ions provide local weakness in the glass structure, and thus faulting could be initiated at one of these weak regions. Subsequent faulting then takes place by a dilation of the structure in a localized region about the fault line. According to Hagan median-radial and lateral cracks were seen to initiate from intersecting fault lines close to the elastic-plastic boundary.[29]

2.5.3   Lawn, Dabbs, and Fairbanks Model[38]

The model of Lawn et al.[38] provides a comprehensive picture of median-radial crack initiation from Vickers indentation in soda-lime-silica glass. The effects of maximum indentation force, contact duration (loading rate), temperature, and water were studied. Their work shows that these variables influence the overall crack initiation behavior. Key points from their work are summarized below:

1. Median-Radial crack initiation is contact-time dependent:

(i) For long contact durations, cracks pop-in on unloading, during indenter contact.

(ii) For short contact durations, cracks pop-in *after* complete indenter removal, with considerable time delay.

2. Time is needed to develop a critical nucleus:

(i) Increasing environmental water content reduces the time-to-initiation, which is highly water sensitive, causing cracks to form sooner on unloading, for fixed total contact time.

(ii) Increasing the peak contact load also reduces the time-to-initiation, for fixed total contact time.

(iii) At large enough contact times, the time-to-initiation is independent of

peak contact load, for fixed total contact time.

3. **Entry of water into shear fault interfaces causes breaking of Si-O-Si bonds and formation of Si-OH. Water diffuses in from top surface of indentation.**

(i) Rate dependence of pop-in depends on rate of diffusion and subsequent reaction of water, i.e., a two-step process is at work.

(ii) Increasing temperature increases activity of water, and hence time-to-initiation decreases, for fixed total contact time.

(iii) For short contact durations the time-to-initiation decreases as moisture content increases; however, for long contact durations it is independent of moisture content.

Lawn et al.[38] believed the increase in peak contact force increased the size of the shear faults, without increasing the shear stress on the fault interfaces (geometric similarity in the stress field), thus making diffusion and reaction of water easier, and hence decreasing the time-to-initiation. They concluded that initiation of median-radial cracks in soda-lime-silica glass was a two-step process. The first step is the creation of shear faults, followed secondly by median-radial crack initiation from a severe fault close to the surface. This was based on in-situ optical observation of the initiation process from beneath the contact site using an inverted microscope, and post-test SEM (scanning electron microscope) examinations.

<u>(1. Shear Fault Formation)</u>

According to Lawn et al.[38] as the Vickers indenter displaces into the sample a series of faults are 'punched' into the material, which are mostly contained within the contact impression. The faults arise due to high shear stress along the indenter/sample interface. Longer faults are expected to form as contact forces increase, since the length of the diamond edge in contact with the specimen increases with contact force. The faults are the result of intermittent shear failure occurring at levels close to, or at, the theoretical shear strength of the material. As noted by the authors from their SEM observations, minor slipping occurs between major catastrophic shear failures.[38] As penetration proceeds, newly formed faults are overtaken by the expanding contact. Minor stress relief accompanying major shear failures likely occurs, only to rebuild as indentation proceeds.[38]

<u>(2. Median-Radial Crack Initiation)</u>

A median-radial crack then initiates when a critical level of stress intensification is reached along a suitably located shear fault. According to Lawn et al.[38] initiation is most likely to occur from a location near the surface of an outer fault. The researchers cite two ways in which the stress intensification could be achieved:[38] **(i)** *Sub-critical growth of a microcrack,* **(ii)** *Interfacial debonding of a critical shear fault.* In mechanism (i) the

kinetics would be controlled by stress-enhanced corrosion by available water in the environment. Although this would likely take place in a tensile region of the stress field, the researchers acknowledged this could initially take place in a mixed field of shear and tension. In mechanism (ii) the crack is assumed to start from a fault, but with the decohesion of the fault itself, driven by the shear stress across it, being the rate-controlling process.[38] The researchers could not determine which of the two mechanisms was controlling the crack initiation behavior they observed.

2.6   Crack Initiation Resistance and the Loading/Unloading Indentation Cycle

In recording microindentation testing the load and displacement depth of an indenter pushing into a material are simultaneously recorded. On the loading cycle, the initiation of cracks at higher loads in one glass compared to another indicates increased resistance to crack initiation. On unloading, however, the opposite is true. The initiation of cracks at lower loads on the unloading cycle indicates increased resistance to crack initiation. As the load is removed, the net tensile stresses near the surface increase, while the elastic compressive stresses decrease. This is because the residual stress component is tensile at the surface and retains its maximum value at all times during testing. Thus at any fixed location near the surface, the net tensile stresses will increase as the compressive elastic stresses at that location decrease as the load is removed. Thus a glass which needs to be

unloaded to a smaller load compared to another glass, in order to raise the stress to the critical level, is more resistant to crack initiation.

2.7 Compositional Dependence of Crack Initiation Behavior

2.7.1 'Normal' and 'Anomalous' Glass Compositions

Table I summarizes the deformation and fracture behavior of normal and anomalous glasses. A list of glass compositions and corresponding crack initiation behavior obtained from work by previous researchers is presented in Tables II and III. The data represent a diverse group of *silicate* glasses. The compositions are expressed in normalized molar amounts, where each component is normalized to the amount of RO + R_2O, i.e., the alkali and alkaline-earth components, as such:

$$\mathbf{RO_2} = \text{moles } RO_2 / \text{moles } (RO+R_2O)$$

$$\mathbf{R_2O_3} = \text{moles } R_2O_3 / \text{moles } (RO+R_2O)$$

$$\mathbf{RO} = \text{moles } RO / \text{moles } (RO+R_2O)$$

$$\mathbf{R_2O} = \text{moles } R_2O / \text{moles } (RO+R_2O)$$

$$\mathbf{R_2O_5} = \text{moles } R_2O_5 / \text{moles } (RO+R_2O)$$

The RO_2, R_2O_3, and R_2O_5 components are generally considered to be glass network-formers, while the RO and R_2O components are generally considered as glass network-modifiers.[35]

Table I. Deformation and Fracture Characteristics of 'Normal' and 'Anomalous' Glasses.

Glass Type	Primary Deformation Mechanism	Major Crack Systems	Primary Fracture Occurrence
'Normal'	shear-induced faulting (mostly volume conserving)	median-radial and lateral	on indenter *unloading*
'Anomalous'	pressure-induced densification/compaction (mostly volume shrinkage)	ring-cone and median-radial	on indenter *loading*

Table II. Normalized Glass Compositions of Wagner.[*]

Researcher and Glass	Glass Type	RO_2	R_2O_3	RO	R_2O	$RO+R_2O$
Wagner [9] *Soda-lime-silicate*						
SLS com	**N**	2.91	0.04	n/a	n/a	1.00
SLS 76	**N**	3.63	0.01	n/a	n/a	1.00
SLS 80	**N**	4.71	0.01	n/a	n/a	1.00
SLS 82	**A**	5.38	0.01	n/a	n/a	1.00
SLS 85	**A**	6.44	0.01	n/a	n/a	1.00
Borosilicate						
BSL 300	**N**	3.31	0.31		1	
BSL 200	**N**	3.16	0.47		1	
BSL 100	**N**	5.96	0.98		1	
BSL 75	**N**	5.05	1.35		1	
BSL 50	**A**	7.56	2.13		1	
BSL 25	**A**	14.21	3.62		1	
Aluminosilicate						
ALS 25	**N**	4.28	0.24		1	
ALS 50	**N**	2.72	0.53		1	
ALS 100	**A**	5.61	1.02		1	
ALS 130	**A**	6.19	1.31		1	
Tandon and Cook[39]						
Aluminosilicate	**A**	3.00	0.47	0.29	0.71	
Borosilicate	**A**	15.54	2.96	0.14	0.86	

[*] After Wagner[9]. SLS = soda-lime-silicate, BSL = borosilicate, ALS = aluminosilicate. R_2O_3 in SLS glasses most likely contamination from alumina crucibles used to melt glasses.

Wagner, whose results are shown in Table II, found a transition from 'normal' to 'anomalous' crack initiation behavior in the three series of glasses he examined.[9] In terms of the normalized network former (NNF) ratio, which will be defined here as **$RO_2+R_2O_3+R_2O_5$**, the transition ranges were:

(i)   soda-lime-silicate: **$RO_2+R_2O_3$: 4.72 to 5.39** (N) → (A), respectively

(ii)   sodium aluminosilicate: **$RO_2+R_2O_3$: 4.52 to 6.63** (N) → (A), respectively

(iii)   sodium borosilicate: **$RO_2+R_2O_3$: 6.94 to 9.69** (N) → (A), respectively

It is recognized this classification may not always be accurate due to specific structural considerations. For example, when $[R^+]/[Al] < 1$, or $[R^{2+}]/[Al] < 0.5$, not all Al^{3+} ions will be in network-forming positions.[35]

Although no median-radial cracks initiated on the loading cycle in any of the 'anomalous' glasses tested by Wagner except for a few in v-SiO_2, ring-cone cracking was observed in most of the 'anomalous' glasses when indented to 1400 g load (Cook and Pharr[11] found that median-radial cracks initiated on loading in the two 'anomalous' glasses they tested, v-SiO_2 and borosilicate glass).[9] The frequency of ring-cone cracking increased in all 'anomalous' glasses when the load was increased to 2 Kg. In three samples (BSL 50, SLS 82, and SLS85) no cone cracks were observed at 1400 g load; however, ring-

cone cracks did form when the load was increased to 2 Kg. That is, the
transition was dependent on the maximum load in these three samples.

Table III. Additional Normalized Glass Compositions.[*]

Researcher and Glass	Glass Type	RO_2	R_2O_3	RO	R_2O
Arora et al.[7]					
Borosilicate	A	20.58	3.40	0.00	1.00
Soda-lime-silica	N	2.60	0.044	0.48	0.52
Lead-alkali	N	3.45	0.13	0.37	0.63
Aluminosilicate	N	2.25	0.60	0.96	0.04
Cook and Phar[11]					
Borosilicate	A	24.43	1.57	0.11	0.89
Soda-lime-silica	N	2.82	0.07	0.59	0.41
Aluminosilicate	N	3.00	0.47	0.29	0.71
Cleary[40]					
Soda-lime-silica	N	2.80	0.04	0.51	0.49
Borosilicate	A	20.25	3.75	1.00	0
Canfield[10]					
Mixed Alkali/Mixed Alkaline Earth	N	3.00	0.00	0.40	0.60
Alkali/Mixed Alkaline Earth	N	2.70	0.00	0.37	0.63
Peter[12]					
Soda-silica	A	5.67	0.00	0.00	1.00
Soda-lime-silica	N	3.17	0.00	0.42	0.58
Hagan and Van der Zwaag[8]					
SLS 1	A	5.67	0.00	0.47	0.53
SLS 2	A	5.67	0.00	0.33	0.67
SLS 3	N	4.00	0.00	0.50	0.50
SLS 4	N	3.00	0.00	0.48	0.52
SLS 5	N	2.33	0.00	0.50	0.50
SLS 6 (commercial glass)	N	3.43	0.00	0.33	0.67

[*] 'A' for 'Anomalous' and 'N' for 'Normal' behavior. Data was compiled from past research, as indicated. SLS=soda-lime-silicate.

Wagner's work thus showed the transition from 'normal' to 'anomalous' behavior was affected by glass composition and maximum indentation load.

It is also apparent from Wagner's results that, as the normalized amount of network forming oxides (**RO$_2$** and **R$_2$O$_3$**) increase, the glasses become more 'anomalous.' For the soda-lime-silicate glasses, Wagner[9] found that below about 16 mol % alkali + alkaline-earth content, glasses are 'anomalous,' while above this amount they are 'normal.' The creation of non-bridging oxygen's (NBO's) in the structure likely facilitates shear flow, and thus 'normal' behavior results.

For the sodium-borosilicate glass series, when the molar ratio of Na$_2$O to B$_2$O$_3$ was 0.74 or greater the glasses were 'normal,' while below this value they were 'anomalous.' Wagner[9] suggested this is because at low relative sodium concentrations 3-fold-coordinated boron is converted to 4-fold-coordinated boron, with no NBO's created. However, once the sodium concentration is high, NBO's are created, and 'normal' behavior results.

For the sodium-aluminosilicate series, when the molar ratio of Na$_2$O to Al$_2$O$_3$ was greater than 1.0, the glasses behaved 'normal,' while 'anomalous' behavior resulted for a ratio of 1.0 or less. Wagner[9] suggested that at low relative concentrations of sodium all Al^{3+} ions are in tetrahedral, i.e., network-forming, positions in the glass structure, thus eliminating any NBO's and resulting in 'anomalous' behavior. At higher ratios extra Na$^+$ ions

exist, since all AlO_4 units are charge compensated, resulting in NBO formation and 'normal' behavior.

Thus in all three glass series the NBO content emerges as an important factor in controlling the crack initiation behavior. In general, higher NBO contents favor 'normal' behavior, while lower contents favor 'anomalous' behavior. But as pointed out by Wagner[9] two of the borosilicate glasses which were predicted to have no NBO's behaved 'normal.' He suggested this could be the result of inaccuracies in the structural model which was used to determine the NBO amount, or these glasses were phase-separated.

Data from other researchers also show similar dependence of the transition from 'normal' to 'anomalous' behavior.[8,10,12] Hagan and Van der Zwaag[8] found that soda-lime-silicate glass with **$RO_2 = 4.0$** was 'normal,' while one with **$RO_2 = 5.67$** was 'anomalous.' This range agrees fairly well with that found by Wagner, as do the results of Peter[12] shown in Table III.

Tandon and Cook[39] found that for aluminosilicate glass with **$RO_2 + R_2O_3 = 3.47$** the behavior was 'anomalous.' However, Wagner[9] found that for aluminosilicate glass with **$RO_2 + R_2O_3 = 4.52$** the behavior was 'normal.' The reason that a glass with a smaller NNF ratio would behave 'anomalous' compared to a glass with a much larger NNF ratio lies in the maximum indentation load used. Tandon and Cook[39] used an indentation load of ~ 3.1 Kg, while Wagner[9] used only 1.4 Kg. The effect of using a higher maximum

indentation load likely caused a transition from 'normal' to 'anomalous' behavior in the aluminosilicate glass of Tandon and Cook[39].

2.7.2   Crack Initiation Resistance and Glass Composition

Wada et al.[41] studied the crack initiation resistance of several series of silicate glasses by conventional Vickers indentation testing.   The load at which there was 50% median-radial cracking (an average of two corners exhibiting median-radial cracks) around an indentation after testing, was used as a measure of the crack resistance of each glass. Their data are shown in Table IV, along with the normalized glass compositions.   All the glasses studied by Wada et al.[41] behaved 'normal,' since according to the researchers no glasses exhibited ring-cone fracture. As shown in Figure 3, the glasses with higher normalized-network-former ratio in general show higher load at

Table IV. Cracking Data of Wada et al.[*]

Researcher and Glass	Glass Type	RO_2	R_2O_3	RO	R_2O	R_2O_5	Density (g/cm^3)	Load At 50% Crack Formation (g)
Wada et al.								
BSIL	N	7.46	2.57	0.00	1.00		2.30	1000
ALBSIL 1	N	7.73	1.37	0.20	0.80		2.38	800
ALBSIL 2	N	5.13	0.72	0.36	0.64		2.46	240
ALBSIL 3	N	2.01	0.56	1.00	0.00		2.59	110
ALSIL 1	N	2.50	0.43	1.00	0.00		2.61	150
ALSIL 2	N	2.79	0.05	0.46	0.54		2.48	60
LDSIL 1	N	3.26	0.03	0.45	0.55		3.05	63
LDSIL 2	N	2.76	0.09	0.49	0.51		3.21	60
LDSIL 3	N	2.58	0.09	0.57	0.43		3.20	32
LDSIL 4	N	1.97	0.00	0.83	0.17		4.31	28
ALSIL + P	N	6.21	1.40	0.14	0.86	0.08	2.45	800

[*]BSIL=borosilicate,   ALBSIL=aluminoborosilicate,   ALSIL   =   aluminosilicate,
LDSIL=lead silicate, ALSIL+P = phosphorous aluminosilicate.

50% crack formation, i.e., increased resistance to crack initiation. Figure 4 shows that as glass density increases, the tendency is for the load at 50% fracture to decrease. A large gradient in the initiation load centered at a density of ~ 2.5 g/cm^3 is apparent. From Table IV it is seen that glasses with the lowest densities tend to have the highest NNF amounts. This can be understood by considering that, as network-modifying ion concentration decreases relative to network-former concentration, there should be more open space in the glass structure, leading to lower density.

The crack initiation test results of Wagner[9] are shown in Figure 5. The normalized initiation load for the first median-radial cracks to initiate on unloading for the three glass series tested is shown as a function of the NNF ratio. In general, the glasses containing the highest normalized amount of network-forming oxide in each series, i.e., the 'anomalous' glasses, had greater resistance to median-radial crack initiation on unloading (lower normalized loads correspond to increased resistance to initiation). Wagner found that v-SiO$_2$ initiated median-radial cracks at ~ 14% of F$_{max}$ on unloading, which is near the lowest of the soda-lime-silicate glasses, although some median-radials were also seen on loading.

Closer inspection of Wagner's data revealed several more interesting trends regarding the crack initiation load and glass composition. For the soda-lime-silicate glasses, increases in the percent NBO content correlated with decreasing resistance to crack initiation, as shown in Figure 6. The
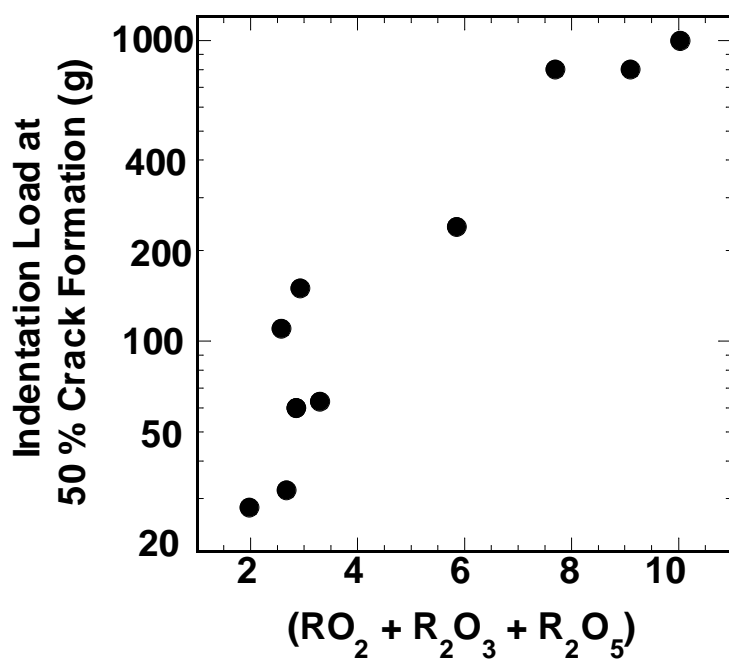
Figure 3. Indentation load for 50% crack formation as a function of the normalized-network-former ratio from the data of Wada et al.[41]
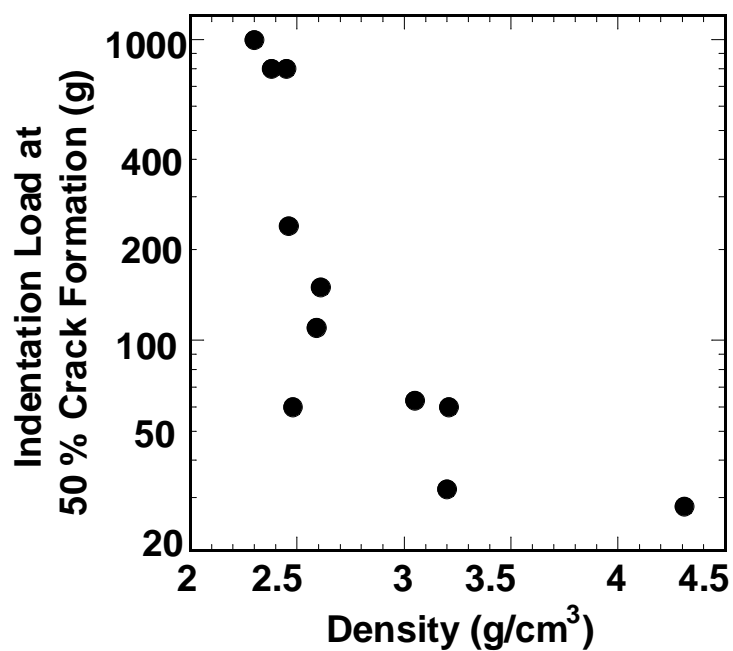
Figure 4. Indentation load for 50% crack formation as a function of the glass density from the data of Wada et al.[41]
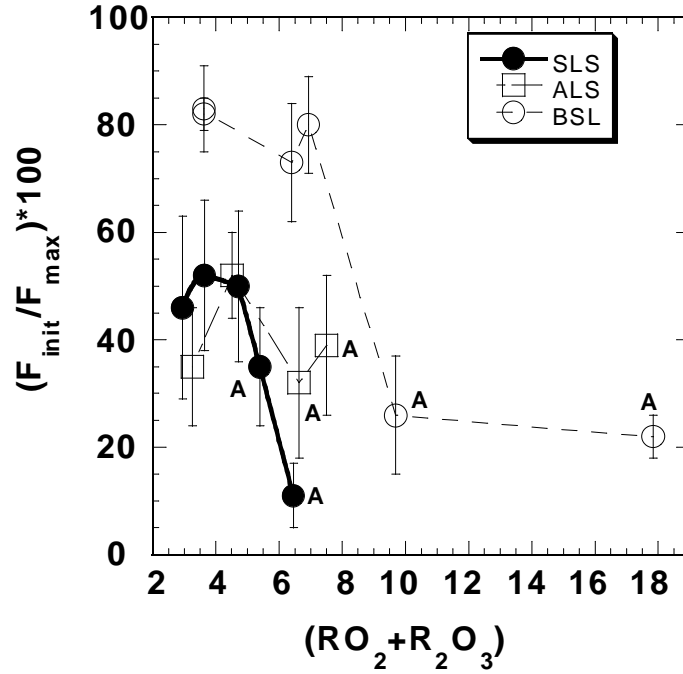
Figure 5. *The normalized initiation load for the first median-radial cracks to initiate on unloading as a function of the NNF ratio for the three series of glasses tested by Wagner[9]. 'A' indicates the 'Anomalous' compositions. Maximum indentation load was 1400 g. Curves are guides for the eye. Data from Wagner[9].*
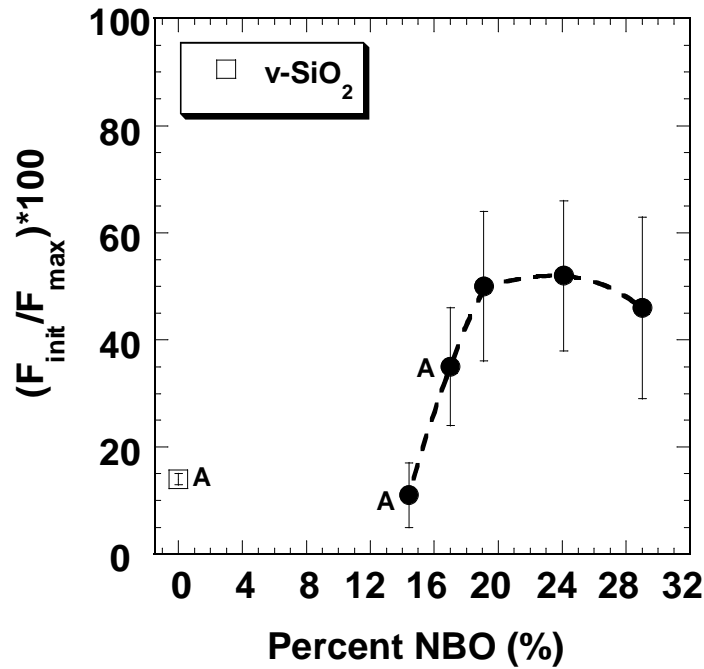
Figure 6. *The normalized initiation load for the first median-radial cracks to initiate on unloading as a function of the percent NBO content of the soda-lime-silicate glass series tested by Wagner[9]. Data from Wagner[9].*

normalized initiation load increased rapidly accompanying the transition from 'anomalous' to 'normal' as the percent NBO increased and then leveled off after ~ 20% NBO. Interestingly, the initiation resistance of v-SiO$_2$ (0% NBO) was similar to the glass containing ~ 15% NBO. This possibly suggests that crack initiation load in soda-lime-silicate glasses is independent of NBO content below a certain threshold.

For the sodium-borosilicate glasses the normalized initiation load for median-radial cracks increased rapidly, then leveled off as the (Na/B) molar ratio increased, as shown in Figure 7. This is presumably also related to the concentration of NBO's in the structure. As the (Na/B) molar ratio increases above a threshold, NBO's are created, resulting in 'normal' behavior and decreased resistance to median-radial crack initiation on unloading.

Another interesting trend arises when the normalized initiation load is plotted as a function of the (Na/Al) molar ratio for the sodium-aluminosilicate glasses of Wagner, as shown in Figure 8. As the (Na/Al) molar ratio increases above 1, NBO's are introduced into the structure, and the normalized initiation load increases, i.e., decreased resistance to crack initiation. When the (Na/Al) molar ratio equals unity, no NBO's should be in the structure, and the normalized initiation load is a minimum. For (Na/Al) < 1 the Al^{3+} ion most likely acts as a network modifier with the creation of NBO's.

The above results suggest that oxide glasses with low NBO content are better able to resist median-radial crack initiation than similar glasses with

37
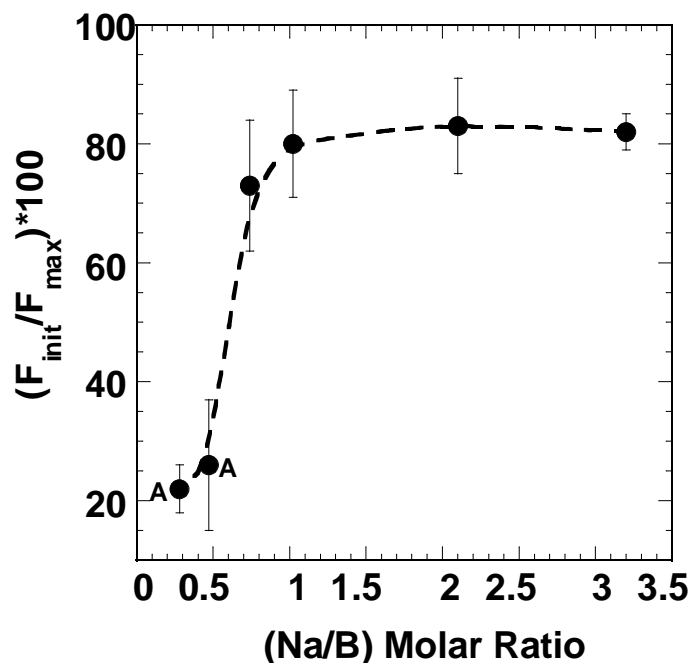
Figure 7. *The normalized initiation load for the first median-radial cracks to initiate on unloading as a function of the (Na/B) molar ratio for the sodium-borosilicate glasses of Wagner[9]. Data from Wagner[9].*
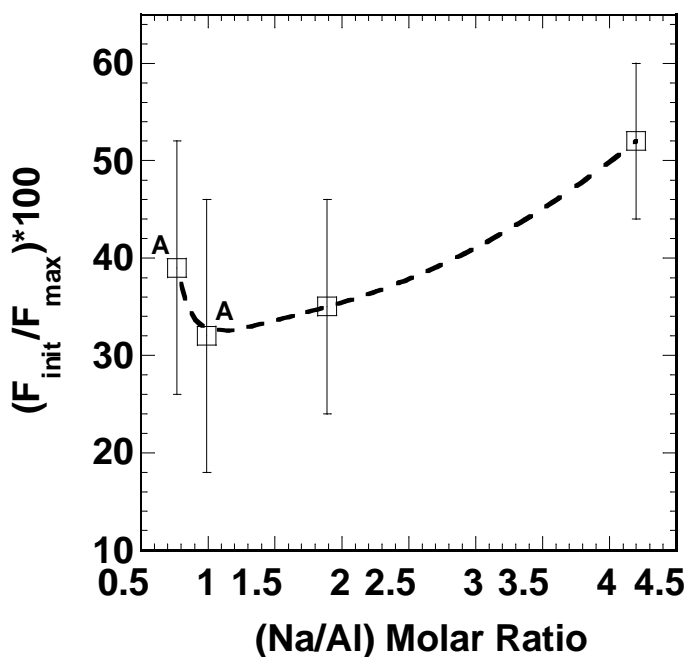
Figure 8. *The normalized initiation load for the first median-radial cracks to initiate on unloading as a function of the (Na/Al) molar ratio for the sodium-aluminosilicate glasses of Wagner[9]. Data from Wagner[9].*

high NBO content. However, such glasses become more susceptible to ring-cone crack initiation. Vitreous B_2O_3 may be one exception. Although this glass should in theory contain no NBO's, it behaves 'normal.'[7] This could be due to the relatively weak van der Waals bonding between sheets of BO_3 triangles, which facilitates shear flow, and likely reduces surface elastic tensile stresses such that ring-cone crack formation is suppressed.

Cook and Pharr[11] found that median-radial cracks initiated on loading in v-SiO_2 and borosilicate glass at 938 g and 1630 g, respectively. Wagner[9] found that lateral cracks for all three series of glasses he tested initiated at less than 5% of F_{max}. Of the three major crack systems, ring-cone, lateral, and median-radial, the last system is the most detrimental to glass strength, and hence assumes more importance in indentation testing.

2.8   Glass Brittleness and Crack Initiation

One challenge that faces any discussion of brittleness, especially in regards to indentation testing of hard materials, is how to define and measure it. Brittleness in the classic sense refers to a lack of ductility, characterized by little or no permanent deformation prior to fracture. Many ceramics and glasses are thus brittle, at least on a macro scale, at low homologous temperatures. However, in sharp indentation testing of glass and other hard materials, *permanent deformation* can be generated, along with cracks from the corners of the indentation. Thus Lawn and Marshall[13] proposed that

brittleness in sharp indentation testing be defined by the ratio of indentation hardness to fracture toughness, H/K_C, which they called the 'index of brittleness,' or simply, brittleness index. Based on this definition, a material with smaller brittleness index relative to another has an indentation response that is *relatively* more deformation controlled than fracture controlled. It is evident the two mechanical processes, deformation and fracture, compete for the energy provided by indentation.[13] Their model, based on indentation fracture mechanics, predicts the initiation threshold for median-radial cracks is higher the smaller the brittleness index.

2.8.1 'Less-Brittle' Glasses

In a recent patent application, Sehgal et al.[42] showed the sand-blast resistance of glass increases as the brittleness index of glass is made smaller. A circular blast of sand, two centimeters in diameter, was made to contact the samples at a pressure of 1 Kg/cm^2 for two minutes. Based on the weight reduction of the samples, the authors calculated the abrasion depth of each glass. Only commercial silicate glasses were examined. A strong trend between decreased abrasion depth of the glass with decreasing brittleness index was evident in the data. This result is significant because it correlates brittleness index with some other physically useful mechanical response of glass. The researchers further found that brittleness index of glass tended to decrease with decreasing glass density.

In another recent paper, Sehgal and Ito[14] showed that brittleness index in ternary soda-lime-silicate glass compositions decreases linearly as molar volume increases. This may indicate that more open glass structures, at least in the soda-lime-silica system, are less brittle. However, the authors point out that v-SiO_2, which has a high molar volume (~ 27.3 cm^3/mol) does not fit the trend. It has a high brittleness index, ~ 9.0 $\mu m^{-1/2}$, compared to commercial soda-lime-silicate glass which has brittleness index ~ 7.1 ± 0.1 $\mu m^{-1/2}$. They suggested the 'anomalous' behavior of v-SiO_2 may be the reason for its high brittleness. The authors measured the hardness at 49 N (5 Kg) using a Vickers diamond pyramid, but used the projected area (d^2/2) rather than the actual area to calculate the hardness.[14] The hardness calculated by using the projected area is about 8% higher than if the actual area were used.

The authors developed a 'new low-brittleness glass,' with brittleness index 5.1 ± 0.1 $\mu m^{-1/2}$, and having lower hardness (4.7 GPa) and higher fracture toughness (0.92 MPa$\sqrt{m}$) than standard soda-lime-silicate glass.[14] The molar volume of this glass was 25.27 cm^3/mole, compared to 23.78 cm^3/mol for the standard glass. According to the authors, the load at which there was 50% crack formation around Vickers indentations (two corners of indentation have median-radial cracks) was ten times higher for the low-brittleness glass compared to the standard glass, i.e., 3500 g compared to 350 g. In addition, all glasses behaved 'normal.' Further, the scratch resistance of the low-brittleness glass was greater, as indicated by less visible damage produced by

a steel roller cutter loaded to 1 Kg and dragged across the surfaces of the glasses, compared to the standard glass. The authors measured the 3-point bend strength of the two glasses after Vickers indentation at 300 g. The strength of the low-brittleness glass was 160 MPa, compared to 60 MPa for the standard glass. The composition of the low-brittleness glass was, in molar %: 13 Na_2O•1 K_2O•4 MgO•1 CaO•2 Al_2O_3•79 SiO_2. Total modifier ion content was 19 mol %. For a standard commercial silicate flat glass, the total modifier content is higher, around 25 mol %.[43] Again, it appears fewer modifier ions and presumably NBO's correlate with increased resistance to median-radial cracking. Of course with continued decrease of modifier content a point will be reached where 'anomalous' behavior will commence, increasing the likelihood of ring-cone and possibly median-radial fracture on loading. The researchers also found that replacing Na^+ with K^+, and Ca^{2+} with Mg^{2+} reduces the brittleness index of glass.

2.8.2 Results of Canfield[10]

Canfield[10] found that as Mg^{2+} replaced Ca^{2+} in two series of silicate glasses the brittleness index decreased. The two series were a mixed-alkali/mixed-alkaline earth, and an alkali/mixed-alkaline earth, both of which behaved 'normal.' The NNF ratios of these glasses are listed in Table III. Canfield monitored the crack initiation in-situ and found that median-radial cracks initiated only on unloading, and that the initiation load decreased nearly

linearly with decreasing brittleness index (H/K_C). *That is, the crack initiation resistance increased with decreasing brittleness index.* The decrease in initiation load also correlated with an increase in atomic molar volume for the mixed-alkali/mixed-alkaline earth silicate series, except for one of the glasses. When plotted as a function of glass density, the load at fracture showed a linear decrease with decreasing density, for all glasses.

2.8.3   Results of Wagner[9]

Using the Vickers hardness and fracture toughness data from the glasses tested by Wagner[9] brittleness indices were calculated for each glass. The brittleness index is plotted as a function of the (Na/B) and (Na/Al) molar ratios for the sodium-borosilicate and sodium-aluminosilicate glass series in Figure 9. The large increase in brittleness index with increasing (Na/B) molar ratio correlates well with the large increase in F_{init}/F_{max} previously shown in Figure 7. At (Na/B) = 1 the brittleness index is a maximum. For the sodium aluminosilicate glasses the brittleness index increases with increasing (Na/Al) molar ratio. This also agrees well with the increase in initiation load, albeit after the small initial decrease, as shown in Figure 8. In Figure 10 the brittleness index is plotted as a function of the percent NBO for the SLS series of glasses from Wagner[9]. One obvious feature is the sharp minimum in brittleness index around 20% NBO. This behavior of the

43
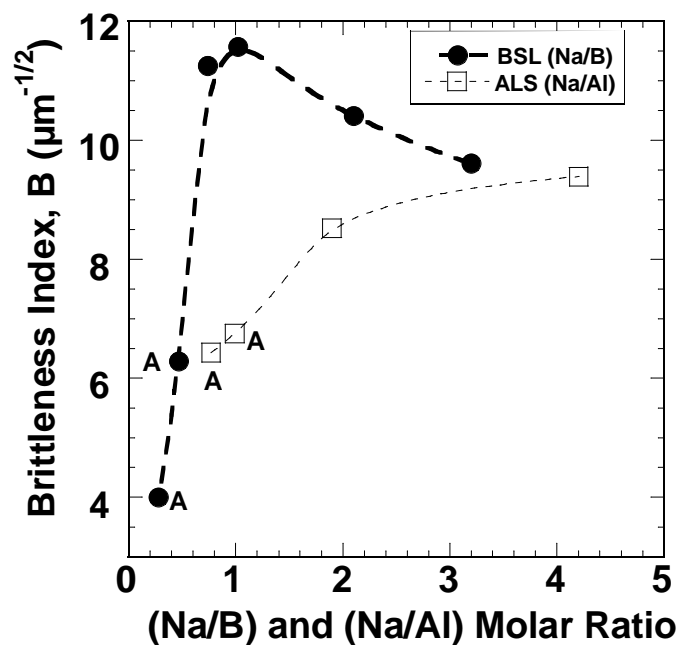
Figure 9. *The variation of brittleness index as a function of (Na/B) and (Na/Al) molar ratio for the BSL and ALS glass series of Wagner[9].*
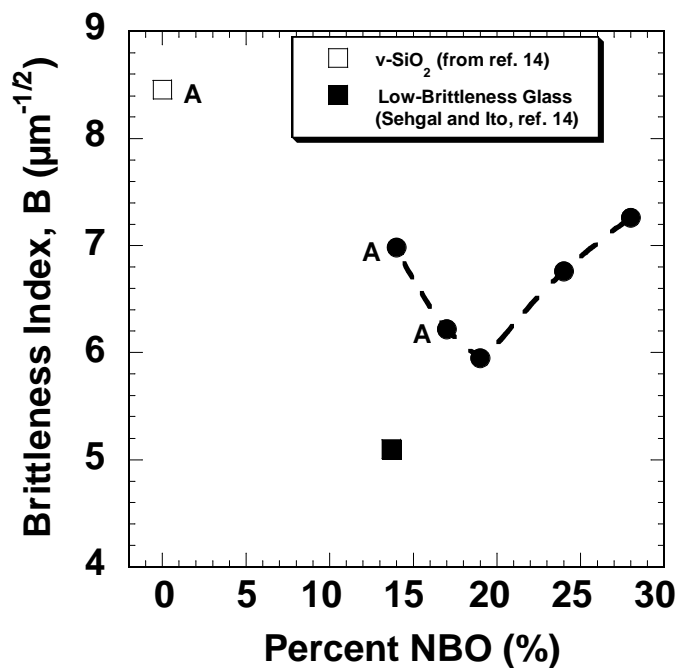
Figure 10. *Brittleness index as a function of percent NBO content for the soda-lime-silicate glasses of Wagner[9]. Also included are data points for v-SiO₂ and the low-brittleness glass of Sehgal and Ito[14].*

brittleness index does not correlate with the trend in initiation load shown in Figure 6, since the initial decrease in brittleness index and corresponding increase in normalized initiation load is opposite than expected. However, the increase in brittleness index with decreasing percent NBO correlates with the increasing tendency for ring-cone crack initiation on loading, i.e., 'anomalous' behavior.

The brittleness index is plotted as a function of the NNF ratio in Figure 11. A turn-around in brittleness is clearly seen in the SLS glass series, occurring just after **RO$_2$+R$_2$O$_3$** = 5. The glasses of Sehgal and Ito[14] fit the trend of the Wagner glasses, with their low-brittleness glass having a NNF ratio just below the normal-to-anomalous threshold. *Whereas the onset of 'anomalous' behavior corresponds to increased brittleness index for the soda-lime-silicate glasses, for the sodium-borosilicate and sodium-aluminosilicate glasses it is characterized by a decrease in brittleness index.*
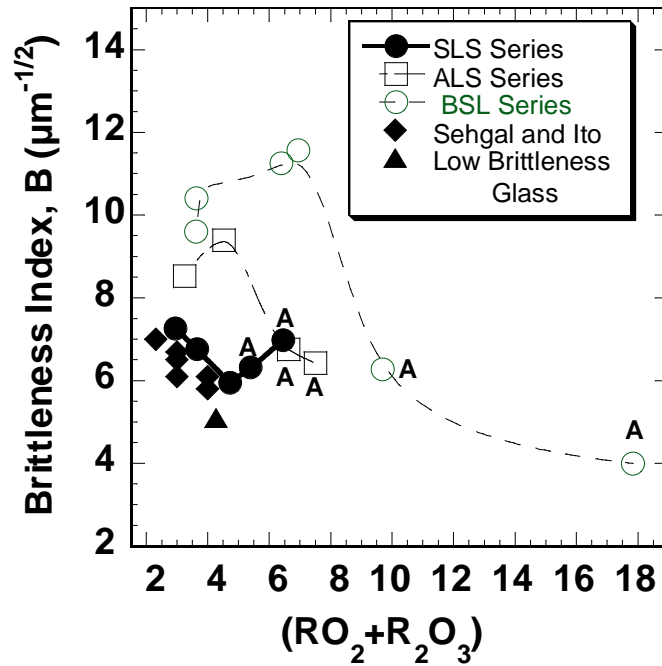
Figure 11. *The variation of brittleness index with normalized network former ratio for the glasses tested by Wagner[9] and Sehgal and Ito[14]. 'A' designates 'anomalous' compositions. Data from Wagner[9] and Sehgal and Ito[14].*

2.9   The Effect of Water on Crack Initiation Behavior of Glass

2.9.1   Results of Lawn et al.[38]

Lawn et al.[38] found the time-to-initiation of median-radial cracks from Vickers indentations in soda-lime-silicate glass depended on the total contact time, peak load, and environment. For short contact durations the crack initiation time was larger than the total contact time, i.e., cracks initiated after complete unloading, for given maximum load. For longer contact durations cracks initiated during the unloading cycle, for given maximum

load. The normalized initiation time ($t_{initiation}/t_{total}$) remained constant at ~ 0.9 for the longer-contact-duration tests. However, for the shorter-contact-duration tests, the normalized initiation time was >1, and increased with decreasing contact time. The invariance of the normalized initiation time at large contact time was cited by the authors as evidence the crack nuclei were developed to such a point that kinetic effects were not influencing the initiation process. This is to say the crack nuclei just needed to experience the appropriate stress conditions for initiation to occur, without having to grow further. The authors attributed the results at short contact durations to a stress-enhanced chemical reaction between crack nuclei and water vapor in the air. According to the authors, these crack nuclei needed to develop further before initiation could occur. This apparently made the nuclei much more susceptible to chemical attack compared to the fully developed nuclei. The shorter the contact duration, the more time is needed after indenter unloading for a nucleus to become critical, hence the normalized initiation time increases. This is presumably because the shorter the amount of time the indenter is in contact with the specimen, the less stress corrosion can occur, i.e., the nuclei do not grow very large, compared to when the indenter contacts the specimen for a longer period of time, in which more severe stress corrosion can likely occur. Of course, stress corrosion continues to occur after indenter unloading due to the residual stress field, but it may not occur as quickly, because the stress is likely to be smaller compared to when the

47

specimen is under load. In addition, the authors found the un-normalized (absolute) initiation time increased as contact duration decreased for the short-contact-duration tests.[38] This further supports the idea that stress corrosion of crack nuclei is more severe the longer the contact duration.

The authors also found that time-to-initiation in (N_2 gas) > in (Air) > in (liquid water). It was clear the type of environment also influences the crack initiation behavior. Higher water content reduced the initiation time, for short total contact time. For larger total contact time, the environment had no effect on the initiation time.

2.9.2   Results of Takata et al.[44]

Takata et al.[44] investigated the mechanical properties and crack initiation behavior of $Na_2O \cdot 2SiO_2$ and $Na_2O \cdot 3SiO_2$ glasses containing up to 12 wt % water. One difference between these experiments and those just discussed by Lawn et al.[38] is the water was incorporated structurally into the bulk glass. This was done by a high-pressure hydrothermal technique, which forced water into the glass structure. At these high water levels some water is likely in molecular form, i.e., not –OH-bound water. According to Ernsberger[45] as-melted silicate glasses contain on the order of a few hundredths of one percent by weight of water, and v-SiO_2 can contain up to 0.1 wt % water, depending on processing method. Wu[46] found that a hydrated silicate glass (mol %: 77% SiO_2, 10.8% Na_2O, 3% K_2O, 1.3% Al_2O_3,

48

7.8% ZnO) with 3.5 wt % water contained molecular water. This was concluded based on the presence of a 1.92 μm band in the infrared absorption spectrum, which is attributed to molecular water.[47] Bands at 2.22 and 2.5 μm were also observed by Wu[46] and attributed to free and hydrogen-bonded silanol (Si-OH) groups, respectively. Whereas cracks from Vickers indentation formed readily in the 'dry' $Na_2O \cdot 3SiO_2$ glass at 1.63 Kg, no cracks formed in the same glass containing 5.4 wt % water at 2.15 Kg. Both Knoop hardness and glass transition temperature decreased continuously at room temperature with increasing water content, indicating increased plasticity of the glass. The researchers suggested the increased resistance to crack initiation was consistent with the decrease in Vickers hardness according to the model of Lawn and Evans[21] where the initiation load is proportional to $1/H^3$.

It is apparent that water can have at least two different effects on crack initiation behavior of glass. When water comes into contact with soda-lime-silica glass and stress corrosion results, crack initiation is made easier, as the results of Lawn et al.[38] showed. However, when large amounts of water were incorporated structurally into soda-lime-silica glass, crack initiation was suppressed, as shown by Takata et. al.[44] In the latter case, the reduced intensity of contact stresses, associated with increased plasticity (lower hardness) and/or decreased sizes of contact-induced flaws, may be responsible for the observed behavior.

2.10   Acoustic Emission and Crack Initiation

Acoustic emissions are transient elastic stress (sound) waves produced by the rapid release of energy stored in a material.[48] When cracks initiate in indentation testing, some of the elastic strain energy released is used to generate fracture surface, and some is transferred to the surrounding medium in the form of a transient elastic stress wave. A very sensitive piezoelectric sensor, usually mounted to the surface of the sample, can be used to detect the sound waves, since the frequencies generally lie in the ultrasonic region (20 KHz to 1 GHz), and provide evidence of crack initiation, even if visual observation is not possible.[48]

An important point concerning the detection of acoustic emissions is that what is actually being measured is the sensor's electrical response to a mechanical disturbance, not the actual characteristics of the source which produced it. In addition, as discussed by Kline[49] it is uncertain whether piezoelectric sensors exclusively measure particle displacement, velocity, stress amplitude, or acceleration. Since the sensor is usually mechanically fixed to the surface of the specimen, further alterations to the stress waves can take place. Despite these drawbacks to the use of piezoelectric sensors in AE detection, they offer several advantages, including very high sensitivity. Acoustic emission (AE) sensors can detect surface displacements as small as 10^{-13} meters.[49] In addition, test set-up is relatively simple.

2.10.1 Acoustic Emission Data

The data generated from modern AE systems include the waveform data (amplitude and frequency as a function of time), and hit data. A hit is any detected AE signal. Hit data include the number of counts, amplitude (maximum voltage), average frequency, rise-time, energy, and signal duration of each hit.[48] Counts represent the number of times the signal crosses the threshold voltage, which can be set by the user. Signals which do not meet the threshold requirement are not analyzed by the AE computer system.

2.10.2 Acoustic Emission Testing and Crack Initiation

Lankford and Davidson[50] monitored acoustic emissions of Vickers indentations made in a number of brittle materials, including single-crystal NaCl, SiC, Ge, and polycrystalline Al_2O_3 and SiC. Using a conventional indenter, in which the load was applied rapidly, then held for 18 seconds, they observed acoustic emission very early in the loading cycle (within the first half-second) for all materials. Radial cracks were deemed responsible for these acoustic emissions, and were confirmed to exist by using scanning electron microscopy. The authors pointed to the possibility that lateral cracking on loading could have contributed to some of the AE activity as well. Below a threshold load no acoustic emission was detected, correlating with

the observation of no radial cracks. The number of AE counts was observed to increase as the indentation load increased, indicating more overall acoustic activity and presumably increased cracking.

Tanikella and Scattergood[51] used acoustic emission detection to study crack initiation in soda-lime-silica glass using a Vickers indenter. No acoustic emission was detected on the loading cycle for indentation loads up to 50 N (5.1 Kg); however, on unloading, acoustic emissions were detected at 0.35, 0.53, and $0.73F_{max}$, as the maximum load increased from 5, 6, and 7 to 25 N, respectively (in the load range from 7 to 25 N, cracks initiated at a constant fraction of F_{max} i.e., $0.73F_{max}$). The authors believed these emissions were from median-radial cracks. Smaller signals were detected on unloading and were attributed to lateral cracks at 0.12 and $0.02F_{max}$, for maximum loads of 7 to 25, and 50 N, respectively. For indentations made at 100 N maximum load the authors noted a large signal at 72 N on loading, which they attributed to median-radial crack formation. Indentations were also made at higher loads, which in addition to the median-radial signal at 72 N, produced other emissions which they attributed to further cracking, or to further development (possibly breakthrough to the specimen free surface) of the median-radial cracks.

Wagner[9] and Canfield[10] utilized acoustic emission detection using a piezoelectric sensor along with in-situ optical observation to monitor the crack initiation behavior of silicate glasses. Both researchers primarily used

the AE data to help identify the onset of crack initiation, but some attempt was made by Wagner[9] to analyze and compare the different waveforms from different crack systems, i.e., median-radial, lateral, and ring-cone. Canfield's[10] results showed that the signal amplitude for the first median-radial cracks to initiate on unloading decreased with decreasing initiation load. This agrees with the assumption that the stored elastic strain energy which is released upon crack initiation is less at smaller loads, and hence a less intense elastic stress wave is produced and detected. Cleary and Varner[52] utilized AE detection for determining the threshold loads at which cracks initiated in v-SiO_2, soda-lime-silica, and borosilicate glasses from Vickers and Hertzian indentation testing.

3.   EXPERIMENTAL PROCEDURES

3.1   Glass Compositions Examined

The crack initiation behavior of nine optical glass compositions, Pyrex™ borosilicate glass (Corning code 7740), a commercial float glass, and a commercial vitreous silica glass‡ were examined in the current work. The optical glasses were primarily a mixture of flint and crown glasses, including a host laser-glass composition. Table V lists the components of the optical glasses, and the approximate molar % composition of each glass. In Table VI the compositions are expressed in normalized molar amounts, and a brief description of each glass type is given. Six of the optical glasses contained silica (SiO_2) and are designated by the prefix 'S.' Three compositions contained no silica (non-silicate) and are designated by the prefix 'NS.' In Table VII the compositions of the float and Pyrex™ borosilicate glasses are given, along with the normalized compositions.

The Suprasil 312 vitreous silica specimen was flame fused from synthetic silica particles, and, according to the manufacturer, contained 216 wt. ppm OH. This means the glass contained approximately 216 µg of OH per gram of glass.

‡Suprasil 312--Heraeus Quarzglas GmbH, Hanau, Germany

Table V. Approximate Compositions of the Optical Glasses in Mol %.

Components	Glass								
	S1	S2	S3	S4	S5	S6	NS1	NS2	NS3
SiO_2	81	67	44	13	8	6			
ZrO_2					6	6	6		
Na_2O	6	7							
K_2O	5							23	
CaO					27	10			6
ZnO		10				7	5		
BaO			27						
PbO	5			58					
MgO									
SrO									
B_2O_3		11	25	22	51	60	60		
Al_2O_3	5	6	6	6				7	
La_2O_3					18	13	18	6	
Y_2O_3							7		
P_2O_5								64	7
Nb_2O_5							5		
KHF_2	1								
LiF									9
CaF_2									8
MgF_2									9
BaF_2									12
SrF_2									26
AlF_3									23
Total (Molar %)	103	101	102	99	100	102	101	100	100

55

Table VI. Normalized Molar Compositions of the Optical Glasses.

Glass	RO_2	R_2O_3	R_2O_5	RO	R_2O	RF	RF_2	RF_3	$RR'F_2$
S1 (lead-alkali-silicate crown)	5.06	0.31		0.31	0.69				0.06
S2 (zinc-silicate crown)	3.94	1.00		0.59	0.41				
S3 (barium-borosilicate dense crown)	1.63	1.15		1.00					
S4 (lead-borosilicate dense flint)	0.22	0.48		1.00					
S5 (lanthanum-borate crown)	0.52	2.18		1.00					
S6 (lanthanum-borate crown)	0.71	4.35		1.00					
NS1 (lanthanum-borate flint)	1.20	17.00	1.00	1.00					
NS2 (potassium-phosphate)		0.56	2.78		1.00				
NS3 (fluoride crown)			1.17	1.00		1.50	9.17	3.83	

Table VII. Float[*] and Corning 7740 Pyrex™ Borosilicate Compositions.

	Float Glass (mol %)	Pyrex™ Borosilicate Corning Code 7740 (mol %)
SiO_2	70.3	81
Al_2O_3	0.4	2
B_2O_3		13
CaO	9.3	
MgO	6.1	
Na_2O	13.7	4
K_2O	0.1	
RO_2	2.41	20.25
R_2O_3	0.01	3.75
RO	0.53	
R_2O	0.47	1.00

[*] from previous study[53]

3.2 The Recording Microindenter Testing System

A recording microindenter was built so that crack initiation using relatively high indentation loads, up to 4 Kg, could be investigated in-situ. The whole assembly rested on a sturdy table, and four rubber pads were positioned between the steel base plate of the indenter and the table in order to dampen any vibrations. A schematic of the system is shown in Figure 12. The soft-PZT piezoelectric actuator[†] pushes the Vickers diamond into the glass sample while the load and displacement of the diamond are simultaneously monitored as a function of time by the strain-gauge load cell[‡], and two capacitance displacement gauges[*], respectively. The load cell had a 22.7 Kg capacity, and the displacement gauges had a measuring range of 500 µm. Before passing to the workstation computer, the signals from both the load cell and capacitance gauges passed through their respective signal conditioners and amplifiers. When combined with the 16-bit digital-to-analog (D/A) card[**] in the computer, the theoretical load and displacement resolutions were ≈ 0.35 g and 7.6 nm, respectively. For driving the piezoelectric actuator, the D/A card was capable of a 12-bit digital-to-analog conversion, which when combined with the 60 µm total displacement capability of the actuator, resulted in a displacement resolution of ~ 14.4 nm. The displacement rate of the actuator, and hence Vickers indenter, was

[†]Model PZL-60, Burleigh Instruments, Inc., Fishers, New York
[‡]Lebow Model 3189-50, Eaton Corp. Lebow Products, Troy, Michigan
[*]Model HPT-40, Capacitec Corporation, Ayer, Massachusetts
[**]Model AT-MIO-16XE-50, National Instruments Corp., Texas
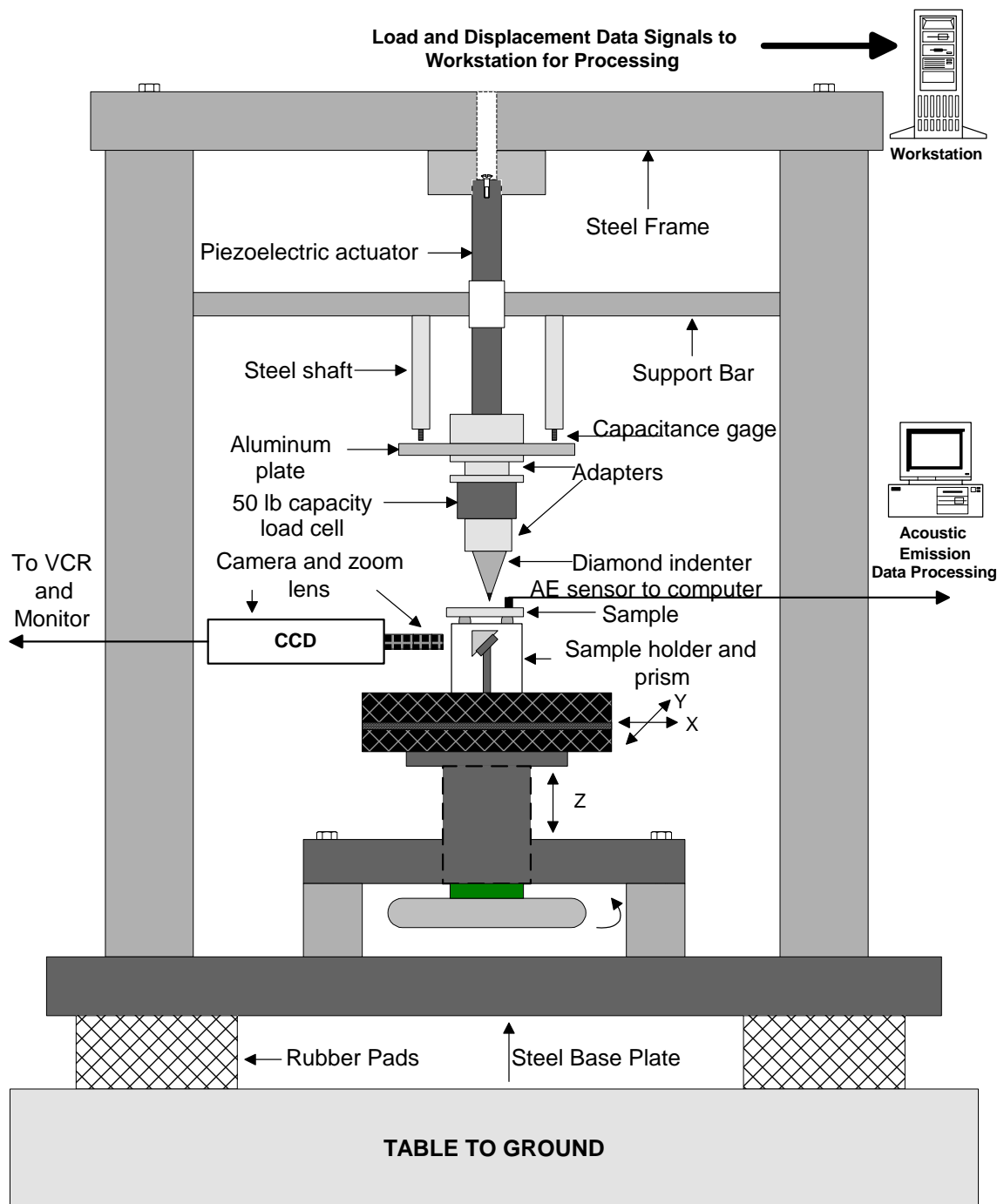
Figure 12. *Schematic diagram of the recording microindenter built for the current study. The indenter was 18 inches tall from the bottom of the steel base plate to the top of the frame, and about 15 inches wide, not including the steel base plate.*

controlled by adjusting the rate of increase of the voltage. The displacement rate was the same on loading and unloading. A program was written using LabView software which allowed total user control over the maximum load and displacement rate desired. The data that were collected from a run were the time, load, and displacement readings from both capacitance gauges. The averaged readings from both gauges were used to calculate a single displacement point for each load. A threshold load of 1.5 grams was used before data were collected in order to prevent false triggering of data collection. This was necessary because of the small amount of electrical noise in the system.

3.2.1 Optical System

A zoom lens was fitted to a CCD camera, which was connected to a 13" Panasonic television, and allowed in-situ optical observation of the indentation crack initiation process from below the specimen. A VCR was also set-up to record the entire indentation process observed on the monitor. Fiber-optic lamps illuminated the indentation site. A glass prism directed the light, by total internal reflection, through a 90° angle into the zoom lens and CCD. By adjusting the zoom lens, the magnification of an image on the monitor could be varied from 116 to 743 X, with a corresponding resolution of 6 to 2.1 μm, respectively. For most of the crack initiation experiments the

magnification was kept at 743 X, permitting relatively detailed observation of the indentation crack initiation process.

3.2.2   Acoustic Emission System

A PAC MISTRAS-2001 acoustic emission system[†] was used to detect the acoustic emissions resulting from the crack initiation tests, in-situ.   The system was fully computerized and capable of simultaneously collecting and processing classical AE features (counts, hits, duration, energy, rise-time, amplitude, frequency, etc.) and perform transient waveform recording as well, all in real-time.   Each detected signal is a 'hit' and is characterized by counts, duration, energy, amplitude, frequency, and rise-time.   A brief description of these signal attributes is given below.

Hits: The number of discrete signals detected by the sensor during the course of an experiment.

Counts: The number of times the detected signal crosses the threshold level, expressed in whole integers. Frequently used as a measure of the magnitude of the source event.

Duration: The length of a hit from the time the threshold is first crossed to when it is last crossed, usually expressed in μs.

Energy: Electrical energy output of the piezoelectric sensor, given by the area under the square of the voltage vs. time, V(t), curve. Value is sensitive to both duration and amplitude of signal. Units are arbitrary.

Rise-Time: The time that elapses between when a signal first crosses the threshold level to when the signal peak (amplitude) is reached.

Amplitude: The maximum signal voltage, expressed in dB.

Frequency: The average frequency response of the sensor, expressed in KHz.

A broadband, resonant-type, single-crystal piezoelectric transducer from Physical Acoustics Corporation (PAC), called PICO, was used as the AE sensor. It measured 5 mm diameter and 4 mm tall. The sensor had a resonance frequency of 513.28 KHz, and an optimum operating range of 200 to 750 KHz. The sensor was connected to a 1220 A preamplifier from PAC, set to a 40 dB gain, which translated into a 100-fold pre-amplification of the signal. The threshold level used in all tests was 32 dB, which translated into a minimum necessary voltage of ~ 40 µV, equivalent to a displacement on the order of 10^{-14} meters at the sensor. If the amplified signal did not meet the threshold requirement, it was not processed. Table VIII lists the test settings used for the collection of AE data for the crack initiation tests. The PDT, HDT, and HLT are timing parameters governing the collection of data. The values chosen for these settings were based on past work and some preliminary testing in the current work as well.[9] The goal was to have a distinct event, e.g., the initiation of a single median-radial crack, produce a single AE hit. The filter values were used to further screen incoming signals, in terms of frequency and counts, but for the most part all signals which passed the threshold requirement were processed. The pre-trigger time told the computer how long to collect data prior to the time when the threshold was crossed. A hit length of 8 kilobytes coupled with the sampling rate of 4

61

MHz allowed a maximum recordable waveform size for each hit of 2048 µs. It
was necessary to keep all AE settings constant for each glass specimen
tested, since changing certain parameters, namely the threshold level and
pre-amp gain, would have influenced the results, and invalidate comparisons
between samples.

Table VIII. Acoustic Emission Test Parameters and Settings.

Parameter	Value
Pre-Amp Gain	40 dB
Threshold	32 dB
Peak Definition Time (PDT)	30 µs
Hit Definition Time (HDT)	400 µs
Hit Lockout Time (HLT)	600 µs
Sampling Rate	4 MHz
Filter-Low	10 KHz
Filter-High	1200 KHz
Pre-Trigger	20 µs
Hit Length	8 K
Filter (Low Level)	3 Counts
Filter (High Level)	3000 Counts

3.2.3 Machine Compliance

In order to assess whether any deformations present in the recording microindenter and associated sample stage were reversible, i.e., elastic, test runs were made on a polished steel disc 51 mm in diameter and 7 mm thick. The disc was placed on the steel sample holder which rested on the x-y-z stage. The sample holder was a steel cylinder measuring 30 mm outer diameter and 30 mm tall. It was hollow in the center with an opening in one side to allow light coming from the sample to pass through the prism, and into the CCD camera. A groove cut into the top of the holder allowed approximately 14 steel ball bearings, each 4 mm in diameter, to rest. The small contact area afforded by the ball bearings on the sample are thought to help minimize tilting and rocking of samples placed on them.

A flat-tipped (~ 1 mm diameter) cone-shaped hardened steel punch was attached to the instrument instead of the Vickers diamond, and test runs were made using a maximum load of 4 Kg and a displacement rate of 0.2 µm/s. Ten runs were made. Contact of this blunt tip on the thick steel disc was assumed to represent an elastic contact situation only. Any displacement measured would thus be the result of elastic deflections of the indenter system itself. A typical run is shown in Figure 13, in which considerable elastic deflection is seen. The 'compliance hysteresis loop' is likely due to the intrinsic behavior of the soft-PZT actuator, which itself has

hysteresis with its voltage-displacement behavior. The residual displacement depth at zero grams load, p_o, was determined to be 0.52 ± 0.17 μm, indicating nearly complete recovery of all deformation, i.e., elastic behavior of the machine and stage.

3.2.4 Accuracy Check

To determine the accuracy of the recording microindenter, Vickers indentations were made on a polished aluminum metal cylinder with a new
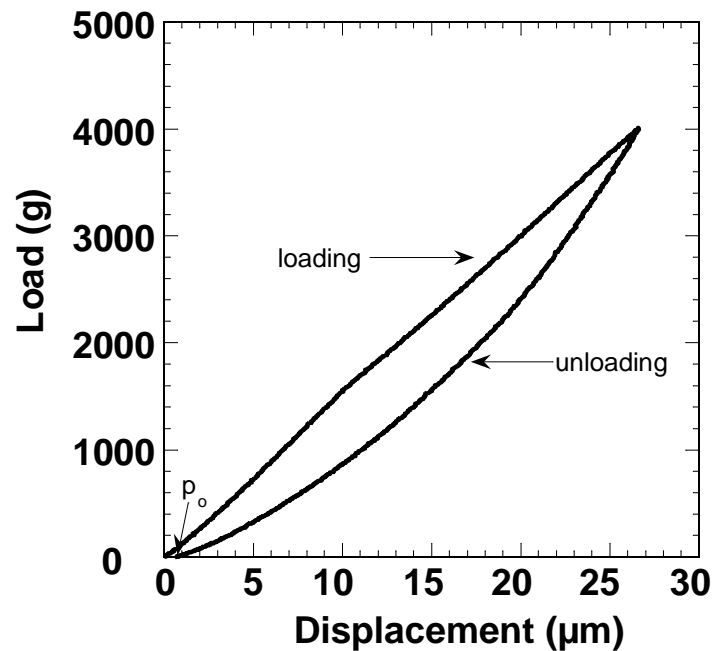
Figure 13. *A typical load-displacement curve obtained from the compliance test runs. 725 individual data points make up this 'curve.'*

Vickers diamond indenter. The cylinder measured 32 mm in diameter and 12 mm thick. A maximum load of 2.4 Kg and a displacement rate of 0.2 µm/s were used. Ten indentations were made. The residual indentation depth values, p_0, from these tests were obtained from the load-displacement curves, and the average value listed in Table IX. This value, along with the value obtained by measuring the depths of several indentations directly with an optical interferometer[‡], differed by only 7%. This was evidence the displacement measuring gages, and the recording microindenter, were functioning correctly.

A standard Vickers hardness calibration block[†] was indented at 200 g load, with a hold time of 15 seconds. Ten indentations were made and the Vickers hardness was calculated and compared to the manufacturer's value of 711 Kg/mm^2. The experimentally determined value was 737 ± 19 Kg/mm^2, which differed from the manufacturer's value by only 4%. This provided further evidence the recording microindenter was functioning properly.

Table IX. Summary of Data from Accuracy Tests of the Recording Microindenter.

p_0 (From Recording Microindenter)	p_0 (Interferometer Measured)
26.9 ± 0.5 µm	25.2 ± 0.7 µm
H_V (Experimental)	H_V (Manufacturer's Value)
737 ± 19 Kg/mm^2	711 Kg/mm^2

[‡]Zygo New View 5000 System, Zygo Corporation, Middlefield, Connecticut
[†]Shimadzu HMV-2000 Hardness Calibration Block, Shimadzu Corporation, Japan

3.3   Sample Preparation

3.3.1   Grinding

The nine optical glasses came in bulk annealed form and were cut into smaller rectangular pieces about 30 mm L x 25 mm W x 4 mm H using a large diamond saw[*].   Approximately four samples were cut for each composition. Grinding and polishing of the samples was then carried out to achieve a flat, near-optical-quality surface with few scratches and pits. No cutting was necessary for the vitreous silica specimen. The float and Pyrex™ borosilicate samples were cut from sheets of glass 3.2 and 3.5 mm thick, respectively, and no grinding was necessary. All specimens, except for the vitreous silica (Suprasil 312), were mounted on circular aluminum metal blocks using thermoplastic glue, in order to facilitate grinding and polishing. The vitreous silica specimen was large enough to grind and polish without using metal blocks. A Buehler grinder[†] was used for grinding. Samples were ground on both sides using SiC paper with either distilled water or polishing oil. First 320-grit, followed by 400-grit, then 600-grit SiC paper was used. The grit numbers correspond to average SiC grain sizes of approximately 34 µm, 22 µm, and 14 µm, respectively. Samples NS1 and S3 were ground with polishing oil to reduce water interaction with the glass, while the rest of the samples, including the vitreous silica specimen, were ground in distilled

[*]Discotom-5 Cutting Saw, Struers Corporation, USA
[†]Buehler Ecomet 3 Variable Speed Grinder/Polisher, Buehler Corporation, USA

water. Each pad was saturated with either the oil or distilled water prior to grinding. Samples were ground five minutes per side. Each sample was rinsed with either water, for the water-ground specimens, or reagent alcohol (90% ethanol, 5% methanol, 5% isopropanol) for the oil-ground specimens, between steps to remove residue. Polishing of the specimens took place next.

3.3.2 Polishing

The two oil-ground specimens were polished using diamond pastes[*] of 15 µm, 6 µm, 3 µm, and 1 µm, in that order. Polishing oil[‡] was put on a pad[**] secured to a polishing wheel spun by a motor, along with some diamond paste. The samples were moved in a circular direction opposite the rotation of the wheel and polished for approximately five minutes per side. Additional polishing oil was squirted onto the pad about every thirty seconds. Between polishing steps, all samples were placed in a beaker containing the reagent alcohol, which was then placed in an ultrasound bath for a couple of minutes to remove residue. Samples were then gently dried with laboratory towels. New pads were used for each diamond paste size. The last step consisted of polishing with a cerium oxide polishing compound[ξ] on a new pad, followed by cleaning. All surfaces were subsequently checked with a light microscope to ensure good quality.

[*]METLAB Diamond Compound, METLAB Corporation, USA
[‡]Polishing Oil, Buehler Corporation, USA
[**]METLAB PAN W Polishing Pads, METLAB Corporation, USA
[ξ]Cerium Oxide Polishing Compound, Buehler Corporation, USA

When necessary, samples were re-polished with the cerium oxide compound to remove any obvious imperfections. The samples were then removed from the aluminum blocks by heating the blocks on a hot-plate until the glue softened, at which point the samples were removed. The samples were then placed, one at a time, in a beaker containing acetone and ultrasonicated for approximately five minutes. This was necessary in order to remove the glue from the samples. The samples were then wiped with reagent alcohol to remove any acetone residue, and then stored in a drying oven held at ~100 °C to help keep away water.

The water-ground specimens were polished using diamond sprays, along with the polishing pads. The sprays came in diamond sizes of 15 μm, 6 μm, and 1 μm. Samples were polished starting with the largest diamond size first. More spray was added every thirty seconds, and samples were polished approximately five minutes per side, and cleaned with the reagent alcohol and ultrasound polishing steps. After polishing with the 6-μm spray, the specimens were polished using the 3-μm diamond paste and a glycol-based diamond thinner fluid. Polishing with the cerium oxide compound was the last polishing step, followed by specimen cleaning and storage, as before.

The float-glass specimens were cleaned with the reagent alcohol and ultrasound, while one side of the 7740 Pyrex™ borosilicate specimens was polished with the 1-μm diamond spray, followed by polishing with the cerium

oxide compound. This was done to remove any surface layers that may have been present.

For glasses NS1 and S3, only the specimens used for the in-situ crack initiation studies were oil polished; the rest of these specimens were polished via the water route described above for all other tests. The toxicity, smell, and greasiness of the oil were some of the reasons why it was not used to prepare all the specimens.

3.3.3 Annealing

The polished glass specimens, except the vitreous silica specimen, were annealed in an electric muffle furnace[§] at 10 K above their respective glass transition (T_g) or annealing (T_A) temperatures to remove any residual stresses. Values of T_g were supplied by the optical glass manufacturer, who used a 2.2 K/minute heating rate. The glass transition temperature of the float glass was determined in a previous study[53] and the annealing temperature of the 7740 Pyrex™ borosilicate glass was found in the literature. Two specimens of the same glass were placed inside the annealing furnace on a piece of platinum foil. The temperature was increased at 10 K/minute until the desired temperature of 10 K above T_g or T_A was reached, at which point the specimen was soaked at this temperature for one hour. After one hour, the temperature was decreased at a rate of ≈ 1 K/minute to

[§]Thermolyne Model 1300, Thermolyne Corporation, USA

room temperature (≈ 22 °C). The specimens were then removed and stored in the drying oven. Table X lists the glass transition and annealing temperatures.

Table X. Glass Transition and Annealing Temperatures.

Glass	T_g (°C), *T_a (°C)
S1	459
S2	528
S3	638
S4	362
S5	650
S6	640
NS1	642
NS2	520
NS3	405
float	554
7740 Pyrex™ Borosilicate	560 *

3.4   Mechanical Properties Measurements

3.4.1   Density

The densities of the polished glasses were measured using the Archimedes method with kerosene as the immersion medium. The dry mass of the specimens were measured on a laboratory balance to the nearest 0.001 g, followed by the wet suspended masses. The temperature of the kerosene was

monitored throughout with a glass-bulb thermometer. The density was

calculated using the following formula:[35]

$$\rho_{glass}(g/cm^3) = \frac{dry\ mass\ (g)}{\left(\dfrac{dry\ mass\ (g) - wet\ mass\ (g)}{\rho_{kerosene}\ (g/cm^3)} \right)} \tag{3}$$

Three density measurements were made per specimen, then subsequently

averaged. The molar volumes (cm^3/mol glass) of the glasses were also

calculated by dividing the molecular masses of the glasses by the measured

densities. In addition, atomic molar volumes (cm^3/mol atoms) were

calculated by dividing the molar volumes by the number of atoms per mole of

glass. Specimens were wiped clean using the reagent alcohol and laboratory

towels after testing.

3.4.2   Young's Modulus and Poisson's Ratio

The elastic (Young's) modulus and Poisson's ratio were determined using

the ultrasonic pulse-echo technique.[54] The specimens used for the density

measurements were used for this. Transit times for shear and longitudinal

sound waves to traverse the thickness of the specimens were measured using

a digital oscilloscope[ξ]. Shear and longitudinal transducers[‡] powered by an

amplifier[*] were used to generate the ultrasonic waves. The transducers were

coupled to the specimens using maple syrup. By dividing the thickness of the

specimens, measured with digital calipers, by one-half the round-trip transit time of the waves, the shear and longitudinal sound wave velocities were calculated. Specimens were cleaned after testing. Young's modulus and Poisson's ratio were then calculated using the following formulas:[54]

$$\nu = \frac{1 - \left[2 \left(\dfrac{V_T}{V_L} \right)^2 \right]}{2 - \left[2 \left(\dfrac{V_T}{V_L} \right)^2 \right]} \qquad (4)$$

where,

ν = Poisson's ratio

V_T = transverse (shear) sound velocity

V_L = longitudinal sound velocity

$$E = V_L{}^2 \rho \frac{(1 + \nu)(1 - 2\nu)}{1 - \nu} \qquad (5)$$

where,

E = Young's modulus

ρ = glass density

Poisson's ratio is the ratio of transverse to longitudinal strains in the material when it is pulled (elongated) in uniaxial tension.[55]

Shear and bulk moduli were also calculated after Young's modulus and Poisson's ratio were determined, using the following formulas:[35]

$$G = \frac{E}{2(1+v)} \qquad (6)$$

where,

G = shear modulus

$$K = \frac{E}{3(1-2v)} \qquad (7)$$

where,

K = bulk modulus

3.4.3   Conventional Vickers Hardness (Hv)

The Vickers hardness is indicative of the mean contact pressure on a glass in an indentation experiment.[21] It is calculated by dividing the indentation load by the surface area of the remaining indentation after unloading. The conventional Vickers hardness of the polished glasses was measured using a Vickers hardness testing machine[†], except for the vitreous silica specimen. This was a conventional hardness testing machine utilizing dead weight loading.   The atmosphere side of the float glass specimen was tested. Specimens were gently cleaned with reagent alcohol and a laboratory towel just before testing.

[†]HMV-2000 Microhardness Tester, Shimadzu Corporation, Japan

An applied load of 200 g, held for 15 seconds, was used for the tests. The exact loading rate was unknown, but complied with ASTM E384-89 specifications[56] and was much faster than the indentation rate of the recording microindenter. Samples rested on a three-ball ring holder to minimize tilting from any unevenness. The two indentation diagonal lengths were measured in reflected light to the nearest tenth of a micrometer for each indentation, using the attached measuring unit. Ten indentations were made per specimen. Temperature ranged from 21 to 23 °C and relative humidity from 14 to 21% during the course of testing all specimens. The Vickers hardness was calculated using the following formula from ASTM E384-89:[56]

$$H_V(\text{Kg/mm}^2) = \frac{1854.4F(g)}{d^2(\mu m)^2} \tag{8}$$

where,

H_V = Vickers hardness

F = indentation load

d = average indentation diagonal length

The average indentation diagonal length, d, was calculated by averaging the two indentation diagonals lengths measured for each indentation. Ten Vickers hardness numbers were calculated for each glass, from which an average and standard deviation were calculated.

3.4.4 Fracture Toughness (K_{IC})

The indentation technique was used to measure the fracture toughness of the glass specimens, except the vitreous silica and Pyrex™ borosilicate glasses, since they behaved 'anomalous.' The same specimens used in the hardness testing were used for the fracture toughness tests. The atmosphere side of the float glass specimen was tested. Twelve Vickers indentations were made on each sample using the same hardness tester used to measure the Vickers hardness. Specimens rested on a three-ball ring holder to minimize tilting from any unevenness. Immediately after making an indentation the four major median-radial crack lengths were measured from the center of indentation to the tip of the cracks using the attached measuring unit. The two indentation diagonal lengths were measured for each indentation as well. Loads ranging from 0.5 Kg to 2 Kg were used, with a 15 s hold time. A load of 1 Kg was used for most specimens. Different loads were needed since for some of the glasses cracking of the indentations was too severe at 1 Kg, while for another glass a higher load was needed (2 Kg) to have 100% of the indentations form cracks. The loads used for each glass will be made clear in the results section. Throughout the course of testing, temperature was 24 ± 2 °C, and relative humidity was 43 ± 7%. The equation used to calculate the fracture toughness was that derived by Anstis et al.[26] in which the half-penny crack geometry is assumed to be the final shape. This assumption turned out

to be valid for the glasses tested in the current work, as fractographic evidence will show. The formula used was:[26]

$$K_{IC} = 0.016 \left(\frac{E}{H} \right)^{1/2} \left(\frac{F}{c^{3/2}} \right)$$

(9)

where,

K_{IC} = Mode I (tensile opening) plane-strain fracture toughness

E = Young's modulus

H = Hardness

F = indentation load

c = crack length measured from center of indentation to crack tip

The Vickers hardness (H_V) was used for the hardness (H) in Eq. 9, and was calculated from the measured indentation diagonal lengths, using Eq. 8. The average crack length of each indentation was used for 'c' in Eq. 9. Twelve fracture toughness values were calculated for each glass, from which an average and standard deviation were calculated.

3.4.5   Fracture Surface Energy (γ_f)

The plane-strain fracture surface energy, γ_f, was calculated using the following fracture mechanics relation:[57]

$$\gamma_f = \frac{K_{IC}^2 (1 - v^2)}{2E}$$

(10)

where,

γ_f = plane-strain fracture surface energy

Values of K_{IC}, E, and ν were obtained from the fracture toughness and Young's modulus measurements. Twelve values of the fracture surface energy were calculated for each glass, one for each indentation, from which an average and standard deviation were calculated.

3.4.6   Brittleness Index (B)

The brittleness index (B) was calculated for each glass using the equation of Lawn and Marshall[13] who proposed that brittleness in indentation testing be defined by the ratio of indentation hardness to fracture toughness:

$$B = \frac{H}{K_C} \qquad (11)$$

The average Vickers hardness and fracture toughness values previously calculated were used to calculate the average brittleness index for each of the glasses.

3.5   Crack Initiation Testing

Crack initiation tests were carried out using the newly-built recording microindenter. Tests were conducted on the nine optical glass specimens, the float, 7740 Pyrex™ borosilicate, and vitreous silica glasses. Tests were conducted at 1 Kg maximum set load with 0.2 µm/s set indenter displacement rate. In addition, tests were conducted at 4 Kg maximum set load for the float glass, Suprasil 312, and optical glasses S1, S3, S5, S6, and NS1 with 0.2 µm/s rate. For the remainder of the optical glasses (S2, S4, NS2, and NS3), additional tests were conducted at 3.5 Kg maximum set load (0.2 µm/s rate), since these glasses were too 'soft,' causing the actuator to run out of displacement before 4 Kg could be reached. All tests to be described for the float-glass specimen were performed on the atmosphere side.

Table XI. Crack Initiation Testing Contact Parameters.

Glass	Maximum Load (Kg)	Displacement Rate (µm/s)
All	1	0.2
S1,S3,S5,S6,NS1, float, silica	4	0.2
S2,S4,NS2,NS3	3.5	0.2

3.5.1   Testing

One sample was tested at a time. A new Vickers diamond indenter was used for the testing. The polished sides of the specimens were tested. All electronic equipment was turned on approximately thirty minutes prior to testing. A polished specimen was placed in a beaker containing the reagent alcohol and then ultrasonicated for approximately two minutes. The specimen was removed and allowed to dry in air. Care was taken to avoid touching the surface to be tested. The acoustic emission sensor was then mounted onto the sample using Dow Corning high-vacuum grease. The specimen was then placed on the holder (previously described in Section 2.3) The x-y-z stage, zoom lens, and fiber optic lamps were adjusted to obtain and image of the Vickers diamond tip. The sample was then raised carefully using the z-stage until it just made contact with the diamond, at which point it was lowered. The x-y stage was then adjusted to reveal a fresh area of sample, and the diamond tip brought back into focus.

After inputting the contact parameters into the computer program, testing commenced by starting all systems (recording microindenter, AE, and VCR) at the same time. Any acoustic emissions produced were visible on the computer screen of the acoustic emission system. All recording microindenter and acoustic emission data were saved after each test. After a single test was performed, the x-y stage was moved to reveal a new area of sample. Care

was taken to space indentations far enough apart to avoid interaction. The acoustic emission sensor remained within 1 to 1.5 cm from the indentation site at all times. Ten indentation tests were made per sample. Data analysis included examining the acoustic emission data, the load-displacement data, and the recorded video data. All were used to determine the type of cracks formed, and the loads at which they initiated.

Testing was conducted under ambient conditions. The temperature and relative humidity were monitored for all tests. The temperature and relative humidity between testing specimens were 23 ± 2 °C, and 28 ± 11%, respectively. An air conditioner was used to help keep the humidity of the laboratory air low and reproducible between tests.

3.5.2   Post-Test Microscopy

After a set of contact parameters was investigated, the sample was removed and the vacuum grease cleaned off. Post-test microscopy of the indentation sites was conducted using a Reichert-Jung optical microscope[*]. Median-radial cracks lengths were measured from the center of indentation to the crack tips in transmitted light. Approximately 90 minutes would pass from the time the first indentation test was performed before the crack lengths could be measured. Lateral crack sizes were measured in reflected light from the center of indentation to the edge of the crack, at approximately

[*]Reichert-Jung POLYVARMET Optical Microscope, Austria

its midpoint. Indentation diagonal lengths were measured for each indentation as well, in reflected light. Vickers hardness numbers were calculated from the measured indentation diagonal lengths using Eq. 8. Digital images of the indentation sites were taken.

3.5.3   Load-Displacement Data Analysis

Examination of the load-displacement curves from the crack initiation tests revealed that, for a majority of the tests, irreversible deformation of the sample stage occurred during testing, resulting in higher-than-normal values of the maximum penetration and residual indentation depth. This deformation was due to 'settling' of the stage in the z-direction (vertical direction), brought about whenever the z-stage was adjusted between tests either to clean the diamond tip, when necessary, or to reposition the specimen. A set of indentation tests were conducted to verify this. Because of this effect, a second set of indentation tests were conducted on the specimens in which the z-stage was not moved.

The load-displacement curves obtained from these additional tests were used to determine elastic recovery, hardness under maximum load (LVH_{max}), maximum penetration depth (p_{max}), and residual indentation depth (p_o). Although a compliance value for the loading portions of the curves obtained in Section 2.3 was calculated (this is *not* p_o shown in Section 2.3), after analysis of the curves using this value, it was decided that more accurate

comparisons between glasses would be obtained if the curves were analyzed as-is, i.e., without accounting for the machine compliance. It should be recognized that even without taking into account the machine compliance, the value of p_o should still be indicative of the actual residual indentation depth, since all elastic deformations are recovered on unloading, leaving only the residual portion of deformation.

The elastic recovery was obtained by subtracting p_o from p_{max}. The last penetration data point on the unloading cycle was taken as p_o, the residual indentation depth. The energy of deformation is the area bound by the loading and unloading curves, and represents the energy consumed in permanently deforming and fracturing the glass. The Kaleidagraph[*] graphing program was used to integrate the loading and unloading curves of the additional tests. The program fitted the curves using a quadratic equation having the form: $y = ax^2+bx+c$. The area bound by the unloading curve, which represented the elastically recovered energy of specimen and machine, was subtracted from the area bound by the loading curve, which represented the total energy put into the specimen and machine. The difference equaled the energy (work) of permanent deformation. The Vickers hardness under maximum load (LVH_{max}) for each test run was calculated using the following formula:

[*]Kaleidagraph Version 3.09, Synergy Software Corp., USA

$$LVH(Kg/mm^2) = \frac{37.84\,F_{max}(g)}{p_{max}^{\,2}(\mu m)^2} \qquad (12)$$

Equation 12 can easily be derived by noting that d^2 in Eq. 8 is equal to 49 p^2, since d = 7p for a Vickers diamond. The computer curve fitting was checked by hand calculation (integration) of a sample curve.

3.5.4   Effect of Larger Indentation Rate

In order to study the effect of indentation rate on the crack initiation behavior of the glasses, a conventional indentation tester, which applies a constant load, was used. A much faster rate of penetration of the indenter on both loading and unloading occurred. Although exact rates of penetration could not be determined, the full load was transferred in several seconds. In comparison, with the 0.2 µm/s displacement rate of the recording microindenter it took about 2 minutes to reach a 1 Kg load in most glasses. With a conventional indentation tester, once the indenter tip touches the specimen and the loading mechanism shifts all mass onto the loading arm, the indenter will sink-in due to the applied load until reaching an equilibrium depth. This would occur at a rate that would likely be faster the greater the contact load and the 'softer' the specimen, especially during the initial stages of contact when the stress is extremely high. On unloading, the

indenter was withdrawn much faster, on the order of fractions of a second, compared to ~ 80 seconds for a test with the recording microindenter.

A LECO conventional hardness tester‡ utilizing a dead-weight loading system was used to make Vickers indentations on the optical and float glass specimens at 1 Kg load. The maximum load was held on the specimens for 5 seconds before being removed. Polished and annealed specimens were cut to ~ 1 millimeter thickness using a small diamond saw and cutting fluid. The bottom (cut) surface was ground with SiC paper and water to reduce thickness to 1 millimeter if the sample was too thick, while the polished surface was left alone. Specimens were then cleaned in reagent alcohol in ultrasound, then gently dried with laboratory towels. A starter crack was introduced onto the polished surface of each specimen by scoring with a diamond cutting wheel.

Indentations were then made in line with the starter crack such that any median-radial cracks which formed were collinear with the starter crack. At least five indentations were made in a straight line, with the tips of the median-radial cracks collinear with each other, but far enough apart so as to avoid interaction. Specimens were placed directly on the stage without a holder, since the small thickness of the specimens would have caused them to bend had a holder been used. Indentations were made in ambient conditions, with the temperature and relative humidity varying 23 ± 3 °C and 45 ± 5%, respectively, over the course of testing all specimens. All optical glasses were

‡LECO V-100-A2 Hardness Tester, LECO Corp., USA

examined, as was the float glass. Digital images of the indentation sites were taken. Measurements of the indentation diagonal lengths and crack lengths were made as well. Vickers hardness was calculated for all indentations in which the indentation diagonal lengths could be accurately measured.

The specimens were then fractured along the starter crack, cleaving the indentations in half, along an indentation diagonal. The halves of the indentations were then examined with the optical microscope, and measurements were made of the features, including the 'plastic' zone width and depth, the depths of cracks, and the depths and widths of the indentations. Digital images of the cross-section fracture surfaces were taken. The same fractured specimens were examined in a scanning electron microscope[*] (SEM) in secondary electron mode, to examine in detail the 'plastic' deformation zones. Other sets of indentations were made at 1 Kg, and the surfaces of the indentations examined in the SEM.

[*]Amray Model 1810 SEM, Amray Corporation, USA

4.   RESULTS AND DISCUSSION

4.1   Classification of Glasses Based on Indentation Deformation and Fracture Behavior

Of the nine optical glasses tested, two glasses (S1 and S2) could best be classified as 'anomalous,' while the rest were 'normal' with respect to their indentation deformation and fracture behavior. The Suprasil 312 vitreous silica and 7740 Pyrex™ borosilicate glasses behaved 'anomalous.' The float glass was interesting in that it exhibited some signs of 'anomalous' behavior, in the form of partial ring cracking at high loads, as well as a lack of well-defined narrow shear-'flow' lines, and so is described as 'normal-anomalous.' The potassium phosphate glass, NS2, also exhibited partial ring cracking at high loads, however, the abundance of relatively fine shear-'flow' lines within the plastic zones indicated this glass deformed in a mostly 'normal' manner. Table XII summarizes this information. Only the most 'anomalous' glasses exhibited extensive ring-cone cracking at high loads. Many of the 'normal' glasses exhibited median-radial cracking on loading, a feature which in the past was thought to be a characteristic of only 'anomalous' glasses.[7,11]

Table XII. 'Normal' or 'Anomalous' Classification of Glasses.[*]

Glass	Glass Type	Ring-Cone Cracking
S1	A	yes
S2	A	yes
S3	N	no
S4	N	no
S5	N	no
S6	N	no
NS1	N	no
NS2	N	partial ring
NS3	N	no
Float	N-A	partial ring
Suprasil 312 v-SiO$_2$	A	yes
7740 Borosilicate	A	yes

[*]'N' for 'Normal' and 'A' for 'Anomalous'

4.2   Crack Initiation Behavior

4.2.1   S1 (Lead-Alkali-Silicate)—'Anomalous'

This glass was 'anomalous' with respect to its permanent deformation behavior. Table XIII summarizes the crack initiation behavior of this glass. Median-radial cracks initiated on both the loading and unloading cycle. However, the majority of growth took place on unloading. In addition, what were thought to be small partial ring cracks, or severe shear faults, formed around the indentations on loading. Usually, two median-radial cracks would initiate simultaneously, followed by the initiation of more median-

Table XIII. Glass S1 Crack Initiation Behavior Summary.[*]

S1	Ring-Cone Loading	First Median-Radials Loading	Last Median-Radials Loading	First Median-Radials Unloading	First Laterals Unloading
1 Kg (0.2 µm/s) *77°F, 49 % RH*	small, partial ring cracks	317 ± 200 g [70 %]	622 ± 182 g	512 ± 298 g (51 ± 30 %) [80 %]	23 ± 21 g (2.3 ± 1.1 %) [100 %]

[*] Numbers in brackets represent percentage of tests displaying that behavior, while numbers in parentheses indicate percentage of the maximum indentation force at which initiation occurred. Errors are ± one standard deviation

radial cracks at separate instances on either loading or unloading. Lateral cracks initiated near complete unloading for all tests.

4.2.1.1 Post-Test Optical Microscopy

Figure 14 shows an indentation and associated fracture for a test in glass S1. The median-radial cracks showed a tendency to not extend from exactly the indentation corners. Three smaller radial cracks are seen near the top and right corners. It is clear that more than one initiation attempt was made at these two corners. Sub-surface lateral cracks are clearly seen, as are shear faults parallel to the indentation sides. The faults appear wide, particularly near the outer indentation edges, are spaced relatively far apart, and appear to more resemble shear-induced cracks than shear-induced flow lines. The top and right median-radial cracks have initiated from an outer shear fault. The faults have a zigzag (staircase) shape as they make their way to the indentation corners. This behavior was seen in other indentations as well. In this particular indentation, all median-radial and secondary (smaller)

radial cracks initiated on indenter unloading. The outermost faults faintly resemble partial ring cracks, although other indentations more clearly showed the partial ring cracks. Bright regions can be seen between some shear faults, indicating lateral surface cracking took place there.

Doremus[28] considers a shear fault to be a distorted region of the structure, several hundred nanometers wide, but with no separation of material. Bonds are broken and reformed, however not necessarily in the same structural configuration as in the pristine glass. On the other hand, a crack is a defect in which distinct solid surfaces are created and separated from each other by several lattice distances.[28] *In the current work all shear-induced markings will be called shear faults.* It will become clear that some of the faults are more crack-like than flow-like, and are best termed shear cracks, while others appear very narrow and are more aptly called shear flow lines. In addition, some shear faults exhibit both types of behavior along their length, making classification difficult. Distinction will be given only when it is clear as to the nature of the marking, otherwise the term shear fault will be used. In either case, compression-induced shear stress produces the faults, with the nature of the fault (crack- or flow-like) dictated by glass composition, and most likely indentation load as well.
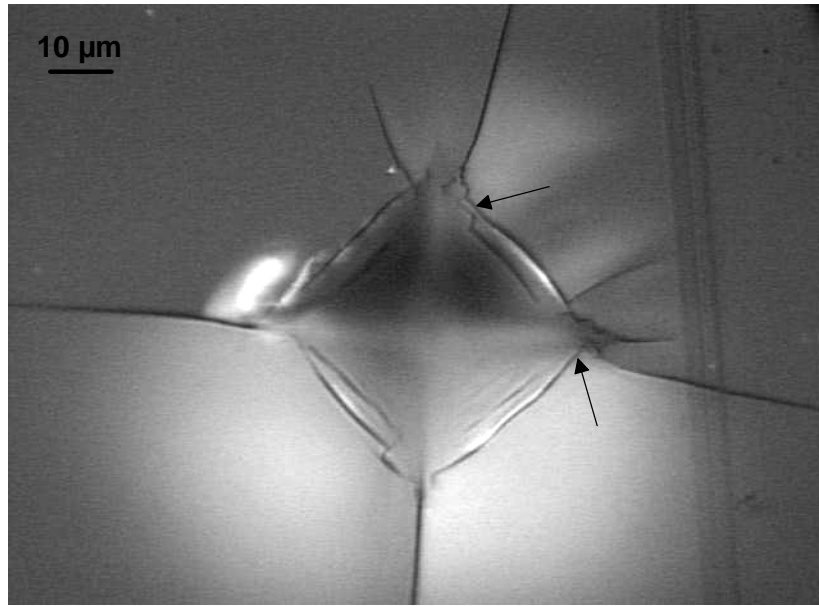
Figure 14. *Indentation and associated fracture produced in glass S1 with the recording microindenter from 1 Kg (0.2 µm/s) test. Top and right median-radial cracks appear to extend from outer shear faults, indicated by arrows. Image width:133 µm. Refl. light, BF, 625x original photo magnification.*

4.2.1.2 Conventional Indenter: Surface and Sub-Surface Examination

The faster penetration rate of the LECO conventional indenter resulted in the formation of ring cracks in various stages of development, around 100% of the indentations at 1 Kg load. Figure 15 shows a typical indentation site. A surface ring crack is evident which extends about three quarters the way around the indentation. One indentation out of ten had some surface chipping from shallow lateral cracks.

Figure 16 is the corresponding cross-section of the right half of the indentation in Figure 15. The median-radial cracks extend well below the permanent deformation zone, which is devoid of shear faults. Two median-radial cracks are seen. The median-radial crack on the left showed some initial constraint at the surface before break-through. Lateral cracks are seen initiating from near the base of the deformation zone, and a portion of a small cone crack is apparent at the top left portion of the plastic zone near the surface.

4.2.1.3 SEM Examination

The scanning electron microscope revealed that some of the shear faults towards the outer edges of indentations were actually shear cracks. Figure 17 illustrates this, which is a portion of an indentation surface. It is also apparent that some of the shear faults alternate between being crack-like and flow-like along their length. In addition, the shear faults become progressively more narrow and less observable the closer to the center of indentation. A high-magnification image of the deformation zone beneath a 1 Kg indentation is shown in Figure 18.
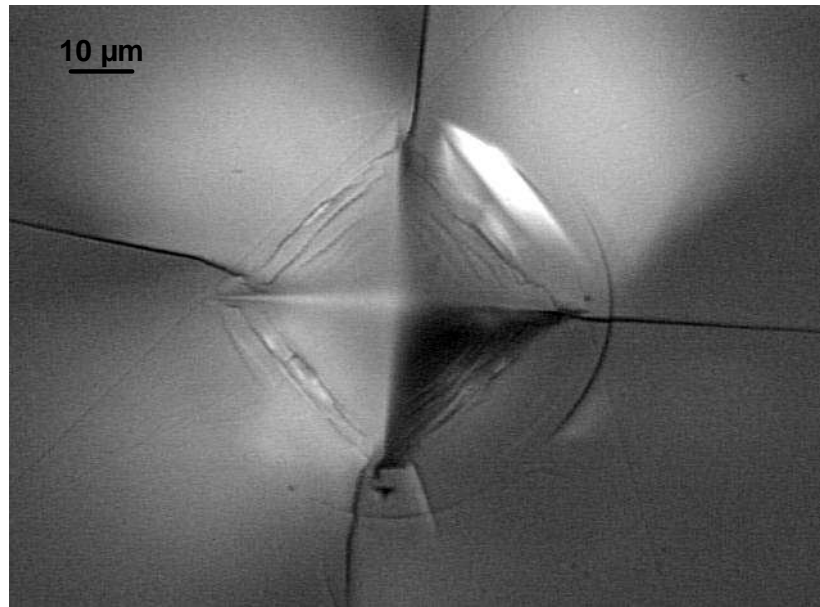
Figure 15. *A 1 Kg indentation site produced with the conventional indenter in glass S1. Image width: 133 µm. Refl. light, DIC (Differential Interference Contrast), 625x original photo magnification.*
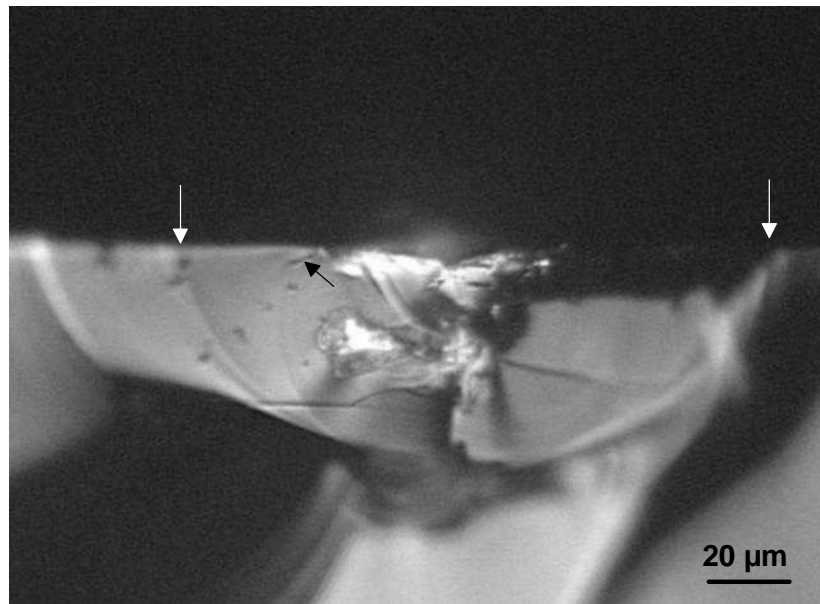
Figure 16. *Cross-section of the right half of the indentation in Figure 15. White arrows indicate approximately where the median-radial cracks terminate along the surface. Black arrow shows part of a sub-surface cone crack. Image width: 203 µm. Refl. light, BF, 400x original photo magnification.*
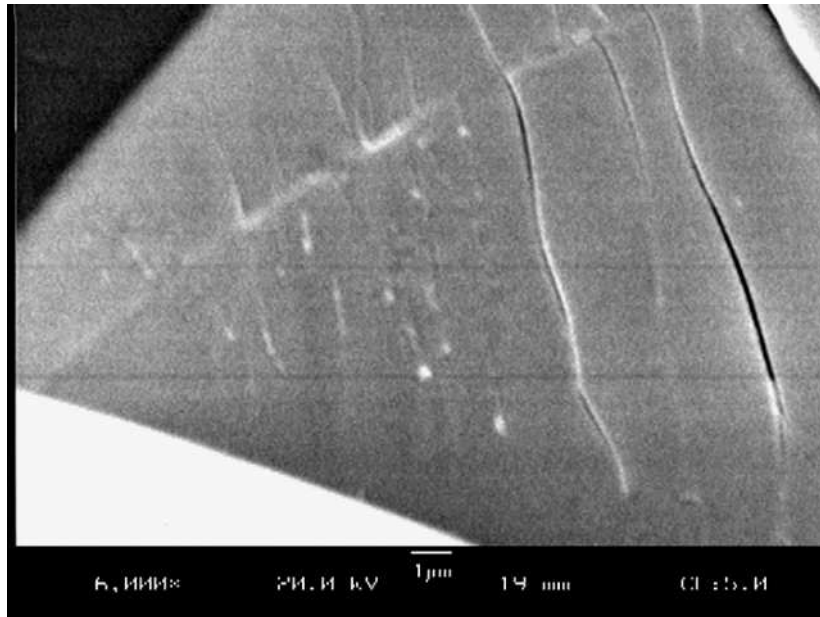
Figure 17. High-magnification image of a portion of a 1 Kg indentation in glass S1. Bar in legend is 1 µm. Secondary electron mode, 6000x original photo magnification.
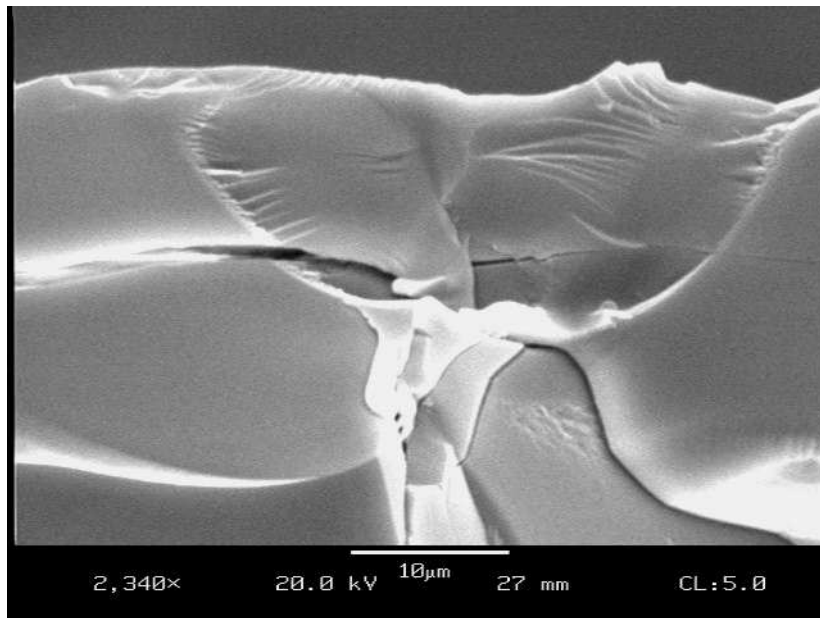
Figure 18. High-magnification image of the deformation zone beneath a 1 Kg indentation made with the conventional indenter in glass S1. Secondary electron mode, 2340x original photo magnification.

4.2.1.4 Surface Profilometry

A surface profilometer[*] was used to profile several indentations in glass S1 made at 1 Kg load with the LECO conventional indenter. One such profile is shown in Figure 19. Figure 20 is an image of the indentation that was profiled. The arrow points in the direction of scanning. A 10 mg stylus force was used, and the stylus tip was made of diamond. The stylus had a vertical range of 65 µm and a vertical resolution of ~ 1 Å. Five different indentations were scanned.

The depths (D) of the indentations were determined by examination of the raw data to find the minimum depth value. The features marked 'H' and 'L' in Figure 19 correspond to the maximum height of displacement above the baseline, and the length over which this displacement occurs, respectively. At first glance it appears that a significant amount of 'pile-up' has occurred around the indentation sides. However, considering this glass is 'anomalous,' and the fact that a steady rise in height begins to occur at a large distance away from the sides of the indentations, suggests that something else has occurred. Marshall et al.[58] noted a similar lifting of surface material around Vickers indentations in soda-lime-silicate glass, which they attributed to lateral cracks creating a compliant layer which is lifted-up after indentation. Although the value of 'L' is larger than the measured lateral crack size (≈ 35 µm from the edge of the indentation to the edge of the lateral cracks in
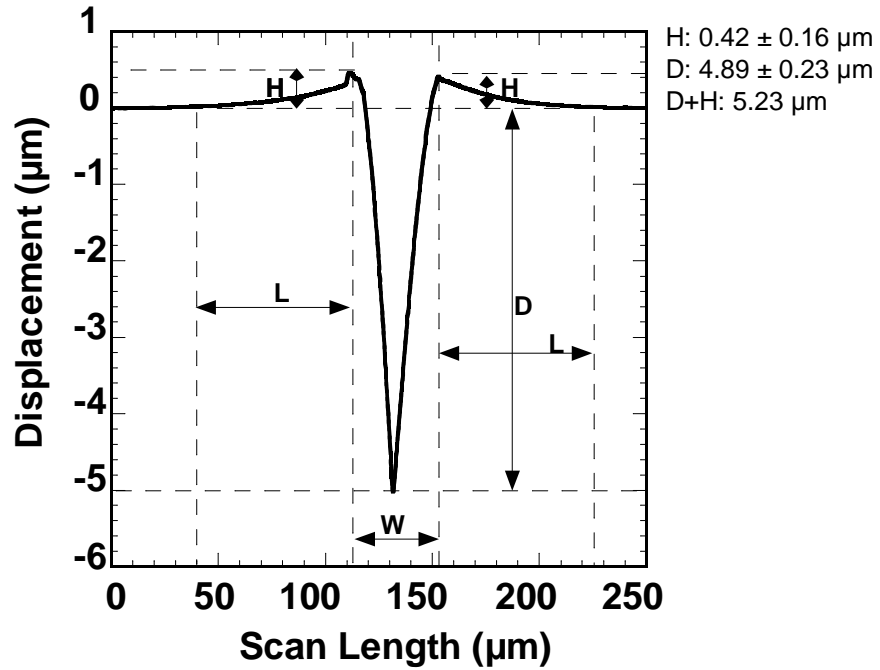
Figure 19. *Profile of an indentation made in glass S1 with the conventional indenter at 1 Kg load.*
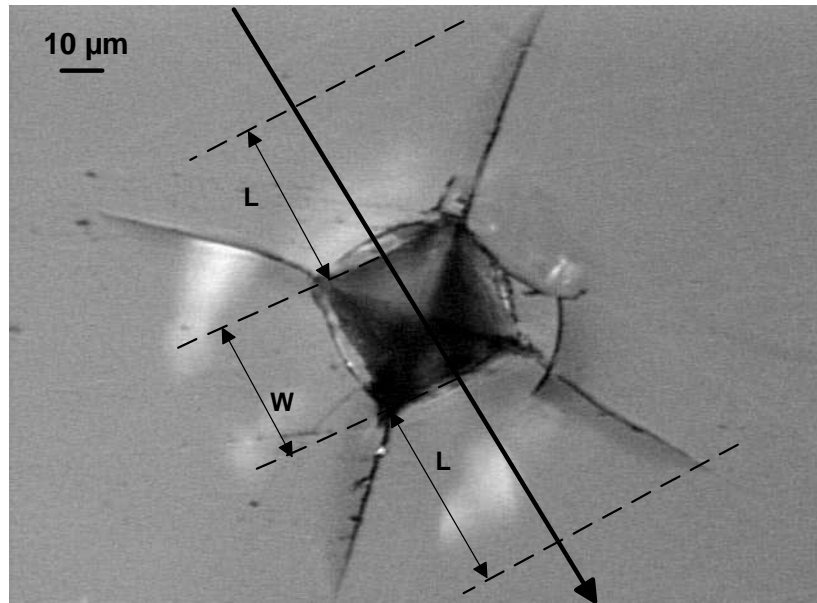
Figure 20. *Image of the indentation scanned in Figure 19. Indentation made with the conventional indenter with a 1 Kg load. Scan length of 250 µm exceeds length of arrow shown. Image width: 203 µm. Refl. light, DIC, 400x original photo magnification.*

Figure 20), it is likely that lifting of material extends beyond the visible indication of lateral cracking seen in this glass. The small, sharp rise in the profile on the left side in Figure 19 may be due to the surface ring crack seen in Figure 20.

4.2.2 S2 (Zinc-Silicate)-'Anomalous'

This glass was 'anomalous' with respect to its permanent deformation behavior. Table XIV summarizes the crack initiation behavior of this glass. Similar to glass S1, some small partial ring cracks appeared to form on loading. Median-radial cracks initiated on the unloading cycle. However in only 30% of the tests did median-radial cracks initiate. This was in contrast to glass S1, which had median-radials initiate for all tests. Lateral cracks only initiated in the three tests in which median-radial cracks initiated.

Table XIV. Glass S2 Crack Initiation Behavior Summary.

S2	Ring-Cone Loading	First Median-Radials Unloading	First Laterals Unloading
1 Kg (0.2 µm/s) *72°F, 21% RH*	small, partial rings	172 g (17.1 %) [30 %]	after unloading [20 %]

4.2.2.1 Post-Test Optical Microscopy

Figure 21 illustrates an indentation site in glass S2. The lateral crack seen exists only in a small area beneath the surface. The median-radial cracks extend from close to, but not exactly from, the indentation corners. A higher magnification image, Figure 22, illustrates this. The cracks appear to be extensions of shear faults. A zigzag pattern to these shear faults is apparent as the faults progress toward the indentation corners, bisecting other shear faults along the way.

4.2.2.2 Conventional Indenter: Surface and Sub-Surface Examination

Several major differences were seen in the fracture patterns between the static and recording microindenter tests at 1 Kg. Foremost, 100% of the indentations had median-radial and lateral cracks initiate, compared to 30% and 20% with the recording microindenter, respectively. A majority of the indentations had median-radial cracks extend from three or more indent corners. Figure 23 shows an indentation made in glass S2 with the conventional indenter. A well-developed ring crack was observed to form around 20% of the indentations, while the other 80% of the indentations had ring-cracks form part way around the indentations, i.e., partial ring cracks. There were more of these partial ring-cracks compared to the recording
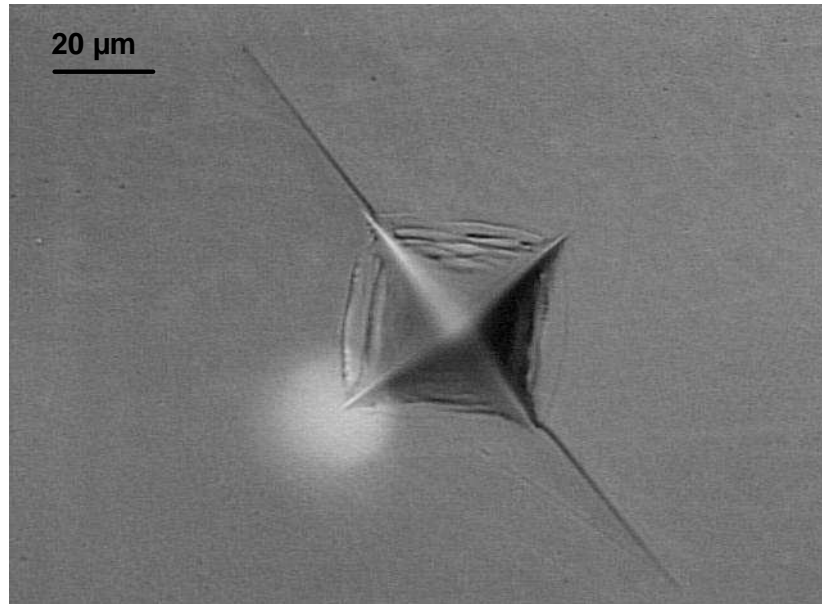
Figure 21. *Indentation and associated fracture produced in glass S2 from 1 Kg (0.2 µm/s) test. Lateral crack is localized in a small area. Image width: 166 µm. Refl. light, DIC, 500x original photo magnification.*
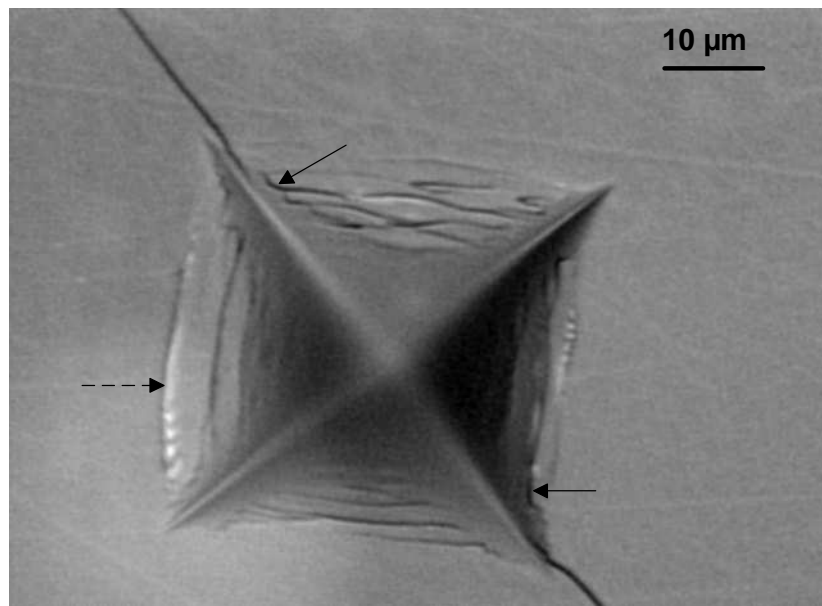
Figure 22. *Higher magnification image of indentation in Figure 21, showing how median-radial cracks, particularly top left crack, appear to extend from outer shear faults, which are indicated by the solid arrows. Dashed arrow indicates a partial ring/shear crack. Significant elastic recovery of indentation sides is evident. Image width: 83 µm. Refl. light, DIC, 1000x.*
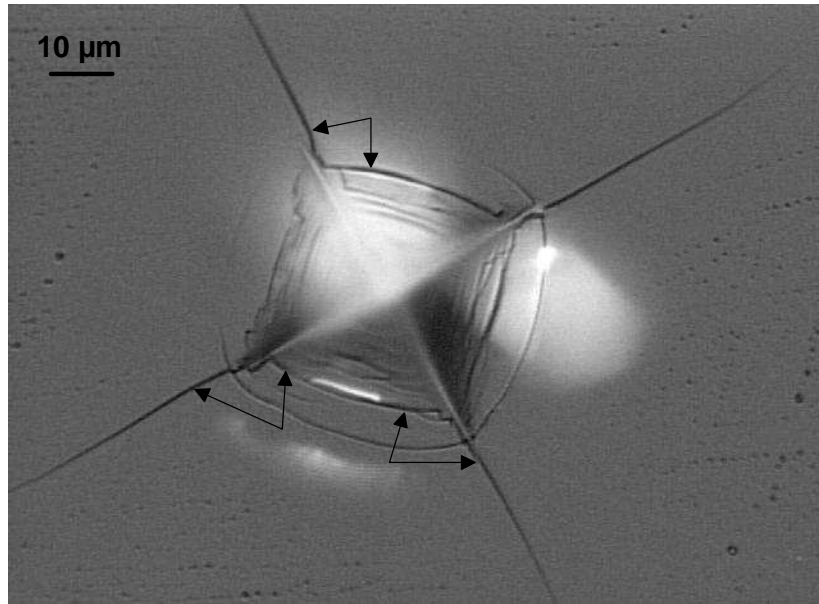
Figure 23. A 1 Kg indentation site in glass S2 produced with the conventional indenter and 1 Kg load. A well-developed surface ring crack is clearly visible. Double arrows indicate shear fault/median-radial crack pair. Image width: 133 µm. Refl. light, DIC, 625x original photo magnification.
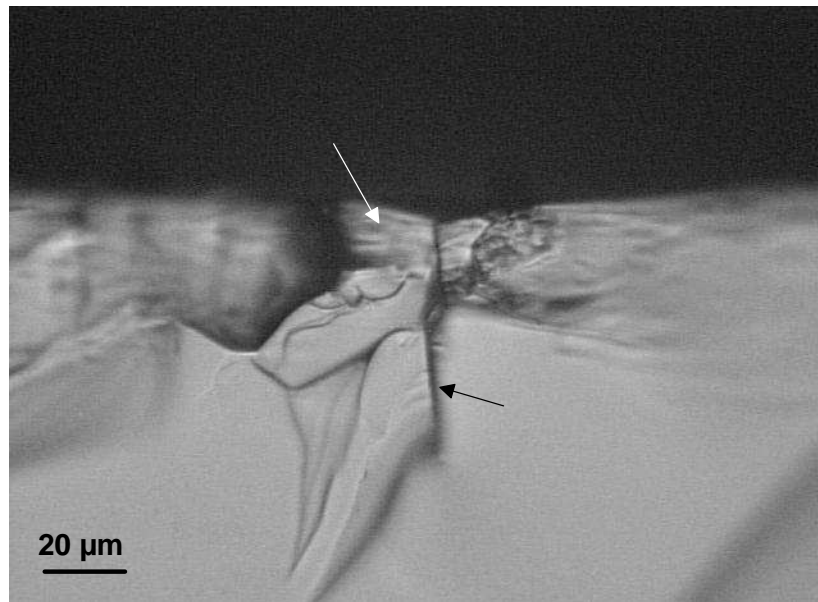
Figure 24. Cross-section of an indentation made in glass S2 with 1 Kg load with the conventional indenter. White arrow indicates deformation ('plastic') zone, and black arrow a median-radial vent. Image width: 203 µm. Trans. light, BF, 400x original photo magnification.

microindenter tests. Median-radial cracks are seen extending from near all four indentation corners. Three such cracks are extensions of outer shear faults, as indicated.

Figure 24 is a cross-section of a 1 Kg indentation in glass S2 made with the conventional indenter viewed in transmitted light. A median-radial vent is seen extending from the rather ill-defined deformation zone. This vent also appears to extend through the entire zone. Several lateral cracks are seen extending from the base of the deformation zone.

4.2.2.3 SEM Examination

Figure 25 is a SEM image of a 1 Kg indentation in glass S2 made with the conventional indenter. Median-radial cracks are seen extending from three indentation corners. A small amount of material has been lifted from the surface in the bottom-left indent face. In Figure 26 a higher magnification image of this indentation site is shown. The compressive stresses in the plastic zone prevent the median-radial crack from propagating further into the indentation.

4.2.2.4 Surface Profilometry

Figure 27 is a profile of an indentation made at 1 Kg with the conventional indenter in glass S2. The measured indentation width, W, is ~ 40 μm. The calculated width is ~ 42.5 μm. The values are in good agreement. Similar features were observed as for glass S1, namely a lifting of surface material most pronounced closest to the sides of the indentation, which gradually decreases further from the sides. Figure 28 shows the indentation that was profiled. The lifting of surface material, indicated by 'H', was less than glass S1.
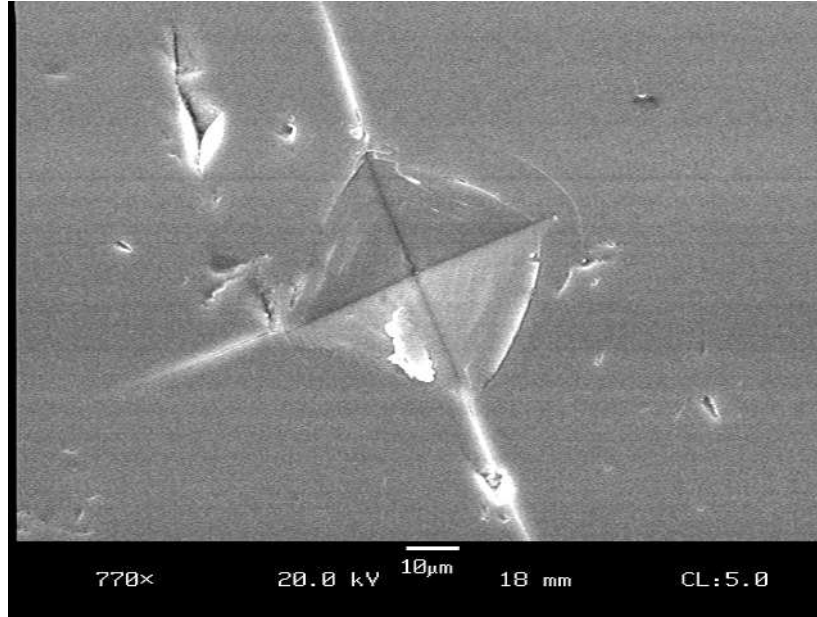
Figure 25. *SEM image of a 1 Kg indentation site in glass S2 made with the conventional indenter. A small partial ring-crack is present outside the right indentation corner. Secondary electron mode, 770x original photo magnification.*
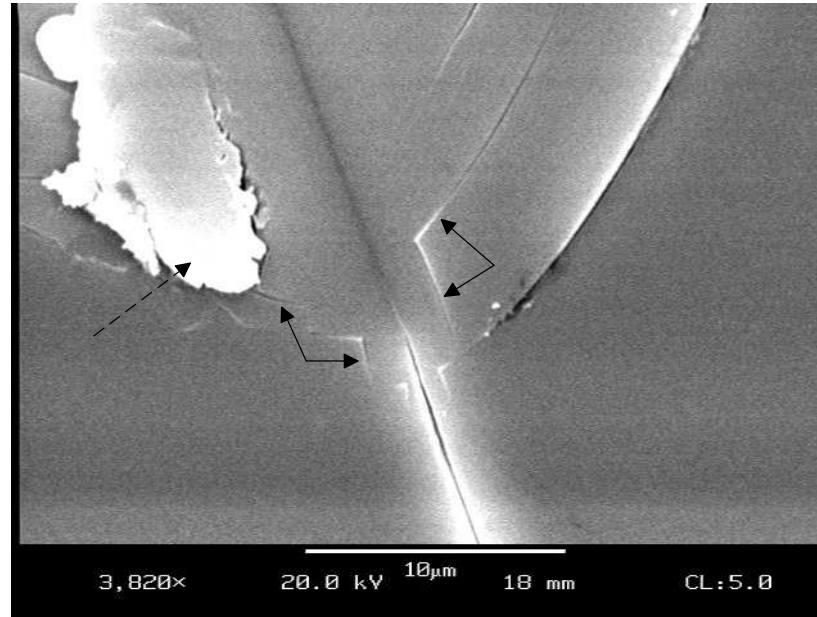
Figure 26. *Higher magnification SEM image of indentation in Figure 25. The two double arrows indicate shear fault/radial crack pairs. The broken arrow designates a glass chip uplifted from the indentation. Secondary electron mode, 3820x original photo magnification.*
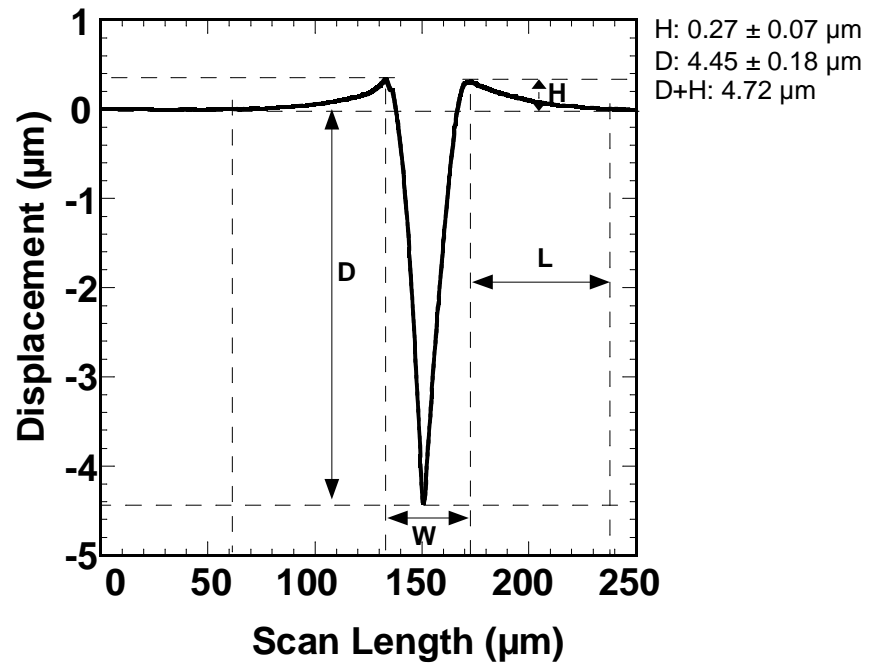
Figure 27. *Profile of an indentation made in glass S2 with the conventional indenter at 1 Kg load.*
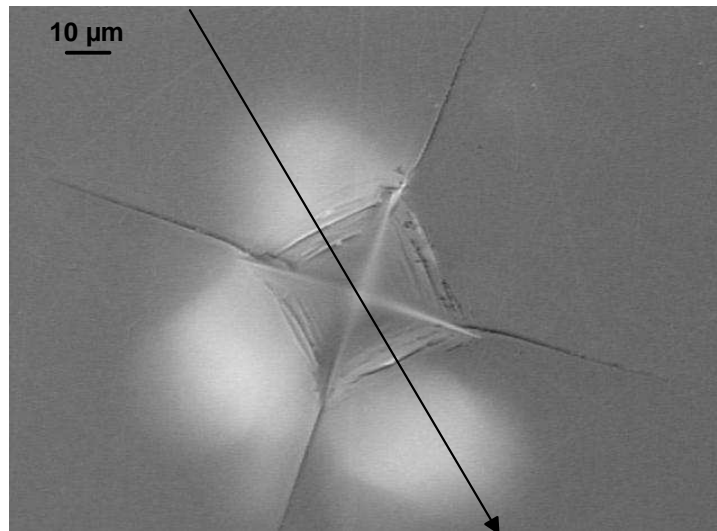
Figure 28. *Image of the indentation profiled. Scan length of 250 µm exceeds length of arrow shown, which indicates scan direction. Image width: 166 µm. Refl. light, DIC, 500x original photo magnification.*

4.2.3 S3 (Barium-Borosilicate)-'Normal'

This glass was 'normal' with respect to its permanent deformation behavior. Table XV summarizes the crack initiation behavior of glass S3. Median-radial cracks initiated on the loading and unloading cycles. On loading, what appeared to be two median-radial cracks would initiate first, followed by additional median-radial cracks, or none at all. The additional median-radial cracks would always initiate at separate instances. The majority of growth of the median-radial cracks took place on unloading. In 50% of the tests all median-radials initiated on unloading. What was thought to be a lateral crack initiated on loading in one test. Lateral cracks initiated on unloading for all tests.

Table XV. Glass S3 Crack Initiation Behavior Summary.

S3	First Median-Radials Loading	Last Median-Radials Loading	First Laterals Loading	First Median-Radials Unloading	First Laterals Unloading
1 Kg (0.2 μm/s) *72°F, 16 % RH*	817 ± 130 g [50 %]	n/a	~ 684 g [10 %]	867 ± 94 g (87 ± 9 %) [100 %]	170 ± 89 g (17 ± 9 %) [100 %]

4.2.3.1 Post-Test Optical Microscopy

Figure 29 illustrates an indentation and associated fracture for these tests. Lateral cracks give rise to the bright reflections beneath the surface. A large shallow lateral crack is present in the bottom-right quadrant, whose leading edge is just below the surface, forming a curved line. A higher magnification image of this same indentation is shown in Figure 30, where the image has been rotated ~ 90°. The shallow lateral crack is in the lower quadrant, where the white reflections are brighter compared to the other quadrants, indicating a more surface-localized crack. The shear faults appear very narrow, and thus resemble 'flow' lines more than cracks. In general, the median-radial cracks extended from closer to the indentation corners compared to 'anomalous' glasses S1 and S2.
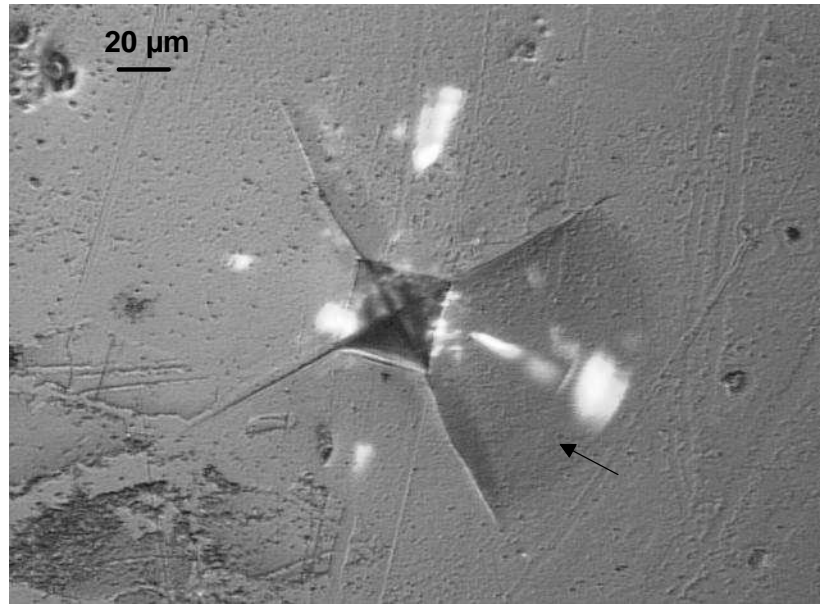
Figure 29. Indentation site produced in glass S3 from 1 Kg (0.2 µm/s) test. Outline of a shallow lateral crack is seen in lower right quadrant, indicated by arrow. Image width: 329 µm. Refl. light, DIC, 250x original photo magnification.
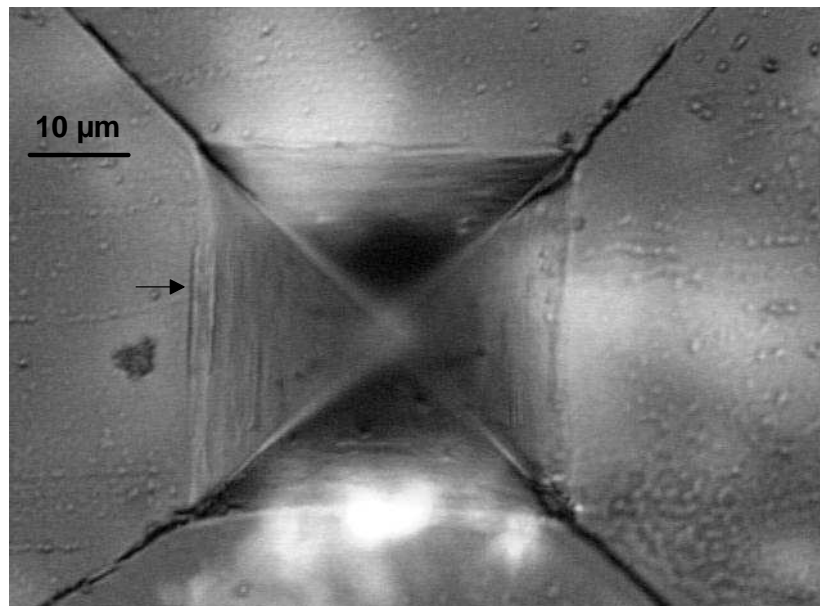
Figure 30. High-magnification image of same indentation shown in Figure 29. Arrow indicates a possible shear crack along the outer indentation edge. Image width: 83 µm. Refl. light, DIC, 1000x original photo magnification.

4.2.3.2 Conventional Indenter: Surface and Sub-Surface Examination

One difference between the conventional and recording microindenter tests was in the percentage of tests in which shallow lateral cracks chipped away surface material. In 40% of the indentations made with the conventional indenter shallow lateral cracks chipped away surface material, compared to 0% with the recording microindenter.

Another difference was that a greater number of shear faults, which also appeared wider, were observed along the outer edges of the indentations. A greater number of these faults appeared more crack- than 'flow'-like, compared to the recording microindenter indentations. The outer faults in general also exhibited more curvature along their length. Figure 31 is one such indentation site in glass S3. Two areas of surface lateral cracks are seen along the top and right indentation sides as well. These cracks were also more numerous in these tests compared to the recording microindenter tests.

The cross-section of the indentation in Figure 31 is shown in Figure 32. The left half of the indentation is shown. The arrest line of a median (full-penny) crack is clearly seen. Judging from the shape of the arrest line, the crack was initially constrained from breaking through to the surface. Two lateral cracks can be seen extending from the base of the deformation zone. One particularly large lateral crack extends from the mid-portion of the
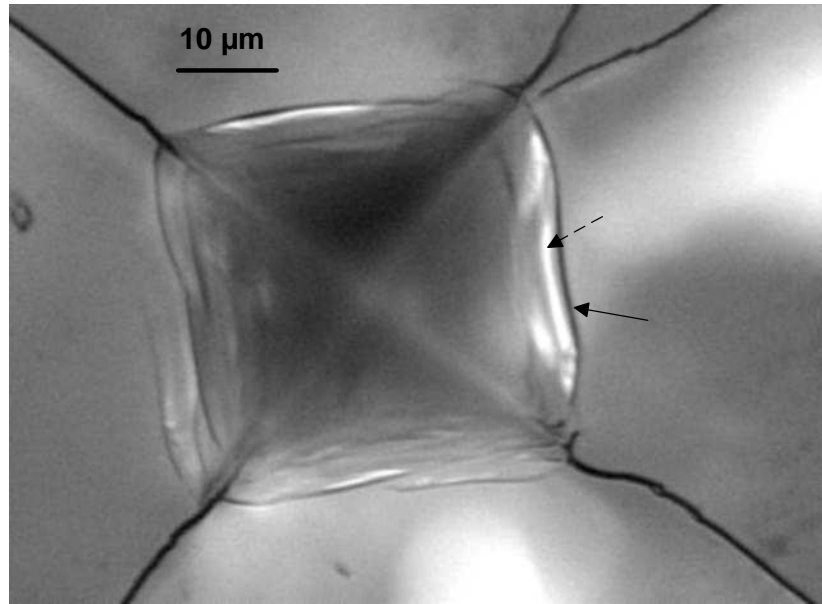
Figure 31. *Indentation site produced in glass S3 with 1 Kg load with the conventional indenter. Solid arrow indicates severe shear fault, while broken arrow illustrates surface lateral-like cracking between faults. Image width: 83 µm. Refl. light, DIC, 1000x original photo magnification.*
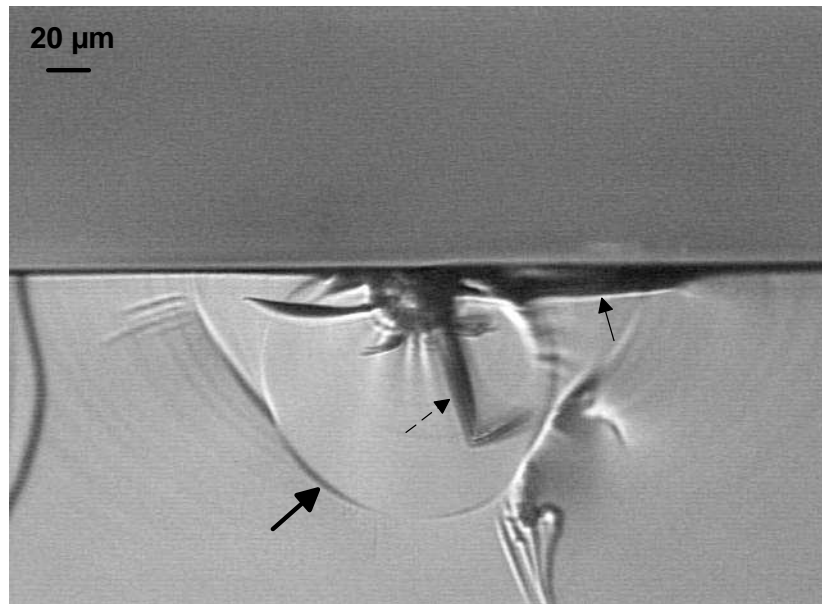
Figure 32. *Cross-section of the indentation shown in Figure 31. Solid arrow indicates shallow lateral crack, broken arrow indicates a median-radial vent crack, and large arrow median-radial arrest line. Image width: 405 µm. Trans. light, BF, 200x original photo magnification.*

deformation zone, on the left side, and curves up toward the surface. In general, a large number of lateral cracks were seen in the cross-section images of this glass. A large shallow lateral crack extends from the top portion of the deformation zone where it intersects the surface. A median-radial (vent) crack is seen extending from the base of the deformation zone, and which curves slightly upward at its lower portion. Most of the indentation cross-sections were similar to that seen in Figure 32.

4.2.3.3 SEM Examination

Figure 33 is a 1 Kg indentation site as seen in the SEM under high magnification. Shear faults are visible and very narrow, less than 1 µm wide. A high-magnification image of the sub-surface deformation zone, beneath a 1 Kg indentation, Figure 34, indicates that fine shear-'flow' lines are present, but are difficult to see because of the cracking.
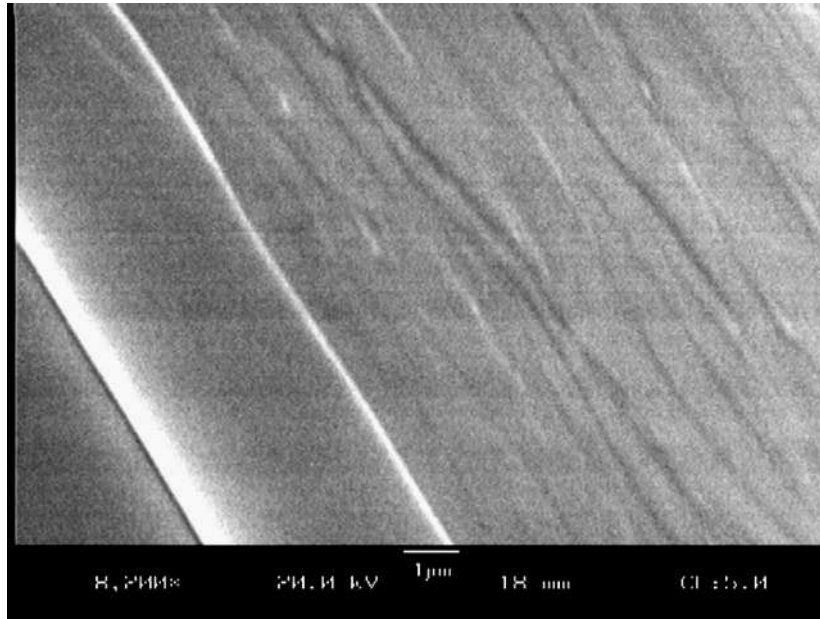
Figure 33. *High-magnification image of a portion of the surface of an indentation in glass S3 made with a 1 Kg load. Shear faults are apparent, and which appear narrow. Secondary electron mode, 8200x original photo magnification.*
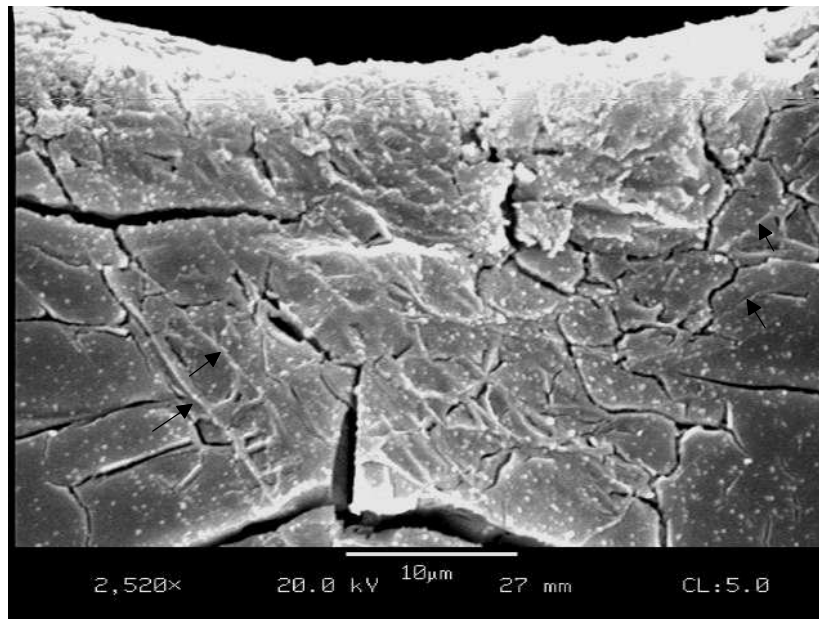
Figure 34. *SEM image of the sub-surface deformation zone beneath a 1 Kg indentation, which consists primarily of many cracks. Arrows indicate shear faults which appear more flow-like than crack-like. Secondary electron mode, 2520x original photo magnification.*

110

4.2.4 S4 (Lead-Borosilicate)-'Normal'

This glass was 'normal' with respect to its permanent deformation behavior. Table XVI summarizes the crack initiation behavior of this glass. Median-radial cracks initiated very early on the loading cycle for all contact conditions, where the majority of growth took place. In addition, compared to glasses S1 and S3, all median-radial cracks initiated on the loading cycle. In addition, lateral cracks initiated in all tests on the loading cycle. Lateral cracks initiated on unloading as well, and at considerably higher loads compared to glasses S1-S3.

Table XVI. Glass S4 Crack Initiation Behavior Summary.

S4	First Median-Radials Loading	Last Median-Radials Loading	First Laterals Loading	First Laterals Unloading
1 Kg (0.2 µm/s) *73°F/25 %*	40 ± 13 g [100 %]	161 ± 49 g [100 %]	370 ± 241 g [100 %]	500 ± 125 g (50 ± 12 %) [100 %]

4.2.4.1 Post-Test Optical Microscopy

Figure 35 shows a typical indentation site in glass S4 from the 1 Kg (0.2 µm/s) crack initiation tests. Median-radial cracks are clearly seen extending from the corners of the indentation. Shallow lateral cracks are present in the top, right, and bottom quadrants, and have partially broken through to the surface, but did not chip away material.

In a high-magnification view of the same indentation, shown in Figure 36, it is apparent that very narrow shear-'flow' lines formed, but shear cracks haven't. In addition, the median-radial cracks extend from very near the indentation corners, and propagate nearly collinear with the indentation diagonals for their entire length. This is in contrast to glasses S1, S2, and S3 to some extent.

4.2.4.2 Conventional Indenter: Surface and Sub-Surface Examination

The largest difference between the conventional and recording microindenter tests was in the percentage of tests in which shallow lateral cracks chipped away material i.e., 90% compared to 10%, respectively. Apparently the faster loading/unloading rate of the conventional indenter provided more driving force for shallow lateral crack breakthrough. A typical indentation site is shown in Figure 37.
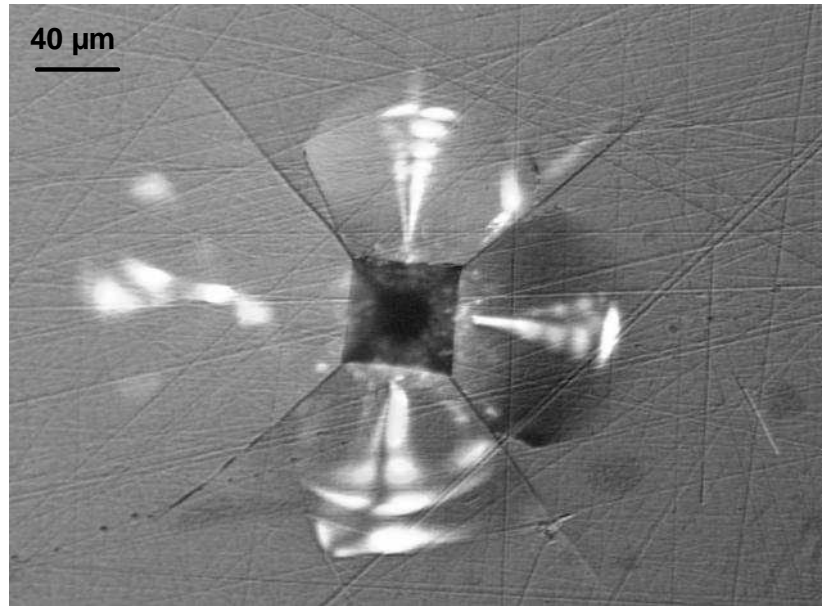
Figure 35. *Indentation site in glass S4 from 1 Kg (0.2 µm/s) test. Shallow lateral cracking is apparent in 3 of 4 quadrants. Image width: 405 µm. Refl. light, DIC, 200x original photo magnification.*
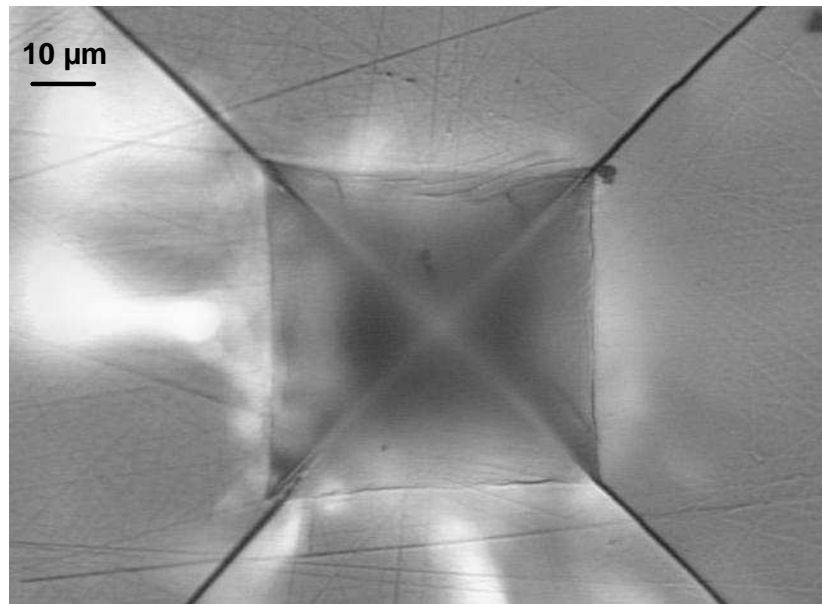
Figure 36. *Higher magnification image of indentation in Figure 35. Shear faults are very narrow. Median-radial cracks extend from very near the indentation corners. Several small cracks are visible within the indentation. Image width: 133 µm. Refl. light, DIC, 625x original photo magnification.*

113
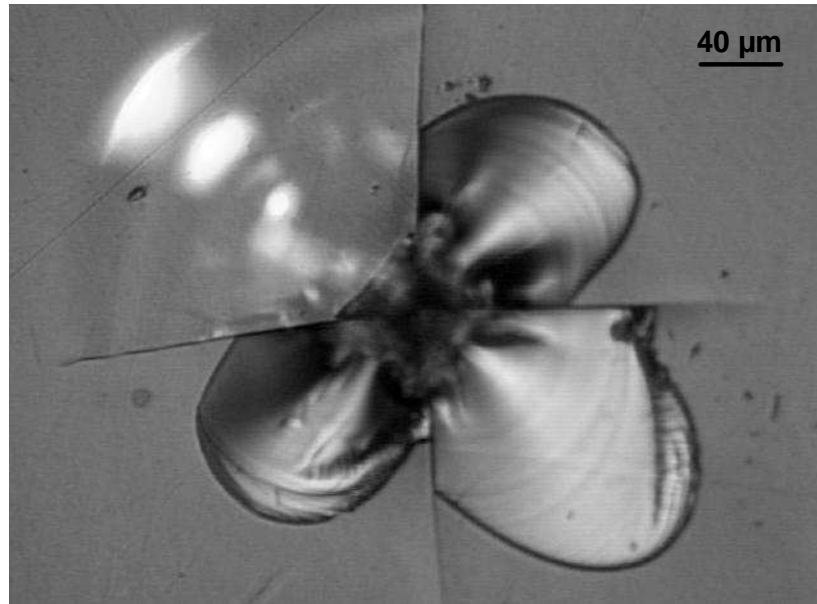
Figure 37. *Indentation site produced in glass S4 with the conventional indenter and 1 Kg load. Shallow lateral cracks have chipped away surface material. Image width: 405 µm. Refl. light, DIC, 200x original photo magnification.*
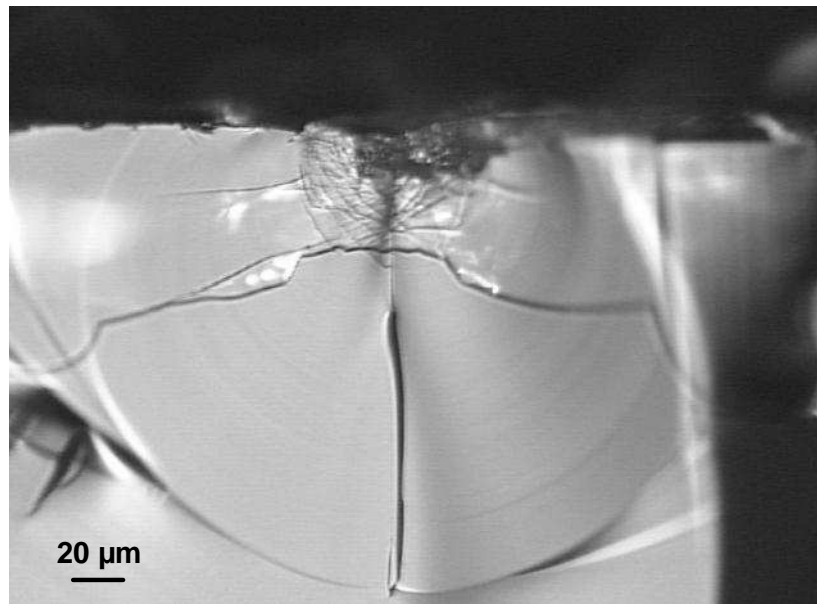
Figure 38. *Cross-section image of indentation site shown in Figure 37, showing the shear fault structure and the broken apart 'core' material comprising the top-central portion of the deformation zone. Image width: 329 µm. Refl. light, BF, 250x original photo magnification.*

114

Figure 38 is the corresponding cross-section of the left half of the indentation in Figure 37. Two well-developed median-radial cracks are seen in the plane of fracture, with a median-radial vent crack between them, extending from the base of the deformation zone. Large lateral cracks extend from the base of the deformation zone, downward into the glass, then level out. The deformation zone consists of well-defined shear faults, and a dark centralized core of material at the top-central portion of the deformation zone is apparent. This region appears very broken apart.

4.2.4.3 SEM Examination

A surface view of a 1 Kg indentation in glass S4 as seen in the SEM is shown in Figure 39, and reveals that shear faults are very narrow, spaced close together, but also difficult to see. A cross-section image of an indentation, shown in Figure 40, reveals a well-developed shear fault structure, with narrow fault lines.

4.2.4.4 Surface Profilometry

A profile of a 1 Kg indentation made in glass S4 is shown in Figure 41. A large amount of surface lifting has taken place on one side of the indentation. A shallow lateral crack chipped away material on the other side of the
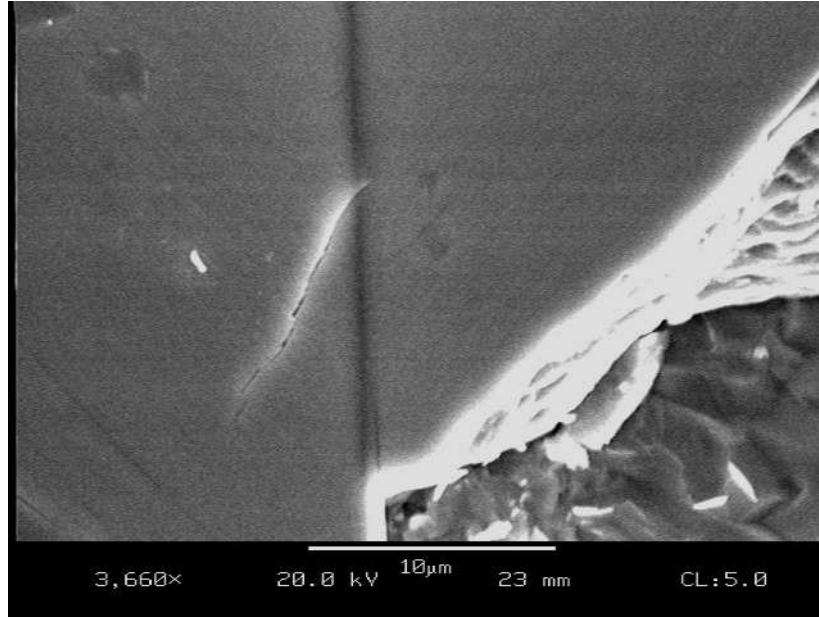
Figure 39. SEM image of a portion of the surface of a 1 Kg indentation in glass S4 made with the conventional indenter. A small crack within the indentation is apparent. Secondary electron mode, 3660x original photo magnification.
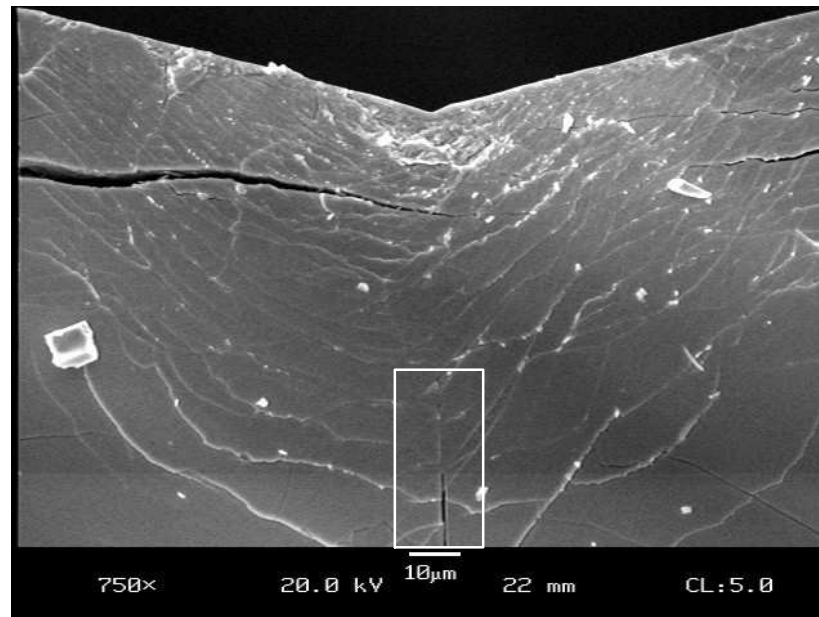
Figure 40. Detailed SEM image of the sub-surface deformation zone beneath a 5 Kg indentation in glass S4, illustrating the network of fine shear fault lines. Box highlights region where median-radial vent crack extends from. Secondary electron mode, 750x original photo magnification.
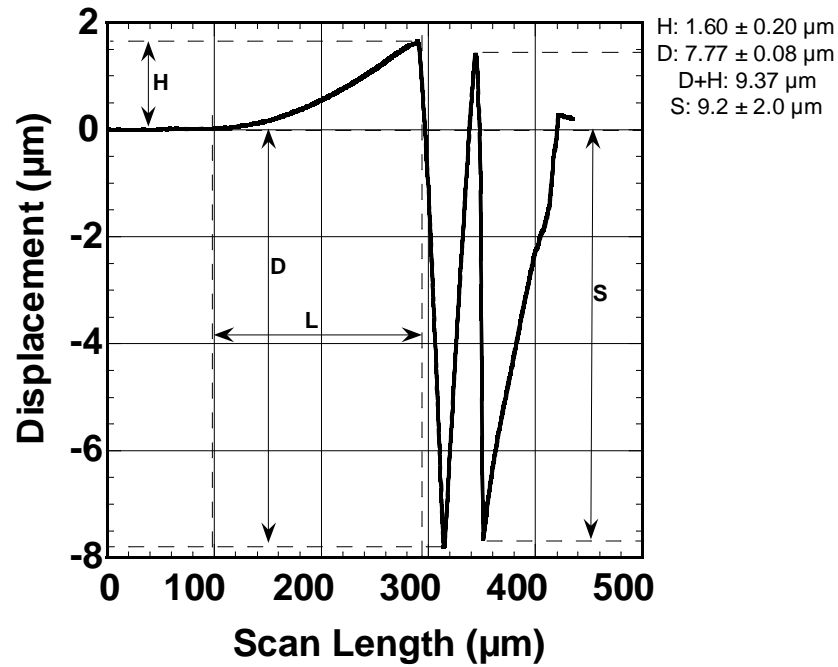
Figure 41. *Profile of a 1 Kg indentation in glass S4 made with the conventional indenter. Scan length ≈ 440 μm.*
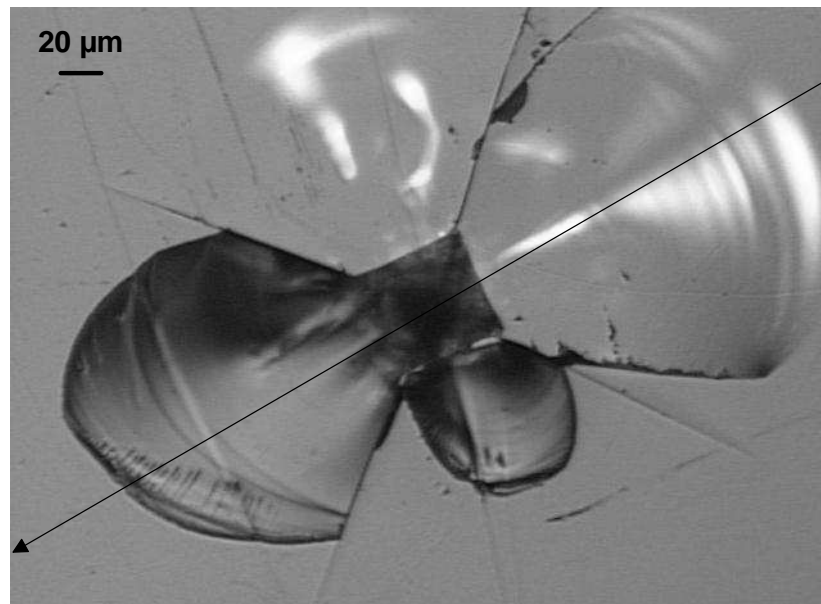
Figure 42. *Image of the indentation scanned in glass S4. Arrow indicates direction of scan. Image width: 405 μm. Refl. light, DIC, 200x original photo magnification.*

indentation, and therefore no surface lifting is seen. Figure 42 is an image of the indentation profiled. The depth of the crater left by the breakthrough of the shallow lateral crack is indicated by 'S', and extends down to roughly the same depth as the indentation. The length of the surface uplift region, 'L', is approximately 190 μm, which is similar to the length of the deep lateral cracks found in this glass i.e., ~ 173 μm.

4.2.5   S5 (Lanthanum-Borate)-'Normal'

This glass was 'normal' with respect to its permanent deformation behavior. The crack initiation behavior for this glass is summarized in Table XVII. Median-radial cracks initiated on both loading and unloading, similar to glasses S1 and S3, although at much lower loads compared to glass S3. In addition, the majority of median-radial growth took place on unloading. What were thought to be lateral cracks initiated on loading for a few tests (40%), though exact loads could not be determined. Lateral cracks initiated on unloading for all tests.

4.2.5.1 Post-Test Optical Microscopy

An indentation site in glass S5 from the crack initiation tests is shown in Figure 43. Median-radial and lateral cracks are apparent. A shallow lateral crack appears in the lower left quadrant. A higher magnification image of

Table XVII. Glass S5 Crack Initiation Behavior Summary.

S5	First Median-Radials Loading	Last Median-Radials Loading	First Laterals Loading	First Median-Radials Unloading	First Laterals Unloading
1 Kg (0.2 µm/s) *77°F/33%*	311 ± 116 g [100 %]	625 ± 230 g	[40 %]	635 ± 252 g (64 ± 25 %) [30 %]	132 ± 43 g (13 ± 4 %) [100 %]

this indentation site is shown in Figure 44. Shear faults are seen parallel to the indentation sides and are quite narrow. The median-radial cracks extend from close to the indentation corners.

4.2.5.2 Conventional Indenter: Surface and Sub-Surface Examination

The faster loading rate of the conventional indenter resulted in 40% of the indentations having shallow lateral cracks chip away surface material, in comparison to 20% for the 1 Kg (0.2 µm/s) indentations made with the recording microindenter. There was also a tendency for the outer shear faults to be slightly wider and more curved, especially near the indentation corners, compared to the recording microindenter indentations. Some surface lateral-like cracking between shear faults occurred for the static microindenter tests as well, which was mainly absent for the recording microindenter tests. Figure 45 illustrates an indentation made with the
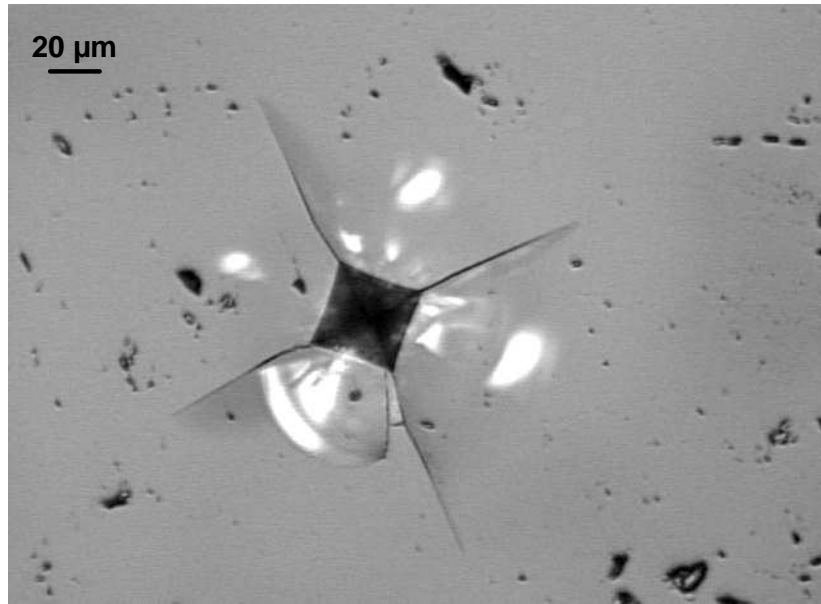
Figure 43. *Indentation site in glass S5 from 1 Kg (0.2 µm/s) test. Image width: 329 µm. Refl. light, DIC, 250x original photo magnification.*
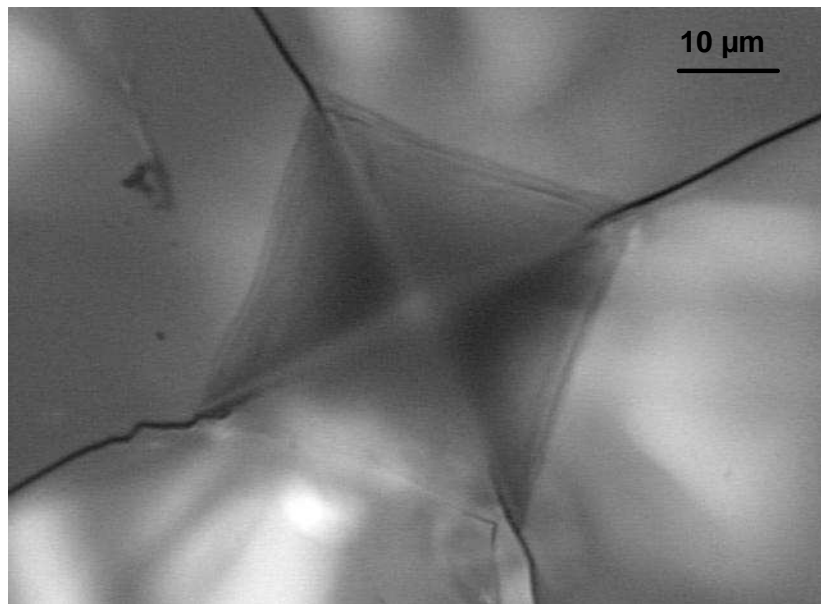
Figure 44. *Higher magnification image of same indentation shown in Figure 43. Image width: 83 µm. Refl. light, DIC, 1000x original photo magnification.*

conventional indenter at 1 Kg load.

Figure 46 is the corresponding cross-section of the indentation in Figure 45. Several features stand out. The deformation zone is completely broken apart, and a small portion of the right side of the indentation has been chipped away by a shallow lateral crack. One deep lateral crack appears to initiate from the base of the deformation zone, while a second extends from part-way down the median-radial vent crack. The two median-radial cracks in the plane of fracture both initiated before the median vent crack. Both of these cracks were initially constrained from breaking through to the surface due to high compressive stresses, as the arrest marks indicate. Arrest marks (lines) give the actual shape of the crack fronts, and hence the state and distribution of stress at the moment they are produced. Thus, these cracks either formed at a relatively high load on loading, or early on the unloading cycle, when the surface compressive stresses were high.

Another geometry seen is shown in Figure 47. Here, the surface compressive stresses must have been relatively low, since when the cracks popped-in, growth took place immediately along the surface. The cracks are concluded to have formed on unloading, since the median-radial vent crack initiated first, leaving the other two cracks to form at either higher loads on
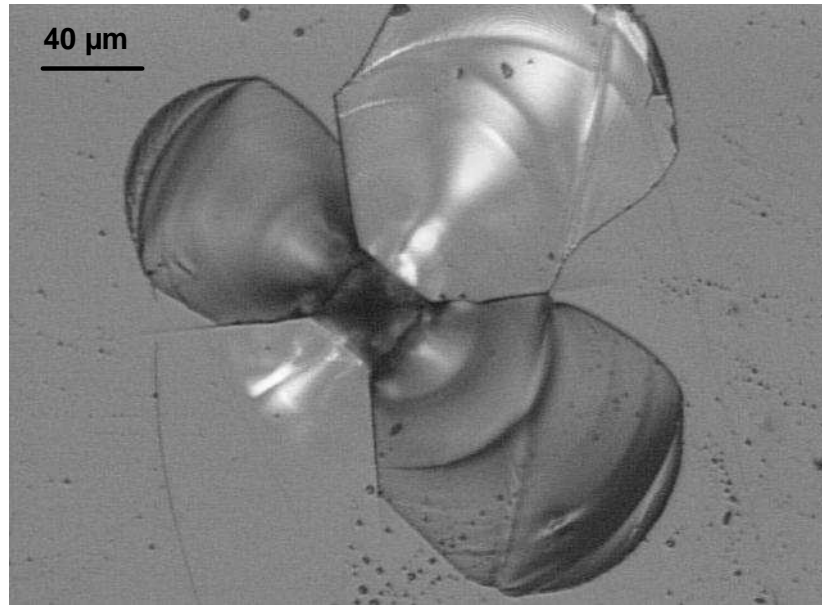
Figure 45. *Indentation site made in glass S5 with the conventional indenter and 1 Kg load. Extensive surface chipping is apparent. Image width: 329 µm. Refl. light, DIC, 250x original photo magnification.*
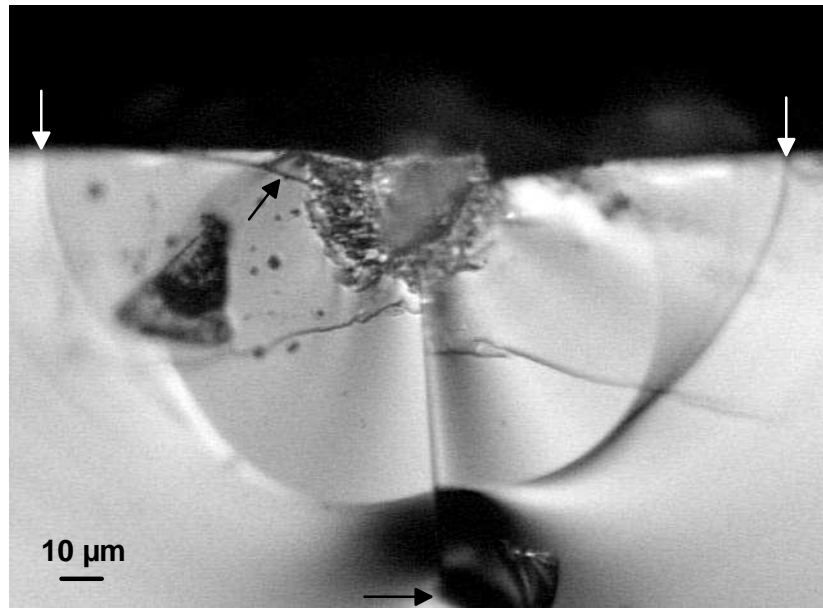
Figure 46. *Cross-section of the indentation shown in Figure 45. White arrows indicate, approximately, end of median-radial cracks along glass surface. Bottom black arrow indicates where median-radial vent crack stops, and top black arrow shows a shallow lateral crack intersecting the surface. Deformation zone is broken apart. Image width: 203 µm. Refl. light, BF, 400x original photo magnification.*

loading (in which case some evidence of surface compression, in the form of constrained crack growth at the surface, would be expected), or on unloading. The latter seems more probable. These observations are consistent with the sequence of initiation observed with the recording microindenter tests. Still another variation to the geometry is shown in Figure 48, a transmitted light image. Here, a full-penny median-radial is in the fracture plane, with a smaller median-radial extending downward from the deformation zone. Figures 47 and 48 illustrate an important point: how an indentation is sectioned determines the fracture pattern seen. If, for example, the indentation in Figure 48 was sectioned along the other diagonal, then a pattern like that seen in Figure 47 would result i.e., two half median-radials instead of the single 'full-penny' median-radial crack. On the other hand, if the indentation in Figure 47 were sectioned along the other diagonal, then a pattern like that in Figure 48 would most likely result. The median-radial vent extending from the base of the deformation zone in Figure 48 represents one of the other mutually orthogonal median-radial cracks (like those in the plane of fracture in Figure 47) intersecting the back free surface of the previously formed 'full-penny' median radial crack. Similar crack morphology behavior was seen in glass S3 as well.
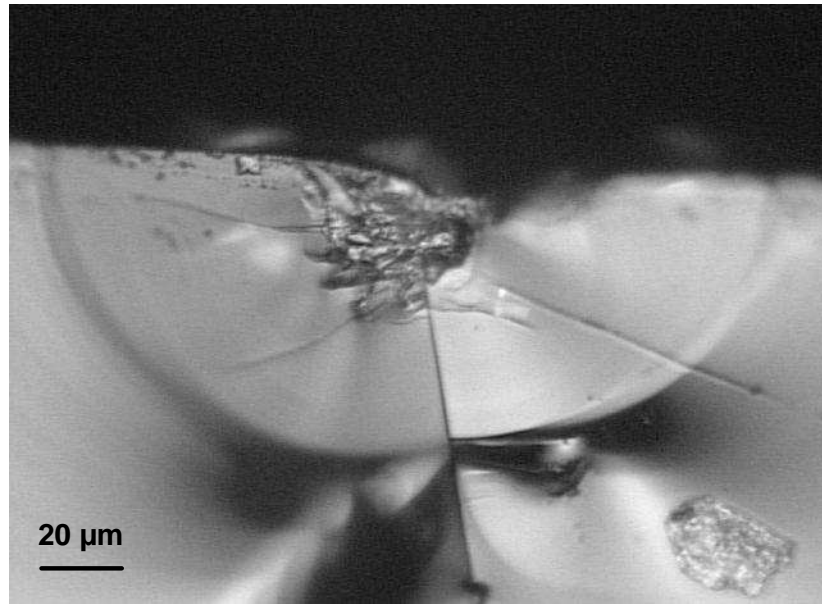
Figure 47. *Cross-section of another 1 Kg indentation made with the conventional indenter. Image width: 203 μm. Refl. light, BF, 400x original photo magnification.*
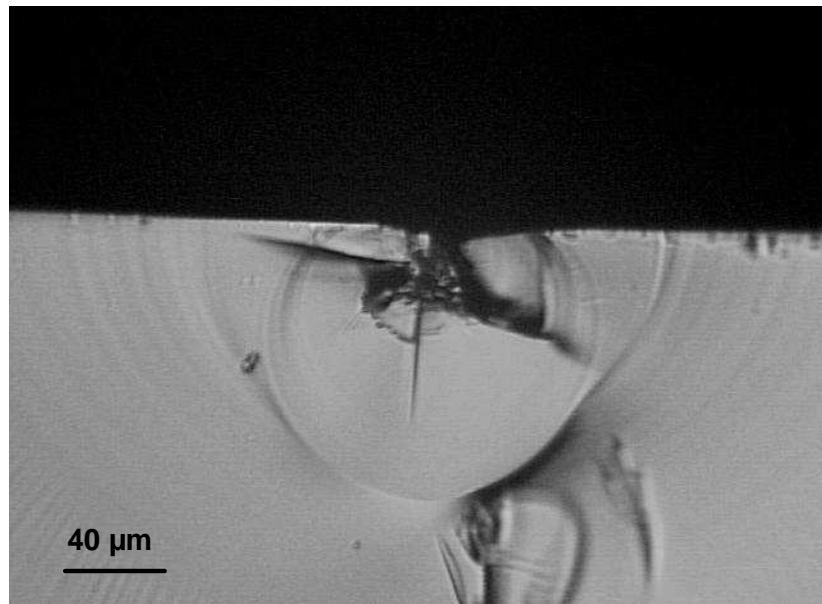
Figure 48. *Cross-section of another 1 Kg indentation made with the conventional indenter in glass S5. Image width: 329 μm. Trans. light, BF, 250x original photo magnification.*

4.2.5.3 SEM Examination

A portion of the surface of a 1 Kg indentation in glass S5 as seen in the SEM is shown in Figure 49. Shear fault lines can be seen on the surface, and they are less than 1 μm wide.

A high-magnification SEM image of the deformation zone beneath a 1 Kg indentation is shown in Figure 50. The central portion of the zone is broken apart, while just outside this, a network of shear fault lines is apparent. The deformation zone has a noticeable cone-shape to it.

4.2.5.4 Surface Profilometry

In Figure 51 a profile of a 1 Kg indentation made with the conventional indenter in glass S5 is shown. Uplift of surface material on both sides of the indentation is seen, similar to the other glasses. The indentation that was profiled is shown in Figure 52. The value of 'L' in Figure 136 is about 75 μm, which corresponds roughly to the surface lengths of lateral cracks (~ 82 μm) in this glass. The average maximum depth of shallow lateral cracks which chipped away surface material was 6.2 μm. The shallow lateral crack in Figure 52 had a maximum depth of about 8 μm, as revealed by another scan in the orthogonal direction through the shallow lateral crack.
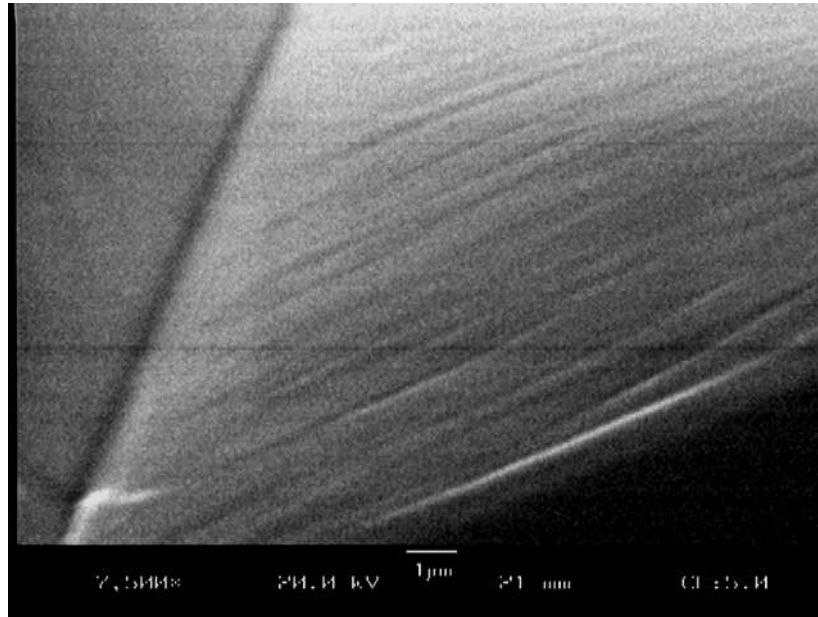
Figure 49. High-magnification SEM image of 1 Kg indentation in glass S5, illustrating array of fault lines on the surface. Fault lines are very narrow, less than 1 μm wide. Dark line across lower half of image is a scanning line from electron beam. Secondary electron mode, 7500x original photo magnification.
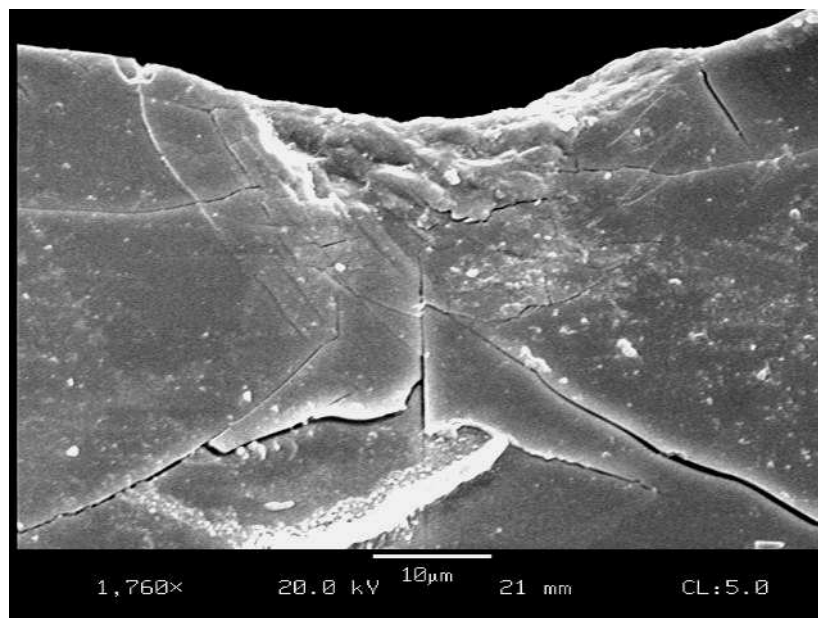
Figure 50. High-magnification image of the deformation zone and cracking beneath a 1 Kg indentation in glass S5 made with the conventional indenter. Secondary electron mode, 1760x original photo magnification.

126

H: 0.66 ± 0.14 μm
D: 4.69 ± 0.36 μm
D+H: 5.36 μm
S: 6.2 ± 1.8 μm
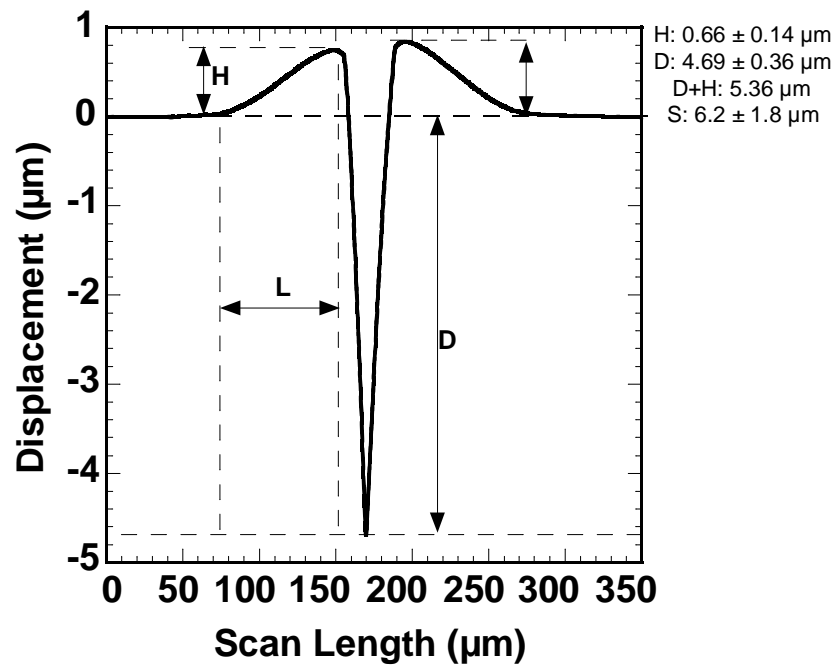
Figure 51. *Profile of a 1 Kg indentation made in glass S5 with the conventional indenter.*
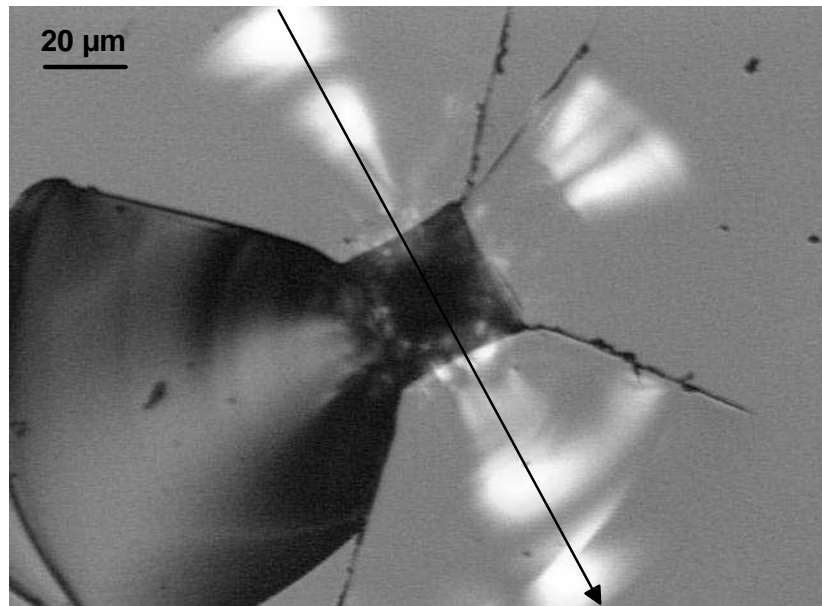
Figure 52. *Image of the indentation used to produce the profile in Figure 51. Arrow indicates scan direction. Scan length of 350 μm exceeds length of arrow shown. Refl. light, DIC, 400x original photo magnification.*

127

4.2.6 S6 (Lanthanum-Borate)-'Normal'

This glass was 'normal' with respect to its permanent deformation behavior. Table XVIII summarizes the crack initiation behavior of glass S6. Overall, the behavior was very similar to that of glass S5. However, median-radial cracks tended to initiate at higher loads on loading. In addition, no lateral cracks were observed to initiate on loading.

4.2.6.1 Post-Test Optical Microscopy

A typical indentation and associated fracture pattern produced from the 1 Kg crack initiation tests on glass S6 is shown in Figure 53. Median-radial cracks exist around all four indent corners. Deep lateral cracks are clearly evident as bright white reflections beneath the surface, as is a shallow lateral crack which broke through to the surface but did not chip away material; 40% of the tests had shallow lateral cracks which intersected the surface and almost removed material. The deep lateral crack below the shallow lateral crack is visible. The median-radial cracks extend from near the indentation corners.

Table XVIII. Glass S6 Crack Initiation Behavior Summary.

S6	First Median-Radials Loading	Last Median-Radials Loading	First Laterals Loading	First Median-Radials Unloading	First Laterals Unloading
1 Kg (0.2 µm/s) *73°F/13%RH*	482 ± 163 g [100 %]	700 ± 139 g	none	728 ± 127 g (73 ± 13 %) [70 %]	121 ± 40 g (12 ± 4 %) [100 %]
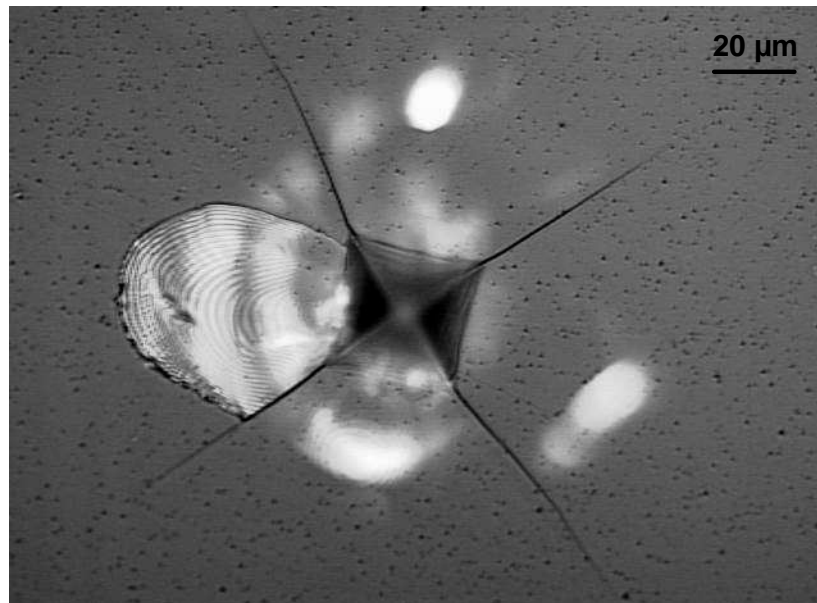
Figure 53. Indentation site produced in glass S6 from 1 Kg (0.2 µm/s) test. Shallow lateral crack in left quadrant broke through to surface, but did not dislodge completely. Image width: 203 µm. Refl., DIC, 400x original photo magnification.

4.2.6.2 Conventional Indenter: Surface and Sub-Surface Examination

Differences between indentations made with the recording and conventional microindenters were not very profound. However, more indentations, 20%, had surface chipping from shallow lateral cracks in the conventional machine compared to the recording microindenter. Similar to glass S5, outer shear faults appeared wider and more curved than in indentations made with the recording microindenter, however the curvature was not as large as observed in glass S5. Figure 54 shows an indentation in glass S6 made with the LECO conventional microindenter.

The corresponding cross-section is shown in Figure 55. Similar features are observed as for glasses S3-S5. Two median-radial cracks in the plane of fracture are seen. Deep and shallow lateral cracks are present, as is a median-radial vent crack. The deformation zone appears broken apart and has a noticeable cone shape to it. Other variations were seen in the cross-section morphology, and were similar to those seen in glass S5, which were presented previously.
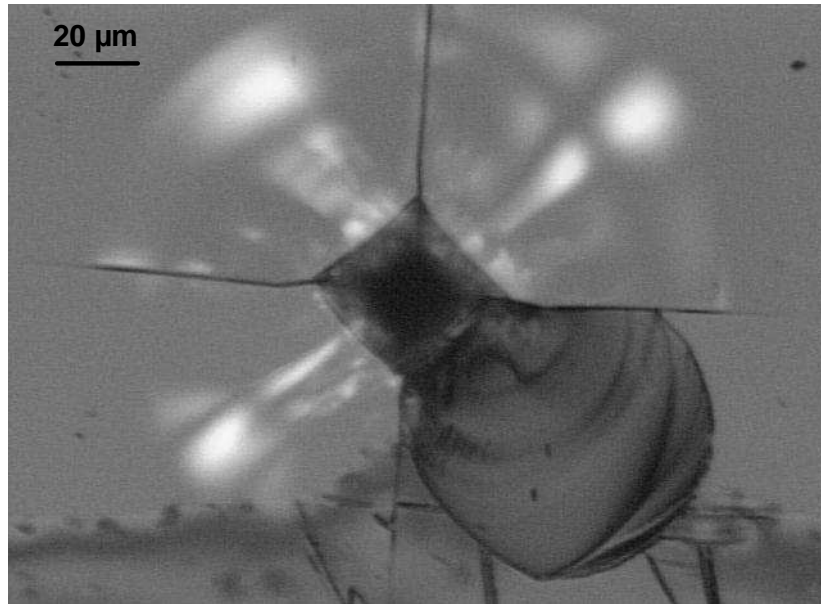
Figure 54. Indentation site in glass S6 from 1 Kg load using the conventional indenter. Image width: 203 µm. Refl. light, DIC, 400x original photo magnification.
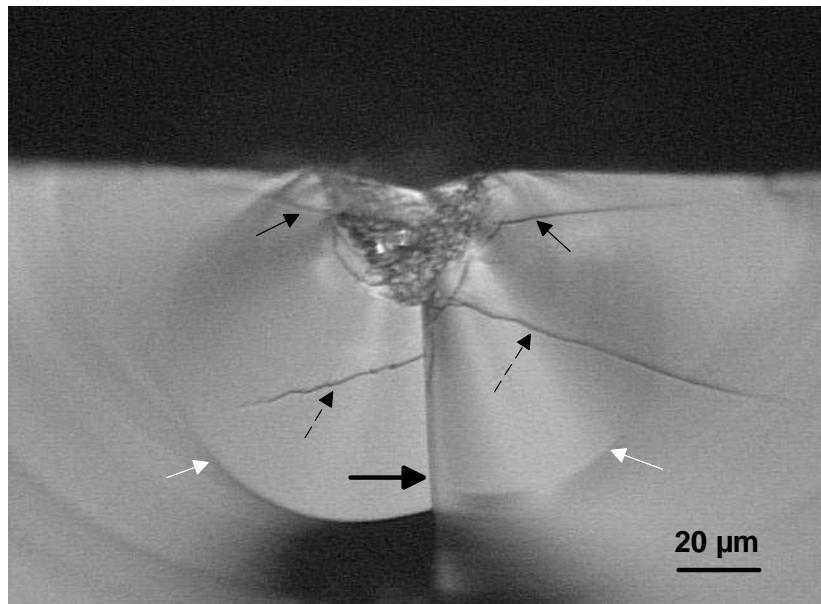
Figure 55. Cross-section of the indentation shown in Figure 54. Small solid black arrows designate shallow lateral cracks, broken arrows deep lateral cracks, white arrows in-plane median-radial cracks, and large black arrow median-radial vent crack. Image width: 203 µm. Refl. light, BF, 400x original photo magnification.

4.2.6.3 SEM Examination

A portion of the surface of a 1 Kg indentation in glass S6 as seen under the SEM is shown in Figure 56. Very narrow shear fault lines are seen, however, some crack-like separation is seen along one of the outer faults.

A cross-section of the deformation zone beneath a 1 Kg indentation is shown in Figure 57. Similar crack features were observed as seen in the optical microscope. However, the broken-apart deformation zone is better seen in the SEM. A shear fault structure is apparent outside the highly damaged core region.

4.2.6.4 Surface Profilometry

A profile of a 1 Kg indentation in glass S6 is shown in Figure 58. The profile shown traversed a shallow crater in the glass surface. The indentation that was profiled is shown in Figure 59. Shallow lateral crack breakthroughs, on average, were deeper than the indentation depths.
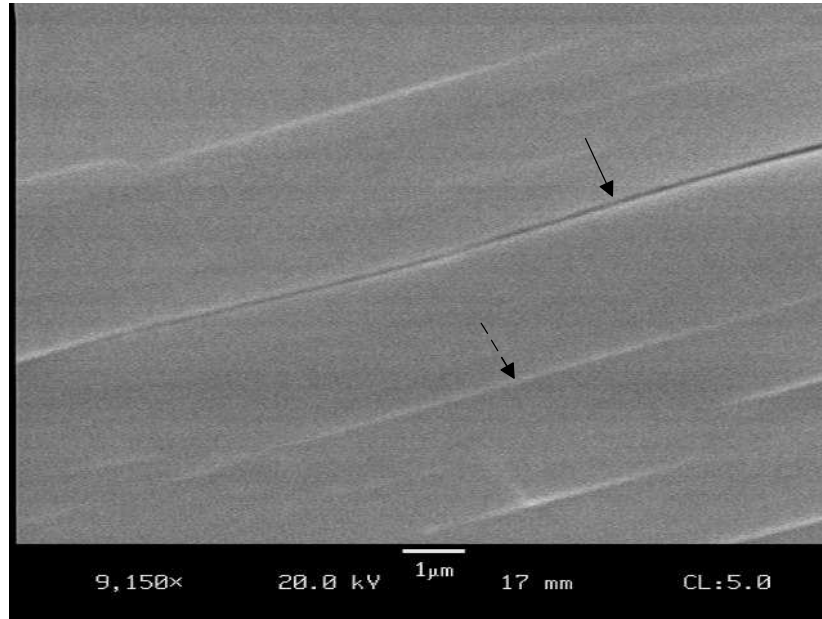
Figure 56. *A high-magnification image of a portion of the surface of a 1 Kg indentation made with the conventional indenter in glass S6. Broken arrow represents a shear fault line that is very narrow and flow-like. Solid arrow represents a shear fault that appears crack-like along a majority of its length. Secondary electron mode, 9150x original photo magnification.*
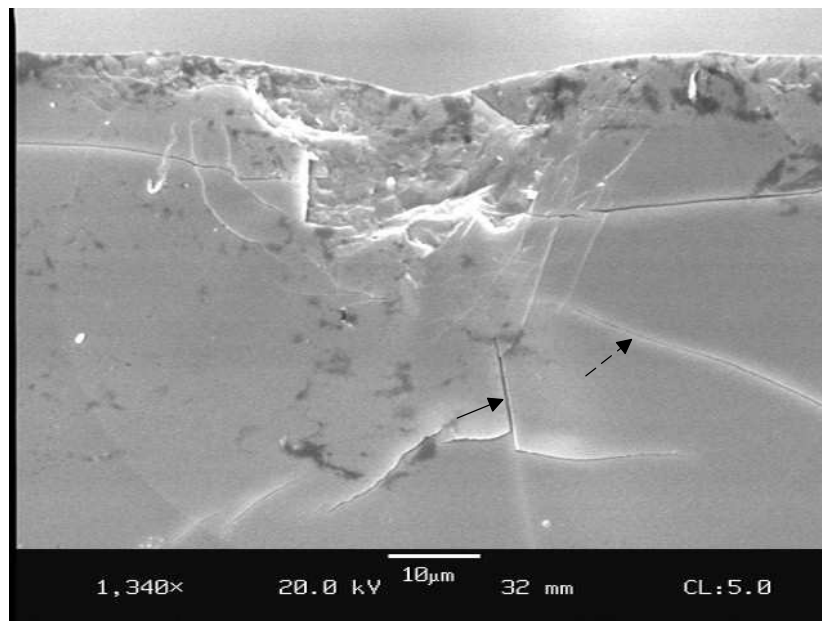
Figure 57. *High-magnification image of deformation zone beneath a 1 Kg indentation in glass S6. Some fault structure is apparent outside broken 'core' region of deformation zone. Solid arrow indicates median-radial vent crack, broken arrow a deep lateral crack. Two cracks are apparent branching off from median-radial vent just below solid arrow. Secondary electron mode, 1340x original photo magnification.*
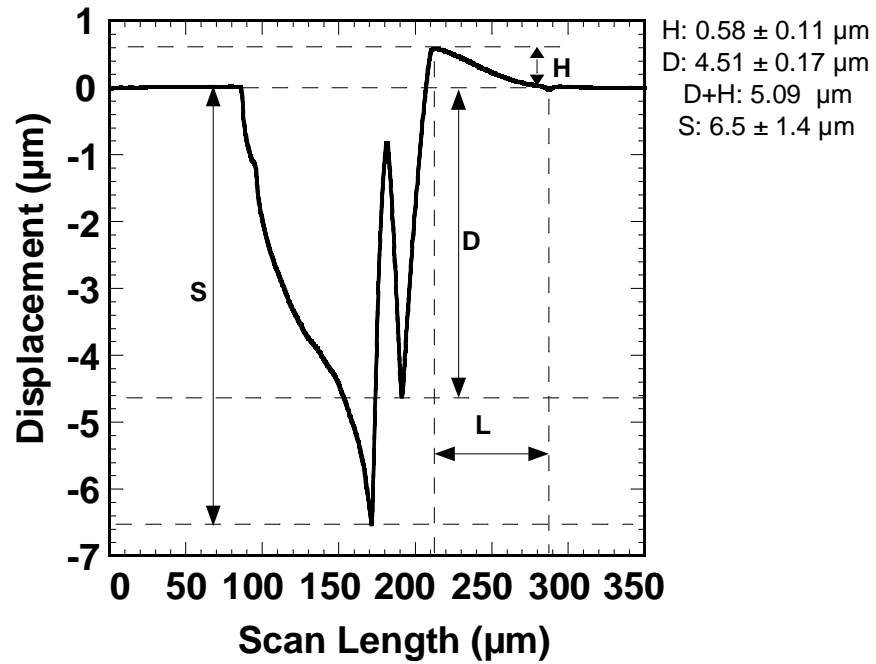
Figure 58. *Profile of an indentation made in glass S6 with the conventional indenter with 1 Kg load..*
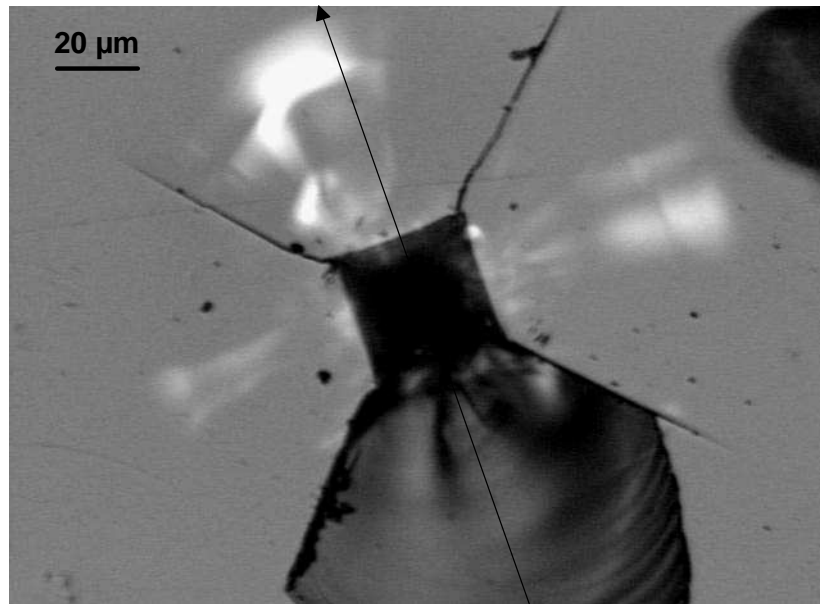
Figure 59. *Image of the indentation scanned in glass S6 to produce the profile. Arrow indicates scan direction. Scan length of 350 μm exceeds length of arrow shown. Image width: 203 μm. Refl. light, DIC, 400x original photo magnification.*

4.2.7   NS1 (Lanthanum-Borate)-'Normal'

This glass behaved 'normal' with respect to its permanent deformation behavior. Table XIX summarizes the crack initiation behavior of glass S6. In comparison to glasses S1, S2, S3, S5, and S6, all median-radial cracks initiated on the loading cycle, similar to glass S4. The majority of crack growth took place on unloading. Some lateral crack formation was observed for several (40%) of the tests on loading. Lateral cracks initiated on unloading for all tests.

Table XIX. Glass NS1 Crack Initiation Behavior Summary

NS1	First Median-Radials Loading	Last Median-Radials Loading	Laterals Loading	First Median-Radials Unloading	First Laterals Unloading
1 Kg (0.2 µm/s) 73°F/21%	257 ± 80 g [100 %]	470 ± 40 g	[40 %]	none	143 ± 48 g (14 ± 5 %) [100 %]

4.2.7.1 Post-Test Optical Microscopy

A typical indentation site in glass NS1 from the 1 Kg crack initiation tests is shown in Figure 60. Median-radial cracks extend from all four indentation corners, and well-developed lateral cracks are present. A small shallow lateral crack is visible in the top left quadrant.

4.2.7.2 Conventional Indenter: Surface and Sub-Surface Examination

The largest difference between the 1 Kg recording and conventional microindenter tests was that 60% of the tests had material chipped away due to shallow lateral cracks, compared to 20% with the recording microindenter. An indentation site is shown in Figure 61. The outer shear faults on several of the indentations were slightly more curved compared to the indentations made with the recording microindenter, and tended to exist outside the main area of indentation.

The corresponding indentation cross-section for the indentation in Figure 61 shown in Figure 62. A well-developed 'full-penny' median-radial crack initiated in the plane of fracture. A dark 'core' region of broken-apart material exists, surrounded by a more defined shear fault structure. Another type of cross-section crack morphology observed consisted of two in-plane median-radials and a median-radial vent orthogonal to both.
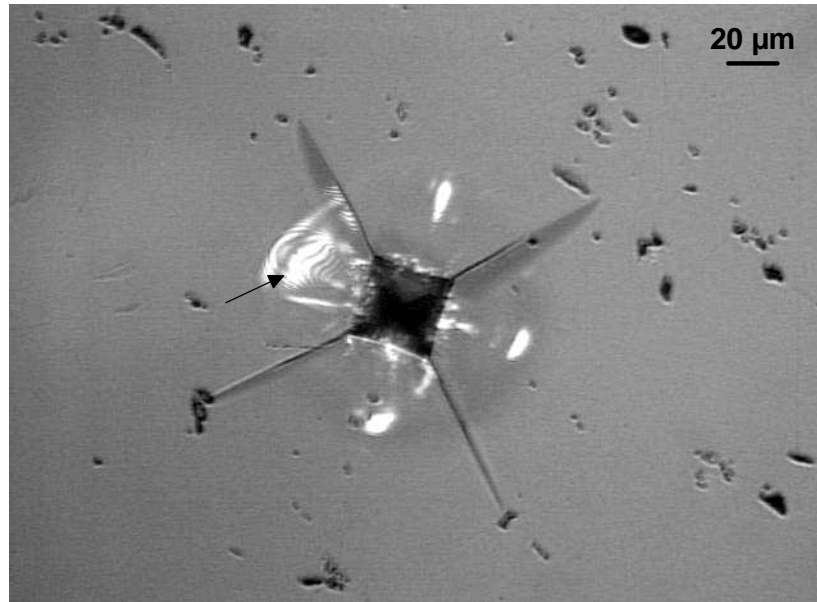
Figure 60. Indentation site in glass NS1 from 1 Kg (0.2 µm/s) test. Arrow indicates shallow lateral crack which is just below the surface. Image width: 329 µm. Refl. light, DIC, 250x original photo magnification.
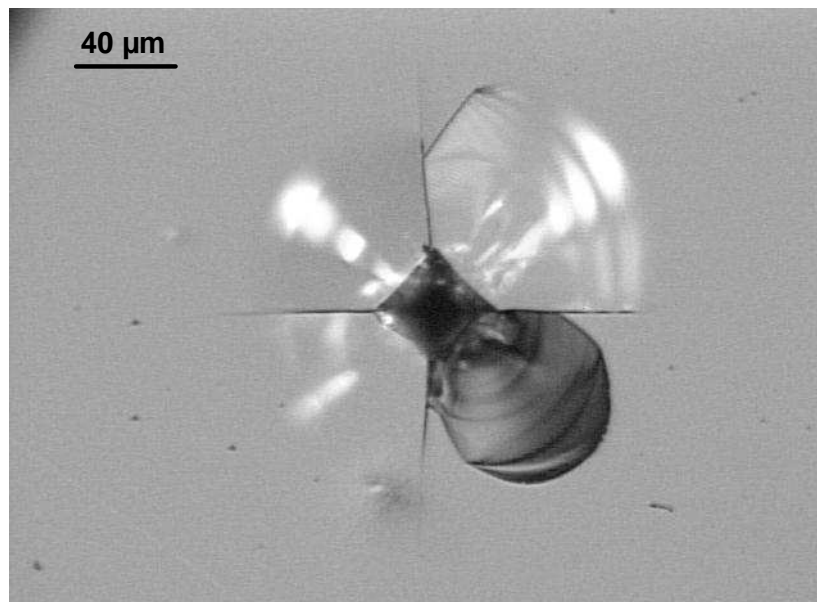
Figure 61. Indentation site in glass NS1 from 1 Kg load with the conventional indenter. Image width: 329 µm. Refl. light, DIC, 250x original photo magnification.
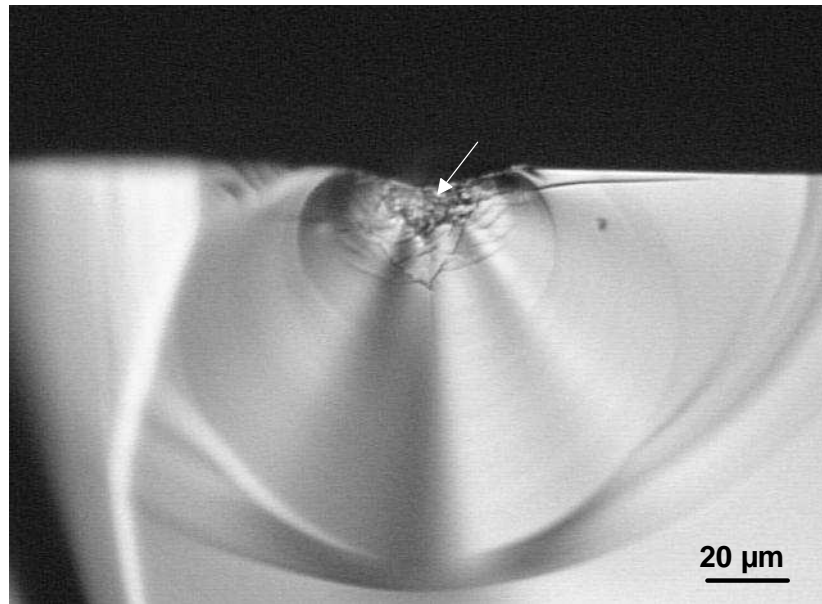
Figure 62. High-magnification image of the cross-section of the indentation in Figure 61, illustrating the fault structure beneath the indentation, and the full-penny median-radial crack. White arrow denotes dark 'core' region which is broken apart compared to surrounding shear fault structure. Image width: 203 μm. Refl. light, BF, 400x original photo magnification.

4.2.7.3 SEM Examination

Figure 63 is a surface view of a portion of a 1 Kg indentation as seen in the SEM. Most of the shear faults are very fine, with the exception of one outer fault which appears white in the image from charging, a sign this fault was wide and crack-like along part of its length.

A cross-section of an indentation as seen in the SEM is shown in Figure 64. The deformation zone is mostly broken apart, corresponding to the dark 'core' seen in the optical micrographs. Remnants of a shear fault structure are
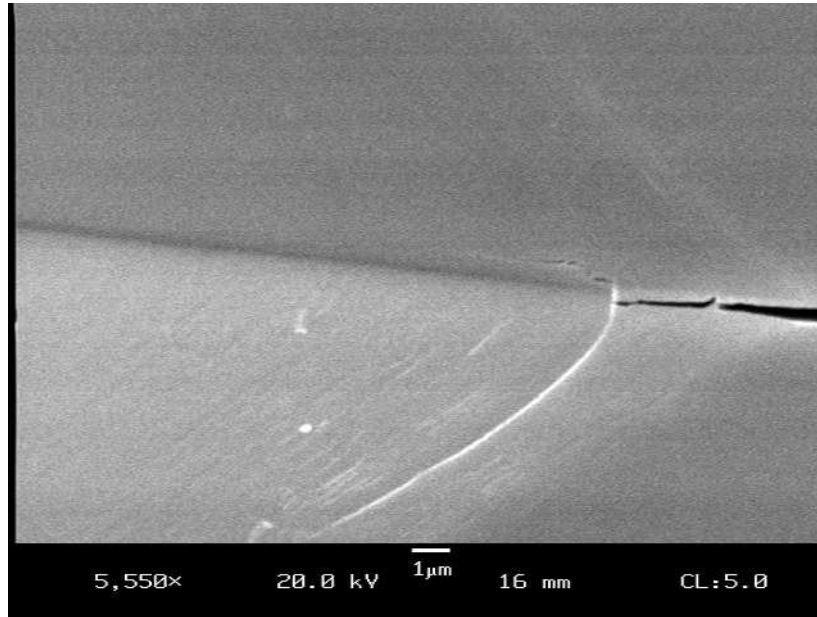
Figure 63. *High-magnification SEM image of a portion of a 1 Kg indentation produced with the conventional indenter in glass NS1. A severe shear fault (bright white), and a median-radial crack that penetrated into the indentation and was clamped shut, are visible. Secondary electron mode, 5550x original photo magnification.*
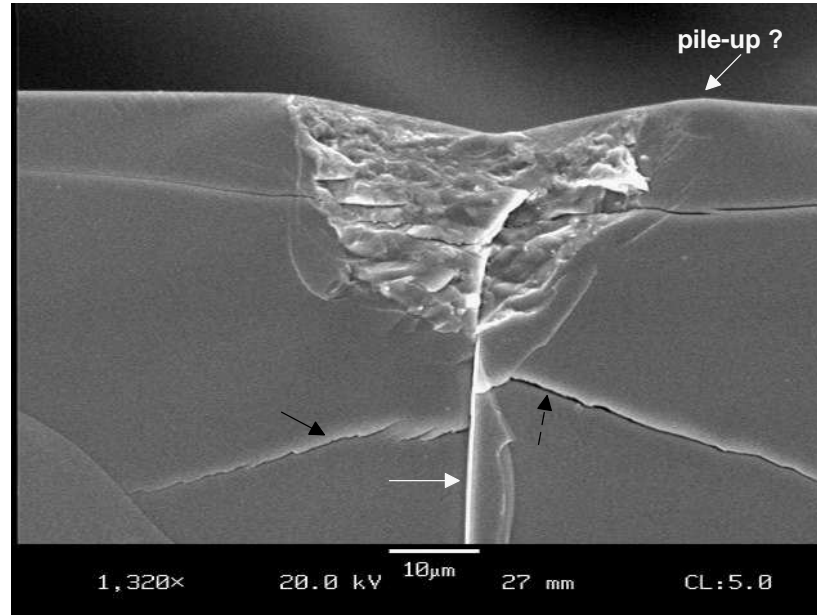
Figure 64. *High-magnification image of deformation zone and surrounding fracture beneath a 1 Kg indentation in glass NS1. Possible pile-up adjacent to the indentation is indicated. Solid black arrow indicates deep lateral crack that appears to extend from the median-radial vent crack (white arrow). Broken arrow indicates deep lateral crack that extends from a shear fault. Secondary electron mode, 1320x original photo magnification.*

139

apparent outside this broken region. The deep lateral crack on the left side of the median-radial vent initiates from a point along this crack, whereas the deep lateral crack on the right appears to extend from a shear fault near the bottom of the deformation zone.

4.2.7.4 Surface Profilometry

A profile of a 1 Kg indentation is shown in Figure 65. The indentation profiled is shown in Figure 66. The lengths of the lateral cracks labeled 'L_1' and 'L_2' in Figure 66 are approximately 79 and 54 µm, respectively. The values of 'L_1' and 'L_2' in the profile are approximately 75 and 58 µm, respectively. This is good evidence the uplift around this indentation is partly due to lifting of the surface by the lateral cracks. However, it is possible that superimposed on this uplift is pile-up near the indentation edge.
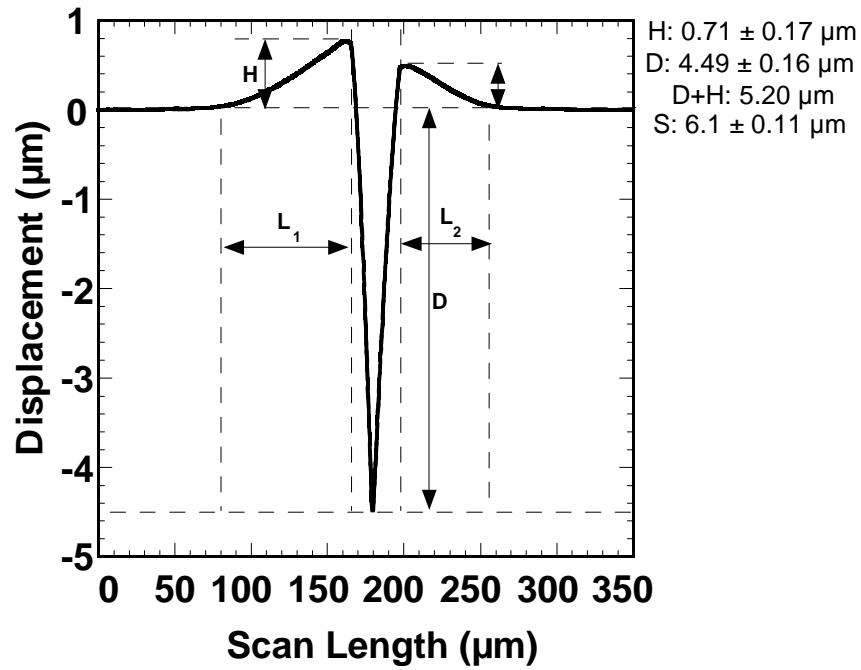
Figure 65. *Profile of an indentation made in glass NS1.*
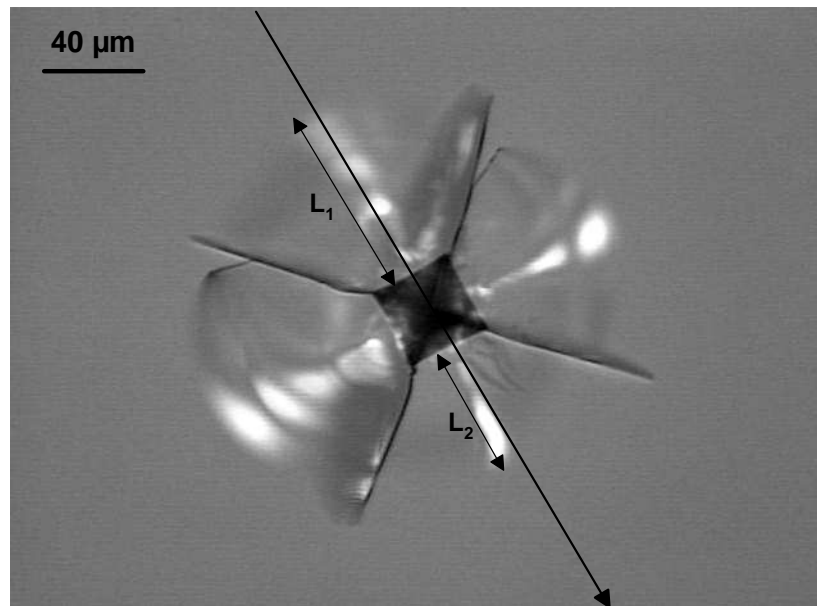
Figure 66. *Image of the indentation whose profile is shown in Figure 65. Indentation made with the conventional indenter and 1 Kg load. Scan length of 350 µm exceeds length of arrow shown. Arrow indicates scan direction. Image width: 329 µm. Refl. light, DIC, 250x original photo magnification.*

4.2.8   NS2 (Potassium-Phosphate)-'Normal'

This glass was 'normal' with respect to its permanent deformation behavior. The crack initiation behavior of this glass is summarized in Table XX. Median-radial cracks initiated on loading at relatively low forces for all tests. All median-radial cracks initiated on the loading cycle, similar to glasses S4 and NS1, however the majority of growth took place on unloading. Similar to glasses S3-NS1, what were thought to be two separate median-radials initiated simultaneously, followed by two additional median-radials which initiated at separate instances. Lateral cracks also initiated on loading in several tests; however, the exact initiation point was difficult to detect, because these cracks developed slowly around the contact site and in a stable manner, i.e., there was no abrupt pop-in. This is similar to that observed in glasses S3, S4, S5, S6, and NS1. Lateral cracks initiated on unloading in all tests.

Effect Of Polishing Medium

In order to see if the water route of polishing this glass had any effect on its crack initiation behavior, another specimen of glass NS2 was ground and polished via the oil route (see section 3). The crack initiation behavior was then investigated at 1 Kg, 0.2 µm/s, and it did not differ noticeably from the water-polished specimen. The first median-radial cracks initiated at 89 ± 35

Table XX. Glass NS2 Crack Initiation Behavior Summary.

NS2	First Median-Radials Loading	Last Median-Radials Loading	First Laterals Loading	First Laterals Unloading
1 Kg (0.2 µm/s) *73°F/21 % RH*	133 ± 33 g [100 %]	205 ± 62 g	[30%]	113 ± 40 g (11 ± 4 %) [100 %]
1 Kg (0.2 µm/s) Oil and Paste Polished *77°F/45 % RH*	89 ± 35 g [100%]	n/a	n/a	83 ± 28 g (8 ± 3 %) [100 %]

g, and the first lateral cracks on unloading initiated at 83 ± 28 g. These values compare favorably with the water-polished specimen, as shown in Table XX. The polishing procedure was thus considered to have had little effect on the crack initiation behavior of this glass.

4.2.8.1 Post-Test Optical Microscopy

An indentation site from the crack initiation tests is shown in Figure 67. Several features stand out. One feature is that the median-radial cracks are considerably longer compared to the lateral cracks. Another is that the well-developed shallow lateral crack that intersected the surface, but did not break away.
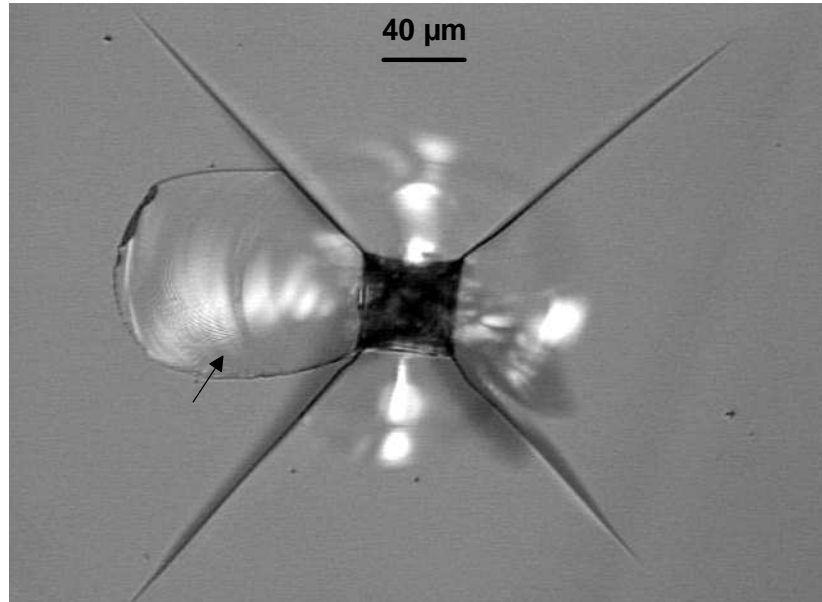
Figure 67. *Indentation site in glass NS2 from the 1 Kg (0.2 µm/s) tests. Median-radial cracks extend well beyond lateral cracks. Arrow indicates shallow lateral crack that intersected surface. Image width: 405 µm. Refl. light, DIC, 200x original photo magnification.*
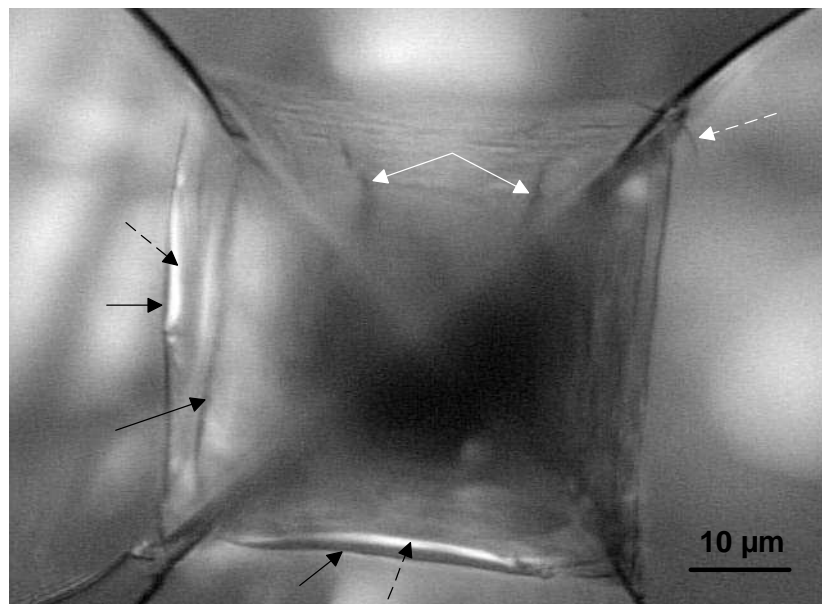
Figure 68. *Higher magnification image of the indentation in Figure 67. Solid black arrows designate severe shear faults, and broken black arrows surface lateral-like cracking between faults. Double white arrow indicates cracks within indentation. Broken white arrow shows small ring-like crack outside of main indentation area. ring crack. Image width: 83 µm. Refl. light, DIC, 1000x original photo magnification.*
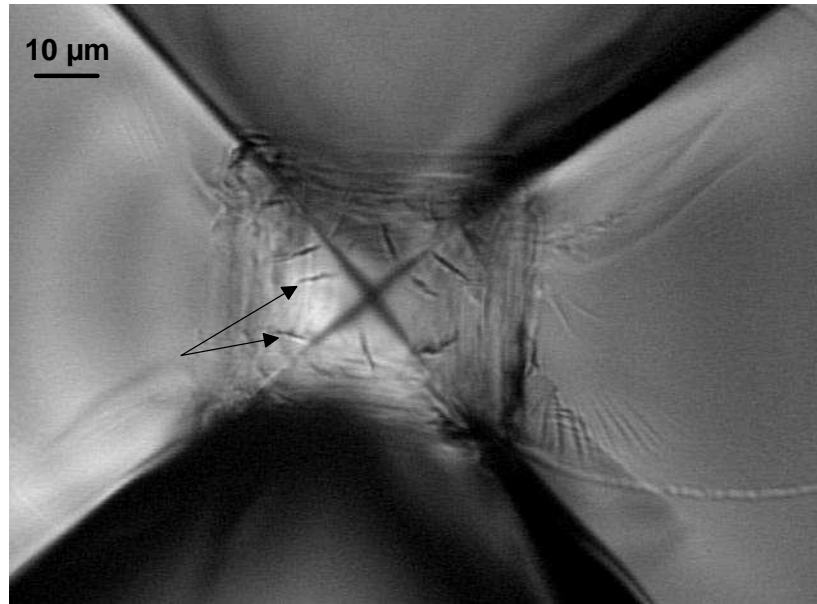
Figure 69. *Another 1 Kg indentation site in glass NS2 seen in transmitted light showing the presence of numerous small cracks within the indentation. Arrows indicate two of these cracks. Image width: 133 μm. Trans. light, BF, 625x original photo magnification.*

A higher magnification image of the indentation is shown in Figure 68. Shear faults were generally severe in this glass with significant surface lateral-like cracks between faults. Another feature observed was that some outer shear fault lines tended to be continuous around the indentation corners, as seen in the lower left and bottom right indentation corners. Small cracks within the indentation area were very numerous compared to all other glasses examined in this study. A transmitted-light image of another indentation, shown in Figure 69, highlights this nicely. A large number of randomly oriented cracks are seen contained within the indentation. Similar

cracks were observed within the indentations of the other normal glasses, i.e., S3, S4, S5, S6, and NS1, but were not so numerous.

4.2.8.2 Conventional Indenter: Surface and Sub-Surface Examination

Similar to the 1 Kg recording microindenter tests, 0% of the tests had shallow lateral cracks chip away surface material, which was surprising. In addition, the surface images showed no sign of shallow lateral cracks intersecting the surface as they did for the recording microindenter tests. An indentation site for these static tests is shown in Figure 70. This particular indentation showed little signs of shear-fault curvature around the indentation corners; however, other tests did.

The cross-section of this indentation is shown in Figure 71. Again, features similar to the other glasses are seen: in-plane median-radial cracks, deep lateral cracks, shallow lateral cracks, a sub-surface deformation zone. In addition, it is possible a ledge formed between the two in-plane median cracks where they intersected, otherwise, a median-radial vent crack is present. These are indicated in the figure.

One common variation of the cross-section morphology was the presence of a full-penny median-radial crack in the fracture plane. An example of this is shown in Figure 72. Another indentation cross-section in this glass, is
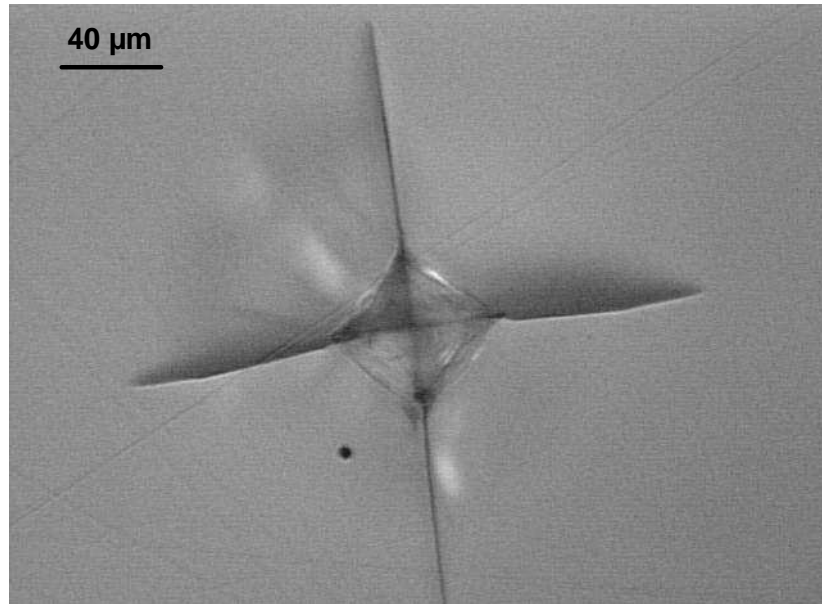
Figure 70. *Indentation site produced in glass NS2 from 1 Kg load with the conventional indenter. Image width: 329 µm. Refl. light, DIC, 250x original photo magnification.*
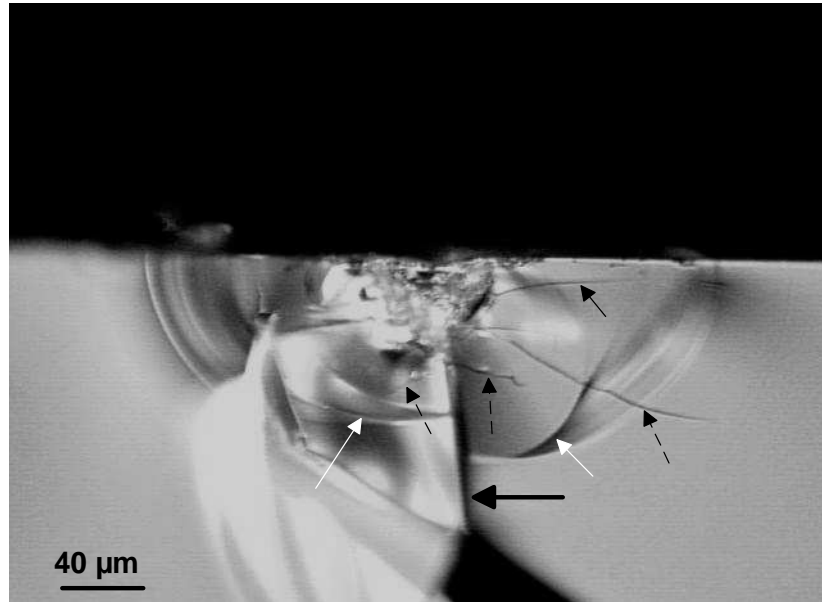
Figure 71. *Cross-section of the indentation show in Figure 70. Small black arrow indicates a shallow lateral crack, large black arrow either a ledge or a median-radial vent crack. Broken arrows represent deep lateral cracks. White arrows indicate in-plane median-radial crack arrest lines. Image width: 405 µm. Refl. light, BF, 200x original photo magnification.*
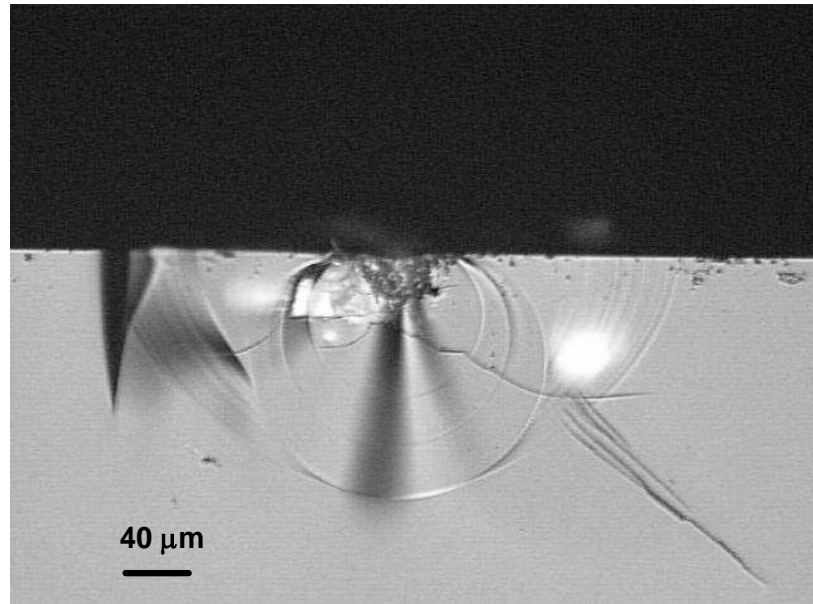
Figure 72. Cross-section of another indentation in glass NS2 from 1 Kg indentation illustrating the full-penny crack morphology seen beneath some indentations. Refl. light, BF, 160x original photo magnification.
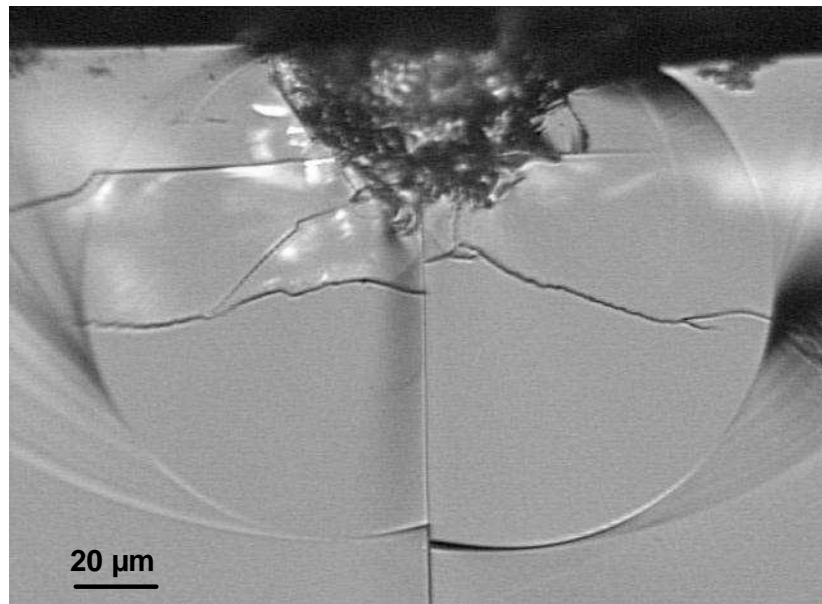
Figure 73. Cross-section image of another indentation in glass NS2 made with the conventional indenter with 1 Kg load. Deformation zone is broken apart. Image width: 203 μm. Refl. light, BF, 400x original photo magnification.

shown in Figure 73, more clearly revealing two in-plane median-radial cracks compared to Figure 71.

4.2.8.3 SEM Examination

Figure 74 is a SEM image of a 1 Kg cross-section in glass NS2. A deformation zone consisting of a 'core' region of broken material, surrounded by a shear fault structure is apparent. In addition, a deep lateral crack appears to have extended from an outer shear fault on the left side of the deformation zone. Similar to glasses S5-NS1, the deformation zone appears cone-shaped, not semicircular.

A surface view of a higher load (5 Kg) indentation examined in the SEM is shown in Figure 75. It is seen that the shear fault structure is not as narrow compared to glasses S3-NS1; i.e., there are more severe faults present.
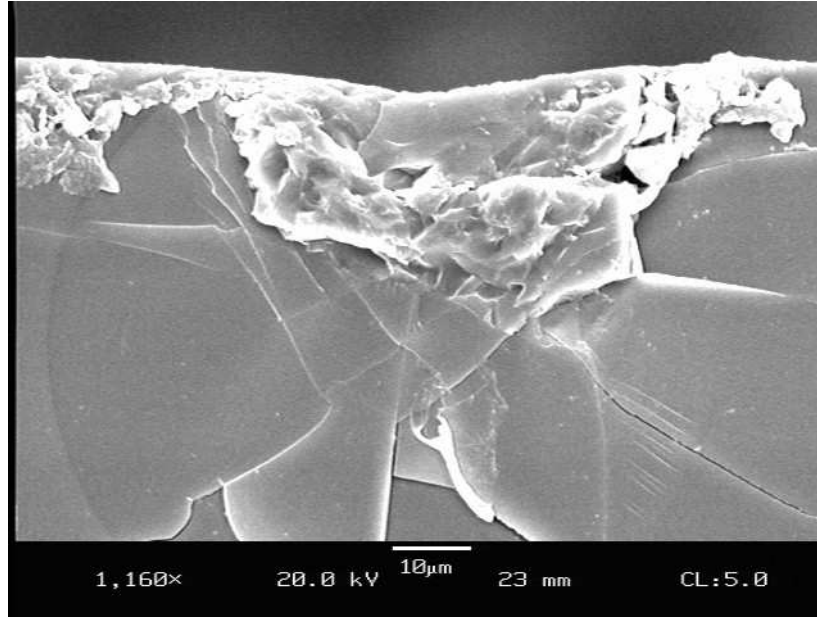
Figure 74. SEM image of the deformation zone shown beneath a 1 Kg indentation in glass NS2. Note how a region of broken apart material exists immediately below the surface, surrounded by a shear fault structure. Secondary electron mode, 1160x original photo magnification.
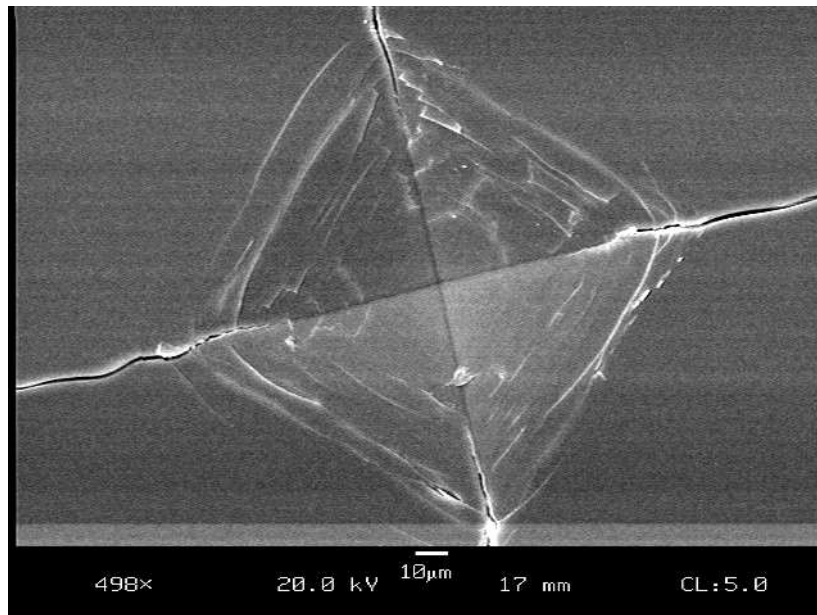
Figure 75. Surface view of a 5 Kg indentation in glass NS2 made with the conventional indenter. Secondary electron mode, 498x original photo magnification.

4.2.9 NS3 (Fluoride)-'Normal'

This glass was 'normal' with respect to its permanent deformation behavior. For all tests, median-radial cracks initiated very early on the loading cycle, seemingly instantaneous in most tests. Median-radial cracks were observed to extend from the indentation corners almost as soon as the indenter made contact, i.e., there was no abrupt, unstable 'pop-in' event. The majority of crack growth took place on loading. Lateral cracks initiated on loading, for all test conditions. These cracks were well-developed, similar to those seen in glass S4 on loading, compared to the other glasses. It appeared the faster displacement rate suppressed the average load at which the first lateral cracks initiated on loading. On unloading lateral cracks initiated as well.

Table XXI. Glass NS3 Crack Initiation Behavior Summary.

NS3	First Median-Radials Loading	First Laterals Loading	First Laterals Unloading
1 Kg (0.2 μm/s) *75°F/34%RH*	instantaneous [100 %]	353 ± 285 g [100 %]	239 ± 54 g (24 ± 5 %) [100 %]

4.2.9.1 Post-Test Optical Microscopy

An indentation site is shown in Figure 76. Well-developed median-radial and lateral cracks are apparent. The median-radials extend nearly parallel to the indentation diagonals.

A higher magnification image of this indentation is shown in Figure 77. The shear faults are very narrow and difficult to see, and this behavior was typical of all the indentations.

4.2.9.2 Conventional Indenter: Surface and Sub-Surface Examination

The faster loading rate of the conventional indenter resulted in 100% of the tests having surface material chipped away, compared to 40% for the 0.2 µm/s recording microindenter tests. In addition, the surface chipping was much more severe, with all tests, except one, having material removed from all four quadrants. Figure 78 is a representative indentation site. Two of the chipped regions have extended beyond the median-radial cracks. The corresponding cross-section of this indentation is shown in Figure 79, in transmitted light. Similar features are observed as for most of the other glasses: median-radial cracks, lateral cracks, a deformation zone, etc. The shallow lateral cracks have severely chipped away the surface. Very little convex shape to the median-radial cracks is apparent, indicating little constraint at the surface. This is consistent with the fact these cracks
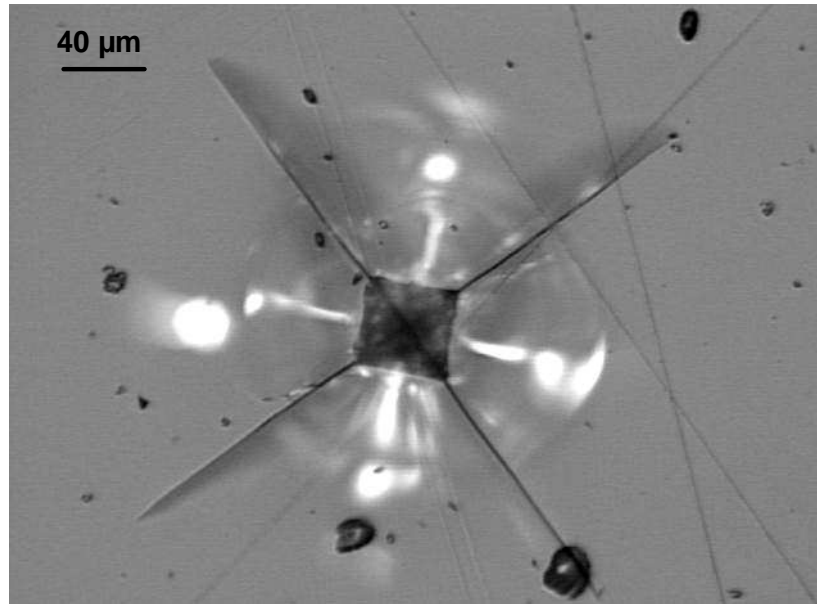
Figure 76. Indentation site produced in glass NS3 from the 1 Kg (0.2 µm/s) crack initiation tests. Image width: 405 µm. Refl. light, DIC, 200x original photo magnification.
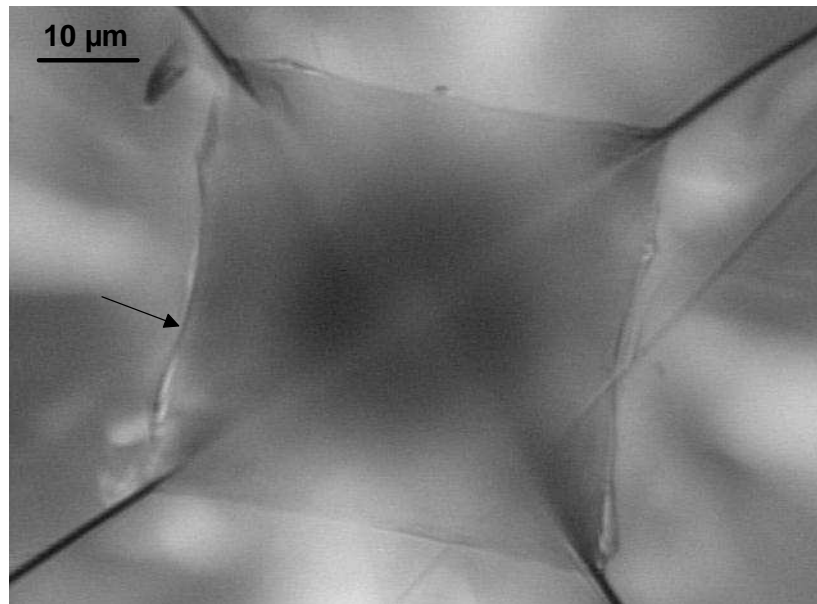
Figure 77. Higher-magnification image of the indentation in Figure 76 illustrating how the shear faults are very fine and difficult to see. Arrow indicates a more visible fault along the edge of the indentation. Image width: 83 µm. Refl. light, DIC, 1000x original photo magnification.
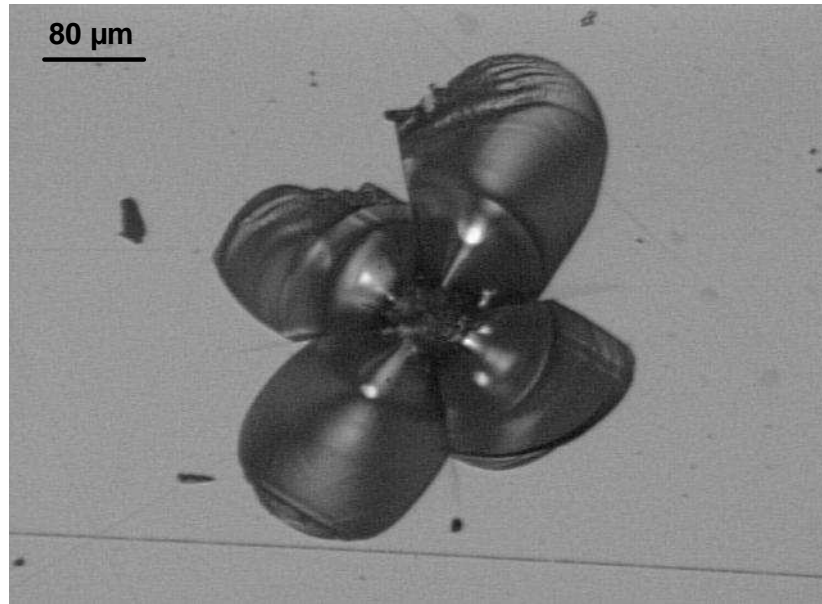
Figure 78. Indentation site produced in glass NS3 from the 1 Kg conventional indentation tests. Severe surface chipping has occurred. Image width: 658 µm. Refl. light, DIC, 125x original photo magnification.
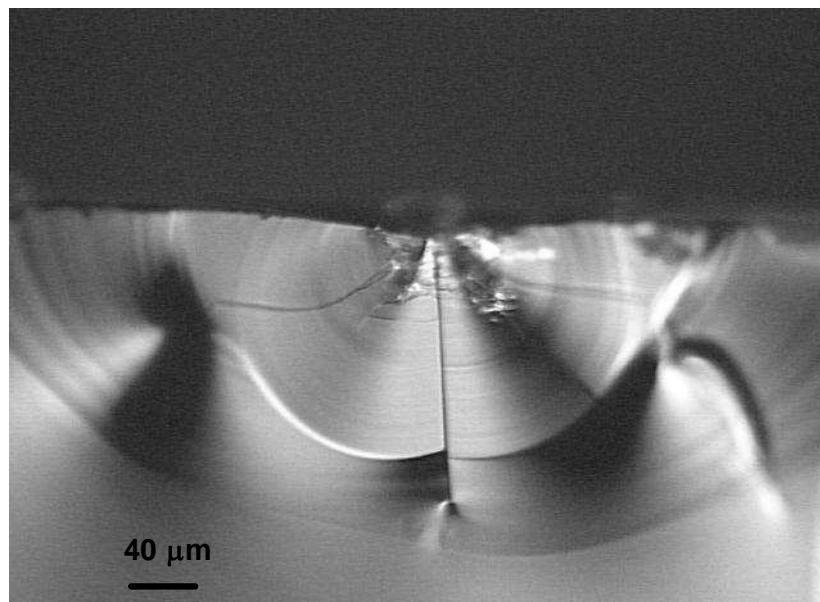
Figure 79. Cross-section of the indentation in Figure 78. Image width: 511 µm. Trans. light, BF, 160x original photo magnification.
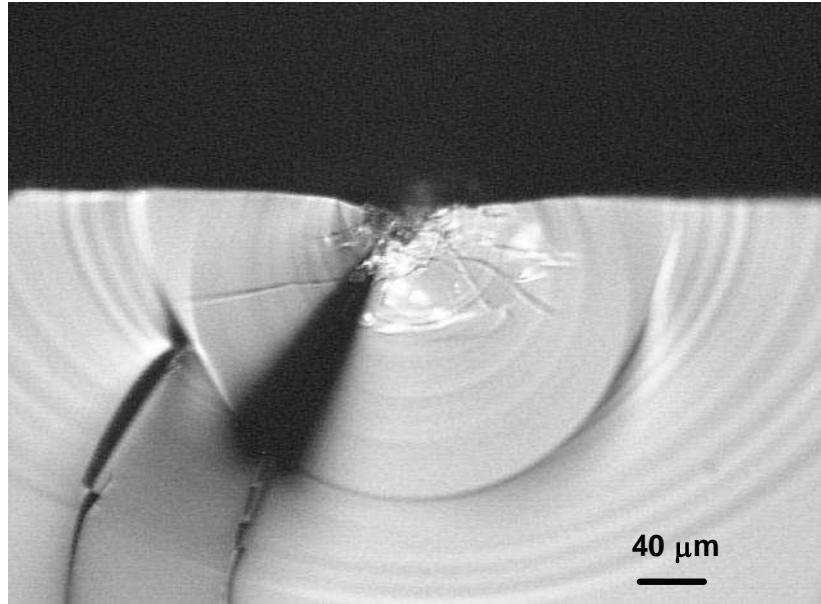
Figure 80. *An example of a full-penny crack morphology seen beneath a 1 Kg indentation site in glass NS3. Refl. light, BF, 160x original photo magnification.*

initiated very early in the loading cycle, where the compressive stresses at the surface would presumably be small. Full-penny crack morphologies were also seen, an example of which is shown in Figure 80.

4.2.9.3 SEM Examination

A high-magnification image of a portion of a 1 Kg indentation in glass NS3 is shown in Figure 81, and reveals that shear faults are present on the surface, but are extremely narrow.
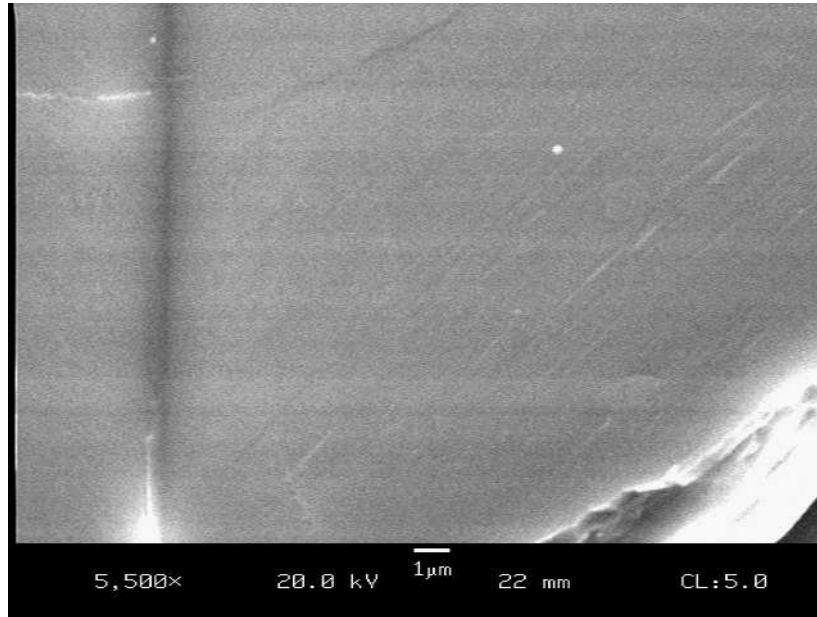
Figure 81. High-magnification image of a portion of a 1 Kg indentation in glass NS3 made with the conventional indenter. Very fine shear fault lines are visible on the surface. Secondary electron mode, 5500x original photo magnification.
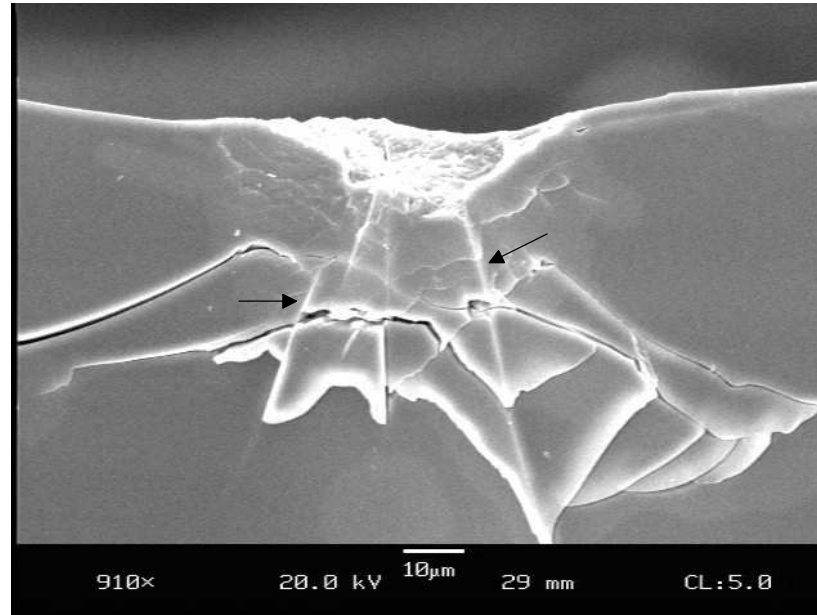
Figure 82. Cross-section of a 1 Kg indentation made with the conventional indenter in glass NS3 examined in the SEM. Arrows indicate radial-like cracks extending down from the deformation zone. Secondary electron mode, 910x original photo magnification.

A cross-section of a 1 Kg indentation in glass NS3 viewed in the SEM is shown in Figure 82. A good portion of the indentation has been chipped away. Several radial-like cracks are seen extending down from the deformation zone. These types of cracks were not seen in any of the other glasses. The shear faults are also not as well-defined as in the other glasses, possibly because they are very narrow, less than 1 μm in width.

4.2.10 Float Glass-'Normal-Anomalous'

As mentioned at the beginning of this section, this glass exhibited some signs of 'anomalous' behavior (see Section 4.3). Median-radial cracks initiated on unloading, where the majority of growth took place. Similar to the other glasses, what appeared to be two median-radial cracks initiated simultaneously, followed by two additional cracks which initiated at separate instances. Lateral cracks then initiated near or at complete unloading after the median-radial cracks. Table XXII summarizes the initiation behavior.

4.2.10.1 Post-Test Optical Microscopy

Figure 83 is an indentation site in float glass from the crack initiation tests. Median-radial and smaller secondary radial cracks are visible, as are deep sub-surface lateral cracks. A higher magnification image of the

Table XXII. Float Glass Crack Initiation Behavior Summary.

Float	First Median-Radials Loading	First Median-Radials Unloading	First Laterals Unloading
1 Kg (0.2 μm/s) *73°F/22% RH*	none	520 ± 163 g (52 ± 16 %) [100 %]	near/after complete unloading [100 %]

indentation is shown in Figure 84, where numerous shear faults can be seen parallel to the indentation sides. Some of the outer faults appear crack-like. In addition, it appears that the lower-left median-radial and secondary radial cracks have extended from shear faults within the indentation.

Other types of fracture patterns were seen as well. Some indentations had more than one median-radial crack initiate from a corner. Others had median-radial cracks which did not extend from a corner, but rather from the sides of the indentation. In this respect, the float glass behaved similar to glasses S1 and S2, which tended to have median-radial cracks not extend/initiate from exactly the indentation corners.

4.2.10.2   Conventional Indenter: Surface and Sub-Surface Examination

Compared to the 1 Kg tests with the recording microindenter, on average more radial cracks (median-radial + secondary radial) initiated around any given indentation, 6.7 ± 2.0 cracks compared to 5.3 ± 0.3 cracks for the 1 Kg (0.2 μm/s) with the recording indenter. Note, however, there was more variability in the conventional tests. For the 1 Kg (2.0 μm/s) tests, a similar

158
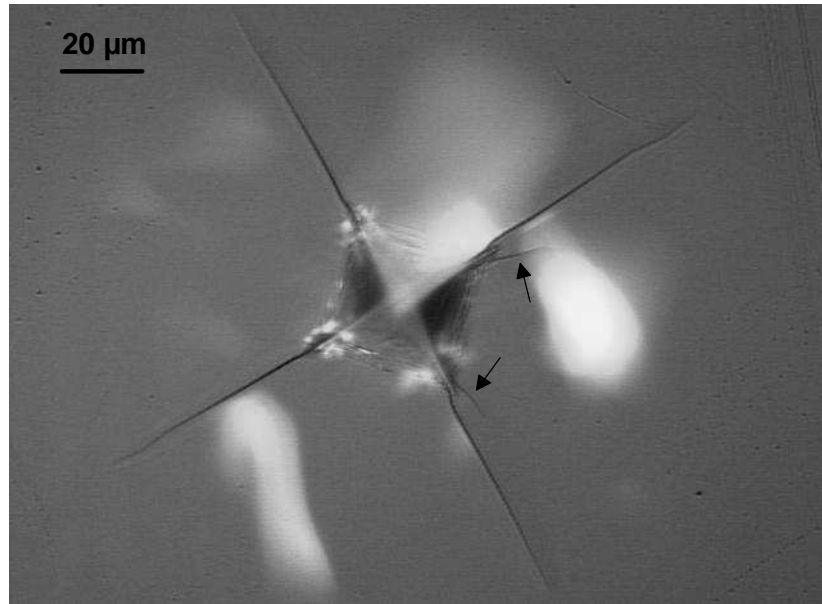
Figure 83. *Indentation site in float glass from 1 Kg (0.2 µm/s) crack initiation test. Arrows indicate small secondary radial cracks. Image width: 203 µm. Refl. light, DIC, 400x original photo magnification.*
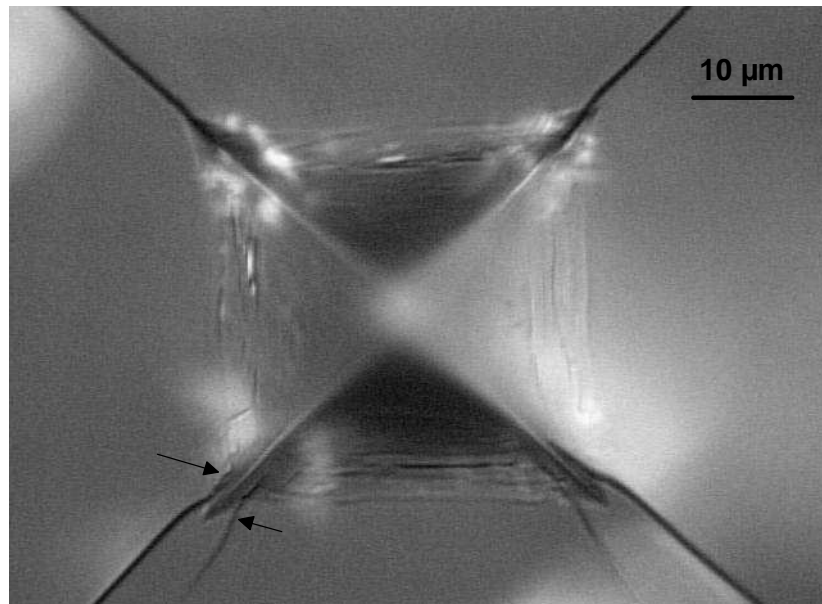
Figure 84. *Higher magnification image of indentation in Figure 83. Shear faults are visible within the indentation. Arrows indicate two cracks that appear to extend from shear faults. Image width: 83 µm. Refl. light, DIC, 1000x original photo magnification.*

number of cracks formed as for the 1 Kg (0.2 µm/s) tests i.e., 5.9 ± 0.9 radial cracks. Fractions (decimals) denote frequency of occurrence. Figure 85 is a 1 Kg indentation site made with the conventional indenter in float glass. The corresponding cross-section of this indentation is shown in Figure 86. Two in-plane median-radial cracks have initiated, and a median-radial vent crack is visible extending downward from the deformation zone. The deformation zone appears to contain numerous cracks. The median-radial vent crack changes direction at the bottom portion, turning parallel to the surface.

Another type of geometry seen is shown in Figure 87, where a single full-penny median-radial crack initiated in the plane of fracture. The final geometry is half-penny. This indentation site was produced with the recording microindenter; however, this geometry was also seen beneath indentations made with the conventional indenter.

4.2.10.3   SEM Examination

Figure 88 is a portion of a 1 Kg indentation in float glass as examined in the SEM. Numerous shear cracks are apparent along the edges of the indentation. These faults are thought to be cracks because of the charging which makes them white, indicating presence of free surfaces in which the Au-Pd coating material could not coat because of their narrowness. The interior portion of the indentation appears shear crack free; however, fine shear-'flow' lines are apparent.
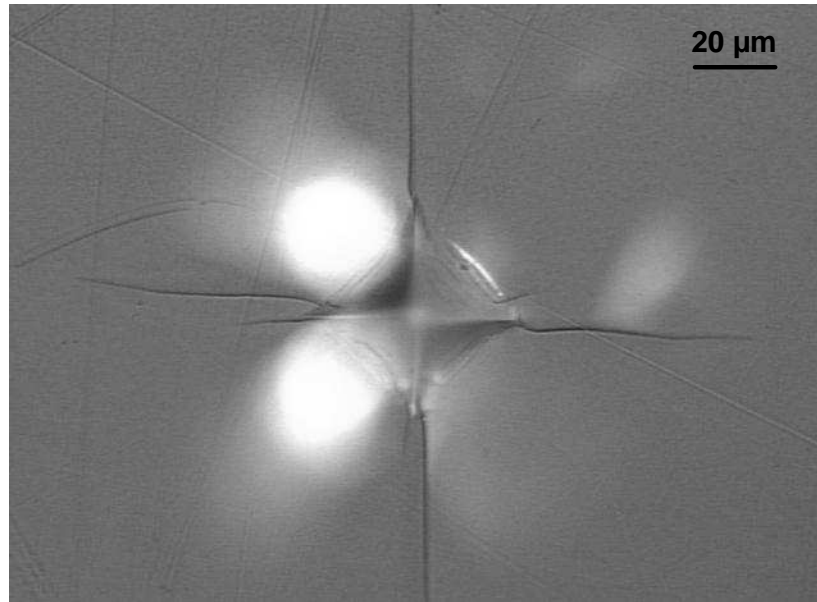
Figure 85. *An indentation site in Float glass made with the conventional indenter and 1 Kg load. Image width: 203 µm. Refl. light, DIC, 400x original photo magnification.*
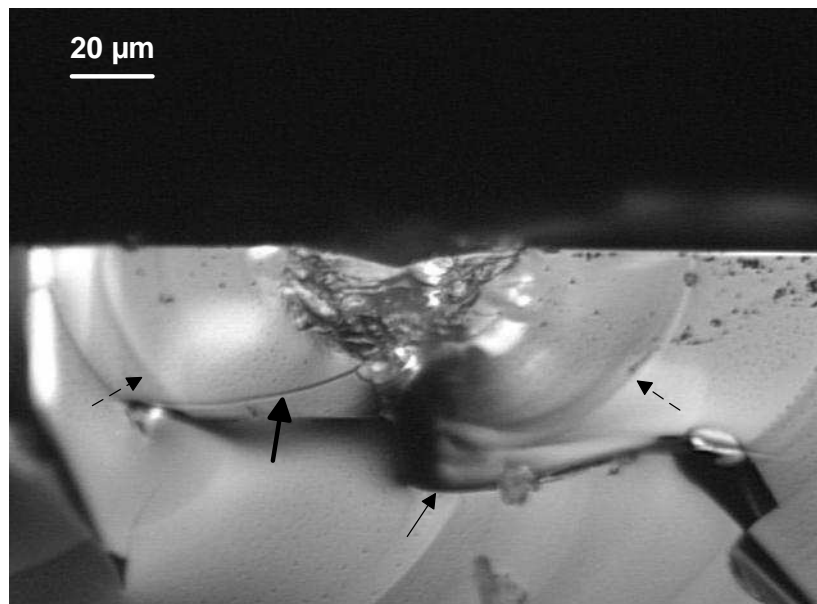
Figure 86. *Cross-section image of the indentation shown in Figure 85. Small solid arrow indicates median-radial vent crack. Broken arrows represent in-plane median-radial cracks, and large solid arrow represents a deep lateral crack. Image width: 203 µm. Refl. light, DIC, 400x original photo magnification.*
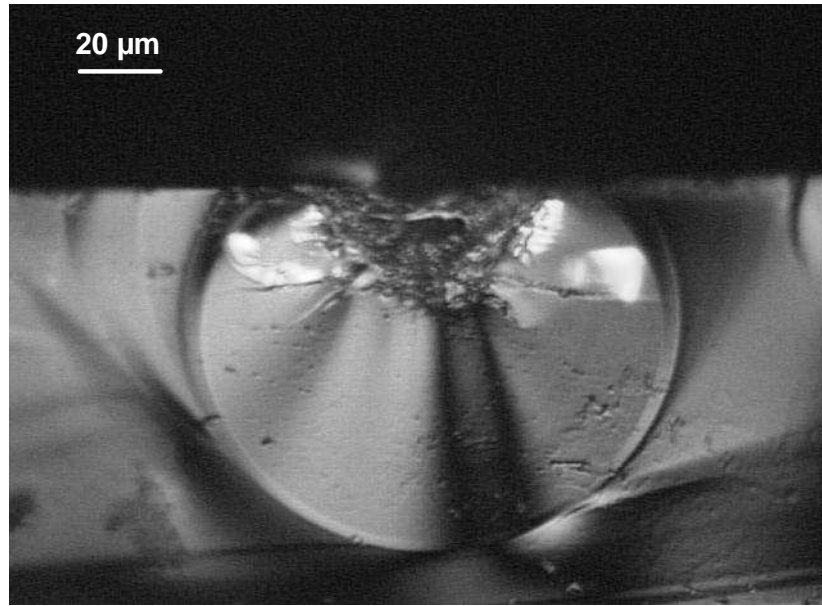
Figure 87. *Cross-section of a 1 Kg (0.2 µm/s) test made in float glass with the recording microindenter. A full-penny median-radial crack popped in on unloading, then broke through to the surface to form a final half-penny geometry. Image width: 203 µm. Refl. light, DIC, 400x original photo magnification.*
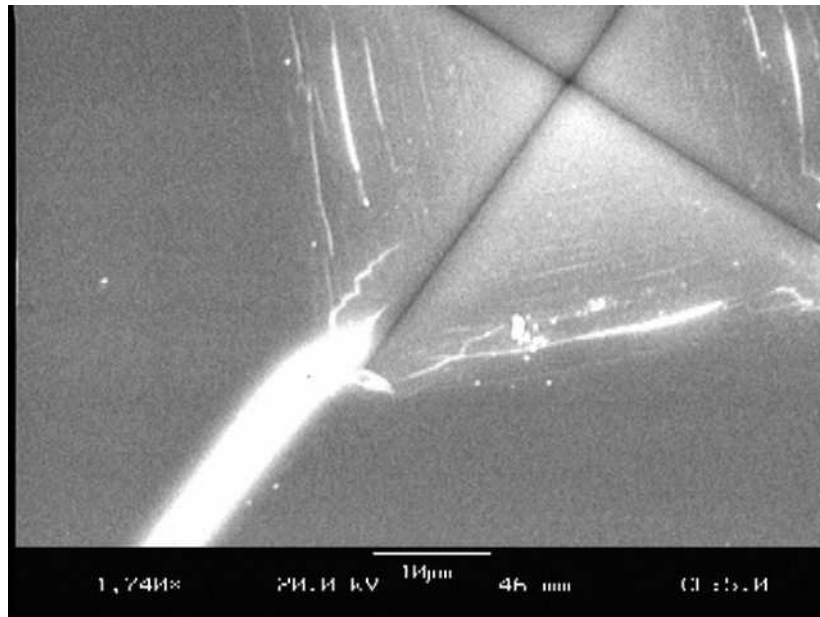
Figure 88. *High magnification image of a portion of a 1 Kg indentation in float glass, illustrating that outer shear faults are crack-like. Secondary electron mode, 1740x original photo magnification.*

162
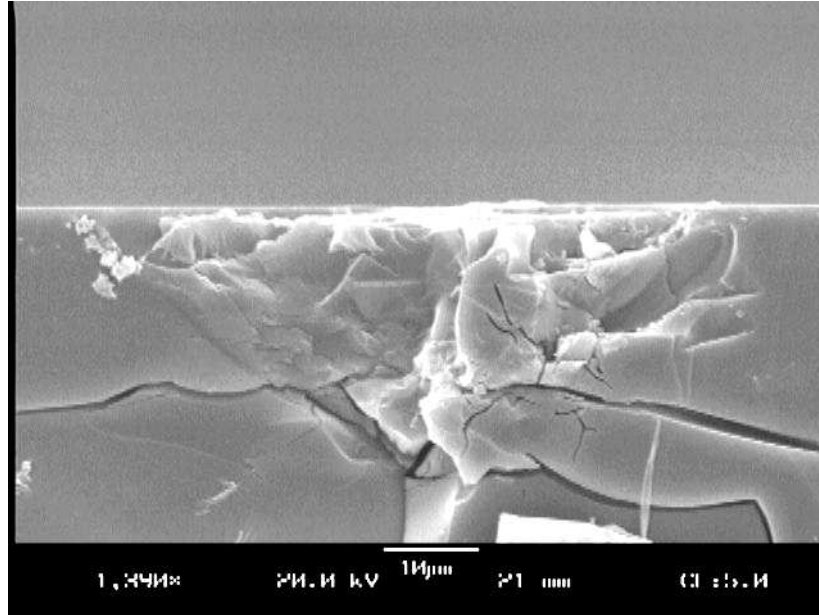
Figure 89. *High-magnification image of the deformation zone beneath a 1 Kg indentation in float glass. Shear faults and cracks comprise the deformation zone. Secondary electron mode, 1390x original photo magnification.*
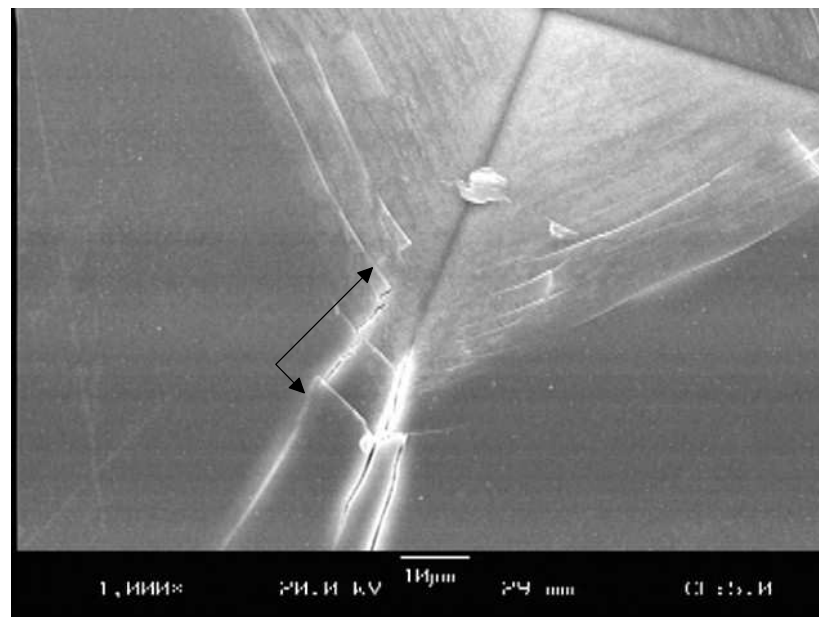
Figure 90. *High-magnification SEM image of a portion of a 5 Kg indentation in float glass. Double arrow indicates a shear crack/secondary-radial crack pair. Secondary electron mode, 1000x original photo magnification.*

A cross-section of the deformation zone beneath a 1 Kg indentation is shown in Figure 89. It contains many cracks, but also fine shear faults. In Figure 90, an image of the surface of another indentation site examined in the SEM reveals that an outer shear fault developed into a median-radial crack.

4.2.10.4   Surface Profilometry

A profile of a 1 Kg indentation made with the conventional indenter in the float glass is shown in Figure 91. Similar to the other glasses which were profiled, an uplift region is apparent on both sides of the indentation. The distance 'L' labeled is about 90 µm. Post-test microscopy found that lateral cracks averaged 63 ± 14 µm, which is good indication the uplift is from the lateral cracks.
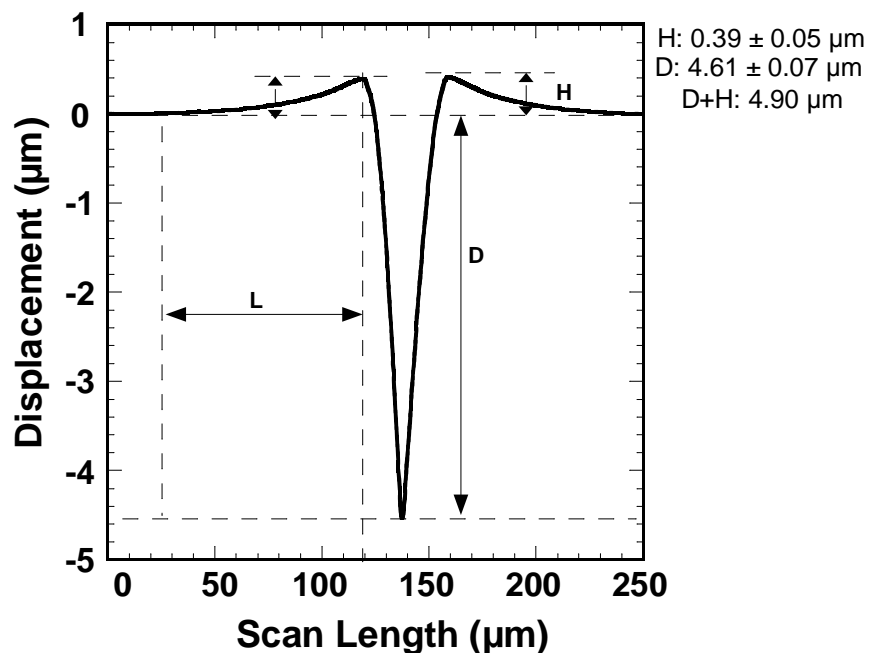
Figure 91. *Profile of a 1 Kg indentation made in float glass with the conventional indenter.*

4.2.11 7740 Pyrex™ Borosilicate

This glass was 'anomalous' with respect to its permanent deformation behavior. Ring-cone cracks initiated in 100% of the tests on loading, with the smallest ring-cones initiating at 191 ± 66 g. Larger ring-cone cracks initiated as the indentation force was increased. The ring-cone cracks popped-in all around the indentation sites. A single large ring-cone crack would emerge as the dominant crack and show the most growth. Numerous white reflections were seen, due to both ring-cone crack formation and shear fault formation. No radial cracks formed on loading up to 1 Kg.

Table XXIII. 7740 Pyrex™ Borosilicate Crack Initiation Behavior.

7740 Pyrex™ Borosilicate	First Ring-Cone Loading	First Median-Radials Unloading	First Laterals Unloading
1 Kg (0.2 µm/s) *72°F/31%*	191 ± 66 g [100 %]	198 ± 10 g (20 ± 1 %) [100 %]	near complete U.L.

On unloading, the dominant cone crack was observed to close slightly, and then at an average force of 198 ± 10 g, the cone crack would 'pop-shut,' appearing to close completely. However, similar to what was observed and described by Arora et al.[7] what was most likely observed was the top part of the cone crack detaching from the bottom part of the same crack. At the same time that the cone crack detached itself, median-radial and secondary radial cracks initiated and grew. All cracks initiated at the same time. Towards complete unloading, lateral cracks initiated. Based on post-test microscopy, both shallow and deep lateral cracks were present, with the shallow lateral cracks tending to be concentrated close to the indentation impression. No large breakthroughs of the shallow lateral cracks was observed; however, there was minor surface chipping near the edges of most indentations. Table XXIII summarizes the crack initiation behavior of the 7740 Pyrex™ borosilicate glass.

4.2.11.1 Post-Test Optical Microscopy

Figure 92 is an image of a 1 Kg (0.2 µm/s) indentation site in the 7740 Pyrex™ borosilicate glass. Multiple, well-developed surface ring cracks are apparent, which flare into cone cracks below the surface. Median-radial cracks are also evident, as are smaller sub-surface radial cracks. Some of the latter cracks are smaller, and some larger, than the surface median-radial cracks. A higher-magnification image of this indentation, Figure 93, shows in greater detail the multiple well-developed surface ring cracks. There is also a lack of shear faults on the surface of the indentation, evidence that less shear
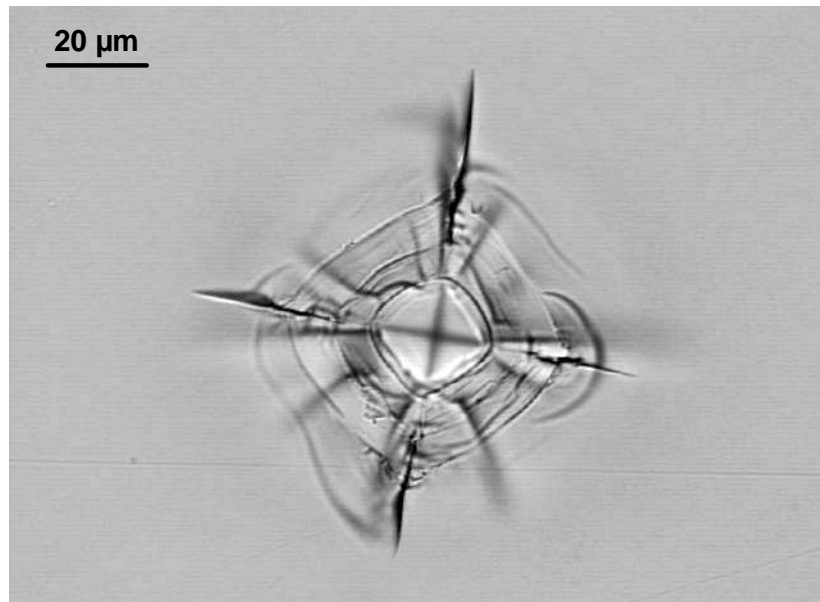
Figure 92. *Indentation site in the 7740 Pyrex™ borosilicate glass from 1 Kg (0.2 µm/s) test. Image width: 166 µm. Trans. light, BF, 500x original photo magnification.*
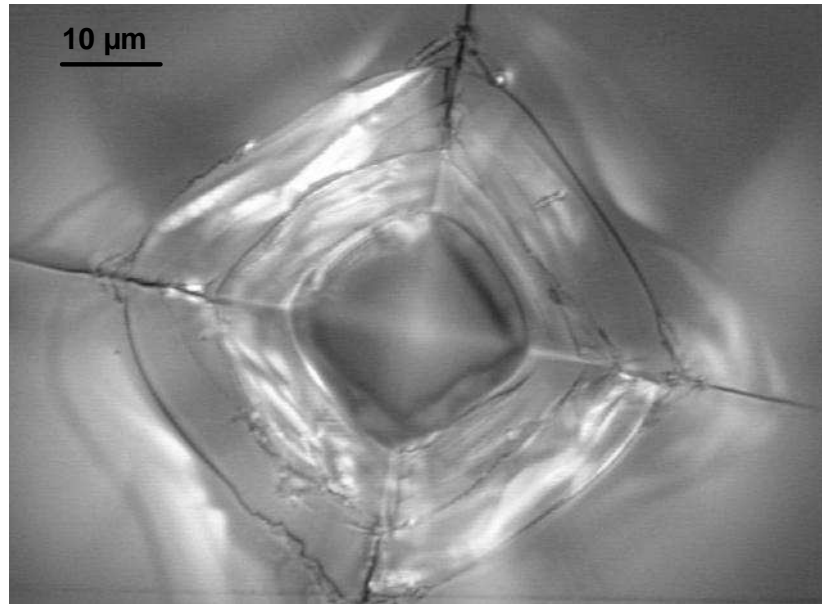
Figure 93. *Higher magnification image of the indentation in Figure 92. Image width: 83 μm. Refl. light, DIC, 1000x original photo magnification.*

deformation, and more densification/compaction, took place in this glass, which would explain its 'anomalous' behavior.

4.2.12 Suprasil 312 Vitreous Silica—'Anomalous'

This glass was 'anomalous' with respect to its permanent deformation behavior. The crack initiation behavior of this glass is summarized in Table XXIV. Ring-cone cracks initiated early on the loading cycle. Multiple ring-cone cracks initiated as the load was increased. Usually a dominant ring-cone cracks emerged and showed the most growth. It was also believed that median-radial cracks initiated on the loading cycle. However, due to the presence of the cone cracks, seeing these cracks initiate was very difficult.

Table XXIV. Suprasil 312 Vitreous Silica Crack Initiation Behavior Summary.

Suprasil 312	First Ring-Cone Loading	Median-Radials Loading	Cone Closure/addn'l Radial Initiation Unloading	First Laterals Unloading
1 Kg (0.2 µm/s) *81°F/31%*	78 ± 28 g [100%]	yes	224 ± 114 g (22 ±11 %) [100 %]	30 ± 10 g (3 ± 1 %) [100 %]

On unloading, the median-radial cracks would start to close. This was followed by violent closure of part of the cone crack, which was simultaneously accompanied by initiation of another set of median-radial cracks, and the extension of the pre-existing median-radial cracks. Lateral cracks initiated on unloading.

4.2.12.1 Post-Test Optical Microscopy

An indentation site from a 1 Kg test is shown in Figure 94. Multiple, well-developed surface ring cracks are apparent. Bright regions are from lateral cracks. A transmitted-light image of the same indentation, Figure 95, clearly shows median-radial cracks extending from the indentation site. Additional radial cracks extend from the sides of the indentation, and are out of focus, indicating they exist just below the surface. Overall, this fracture pattern looks similar to the 7740 Pyrex™ borosilicate glass pattern. A higher-magnification image of the indentation is shown in Figure 96. A very small

amount of surface chipping is apparent. Shear faults appear to be absent on the surface; however, ring cracks are evident. A cursory examination of other indentation sites revealed that the diameter of the innermost surface ring crack scaled with initiation load for the first ring cracks to initiate on loading. Since ring-cone cracks have been found to initiate at the contact periphery for Vickers indentations in vitreous silica, aluminosilicate, and borosilicate glass,[39] this is not surprising.
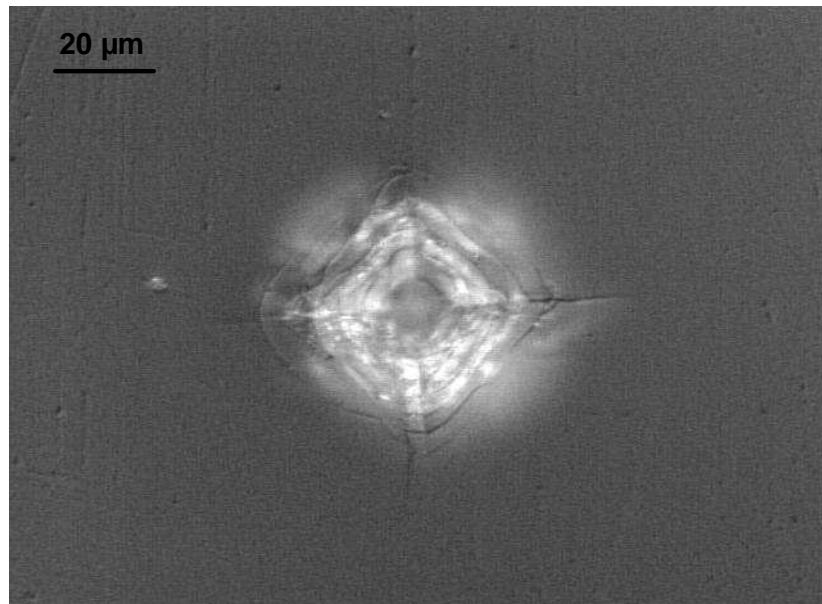
Figure 94. *A 1 Kg (0.2 µm/s) indentation site in the Suprasil 312 v-SiO₂. Image width: 166 µm. Refl. light, DIC, 500x original photo magnification.*
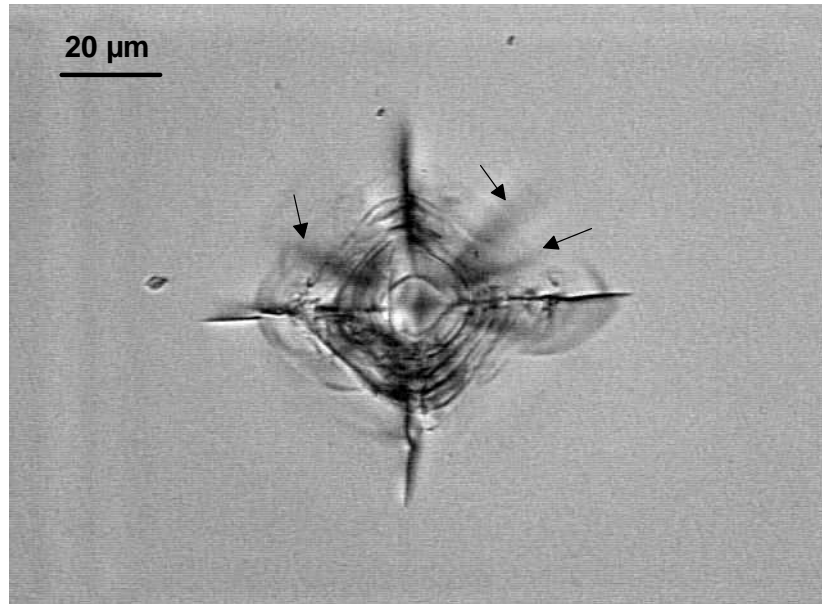
Figure 95. *Transmitted-light image of indentation in Figure 94. Arrows indicate sub-surface radial cracks that to extend from indentation sides. Image width: 166 μm. Trans. light, BF, 500x original photo magnification.*
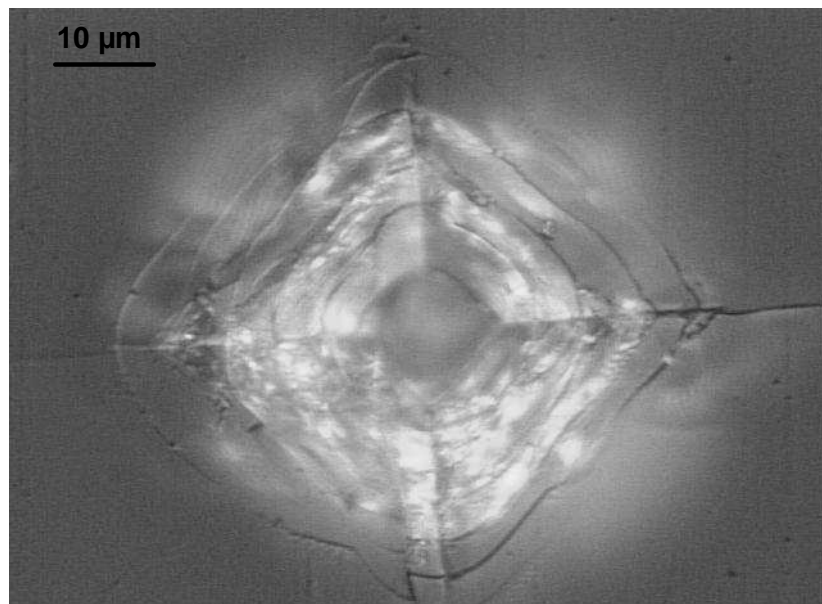
Figure 96. *High-magnification image of the indentation site in Figure 94. Image width: 83 μm. Refl. light, DIC, 1000x original photo magnification.*

171

4.2.12.2 Indentation Cross-Sections

Since the Suprasil 312 specimen was $\approx$ 10 mm thick, it could not be sectioned for observation of indentation cross-sections. Instead, commercial vitreous silica microscope slide glass was used for this purpose. A 1 Kg indentation made with the conventional indenter and its corresponding cross-section are shown in Figures 97 and 98, respectively. A well-developed cone crack and a median-radial vent crack are visible. The angle the major cone crack makes with the free surface is $\approx$ 43°. The median-radial crack extends only $\approx$ 36 µm below the surface, compared to the cone crack which extends down to $\approx$ 62 µm. The deformation zone lacks shear faults, but appears to contain cracks.
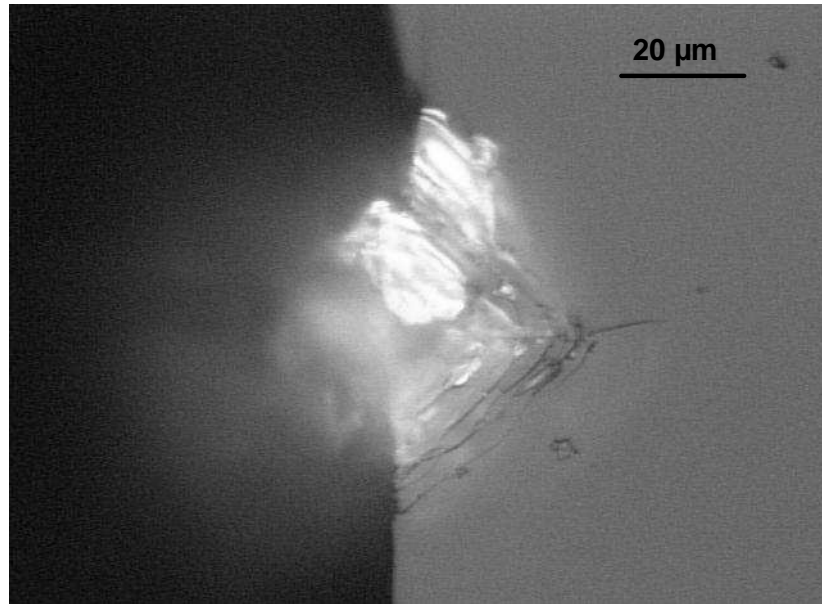
Figure 97. *A 1 Kg indentation in vitreous silica microscope slide glass that was sectioned in half. Image width: 133 µm. Refl. light, DIC, 625x original photo magnification.*
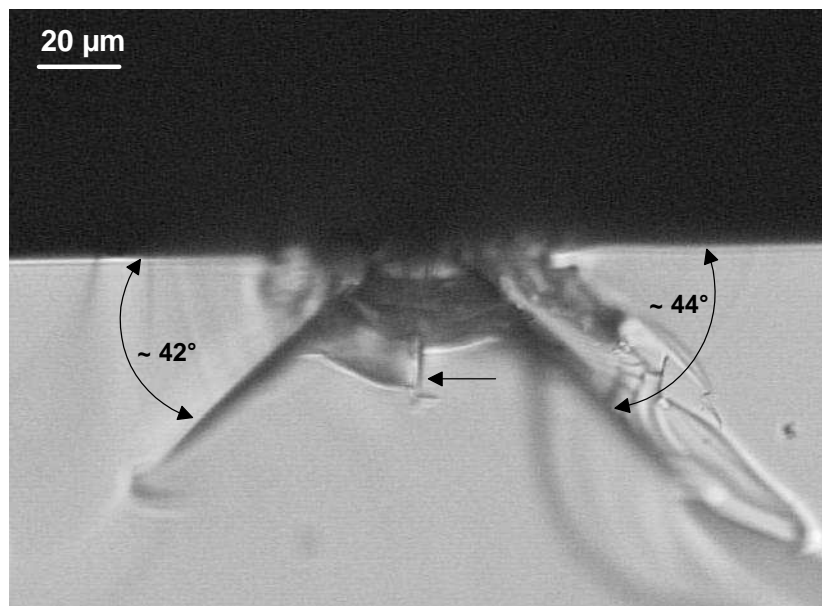
Figure 98. *Corresponding cross-section of the indentation half shown in Figure 97. Cone crack angles were measured using a protractor on the printed image. Image width: 203 µm. Trans. light, BF, 400x original photo magnification.*

4.3   Additional Higher-Load Tests

Additional crack initiation tests were conducted with the recording microindenter on glasses S1, S2, S3, S4, S5, S6, NS2, NS3, and float. The maximum load was allowed to reach 4 Kg for glasses S1, S5, and S6, and 3.5 Kg for glasses S2, S4, NS2 and NS3. For glass S1 the increased maximum load resulted in the formation of well-developed ring-cone cracks. For glass S2, well-developed surface ring cracks initiated; however, in only one test did a well-developed cone crack initiate. Thus, for these two glasses, a transition to 'anomalous' cracking behavior occurred. In addition, median-radial and lateral cracks initiated on unloading for all tests performed at 3.5 Kg for glass S2.

For glasses S3, S5, and S6, increasing the maximum load caused the remainder of the median-radial cracks to initiate on the loading cycle, as opposed to on unloading as for the 1 Kg tests. In addition, lateral cracking on unloading became more frequent at loads greater than 1 Kg.

For the float-glass specimen, increasing the load to 4 Kg resulted in 20% of the tests having all median-radial cracks initiate on loading, with the remainder of the tests initiating all such cracks on unloading. In addition, small partial ring cracks were present around the corners of these higher-load indentations. An example of this is shown in Figure 99. For the phosphate glass, NS2, a similar type of partial ring cracking was seen around

174
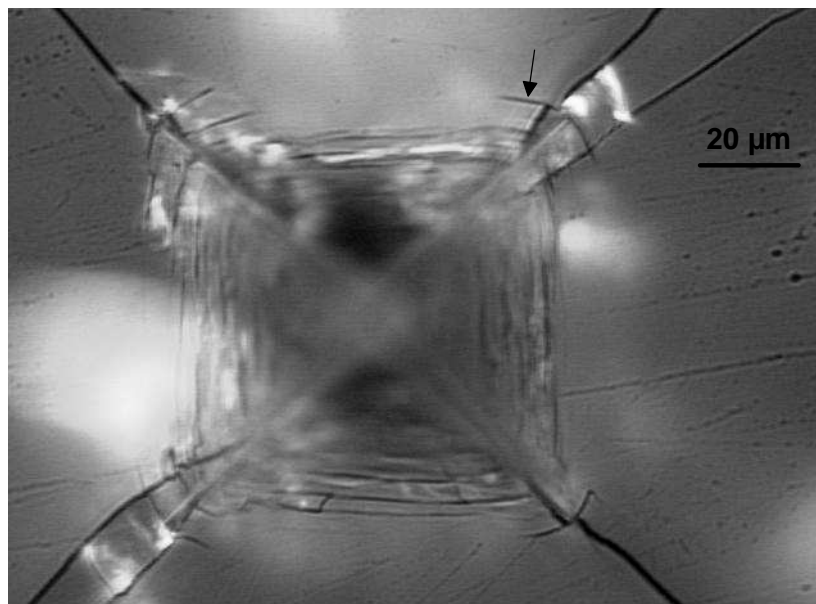
Figure 99. *High-magnification image of a 4 Kg indentation site in float glass produced with the recording microindenter. Arrow indicates one of many partial ring cracks that formed around the 4 Kg indentations. Image width: 166 µm. Refl. light, DIC, 500x original photo magnification.*

indentations at 3.5 Kg load. However, increases in load did not cause this behavior for glasses S4 and NS3.

In addition, one of Wagner's original glass specimens, ALS100, was tested to 4 Kg maximum load as well. In 100% of the tests well-developed ring-cone cracks initiated. This was in comparison to 56% of the tests that Wagner[9] observed these cracks to initiate when indented to 1400 g load. Thus, increasing the maximum load on this glass resulted in more tests exhibiting 'anomalous' behavior. Suprasil 312 vitreous silica was also believed to have initiated median-radial cracks at > 1 Kg when it was indented to 4 Kg.

4.4　　　　　　Mechanical Properties Results and Discussion

4.4.1　Density

The density, molecular weight, molar volume, and atomic molar volume results for the glasses are shown in Table XXV. The molecular-weight data were provided by the glass manufacturer. The atomic-molar-volume values should be approached with some caution, since the calculation of this number was dependent on the actual compositions of the glasses, which in the current work was known to within about 5 molar percent.

It is apparent the 'anomalous' glasses all have densities below about 2.5 g/cm^3. However, v-B$_2$O$_3$ is one exception. It presumably behaves 'normal' in

Table XXV. Density, Molecular Weight, Molar Volume, and Atomic Molar Volume Data.

Glass	Density (g/cm^3)	Molecular Weight (g/mol glass)	Molar Volume (cm^3/mol glass)	Atomic Molar Volume (cm^3/mol atoms)
S1 (A)	2.50	67.36	26.94	8.24
S2 (A)	2.46	64.82	26.35	8.05
S3 (N)	3.55	89.99	25.35	7.43
S4 (N)	6.16	160.41	26.04	8.83
S5 (N)	3.47	88.57	25.52	6.53
S6 (N)	3.74	105.10	28.10	6.38
NS1 (N)	4.29	136.27	31.76	6.17
NS2 (N)	2.57	124.34	48.38	8.62
NS3 (N)	3.66	93.58	25.57	7.61
Float (N-A)	2.52	59.28	23.52	8.25
7740 Pyrex ™ Borosilicate	2.23	62.23	27.91	8.46
v-SiO$_2$ (Suprasil 312) (A)	2.23	60.08	26.94	8.98
v-B$_2$O$_3$* (N)	1.81	69.62	38.25	7.65

*from CRC Handbook[59]

indentation testing, because of the weak van der Waals bonding between sheets of BO_3 triangles which would allow this glass to shear more readily rather than compact/densify.[60]

The float glass has a density of 2.52 g/cm^3, and partial ring cracks formed for the 4 Kg tests made with the recording microindenter. Thus, this glass has some 'anomalous' character. The potassium phosphate glass (NS2) also had partial ring cracks form around the 3.5 Kg indentations made with the recording microindenter. It has a density of 2.57 g/cm^3. However, glass NS2 is classified as 'normal' since numerous fine shear flow lines formed beneath the indentations. The most 'normal' glasses are characterized by higher densities, implying less 'free-volume.' The lower densities of the 'anomalous' glasses are consistent with a more open structure, which is capable of accommodating the penetrating indenter by more compaction/densification rather than by shear-induced faulting/flow, resulting in greater elastic surface stresses and higher probability of ring-cone cracking.

4.4.2 Elastic (Young's) Modulus

The results of the Young's modulus testing of the glasses is shown in Table XXVI. The bulk and shear moduli are listed as well, as is Poisson's ratio and the sonic velocities for the longitudinal and shear sound waves.

Table XXVI. Elastic Moduli Data.

Glass	Young's Modulus, E (GPa)	Shear Modulus, G (GPa)	Bulk Modulus, K (GPa)	Poisson's Ratio, ν	V_L (m/s)	V_S (m/s)
S1 (A)	63.3 ± 1.3	27.4 ± .4	31.0 ± .6	0.156 ± .022	5567 ± 50	3470 ± 17
S2 (A)	70.1 ± .5	29.7 ± .3	36.5 ± .3	0.182 ± 0.013	5189 ± 94	3309 ± 26
S3 (N)	88.1 ± .6	34.8 ± .2	63.8 ± .4	0.267 ± 0.006	5551 ± 50	3129 ± 9
S4 (N)	48.6 ± .8	19.1 ± .2	35.2 ± .6	0.268 ± 0.011	3149 ± 72	1761 ± 10
S5 (N)	112.8 ± 1.8	44.6 ± .8	78.3 ± 1.3	0.264 ± 0.010	6336 ± 85	3588 ± 31
S6 (N)	114.2 ± 2.8	45.0 ± 1.1	82.7 ± 2.1	0.269 ± 0.016	6170 ± 119	3467 ± 42
NS1 (N)	123.0 ± 2.0	47.8 ± 1.0	97.6 ± 1.6	0.288 ± 0.019	6119 ± 127	3335 ± 33
NS2 (N)	49.7 ± .6	19.9 ± .2	33.1 ± .4	0.249 ± 0.013	4816 ± 68	2781 ± 11
NS3 (N)	78.9 ± 1.2	30.7 ± .5	62.6 ± 1.0	0.285 ± 0.009	5286 ± 61	2895 ± 24
Float (N-A)	73.6 ± 1.4	30.1 ± .3	43.8 ± .8	0.221 ± 0.019	5782 ± 126	3459 ± 15
7740 Pyrex Borosilicate[‡](A)	62.7	26.1	34.8	0.20	n/a	n/a
v-SiO$_2$ (Suprasil 312) (A)	74.6 ± .4	31.8 ± .2	37.7 ± .2	0.17 ± .01	5908 ± 30	3824 ± 12
v-B$_2$O$_3$ * (N)	17.0	6.9	12.1	0.262	n/a	n/a

[*] from G.H. Frischat[61]

[‡] from Engineered Materials Handbook[62]

4.4.2.1 Elastic (Young's) Modulus Discussion

Young's modulus is a measure of a materials resistance to uniaxial elongation or compression. It is the slope of the stress-strain curve in the linear elastic region of a uniaxial tensile test, and thus the proportionality constant between stress and strain i.e., s = E, where E is Young's modulus.[55] For given applied tensile stress, it dictates how much strain the material undergoes, and vice versa. Highly 'elastic' materials, such as rubber, have relatively low Young's modulus, where more 'rigid' materials, such as silicate glasses, have relatively high Young's modulus. Thus, Young's modulus is a

measure of structural rigidity, or stiffness.

4.4.2.2 Atomic Description of Young's Modulus

On an atomic scale, the Young's modulus measures the resistance to the stretching or compression of bonds between two atoms, and its magnitude is related to the slope of the curve of interatomic force vs. separation at the equilibrium bond distance, r_0.[55] This can be expressed as follows:[55]

$$E \approx -\frac{1}{r_0}\left(\frac{dF}{dr}\right)_{r_0} \tag{19}$$

For ionic crystals the following expression for Young's modulus can be derived:[63]

$$E = 2\alpha\frac{U}{r_0^3} \tag{20}$$

where,
E = Young's Modulus
α = Madelung constant
U = electrostatic energy of attraction (binding energy)
r_0 = equilibrium interatomic separation distance

The quantity $\alpha \cdot U$ is the Madelung energy, U_m. Thus, Young's modulus for ionic crystals is two times the Madelung energy per volume r_0^3.[63] Thus materials with high binding energy and short equilibrium length bonds are predicted to have high Young's modulus.

Using the method of Makishima and Mackenzie[63] the dissociation energy

per unit volume glass was calculated based on the following equation:

$$G = \sum_i G_i X_i \qquad (21)$$

where,

G = dissociation energy per unit volume glass

G_i = dissociation energy for oxide component i

X_i = mole fraction of component i

Values of G_i from the work of Makishima and Mackenzie[63] were used to

calculate G for most of the current glasses. The results are shown in Table

XXVII, along with the values of G_i used in the calculations. The packing

density of ions, V_t, is also shown in the table, and represents, approximately,

the volume fraction the ions occupy in the glass. Several of the glasses

contained components whose G_i values were not known, hence calculations

were not performed on these glasses. In addition, a modified value of G_i was

used for the 7740 Pyrex™ borosilicate glass, which took into account that

only a fraction of the boron was in four-fold coordination. The calculation

assumed the 8 moles of Na^+ ions in this glass converted 8 of the 26 moles of

BO_3 groups to BO_4 groups. The bond dissociation energy for 3-fold

coordinated boron is around 3.9 Kcal/cm³, compared to about 18.6 Kcal/cm³

for 4-fold coordinated boron.[63] The equation for the modified G term is:[63]

$$G_B = \gamma(G4 - G3) + G3 \qquad (22)$$

where,

G_B = modified bond dissociation energy

γ = fraction of 4-fold coordinated boron, i.e., BO_4

$G4$ = bond dissociation energy for 4-fold coordinated B (BO_4; 18.6 Kcal/cm^3)

$G3$ = bond dissociation energy for 3-fold coordinated B (BO_3; 3.9 Kcal/cm^3)

Table XXVII. Dissociation Energy Per Unit Volume for Oxide Components and Glasses.[*]

Component	G_i (Kcal/cm^3)	Glass	G (Kcal/cm^3)	Packing Density, V_t
Al_2O_3	32.0	S1 (A)	15.09	0.542
ZrO_2	23.2	S2 (A)	15.89	0.551
B_2O_3	18.6	S3 (N)	15.96	0.638
Y_2O_3	17.7	S4 (N)	10.45	0.556
La_2O_3	16.2	S5 (N)	17.59	0.683
CaO	15.5	S6 (N)	18.01	0.698
SiO_2	15.4	NS2 (N)	14.10	0.616
P_2O_5	15.0	Float (N-A)	14.84	0.545
ZnO	9.9	7740 Pyrex ™ Borosilicate (A)	14.57	0.535
BaO	9.7	v-SiO$_2$ (A)	15.40	0.520
Na_2O	8.9			
K_2O	4.5			
PbO	4.2			

[*] G_i data from Makishima and Mackenzie[63]

For the other glasses, boron was assumed 4-fold coordinated based on considerations of structure. Considerations of structure are examined later when the crack initiation results are discussed in more detail.

Figure 100 shows the Young's modulus as a function of the dissociation energy per unit volume of the glasses. The agreement is only fair; however, it appears that high dissociation energy per unit volume favors high Young's modulus. In Figure 101 the Young's modulus is plotted as a function of the atomic molar volume of the glasses. Here the agreement is very good; however, two clear exceptions are the two pure glass-formers, v-SiO$_2$ and v-B$_2$O$_3$. The sheet-like structure of v-B$_2$O$_3$ with weak van der Waals bonds holding sheets together is the reason for its lower Young's modulus compared to glasses with similar atomic molar volume, e.g., glasses S3 and NS3. Vitreous silica has a higher Young's modulus than expected compared to glasses with similar atomic molar volume, e.g., glass S4. This may be due to the fact that despite the open structure of v-SiO$_2$, the bond strength of the Si-O bond is very high (~ 106 kcal/mole), and bonding exists in all three spatial dimensions, which probably makes up for the high atomic molar volume (low bond density).[35] Both these figures illustrate that both the bond strength (through G) and glass structure, e.g., atomic molar volume, contribute to the value of Young's modulus of these glasses, in agreement with the theoretical analysis presented earlier.
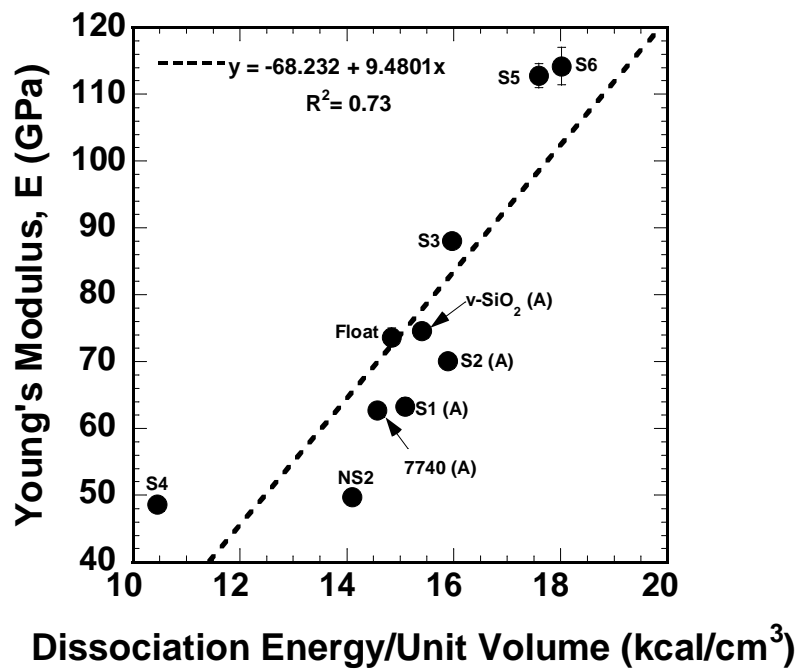
Figure 100. Young's modulus as a function of the dissociation energy per unit glass volume.
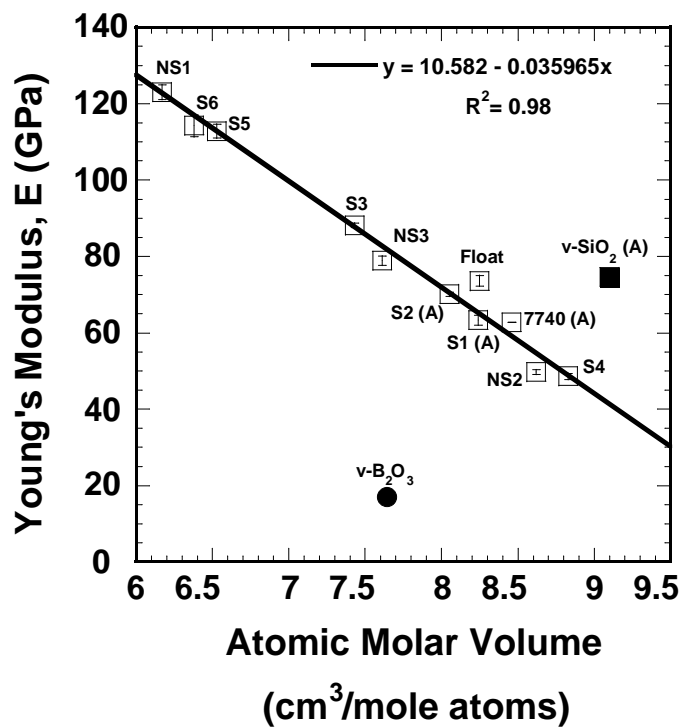
Figure 101. Young's modulus as a function of the atomic molar volume of the glasses.

4.4.3 Vickers Hardness

The Vickers hardness of the glasses is summarized in Table XXVIII. The ratio (E/H_V) is also shown, and was calculated by dividing the average Young's modulus by the Vickers hardness value obtained from each indentation. This ratio appears in many fracture mechanics relations, including the fracture toughness formula used in the current work, and in many crack initiation models, such as those by Chiang et al.[24] and Cook and Pharr[11]. This ratio will be examined further when the crack initiation results are discussed. But briefly, higher values of (E/H_V) are associated with 'softer' materials, and increased crack driving force for initiated cracks. The ratio of shear modulus to bulk modulus, G/K, is also listed, and will be discussed shortly. All of the indentations had median-radial cracks around them, except for the 7740 Pyrex™ borosilicate glass.

4.4.3.1 Vickers Hardness Discussion

The Vickers hardness number has units of stress, thus implying a mean contact pressure. The hardness ranges from 2.01 GPa for v-B_2O_3 to 8.02 GPa for glass NS1, which is about a factor of four difference.

According to Yamane and Mackenzie[64] shear and compressive stresses give rise to the permanent indentations observed in glass from indentation

Table XXVIII. Vickers Hardness Data.

Glass	Vicker's Hardness, H_V (GPa)	Indentation Diagonal Width, d (µm)	E/H_V	G/K	Median-Radial Cracks (µm)
S1 (A)	4.71 ± 0.11	27.80 ± .32	13.45 ± .40	*0.884*	~ 30 (100 %)
S2 (A)	5.36 ± 0.09	26.05 ± .22	13.07 ± .39	*0.814*	25 ± 1 (33 %)
S3 (N)	6.23 ± 0.12	24.17 ± .23	14.15 ± .42	0.545	38 ± 2 (100 %)
S4 (N)	3.04 ± 0.07	34.58 ± .37	15.99 ± .48	0.543	62 ± 4 (100 %)
S5 (N)	7.61 ± 0.11	21.86 ± .15	14.82 ± .44	0.570	33 ± 2 (100 %)
S6 (N)	7.81 ± 0.14	21.59 ± .19	14.63 ± .44	0.544	32 ± 1 (100 %)
NS1 (N)	8.02 ± 0.26	21.31 ± .35	15.33 ± .46	0.490	32 ± 2 (100 %)
NS2 (N)	3.63 ± 0.05	31.67 ± .23	13.70 ± .41	0.601	38 ± 2 (100 %)
NS3 (N)	4.31 ± 0.13	29.04 ± .43	18.29 ± .55	0.490	55 ± 3 (100 %)
Float (N-A)	5.28 ± 0.05	26.27 ± .13	13.95 ± .42	0.687	28 ± 2 (92 %)
7740 Pyrex ™ Borosilicate (A)	5.35 ± 0.11	26.06 ± .06	11.71 ± .35	*0.750*	none
v-SiO$_2$ (Suprasil 312)* (A)	6.78 ± 0.40	16.43 ± .52	11.01 ± .33	*0.844*	10 ± 1 (90 %)
v-B$_2$O$_3$ [‡] (N)	2.01	n/a	8.46	0.570	n/a

[*]Vickers hardness obtained from 100 g indentations made with the recording microindenter, with no hold time under load.

[‡]hardness from Frischat[61], 200 g test load

Numbers in parentheses indicate percent of indentations observed having median-radial cracks.

with a Vickers diamond. Each stress produces different types of deformations, which are summarized in Table XXIX below. Obviously, the elastic deformations in glass do not give rise to the permanent indentation directly, but are associated with the degree of elastic recovery of the indentation diagonals (and depth), and thus affect the hardness number. Anelastic effects, other than densification, are not treated. Shear stresses produce shear-'flow' (faulting), which can give rise to a permanent indentation.

185

Table XXIX. Summary of Possible Deformations and Stresses in
Glass Under a Sharp Indenter.[*]

Stress Type	Deformation
Shear	1. Shear Flow (Faulting)

Compression	1. Elastic Deformation
	2. Densification
	  a. with bond breaking
	  b. without bond breaking

[*]after Yamane and Mackenzie[64]

Compressive stresses can cause elastic deformation of the glass, and possibly densification, the latter causing permanent deformation. Two types of densification can be distinguished. One type involves the breaking of bonds and the other does not, and both types are probably present in an indentation test, with one dominating over the other, as shown by Yamane and Mackenzie[64] for vitreous silica and a 50 CaO•50 SiO$_2$ (mol %) glass. The non-recoverable densification is most likely associated with bond-breaking, involving both shear and compressive stresses, whereas the recoverable densification probably involves re-arrangement of SiO$_4$ tetrahedra by bond rotation and kinking into a smaller volume, which as shown by Mackenzie[34] is facilitated by shear stress, but compressive stresses probably cause the majority of this recoverable densification.

Yamane and Mackenzie[64] developed a formula for calculating the Vickers hardness of glass knowing the composition. The authors suggested the following:[64]

1. Resistance to **elastic deformation** in a Vickers indentation test is proportional to the bulk modulus (i.e., $R_e \propto K$),

2. Resistance to **shear** flow (faulting) is proportional to the shear modulus as well as a relative bond strength factor, α, since bond breaking must also occur during shear flow (i.e., $R_f \propto (\alpha G)$.

3. Resistance to **densification** involves both compression and shear, and could involve the breaking of bond (i.e., $R_d \propto [(\alpha G)K]^{1/2}$.

4.4.3.2 Vickers Hardness vs. G and K

The Vickers hardness is shown as a function of the shear modulus, G, in Figure 102. Strong correlation between it and the hardness is apparent. It should be recalled that the shear modulus is the ratio of shear stress to shear strain in the linear elastic region of material behavior.[35]

In Figure 103 the Vickers hardness is shown as a function of the bulk modulus, K, of the glasses. The correlation between Hv and K is not as good compared to H_V and G; the former having an $R^2 = 0.66$ and the latter R^2
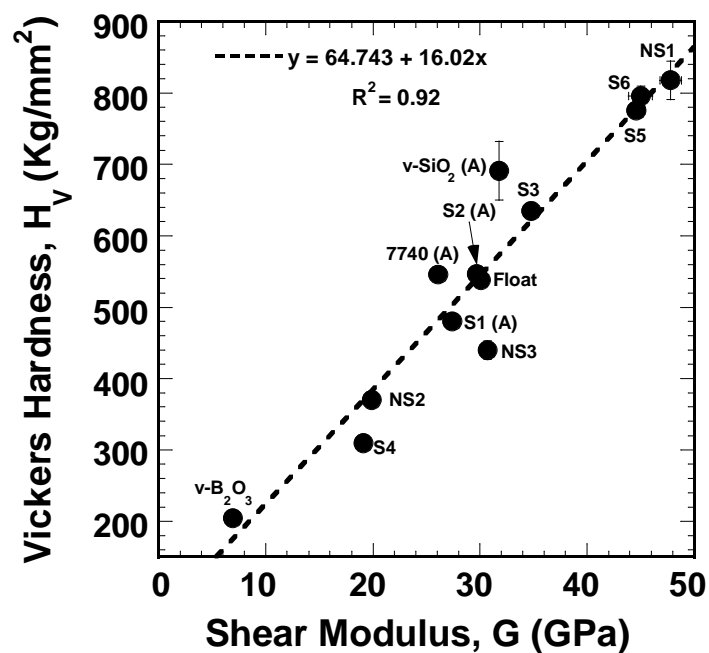
Figure 102. *Vickers hardness as a function of shear modulus of the glasses.*
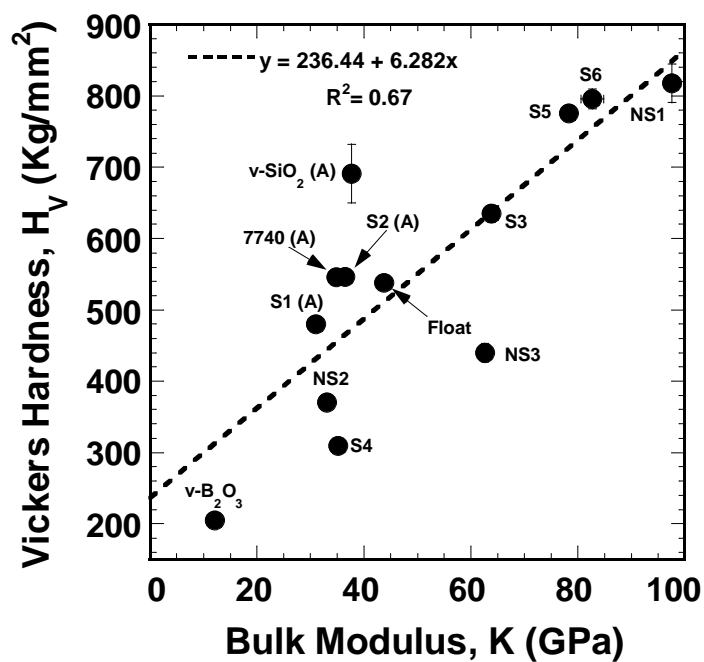
Figure 103. *Vickers hardness as a function of bulk modulus of the glasses.*

188

=0.93. The bulk modulus is the ratio of hydrostatic stress to volumetric strain, in the linear elastic region of material behavior.[35] Hydrostatic conditions mean the stress is applied equally on all sides of a volume element, i.e., equal triaxial stress state. Although the compressive stress component in a Vickers indentation test is not purely hydrostatic, there is a close-enough resemblance to justify its use in analyzing microhardness of glass. Due to the high constraint to material movement that the surrounding elastic material provides in an indentation test, some triaxial stress state is likely in the sub-surface plastic zone. The high constraint arises because the (elastic) specimen volume is so much greater than the small indentation volume.

Since the correlation of Vickers hardness with shear modulus is greater than with bulk modulus, the shear modulus, and hence shear deformation behavior, dictate the indentation response of the current glasses to a greater extent relative to the bulk modulus. This is expected since the shear moduli for all the glasses are lower than the bulk moduli, and thus the glasses will prefer to shear, since this offers the least resistance to deformation.

4.4.3.3 Vickers Hardness vs. Young's Modulus

The Vickers hardness is shown as a function of Young's modulus in Figure 104. Good correlation is seen between H_V and E, but this is due to the linear
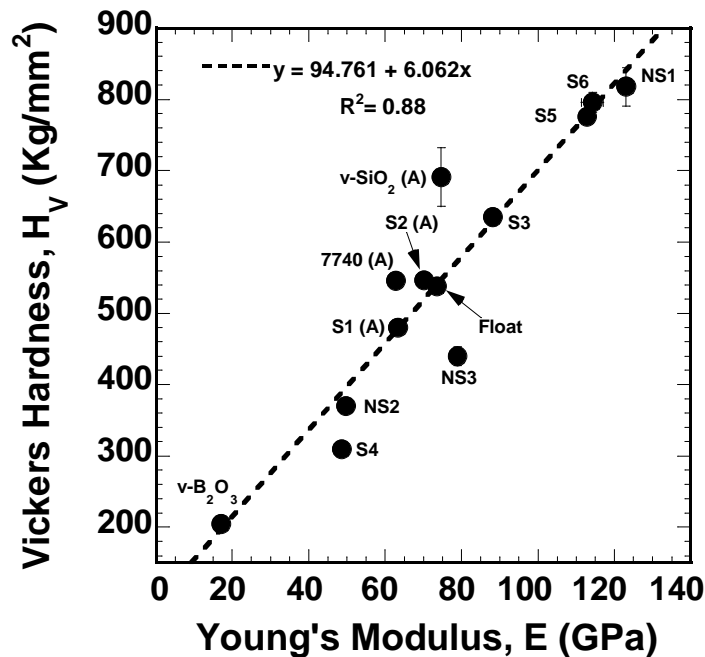
Figure 104. *Vickers hardness as a function of Young's modulus of the glasses.*

relationship of E with G (which is only a function of Poisson's ratio; see Eq. 6); and, as previously shown, H_V correlates highly with G. Young's modulus is expected to have some influence on hardness in and of itself, since elastic recovery of the indentation diagonals occurs in indentation testing of glass, thus affecting the calculated hardness number.[65]

4.4.3.4 Vickers Hardness vs. Atomic Molar Volume

The Vickers hardness is shown as a function of the atomic molar volume in Figure 105, and in general it increases with decreasing atomic molar volume. However, similar to the variation with Young's modulus, the pure network

formers, i.e., v-SiO$_2$ and v-B$_2$O$_3$, do not fit the trend. Also, the fit is not as good compared to the variation of E with atomic molar volume. This suggests the atomic molar volume has less of an influence on hardness than it does on Young's modulus.

4.4.3.5 Vickers Hardness vs. Dissociation Energy/Unit Volume

The Vickers hardness is shown as a function of the dissociation energy per unit volume of glass in Figure 106, for the glasses in which this value was calculated (Table XXVII). The agreement is fair, but highlights the fact that not one single factor can completely predict the hardness number of glass. Similar to the Young's modulus, the structure of the glasses, viz. the atomic molar volume, also plays a role.

4.4.4   Fracture Toughness and Related Data

The data from the fracture toughness testing is shown in Table XXX. The fracture toughness varies from 0.258 MPa•m$^{1/2}$ to 1.010 MPa•m$^{1/2}$, a factor of about four. The crack length values used in the calculation are shown, but should not be compared between the different glasses, since the toughness determinations were made at different loads.
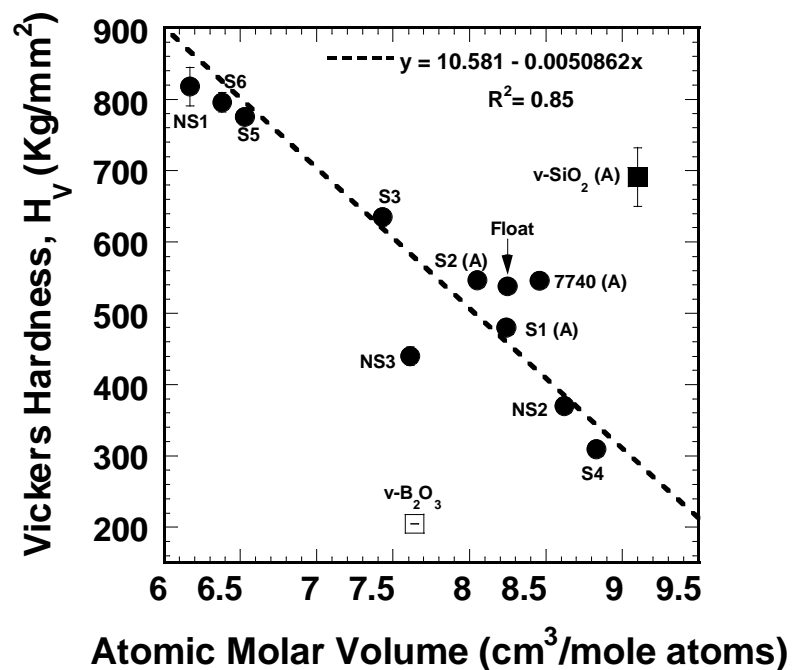
Figure 105. *The Vickers hardness as a function of the atomic molar volume of the glasses.*
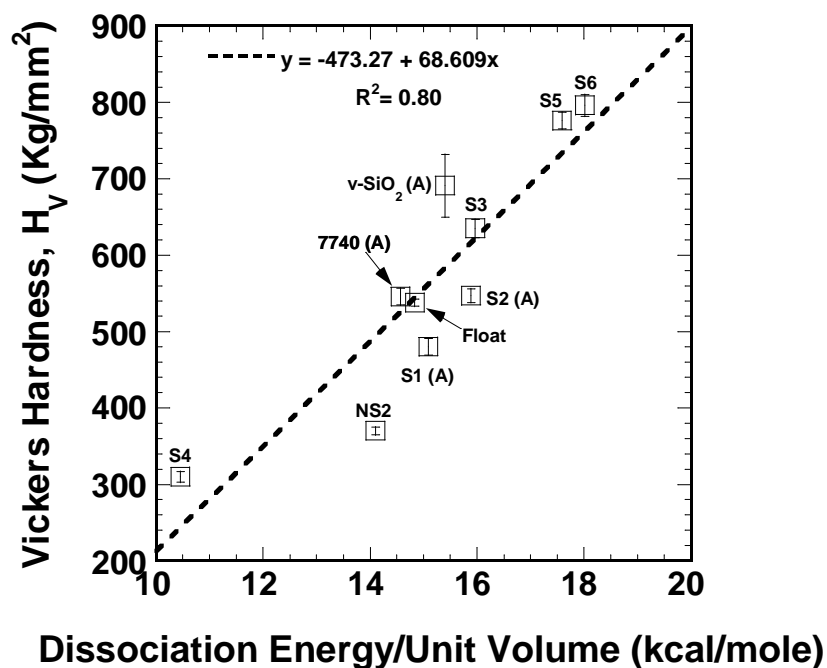
Figure 106. *The Vickers hardness as a function of the dissociation energy per unit volume of the glasses.*

Table XXX. Summary of Data from Fracture Toughness Testing.

Glass	K_{IC} (MPa√m)	H_V (GPa)	Median-Radial Crack Length, c (µm)	Indentation Diagonal Width, d (µm)	γ_f (J/m²)
S1 (A) (1 Kg)	.784 ± .079	4.43 ± 0.05	84 ± 7	64.0 ± .5	4.67 ± 0.75
S2 (A) (2 Kg)	1.010 ± .110	5.14 ± 0.15	110 ± 7	84.0 ± 1.6	6.70 ± .63
S3 (N) (1 Kg)	.508 ± .023	6.19 ± 0.15	111 ± 6	54.2 ± .8	1.36 ± .12
S4 (N) (0.5 Kg)	.258 ± .010	3.04 ± 0.09	114 ± 4	54.6 ± 1.1	.64 ± .05
S5 (N) (1 Kg)	.646 ± .025	7.33 ± 0.19	97 ± 4	49.9 ± .9	1.72 ± .13
S6 (N) (1 Kg)	.687 ± .042	7.33 ± 0.15	93 ± 5	49.9 ± .7	1.92 ± .24
NS1 (N) (1 Kg)	.692 ± .027	7.64 ± 0.07	94 ± 4	48.7 ± .6	1.79 ± .14
NS2 (N) (0.5 Kg)	.440 ± .021	3.61 ± 0.05	76 ± 3	50.2 ± 0.4	1.63 ± .27
NS3 (N) (0.5 Kg)	.349 ± .024	4.36 ± 0.16	97 ± 3	45.6 ± 1.2	.67 ± .07
Float (N-A) (1 Kg)	.715 ± .024	5.13 ± 0.04	88 ± 2	59.6 ± .2	3.30 ± .22
7740 Pyrex Borosilicate (A) [‡]	.758 ± 0.01	5.35 ± 0.11 (200 g)	52 ± 4	n/a	4.75 ± .13
v-SiO$_2$ Suprasil 312 (A) [‡] (1 Kg)	.798 ± 0.023	6.78 ± 0.40 (100 g)	46 ± 3	58.4 ± 1.2	4.42 ± .25
v-B$_2$O$_3$ (N) [š]	0.954	2.01	n/a	n/a	24.9

[‡] K_{IC} and γ_f from Wiederhorn[66]

[š] K_{IC} and γ_f from Miyatta and Jino[67], and H_V from Frischat[61]

One justification for taking the measured values of the fracture toughness of all the glasses as representative of the actual values, comes from comparing the value for the phosphate glass in this study (0.440 MPa√m) with the value given by the manufacturer (0.48 MPa√m). This represents about an 8 % difference. Also, the value for the float glass in this study (0.715

MPa√m) compared well to the value of a similar commercial soda-lime-silicate glass tested by Wiederhorn[66] (0.749 MPa√m). The composition of the glass tested by Wiederhorn[66] was, in mol %: 71.6 $SiO_2 \cdot 1.2$ $Al_2O_3 \cdot 13.1$ $Na_2O \cdot 0.6$ $K_2O \cdot 6.0$ $MgO \cdot 7.5$ CaO (mol %). This is similar to the composition of the float glass tested in the current work (see Table VII).   Another justification is that Anstis et al.[26] found excellent agreement between fracture toughness values calculated using Eq. 9 and those determined by conventional methods using double cantilever beam and double-torsion, for a wide range of materials, including soda-lime, aluminosilicate, and lead-alkali glasses, and numerous polycrystalline and single crystal ceramics.

4.4.4.1 Crack Length vs. K_{IC} and γ_f

Fracture toughness, K_{IC}, measures intrinsic resistance to crack propagation. Solving for the crack length, 'c' in Eq. 9 yields:

$$c = \left\{ 0.016 \left[\frac{\left(E/H \right)^{1/2}}{K_{IC}} \right] \right\}^{2/3} F^{2/3} \tag{23}$$

From equation 27 it is seen that crack length depends on the ratio (E/H), K_{IC}, and of course the indentation load, F. For constant indentation load, the crack length is expected to decrease as (E/H) decreases, and as K_{IC} increases.

The median-radial and lateral crack lengths from the 1 Kg recording microindenter crack initiation tests are shown as a function of K_{IC} in Figure 107. It can be seen that in general crack length decreases as fracture toughness increases, for both crack types. Since it was believed that slow crack growth influenced the results for glass NS2 (potassium-phosphate glass) experiments were repeated ensuring that crack lengths were measured even quicker after indenting than the first time. These values are the 'no slow crack growth' values, and are lower than the first values obtained.

The median-radial and lateral crack lengths are shown as a function of the fracture surface energy in Figure 108. A very similar trend to Figure 107 is seen. This is not surprising given the relationship between K_{IC} and the fracture surface energy i.e., $K_{IC} = [(2E\gamma_f)/(1-\upsilon^2)]^{1/2}$ for plane-strain conditions.

4.4.4.2 Crack Length vs. E/Hv

In Figure 109 the median-radial and lateral crack lengths are shown as a function of the ratio E/H_V. Although there is much scatter in the data, in general the crack length is seen to increase with the value E/Hv, as Eq. 9 predicts. The ratio E/H_V is a measure of the driving force for crack growth provided by the residual stress field.[26] Glasses with high E/H_V are termed
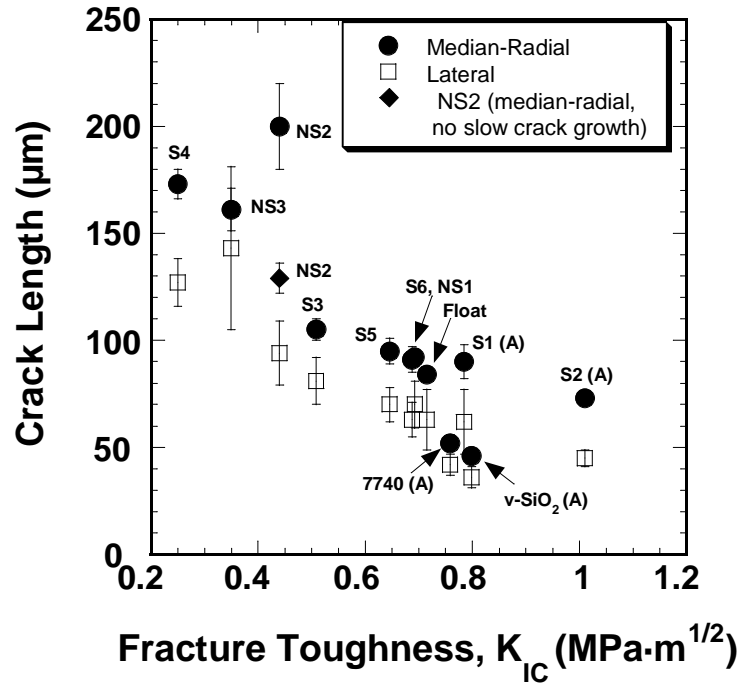
Figure 107. *Median-radial and lateral crack lengths from the 1 Kg recording microindentation crack initiation tests as a function of fracture toughness for the different glasses.*
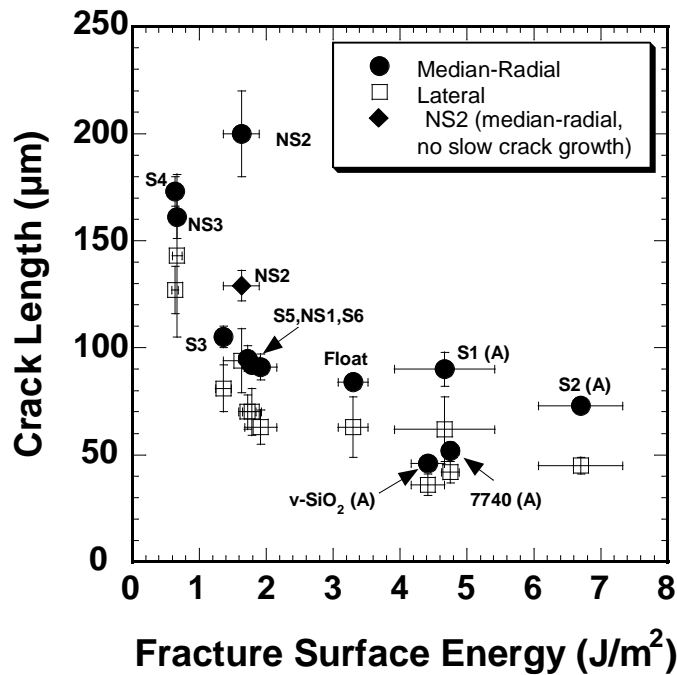
Figure 108. *Median-radial and lateral crack lengths from the 1 Kg recording microindentation crack initiation tests as a function of fracture surface energy for the different glasses.*
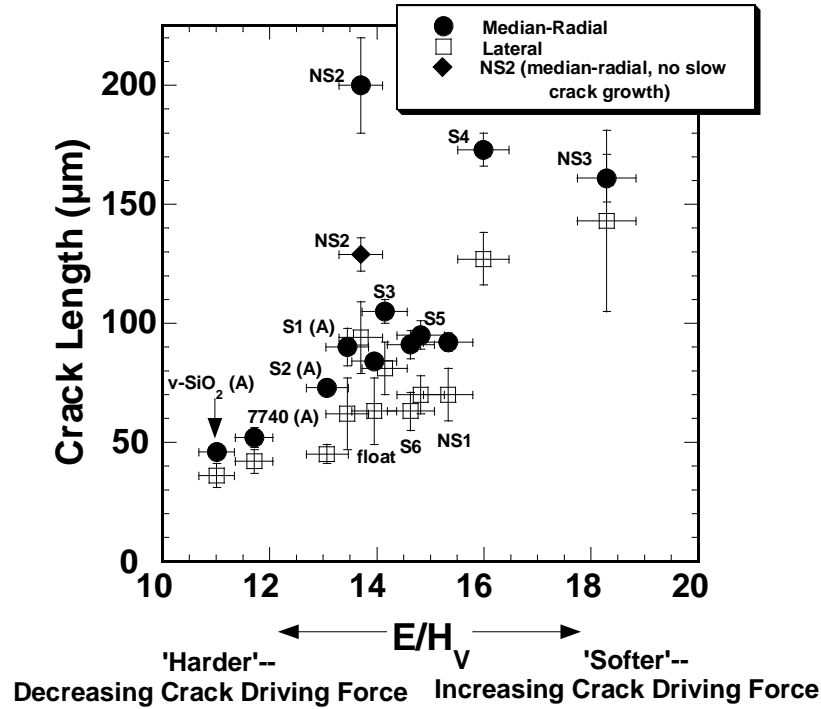
Figure 109. *The variation of median-radial and lateral crack lengths as a function of the ratio E/H_V for the different glasses.*

'soft,' and those with low E/H_V are termed 'hard'.[26] Figure 109 shows that in general the 'softer' glasses have larger crack lengths compared to the 'harder' glasses. Two exceptions are glasses NS2 (phosphate) and glass S4 (lead-silicate). The former is susceptible to slow-crack growth, which may account for the separation of this data point from the rest of the data points. Glass S4 had the lowest Vickers hardness, and significant pile-up may exist around indentations. If significant pile-up or densification of material takes place around indentations, then the fracture mechanics equations are not strictly valid.

4.4.4.3 K_{IC}, γ_f and E

Figures 110 and 111 show the variation of K_{IC} with the fracture surface energy and Young's modulus, respectively. Good agreement is seen between K_{IC} and γ_f, but poor agreement is apparent with Young's modulus. It should be recalled that Eq. 10 indicates there is no direct relationship between K_{IC} and either γ_f or E. The good agreement between K_{IC} and γ_f suggests the fracture surface energy has more influence on the fracture toughness than does Young's modulus. In Figure 112 the fracture surface energy is shown as a function of Young's modulus. No overall correlation is seen. However, it is apparent that all of the 'anomalous' glasses, and the float glass, have the highest fracture surface energies and intermediate values of Young's modulus. That is, the glasses with lower and higher Young's modulus have low fracture surface energies, i.e., they are brittle. This suggests a certain balance exists between the stiffness (E) of the glass, and the ease with which cracks propagate through the structure. High stiffness means less ability to absorb energy 'plastically,' while too low a stiffness means not enough resistance is offered to bond breaking (v-B_2O_3 is one exception). In both situations the resistance to crack propagation, i.e., fracture toughness, is low.
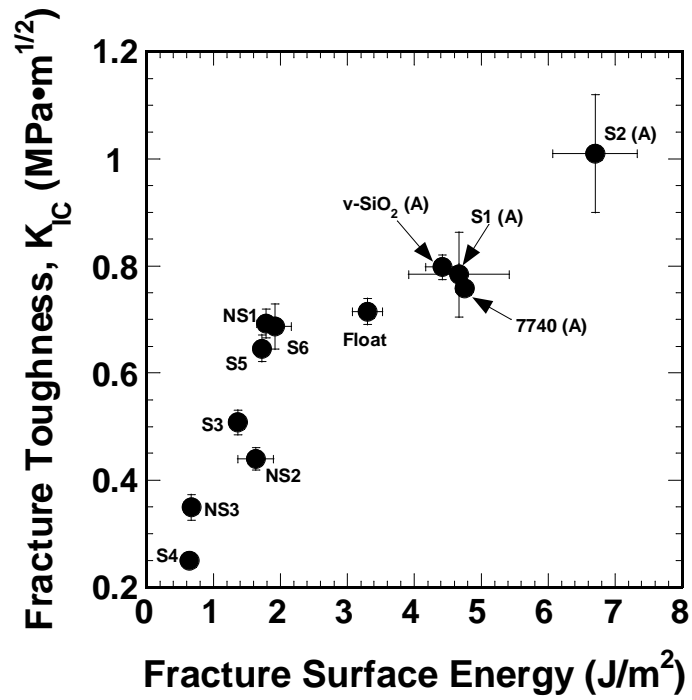
Figure 110. *Fracture toughness as a function of fracture surface energy for the different glasses.*
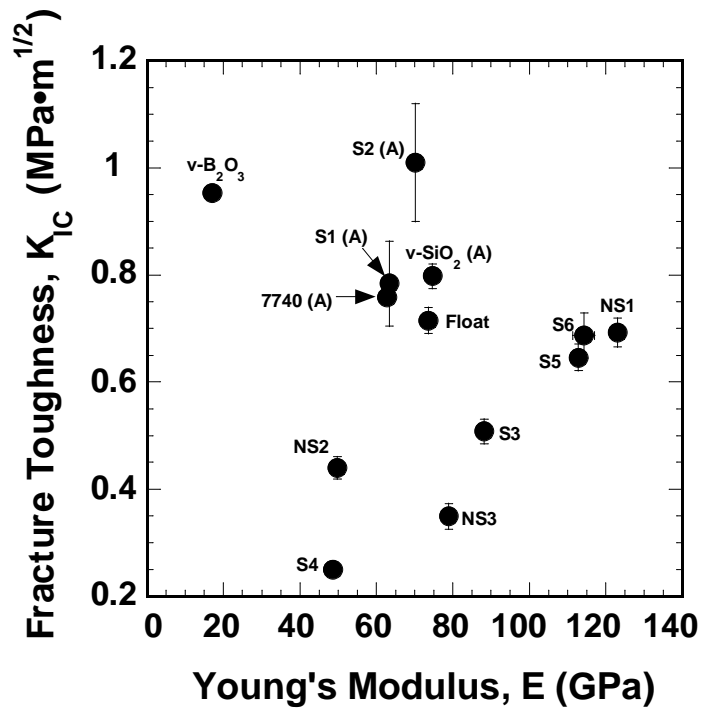
Figure 111. *Fracture toughness is shown as a function of Young's modulus for the different glasses.*

4.4.4.4 K_{IC} and NNF Ratio

Figure 113 shows that there is some correlation with fracture toughness and the normalized network-former amount, at least when the glasses are divided into silicate and non-silicate groups. It appears that, in general, higher NNF is associated with increased fracture toughness; although the 7740 Pyrex™ borosilicate specimen doesn't fit this trend.

4.4.5 Indices of Brittleness

As stated in Section 9, one challenge that faces any discussion of brittleness is how to define and measure it. The brittleness index of Lawn and Marshall[13] is one definition of brittleness. However, the real value of such definitions rest in their ability to predict material behavior under the conditions of interest, i.e., what other useful characteristics or responses of glass is such an index useful for predicting? The resistance to crack initiation on glass surfaces from particle impacts is of prime interest, of course. Thus, being able to correlate the critical load required to generate median-radial cracks in glass with H/K_C would be one such use of such a brittleness index. This correlation is examined in the next section with regards to the crack initiation results.

Quinn and Quinn[68] have listed some thirteen different indices of brittleness that have been proposed in the past, including their own, which
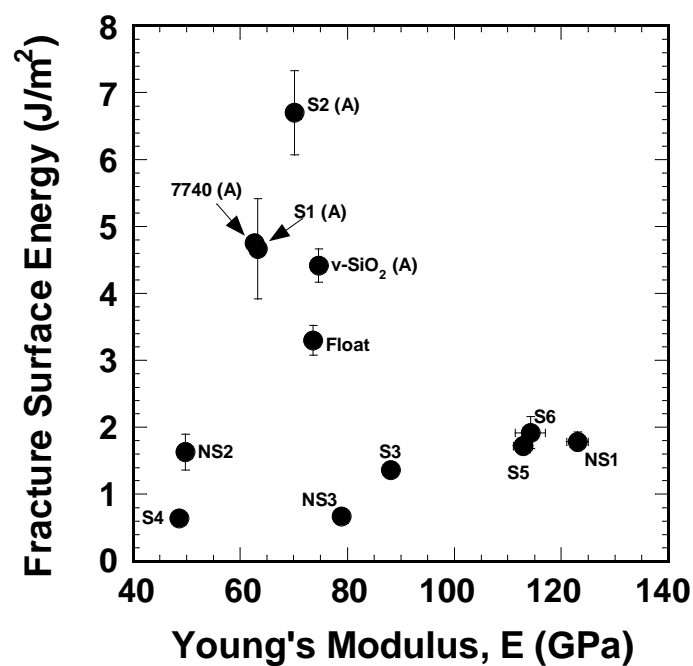
Figure 112. *The fracture surface energy as a function of Young's modulus for the different glasses.*
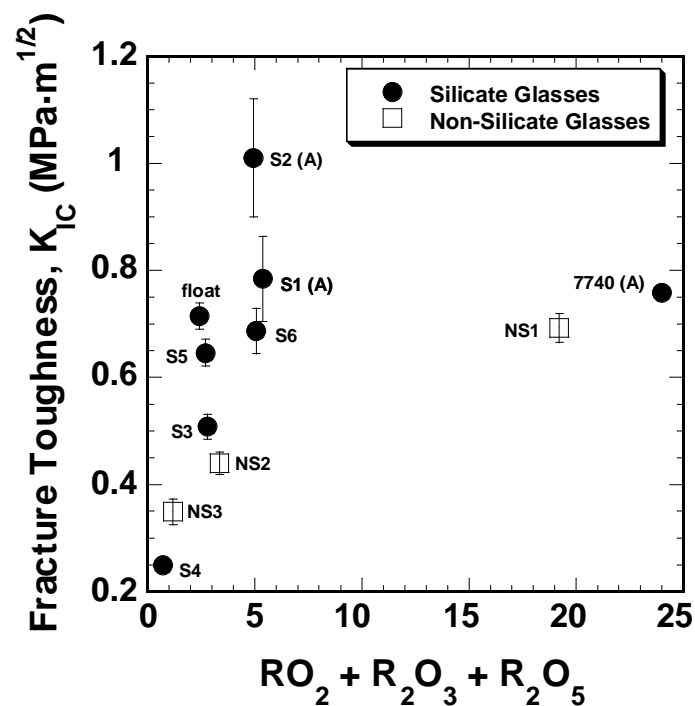
Figure 113. *The fracture toughness as a function of the normalized network former (NNF) ratio of the glasses.*

will be applied to the current glasses shortly. Different possible interpretations of brittleness are briefly described below.

1. Brittleness ≡ H/K$_C$

This index combines the attributes of 1) and 2) above, and is how Lawn and Marshall[13] defined brittleness. Materials with low resistance to deformation (low H), and high resistance to fracture (high K$_{IC}$), are considered less brittle than materials with the opposite characteristics. That is, materials with lower brittleness index are considered to have an indentation response that is relatively more deformation controlled than fracture controlled. The critical load to fracture for such materials, F$_c$, is predicted to increase with decreasing brittleness index.[13]

2. 'c/a' Ratio

The ratio of crack length to indentation size is considered a measure of brittleness according to Sehgal et al.[69] for constant indentation load. This ratio is similar to that of Lawn and Marshall's[13] above, but does away with the unusual units of (length)$^{-1/2}$. The brittleness index proposed by Sehgal et al. is: B = $(1/0.0056)^{3/2} \cdot (c/a) \cdot P^{-1/4}$, which does have units of (length)$^{-1/2}$.[69] However, for constant load, the brittleness index is just a function of c/a, which is unitless. The c/a ratio by itself relates directly the deformation response relative to the fracture response (deformation/fracture).

3. $B \equiv (EH_c)/(K_{IC})^2$

This is the Quinn and Quinn[68] brittleness index. H_c is the 'critical' value of Vickers hardness at which the hardness transitions from being load-dependent to load-independent. Further discussion of this ratio is warranted. As shown by Quinn and Quinn this ratio can be represented as:

$$B \equiv \frac{EH_c}{K_{IC}^2} = \frac{EH_c}{2E\gamma_f} = \frac{H_c}{2\gamma_f} \tag{24}$$

The fracture mechanics relation, $K_{IC} = (2E\gamma_f)^{1/2}$, which is valid for plane-stress conditions was substituted in the denominator in Eq. 24.[57] A units analysis of Eq. 24 reveals the following:

$$[m^{-1}] = \frac{\left[N/m^2\right]\left[\dfrac{m}{m}\right]}{\left[J/m^2\right]} = \frac{\left[J/m^3\right]}{\left[J/m^2\right]} = [m^{-1}] \tag{25}$$

Therefore, the Quinn and Quinn brittleness index is a measure of energy per unit deformation volume, characterized by the hardness, to energy per unit area of fracture, characterized by the fracture surface energy. A material that has higher brittleness index compared to another with a low brittleness

index can be viewed as requiring more energy to produce unit volume deformation relative to unit area by fracture. As the ratio (deformation energy/fracture energy) decreases, the indentation energy is partitioned more equally between the two mechanical responses. Quinn and Quinn[68] showed the change in Vickers hardness from load dependent to load independent is abrupt and easily detectable for materials with high brittleness index, such as α-SiC, compared to materials with lower brittleness index, such as Si_3N_4.

4. Brittleness $\propto K_{IC}^{-1}$

If brittleness is defined as resistance to fracture, then materials with high fracture toughness are considered less brittle than materials with lower fracture toughness, since high-fracture-toughness materials have greater intrinsic resistance to fracture than lower-fracture-toughness materials.

5. Brittleness $\propto \gamma_f^{-1}$

If brittleness is defined as the energy necessary to create unit area of fracture surface in a material, then materials with low fracture surface energy are considered more brittle compared to those with higher fracture surface energy, since less energy per unit fracture area is needed to cause fracture in the former than the latter.

6. Brittleness $\propto H_V$

Defining brittleness as a lack of ductility, then hardness of glass could be considered a measure of brittleness. Using this definition, the brittleness of glass would decrease with decreasing hardness, since for given indentation load 'softer' materials would plastically deform more compared to 'harder' ones, and thus be considered less brittle. Presumably more energy would go into relieving stress by 'flow' rather than 'fracture' in 'softer' materials.

'Harder' materials may be considered more brittle because they concentrate stress to greater extent compared to 'softer' materials, which could lead to cracking (the elastic contact, Boussinesq, stress field around an indentation increases with hardness).[18]

7. Brittleness $\propto$ Young's Modulus, E

Since Young's modulus is a measure of structural rigidity, then materials with high Young's' modulus may be considered more brittle than materials with lower Young's modulus.

8. Brittleness $\propto F_{C(M-R)}^{-1}$, Under Load

Defining brittleness as the critical (minimum) load needed to initiate median-radial cracks around an indentation in a material ($F_{C(M-R)}$), then materials with low $F_{C(M-R)}$ are considered more brittle than materials with high $F_{C(M-R)}$. This index may be the best way to describe the brittleness of

glasses in the current work, since surface flaws degrade the intrinsic strength of glass.

The median-radial crack was chosen for this classification for two reasons: 1) median-radial cracks initiated in all the glasses observed in the current work, and 2) in general median-radial cracks are more detrimental to glass strength because of their nearly or actually perpendicular orientation to the surface compared to, for example, ring-cone cracks. However, it is recognized that ring-cone cracks in vitreous silica in particular, which are steeply oriented to the surface, may be just as detrimental to strength, since they appear larger than the median-radial cracks which form. For the other 'anomalous' glasses, S1 and S2, well-developed ring-cone cracks formed at the higher loads, as did median-radial cracks.

4.4.5.1 Ranking of Glasses According to Various Brittleness Indices

The ranking of the 'brittleness' of the glasses according to the different indices discussed above is shown in Table XXXI. The indices given by H_V/K_{IC}, 'c/a', EH_V/K_{IC}^2, K_{IC}, and γ_f produce nearly similar rankings of the different glasses. However, the Vickers hardness classification of brittleness of the glasses does not agree with the rest of the rankings; the only exception is v-B_2O_3, which has the lowest hardness, and is one of the least 'brittle' glasses.

This suggests that using hardness to rank the brittleness of materials is not valid. The same appears true for Young's modulus.

Although some of the positions switch slightly between the different indices (1-5) it is apparent that the anomalous glasses, float, and v-B_2O_3 are the least brittle, while the more 'normal' glasses (S3, S4, S5, S6, NS1, NS2, and NS3) are the most brittle. Comparing brittleness index #'s 1-5 with that based on median-radial crack initiation forces under loading, # 7, it is apparent that lower brittleness in general correlates with increased resistance to median-radial crack initiation. Glass S1 is one notable exception, in which, despite having relatively low brittleness indices, median-radial cracks initiated relatively early on loading, and is the only 'anomalous' glass in which this occurs. Although median-radial cracks were believed to initiate in the Suprasil 312 v-SiO_2 specimen after the initiation of ring-cone cracks on loading, the exact load was not known. Wagner[9] noted that some median-radials were seen on loading in vitreous silica up to 1400g, but an exact initiation load could not be given. Cook and Pharr[11] noted that median-radial cracks initiated at ~ 938 g on loading in v-SiO_2. This value was used to rank the Suprasil 312 v-SiO_2 in the current work, since it somewhat agrees with the observations in the current work and with Wagner's[9] work.

Table XXXI. Ranking of the Glasses According to the Different Brittleness Indices.

	#1 H/K_{IC} ($\mu m^{-1/2}$)	#2 'c/a'	#3 EH_V/K_{IC}^2 (μm^{-1})	#4 K_{IC} (MPa•m$^{1/2}$)	#5 γ_f (J/m^2)	#6 $H_{V\,(200\,g)}$	#7 E (GPa)	#8 $F_{c(M-R)}$ Under Load (g)
Least 'Brittle'	v-B$_2$O$_3$ (2.11)	v-SiO$_2$(A) (1.58)	v-B$_2$O$_3$ (40)	S2 (A) (1.01)	v-B$_2$O$_3$ (24.9)	v-B$_2$O$_3$ (205)	v-B$_2$O$_3$ (17.0)	S2 (A) (172 UL)
	S2 (A) (5.25)	7740 (A) (1.78)	S2 (A) (396)	v-B$_2$O$_3$ (0.954)	S2 (A) (6.70)	S4 (310)	S4 (48.6)	7740 (A) (198 UL)
	S1 (A) (6.29)	v-B$_2$O$_3$ (2.13)	S1 (A) (528)	v-SiO$_2$(A) (0.798)	7740 (A) (4.75)	NS2 (375)	NS2 (49.7)	Float (520 UL)
	v-SiO$_2$(A) (6.65)	S2 (A) (2.49)	7740 (A) (564)	S1 (A) (0.784)	S1 (A) (4.67)	NS3 (440)	7740 (A) (62.7)	v-SiO$_2$(A) (938 L†)
	7740 (A) (7.06)	Float (2.89)	v-SiO$_2$(A) (600)	7740 (A) (0.758)	v-SiO$_2$(A) (4.42)	S1 (A) (480)	S1 (A) (63.3)	S3 (817 L)
	Float (7.56)	S1 (A) (2.97)	Float (819)	Float (0.715)	Float (3.30)	Float (538)	S2 (A) (70.1)	S6 (482 L)
	NS2 (8.36)	NS2 (3.66)	NS2 (1128)	NS1 (0.692)	S6 (1.92)	v-SiO$_2$(A) (541)	Float (73.6)	S1 (A) (317 L)
	S6 (10.88)	S6 (3.68)	S6 (1946)	S6 (0.687)	NS1 (1.79)	7740 (A) (546)	v-SiO$_2$(A) (74.6)	S5 (311 L)
	S5 (11.19)	S5 (3.78)	S5 (2101)	S5 (0.646)	S5 (1.72)	S2 (A) (547)	NS3 (78.9)	NS1 (257 L)
	NS1 (11.49)	NS1 (3.82)	NS1 (2222)	S3 (0.508)	NS2 (1.63)	S3 (635)	S3 (88.1)	NS2 (133 L)
	S4 (11.90)	S3 (3.86)	S3 (2264)	NS2 (0.440)	S3 (1.36)	S5 (776)	S5 (112.8)	S4 (40 L)
	S3 (12.12)	S4 (4.49)	S4 (2398)	NS3 (0.349)	NS3 (0.67)	S6 (796)	S6 (114.2)	NS3 (1 L)
Most 'Brittle'	NS3 (12.73)	NS3 (5.02)	NS3 (3315)	S4 (0.258)	S4 (0.64)	NS1 (818)	NS1 (123.0)	
		NS2 (5.68*)						

Values for each of the indices are indicated in parentheses
For #8, 'L' = loading, 'UL' = unloading
* based on stress-corrosion crack length values
† based on crack initiation load observed by Cook and Pharr[11]

In conclusion, the 'anomalous' glasses in general, and the float glass, are the least brittle according to all the indices, with the possible exception of glass S1, and have the greatest resistance to median-radial crack initiation.

The more 'normal' glasses, including S3, S4, S5, S6, NS1, NS2, and NS3, have the poorest resistance to median-radial crack initiation, and in general the highest values of the brittleness indices.

4.4.5.2 Brittleness and Glass Structure

Some indication of the effect of the structure of the current glasses on brittleness is shown in Figure 114, where the Quinn and Quinn[68] and 'c/a' brittleness indices are shown as a function of glass density. In general, both indices of brittleness increase with increasing glass density, although a few exceptions are apparent. There was a much higher degree of scatter, i.e., less correlation, when these brittleness indices were plotted as functions of the molar volume or atomic molar volume. Since calculation of the atomic molar volume requires knowing the exact compositions of the glasses, which however were only known to within ± 5 % in the current work, these errors could mask any relationships. Measurement of density, on the other hand, is independent of knowing composition. The higher the density of glass, the less open-volume is available for deformation to occupy. Therefore, it is expected that more shear flow will take place relative to compaction (densification) in order to accommodate the volume of the indenter. Comparing the G/K ratios with the density of the glasses shows that, to some extent, this does occur, as seen in Figure 115. All the 'anomalous' glasses have high G/K ratios and low densities, whereas the 'normal' glasses have
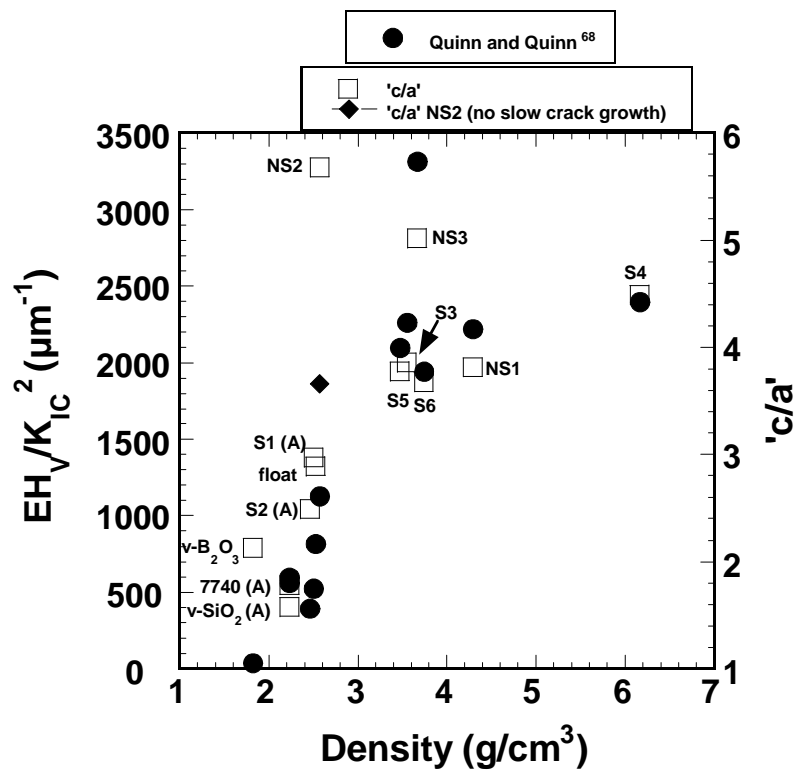
Figure 114. *The variation of the Quinn and Quinn[68] and 'c/a' brittleness indices as a function of glass density.*
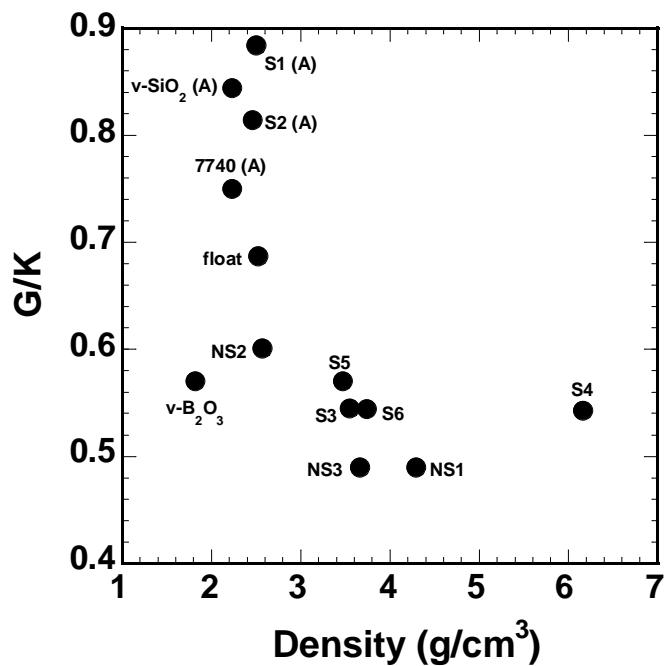
Figure 115. *The variation of G/K ratio as a function of glass density.*

lower G/K ratios and higher densities. Vitreous boron oxide is one exception. It has low density, but also low G/K. As discussed earlier, it has unusually low resistance to shear because of its sheet-like structure with weak van der Waals bonding between sheets. Another exception is glass S4, which has a somewhat higher G/K ratio than expected based on the trend formed with the other glasses.

In Figure 116 the G/K ratio is plotted as a function of the Quinn and Quinn[68] brittleness index. In general the brittleness index increases as the ratio G/K decreases. Again, however, v-B_2O_3 does not fit the trend of the other glasses.

4.4.6   G/K Ratio and Deformation Response of Glass

The ratio G/K for the glasses was previously presented. Since in an indentation test on glass the permanent impression arises from the shear and hydrostatic components of the stress field, the ratio G/K may indicate what deformation mode is more dominant, and consequently whether the glass behaves more 'normal' (shear-induced faulting/'flow'), or more 'anomalous' (hydrostatic pressure-induced densification/compaction). The 'anomalous' glasses, S1, S2, 7740 Pyrex™ borosilicate, and v-SiO_2, have relatively high G/K ratios, ranging from 0.750 to 0.884. The normal glasses have G/K ratios ranging from 0.490 to 0.687. The float-glass specimen has a G/K ratio of
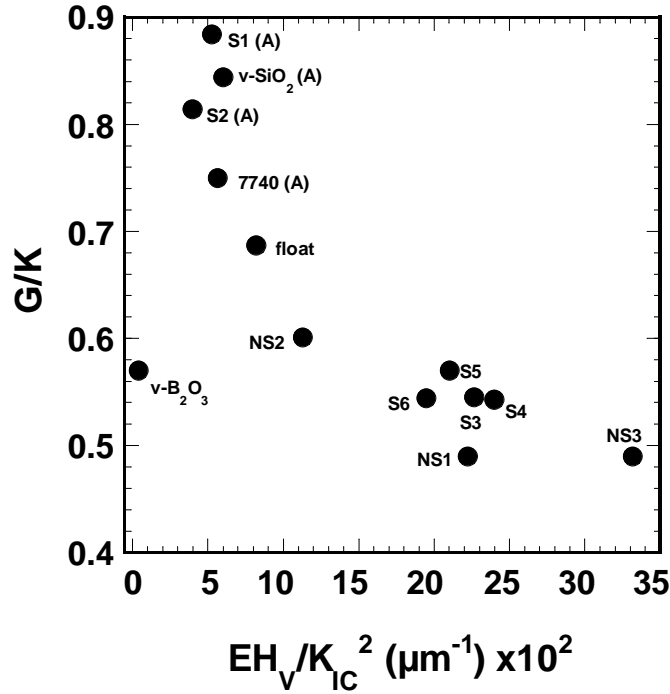
Figure 116. *The variation of G/K ratio with the Quinn and Quinn[68] brittleness index.*

0.687, on the high side, which is possibly indicative of its borderline 'anomalous' behavior, since significant partial ring-cone cracking occurred for the 4 Kg crack initiation tests.

Lower values of G/K indicate a deformation response that is more 'normal,' i.e., shear-'flow' controlled, thus favoring 'normal' crack initiation behavior, i.e., no ring-cone crack formation on loading. Higher values of G/K indicate a deformation response that is relatively more 'anomalous,' i.e., densification/compaction controlled, thus favoring 'anomalous' crack initiation behavior, sometimes manifested by ring-cone cracking early in the loading cycle, such as for the 7740 Pyrex™ borosilicate and v-SiO₂ glasses. The ratio (G/K) is thus analogous to a ratio of ('flow'/compaction), where

higher G/K ratios indicate more compaction and less flow, since the resistance to shear-'flow' increases with increasing G, and that to compaction with increasing K.

The sub-surface deformation zones of the glasses support this notion. The 'anomalous' glasses had few if any shear-fault lines below the surface, indicating a densification/compaction mode was operating. This is in contrast to the 'normal' glasses, which, as the cross-sections showed, contained many shear-fault lines. In general, the 'anomalous' glasses examined in this work have relatively open (low atomic molar volume) three-dimensional structures with strong Si-O bonds, whereas the 'normal' glasses studied have less 3-D connectivity, fewer strong Si-O bonds, or none at all, and more close-packed (low atomic molar volume) structures. The packing density of ions is greater, in general, for the 'normal' glasses compared to the 'anomalous' glasses. Recall the packing density, V_t, is the volume fraction of ions in the glass. A compaction mode is thus favored for the 'anomalous' glasses, and a shear-'flow' mechanism for the 'normal' glasses. It should also be noted that Poisson's ratio, which is also indicative of the extent of compressibility of a solid, is low for the 'anomalous' glasses and higher for the 'normal' glasses. As Poisson's ratio approaches 0.5, the bulk modulus approaches infinity, indicating incompressibility, and hence favoring shear deformation, i.e., 'normal' behavior. The G/K ratio of the glasses in the current study, as well

213
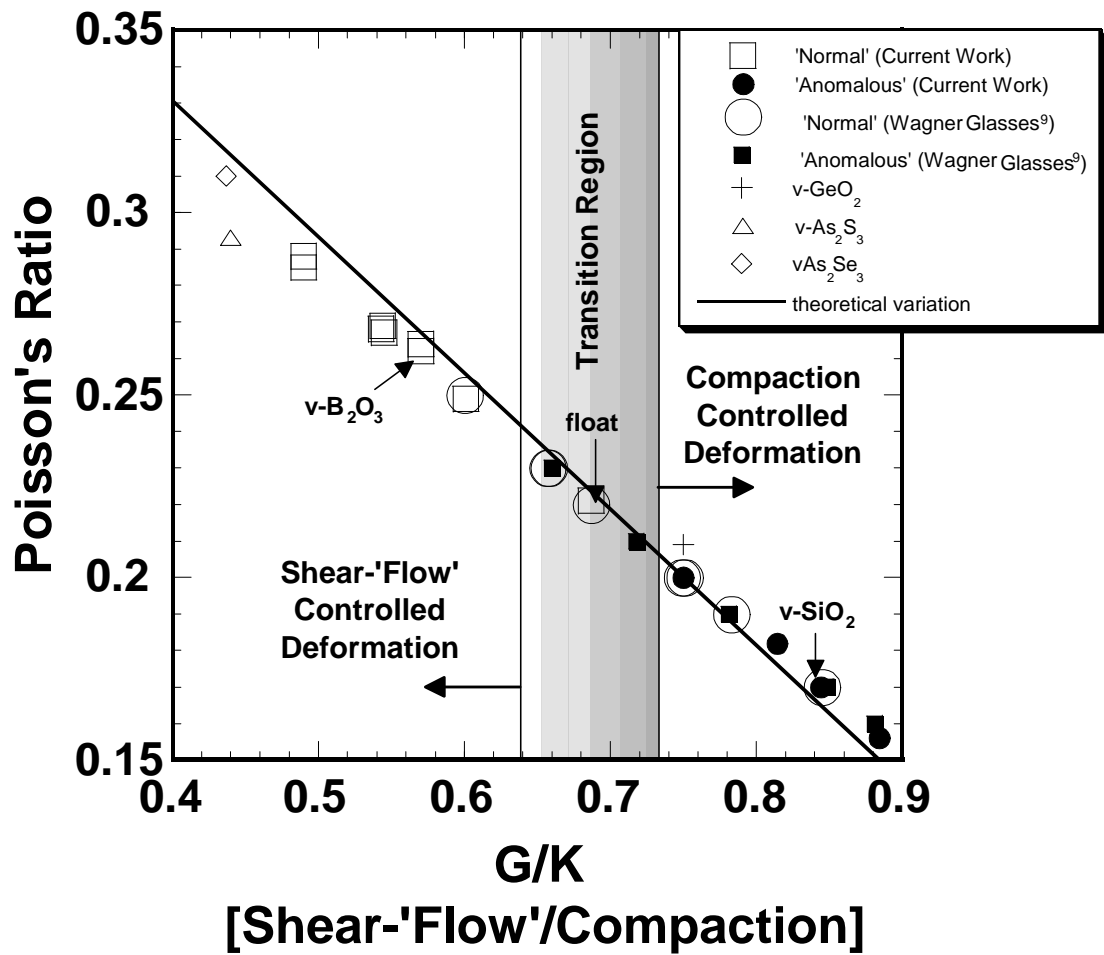
Figure 117. *Shear-'flow'/compaction diagram showing Poisson's ratio as a function of G/K ratio for the glasses examined in the current study, as well as Wagner's glasses.[9] Data for v-GeO₂, v-As₂S₃, and v-As₂Se₃ from Frischat[61]; the first glass is predicted to behave 'anomalous,' while the latter two 'normal.' Solid line represents theoretical variation of G/K with Poisson's ratio.*

as the Wagner glasses[9], is shown as a function of Poisson's ratio in Figure 117. Values of G and K were calculated for Wagner's glasses using his measured values of Poisson's ratio and Young's modulus, and equations 6 and 7. A nearly straight-line relationship is seen. According to theory G/K = 3(1-2ν)/2(1+ν); i.e., G/K is just another statement of Poisson's ratio. The plot

represents a convenient way to group the data, and thinking about deformation processes in relation to G/K is easier than Poisson's ratio, at least in an indentation test. The theoretical variation of G/K with Poisson's ratio is also plotted. Although G and K are elastic properties, it is interesting that they describe the indentation response (where much inelastic deformation is occurring) quite well. One reason for this may be because the majority of the deformation in these glasses is elastic (see Section 7). The elastic behavior of the surrounding material is thus governing the inelastic response in the 'plastic' zone. This is because the elastic material surrounds and constrains the 'plastic' zone. Compaction and shear-'flow' controlled deformation regions are indicated. A transition region centered approximately around G/K = 0.68 is indicated. In this region the deformation behavior is thought to be intermediate between shear-'flow' and 'compaction,' and hence the crack initiation behavior between 'normal' and 'anomalous.' The crack initiation behavior of glasses in this region would be expected to be dependent on the maximum load. The float glass lies in this region, as do 'normal' glasses ALS25, BSL 300, BSL 75, and 'anomalous' glasses BSL 50 and ALS 100. The float glass did show a small transition, as previously discussed, and recall Wagner[9] found a transition with maximum load for glass BSL 50. In addition, glass ALS 100 also showed a transition to more anomalous behavior, in which 100% of the tests had significant ring-cone crack development when tested at 4 Kg in the current work, compared to 56%

at 1400 g maximum load with the recording microindenter when tested by Wagner.[9] Glass ALS 25 did not show a transition up to 3.8 Kg, and glasses BSL 300 and BSL 75 were not tested at higher loads in the current work, because no sufficiently sized specimens were available.

It is also apparent that two Wagner 'normal' glasses[9] lie deep in the region occupied by the 'anomalous' glasses. As noted by Wagner[9] one of these glasses, BSL 100, may have been phase-separated, which could result in more 'normal' behavior than otherwise expected due to regions rich in alkali ions promoting shear. The other glass, SLS 76, may not have been indented to a high enough load to cause 'anomalous' behavior.

A certain critical load may need to be reached before such glasses, e.g., float, achieve a significant (critical) amount of densification, whereupon increased load then causes the build-up of surface tensile stresses and the formation of ring-cone cracks. For vitreous silica, this critical densification occurs early, since ring-cone cracks form at low loads during loading. For glasses containing some modifying ions, the critical densification occurs at higher loads because of shear deformation along modifier/NBO pathways. The glasses with very low values of G/K are believed to always have 'normal' deformation with respect to a sharp indenter, since these glasses will have little tendency to densify because of their closely packed structures and tendency to shear readily. Those glasses in the transition region with intermediate G/K ratios will have a load-dependent deformation behavior,

whereas those glasses with high values of G/K will always have predominantly 'anomalous' deformation behavior. All of the glasses categorized as 'anomalous' have G/K ratios greater than 0.64.

4.5   Crack Length and Related Data from Crack Initiation Tests

4.5.1   Recording Microindenter Data

The crack length, indentation diagonal length, hardness data, and percentage of tests having surface chipping from the recording microindentation crack initiation tests, is summarized in Table XXXII. The hardness data for Suprasil 312 v-SiO_2 needs to be accepted with caution, since the extensive surface ring cracking and crushing of material made accurate determinations of indentation diagonals difficult.

4.5.2   LECO (Conventional Indenter) Data

The data from the tests made with the conventional ('static') indenter are shown in Table XXXIII. The term static is somewhat of a misnomer. Although the maximum load was held 'static' for five seconds on the specimens, the rate of indenter penetration and withdrawal was much greater than in the recording microindenter crack initiation tests, so in this respect these tests are much more dynamic.

Table XXXII. Indentation Characteristics from 1 Kg Recording Microindenter Tests.

Glass	Median-Radial Crack Length (µm)	Lateral Crack Size (µm)	Indentation Diagonal Length (µm)	H_V (GPa)	Tests with Surface Chipping (%)
S1 (A)	90 ± 8	62 ± 15	60.7 ± 1.4	4.93 ± 0.12	0
S2 (A)	73 ± 1	45 ± 4	58.7 ± 0.4	5.31 ± 0.02	0
S3 (N)	105 ± 5	81 ± 11	54.4 ± 0.5	6.16 ± 0.10	0
S4 (N)	173 ± 7	127 ± 11	77.1 ± 0.3	3.07 ± 0.01	10
S5 (N)	95 ± 6	70 ± 8	50.3 ± 0.3	7.23 ± 0.08	20
S6 (N)	91 ± 6	63 ± 8	49.4 ± 0.3	7.47 ± 0.06	0
NS1 (N)	92 ± 4	70 ± 11	48.2 ± 0.5	7.95 ± 0.17	20
NS2 (N)	200 ± 20	94 ± 15	70.4 ± 0.5	3.68 ± 0.04	0
NS3 (N)	161 ± 10	143 ± 38	64.1 ± 0.8	4.44 ± 0.08	40
Float (N-A)	84 ± 3	63 ± 14	58.1 ± 0.6	5.40 ± 0.09	0
7740 Pyrex Borosilicate (A)	52 ± 4	42 ± 5	n/a	n/a	0
v-SiO$_2$ (Suprasil 312) (A)	46 ± 3	36 ± 5	58.4 ± 1.2	5.31 ± 0.16	0

Table XXXIII. Indentation Characteristics from 1 Kg Conventional Indenter Tests.

Glass	Median-Radial Cracks (µm)	Lateral Cracks (µm)	Diagonal Length (µm)	Vicker's Hardness, H_V (GPa)	Tests with Surface Chipping (%)	Median-Radial Depth (µm)	Lateral Depth (µm)	'Plastic' Zone Depth (µm)	'Plastic' Zone Width (µm)
S1 (A)	95 ± 7	59 ± 5	64.5 ± 1.0	4.37 ± 0.14	0	64 ± 10	41 ± 6	22 ± 2	48 ± 7
S2 (A)	74 ± 4	39 ± 6	60.1 ± 0.3	5.04 ± 0.05	0	63	32	19	54
S3 (N)	108 ± 6	99 ± 21	55.0 ± 0.5	6.00 ± 0.10	40	110 ± 18	54 ± 15	32 ± 4	52 ± 2
S4 (N)	181 ± 8	173 ± 26	78.3 ± 0.6	2.96 ± 0.05	90	186 ± 10	105 ± 15	55 ± 4	77 ± 3
S5 (N)	96 ± 4	82 ± 10	50.6 ± 0.6	7.10 ± 0.17	40	105 ± 10	59 ± 9	33 ± 2	49 ± 2
S6 (N)	93 ± 4	72 ± 8	49.7 ± 0.2	7.36 ± 0.06	20	103 ± 3	46 ± 15	33 ± 3	49 ± 2
NS1 (N)	92 ± 4	83 ± 8	48.3 ± 0.3	7.80 ± 0.10	60	95 ± 3	26 ± 16	32 ± 2	49 ± 1
NS2 (N)	183 ± 15	101 ± 11	72.1 ± 0.5	3.50 ± 0.05	0	148 ± 11	79 ± 11	44 ± 5	73 ± 8
NS3 (N)	151 ± 5	127 ± 13	67.6 ± 2.9	4.08 ± 0.25	100	182 ± 8	68 ± 9	50 ± 2	66 ± 5
Float (N-A)	88 ± 4	69 ± 4	57.9 ± 0.2	5.13 ± 0.04	0	59 ± 6	41 ± 5	30 ± 3	59 ± 3

4.5.3 Comparison of Data

Overall, the length of median-radial and lateral cracks from the recording microindenter and conventional indenter tests were similar. This is not unexpected, since the driving force for crack growth should increase primarily with the maximum load.

The Vickers hardness values were, on average, slightly higher for the tests performed with the recording microindenter. It is possible that since the load does not equilibrate at each instance of time in the recording microindenter tests (since a constant displacement is being applied), as compared to the conventional indenter where the maximum load was held for 5 seconds, an equilibrium size is not reached, resulting in slightly higher hardness. In addition, the difference appears to be greatest for the 'anomalous' glasses S1 and S2. It is possible the more open structure of these glasses make them more susceptible to rate effects.

The degree of surface chipping of material from shallow lateral cracks increased for glasses S3, S4, S5, S6, NS1, and NS3 as the loading rate increased. A comparison of the 1 Kg tests of the recording microindenter at 0.2 μm/s with the 1 Kg tests of the conventional indenter reveals that a higher percentage of tests had surface chipping, presumably due to the faster rate of load application, particularly on unloading. This suggests that for

true impact situations greater surface chipping is expected in these glasses compared to the others.

Examination of the median-radial crack depths from the conventional indenter data reveals them to be of the same size as the length of the surface traces. This is not surprising considering the near symmetric half-penny shape observed for these cracks. In addition, the widths of the observable deformation ('plastic') zones were on the order of the indentation size on the surface, while the depths of the deformation zones were about half the diagonal length size; however, as shown in the cross-section images, for glasses S3, S5, S6, NS1, and NS2 the deformation zones also were slightly cone-shaped.

4.6   Mechanical Properties/Characteristics vs. Crack Initiation Loads

In this section the median-radial crack initiation forces from the 1 Kg crack initiation tests are compared to the various mechanical properties of the glasses. Crack initiation is assumed to occur when the stress at a flaw reaches a critical level. It is not the actual level of stress that is important, but rather at what load the critical stress level is reached in a particular glass. The Wagner glasses[9] are also examined using mechanical properties data from his work.

4.6.1 Fracture Toughness

The crack initiation loads for the first median-radial cracks to initiate on loading are shown as a function of the fracture toughness of the glasses in Figure 118. Overall there is no conclusive trend of initiation load with the fracture toughness. However, the glasses with the lowest fracture toughness (S4, NS2, NS3) had the least resistance to median-radial crack initiation.

In Figure 119 the load for the first median-radial cracks to initiate on unloading is shown as a function of the fracture toughness. There is a trend of decreasing initiation load on unloading as fracture toughness increases. Recall that initiation at lower loads on unloading is indicative of increased crack initiation resistance.

The critical stress conditions for initiation on unloading are probably controlled by the extension of flaws produced on loading to a critical size, most likely due to stress corrosion, upon which pop-in then occurs. This is one of the mechanisms first proposed by Lawn et al.[38] and previously discussed in the review section. Although it is tempting to suggest the glasses with higher fracture toughness have increased stress corrosion resistance, which would help explain the results, it is probably not correct to do so. The data of Wiederhorn et al.[27] show that for maintaining a crack velocity of 10^{-7} m/s in borosilicate crown, 61% lead, soda-lime-silicate, and aluminosilicate glasses at 25 °C, mode I stress intensities (K_I) of
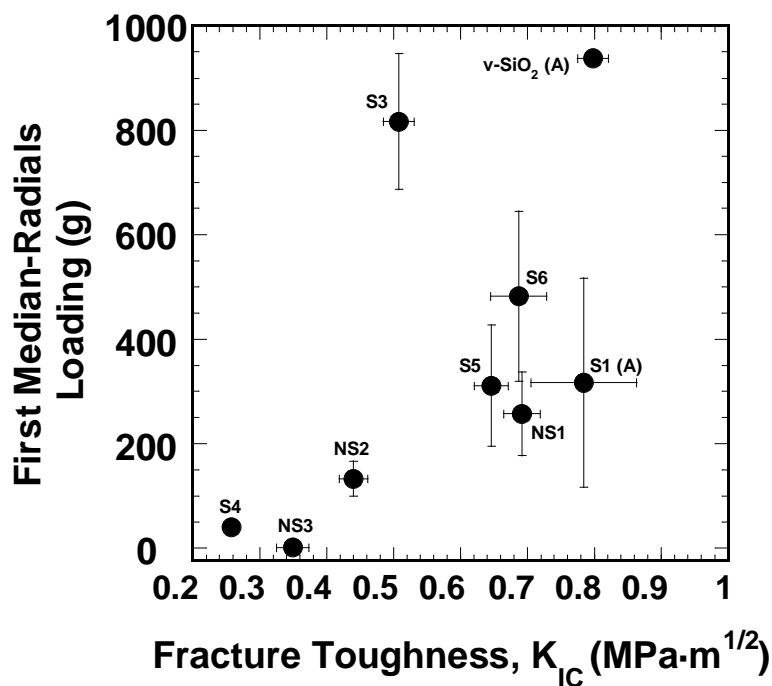
Figure 118. *The first median-radial cracks to initiate on indenter loading for the 1 Kg (0.2 µm/s) tests as a function of the fracture toughness of the glasses.*
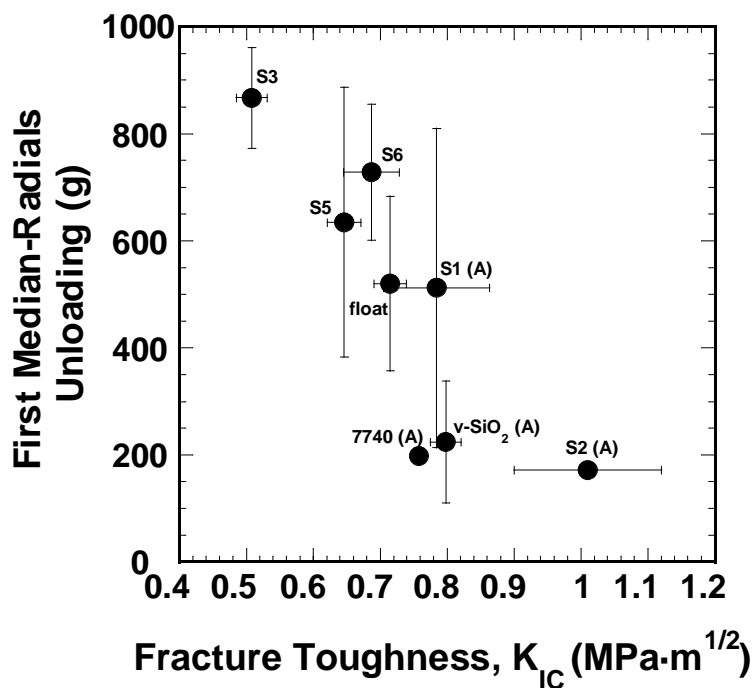
Figure 119. *The first median-radial cracks to initiate on indenter unloading for the 1 Kg (0.2 µm/s) tests as a function of the fracture toughness of the different glasses.*

approximately 0.85, 0.58, 0.68, and 0.82 MPa√m are needed, respectively. The critical stress intensity factors, K_{IC}, of the glasses are 0.62, 0.87, 0.81, and 0.68 MPa√m, respectively. The glasses that had the lowest fracture toughness (i.e., borosilicate crown and aluminosilicate) required the greatest stress intensity to propagate the pre-crack at 10^{-7} m/s compared to the soda-lime-silicate and 61% lead glass. That is, it can not be assumed that greater fracture toughness of glass is always associated with greater stress corrosion resistance. Thus, the fact the initiation loads on unloading show a trend with fracture toughness is possibly because the glasses with the greater fracture toughness may happen to have greater stress corrosion resistance. This seems likely for the v-SiO₂, 7740 Pyrex ™ borosilicate, and S2 glass specimens based on their compositions.

The fact that glass S3 had median-radials initiate at such a high force on unloading may be due to its very high susceptibility to stress corrosion. According to the manufacturer, this glass had the least resistance to water vapor attack of all the glasses. The climatic resistances of the glasses, according to the manufacturer, is shown in Table XXXIV (the manufacturer tests each optical glass for climatic resistance (CR). Each of the nine optical glasses had been given a climatic resistance number based on an accelerated test in which the glasses were exposed to a water-vapor-saturated atmosphere, with temperature fluctuating between 40 and 50 °C. According to the manufacturer, polished and uncoated plates of each glass were used,

and tested in the saturated conditions for 30 hours. After testing, the transmission of visible light is measured and compared to the value before testing. The difference, Δ H (transmission haze), is a measure of how much the water vapor has attacked the surface. The glasses are then ranked into four classes: CR 1 (Δ H <0.3%), CR 2 (Δ H 0.3% to <1.0%), CR 3 (Δ H 1.0% to < 2.0%), and CR 4 (Δ H $\geq$ 2.0%). According to the manufacturer, CR 1 glasses show no signs of surface attack after 30 hours, while glasses in CR 4 are very sensitive to climatic conditions and should be processed and stored carefully to avoid water vapor attack. However, this reasoning does not explain why glass S3 had high resistance to crack initiation on loading when compared to glasses S5, S6, NS1, NS2, NS3, all of which had increased climatic resistance.

In Figure 120 the normalized initiation force for the first median-radial cracks to initiate on unloading in the Wagner glasses[9] is shown as a function of the fracture toughness. For the soda-lime-silicate series the normalized initiation force increases as the fracture toughness increases. The increase in fracture toughness from $\approx$ 0.63 to $\approx$ 0.73 MPa$\sqrt{m}$ was associated with an increase in total alkali + alkaline earth content of ~ 13.5 mol % to 25.4 mol %, respectively. Thus, it is presumed the increased modifier content, while increasing the fracture toughness, decreased the stress corrosion resistance, causing increased slow crack growth and crack initiation earlier on the

Table XXXIV. The Climatic Resistance Class For Each Glass.[*]

Glass	CR Class
S1	1
S2	1
S3	4 (2.0%)
S4	4 (1.8%)
S5	3
S6	3
NS1	1
NS2	3
NS3	2

[*]Numbers in parentheses indicate the percent transmission haze (ΔH) for that glass
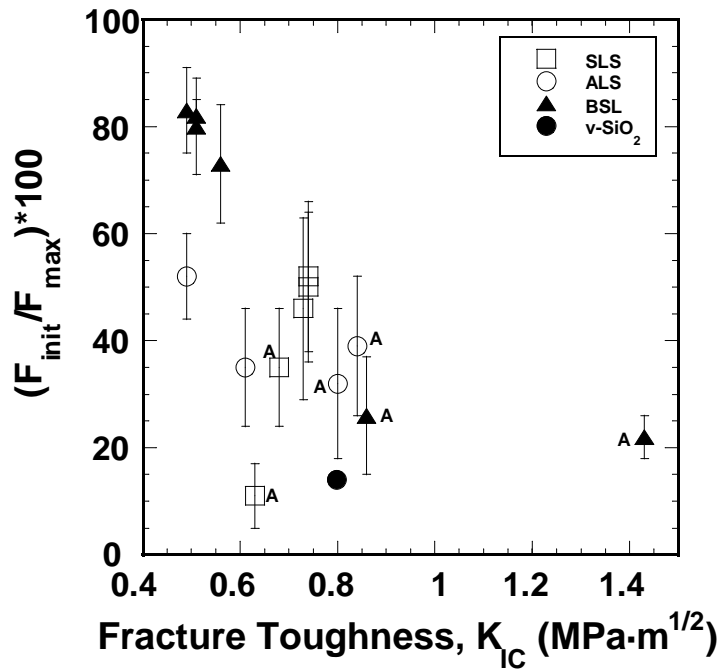
Figure 120. *The variation of normalized initiation force for the first median-radial cracks to initiate on unloading for the three series of glasses examined by Wagner[9]. F_{max} was 1400 g, and indenter displacement rate was 0.2 µm/s. 'A' indicates 'anomalous' glasses. Data from Wagner[9].*

unloading cycle. For the sodium aluminosilicate glasses the increase in fracture toughness was associated with a decrease in the Na/Al molar ratio, and thus a decrease in the total number of NBO's. Thus, stress corrosion resistance, and hence crack initiation resistance, increased. For the sodium borosilicate glasses, the increase in fracture toughness was associated with a decrease in Na/B molar ratio, and thus a decrease in NBO content as well. Stress corrosion resistance is therefore expected to increase with fracture toughness, and hence increased crack initiation resistance.

The above results and discussion suggest it may be the resistance to stress corrosion that partially governs resistance to crack initiation on unloading, and that correlations with fracture toughness only reflect the correlation between fracture toughness and stress corrosion resistance of the glasses. Similar reasoning could be applied to the initiation of median-radial cracks on loading. However, it is noted that glass NS1, in which liquid water had little effect on crack initiation loads, has low resistance to crack initiation on loading. This suggests that other factors besides stress corrosion resistance govern initiation on loading, and possibly unloading as well. If the critical stress level is not reached via sub-critical crack growth, which is a possibility pointed out by Lawn et al.[38] then the crack nucleus (assumed to be a shear fault by Lawn et al.[38]) will spontaneously pop-in when the appropriate critical stress level is reached. In this situation, it then is possible that the fracture

toughness plays a more direct role, since presumably the critical stress level for crack initiation may increase with increasing fracture toughness.

4.6.2   Brittleness Indices (H_V/K_{IC}, EH_V/K_{IC}^2, 'c/a')

In Figure 121 the median-radial crack initiation loads on loading are plotted as a function of the ratios H_V/K_{IC} and EH_V/K_{IC}^2. There is no overall correlation between either brittleness indices and the median-radial initiation load.

In Figure 122 the load at which the first median-radial cracks initiated on unloading as a function of the same two brittleness indices is shown. Although there is much scatter in the data, in general it appears the initiation force on unloading increases with increasing brittleness index.

In Figure 123 the normalized initiation load for the first median-radial cracks to initiate on unloading for Wagner's series of glasses[9] is shown as a function of the brittleness index H_V/K_{IC}. The 'anomalous' glasses in the borosilicate series have the lowest value of the brittleness index and lowest normalized initiation forces. Increased brittleness index in this series is met with large increases in normalized initiation load. For the aluminosilicate series, as brittleness index increases, the normalized initiation load drops slightly, then increases. For the soda-lime-silicate series, there is no trend with the brittleness index.
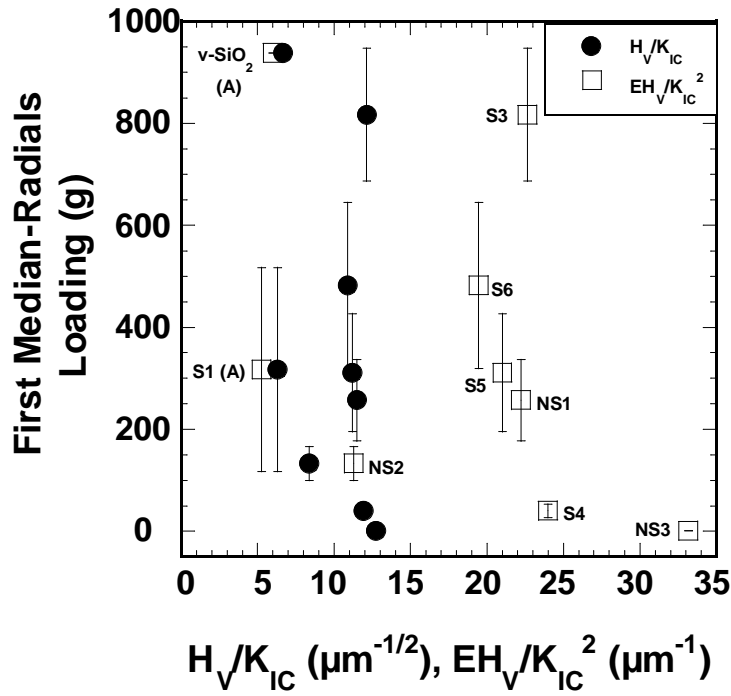
Figure 121. *The variation of first median-radial cracks on indenter loading for the 1 Kg (0.2 µm/s) tests with two different brittleness indices.*
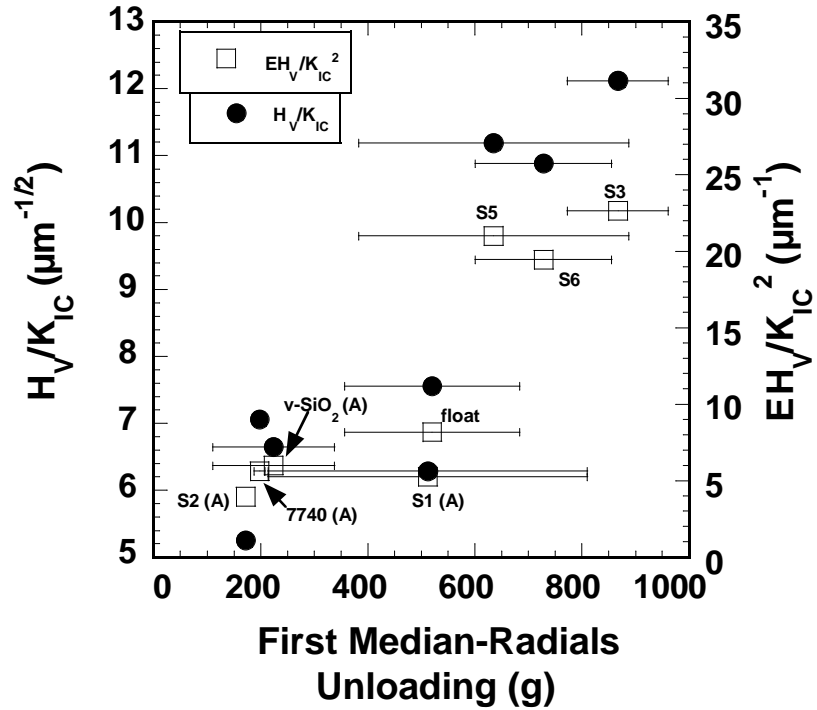
Figure 122. *First median-radial cracks on indenter unloading for the 1 Kg (0.2 µm/s) tests as a function of two brittleness indices.*
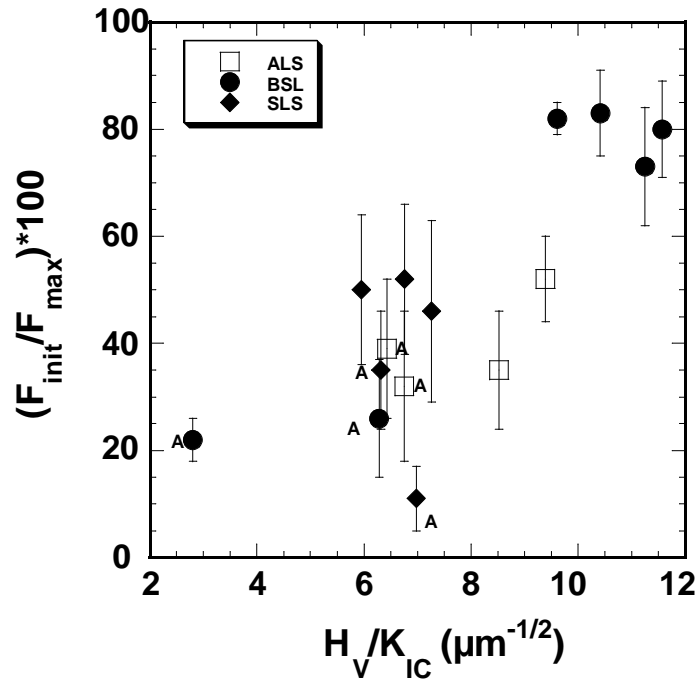
Figure 123. *The normalized initiation load for the first median-radial cracks to initiate on unloading for the Wagner glasses[9] as a function of the brittleness index H_V/K_{IC}. Maximum load was 1400 g, and displacement rate of 0.2 µm/s was used. From data of Wagner[9].*

In Figure 124 the first median-radials to initiate on loading and unloading are plotted as a function of the 'c/a' ratio at 1 Kg. No correlation exists between the 'c/a' ratio and median-radial initiation load on loading. Some correlation is seen between the 'c/a' ratio and the median-radial initiation load on unloading, however. As 'c/a' ratio increases, median-radials appear to initiate at higher loads. The 'anomalous' glasses, with the exception of S1, had median-radials initiate at the lowest load on unloading, and have the
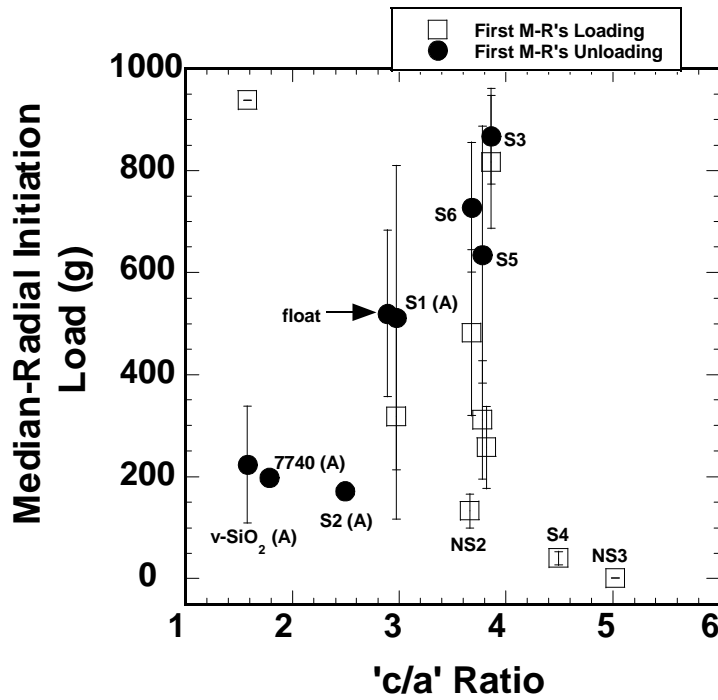
Figure 124. *The median-radial crack initiation load on loading and unloading for the 1 Kg (0.2 µm/s) tests as a function of the 'c/a' ratio of the different glasses.*

Figure 125. *The variation of normalized initiation load with 'c/a' ratio for the Wagner glasses[9].*

lowest 'c/a' ratios. The variation of initiation load with 'c/a' ratio is qualitatively the same as with H_V/K_{IC}. Wagner's crack initiation data[9] is plotted as a function of 'c/a' ratio in Figure 125. The variation of normalized initiation load with 'c/a' ratio is qualitatively the same as with H_V/K_{IC}.

4.6.3   Vickers Hardness

The variation in median-radial initiation load with the Vickers hardness of the glasses is shown in Figure 126. No overall trend is apparent. The Vickers hardness of the glasses does not appear to govern the initiation load in any predictable way. However, the glasses with the lowest Vickers hardness (S4, NS2, NS3) have the lowest initiation load for median-radials on loading. A similar lack of overall correlation with Vickers hardness was seen with the Wagner glasses[9], as shown in Figure 127.

4.6.4   Fracture Surface Energy

In Figure 128 the median-radial initiation load is shown as a function of the fracture surface energy of the glasses. No overall trend is apparent for the median-radials which initiated on loading. However for the 'normal' glasses NS1, NS2, NS3, S4, S5, S6, and the 'anomalous' v-SiO$_2$, it appears the initiation load on loading increases with increasing γ_f. Glasses S3 and S1 do not fit this trend, however.
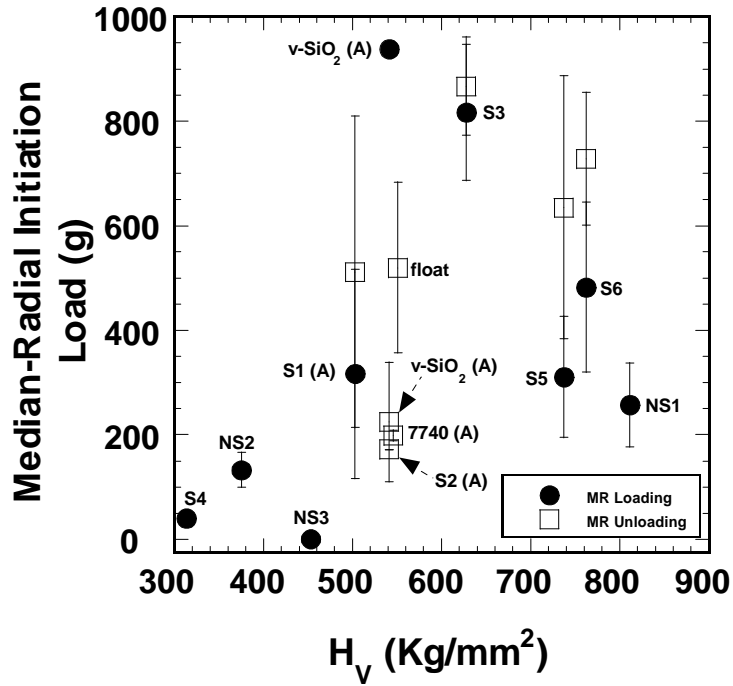
Figure 126. *The variation in median-radial initiation load with Vickers hardness of the glasses. Vickers hardness from the 1 Kg (0.2 µm/s) tests shown.*
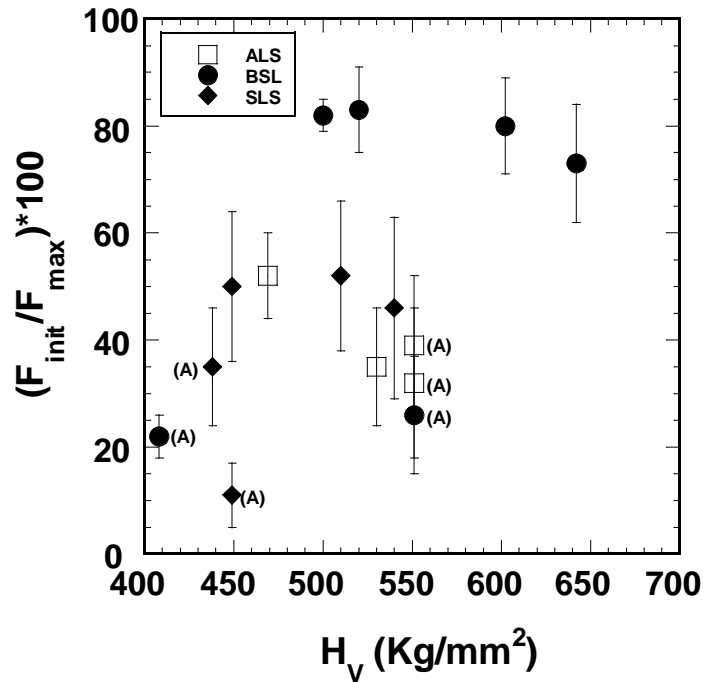
Figure 127. *The variation of normalized initiation load with Vickers hardness for the Wagner glasses[9]. Data from Wagner[9].*

232
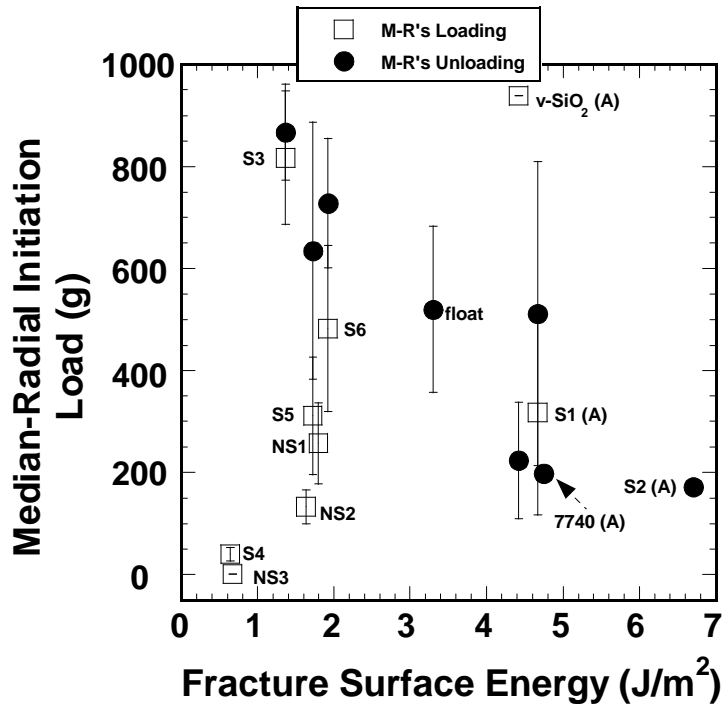
Figure 128. The variation of median-radial initiation load for the first median-radial cracks to initiate for the 1 Kg (0.2 µm/s) tests, as a function of fracture surface energy.

There does appear to be a trend of decreasing initiation load on unloading with increasing fracture surface energy. This trend is similar to that seen with the fracture toughness. This is not surprising considering the good correlation between K_{IC} and γ_f of the glasses.

4.6.5 Young's Modulus

The median-radial crack initiation loads are shown as a function of Young's modulus in Figure 129 for the glasses tested in the current study. There is no correlation with Young's modulus. The normalized initiation
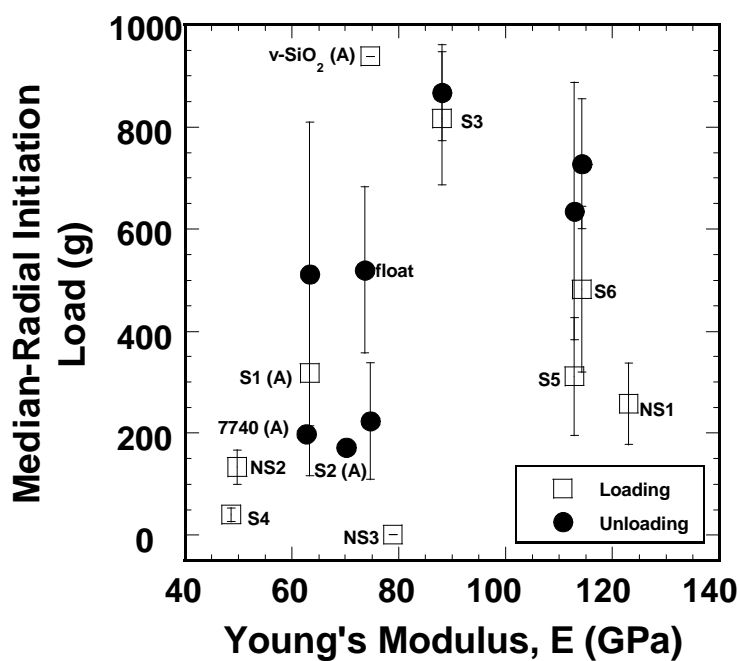
Figure 129. *The median-radial crack initiation load on unloading and loading for the 1 Kg (0.2 µm/s) tests, as a function of Young's modulus of the glasses.*

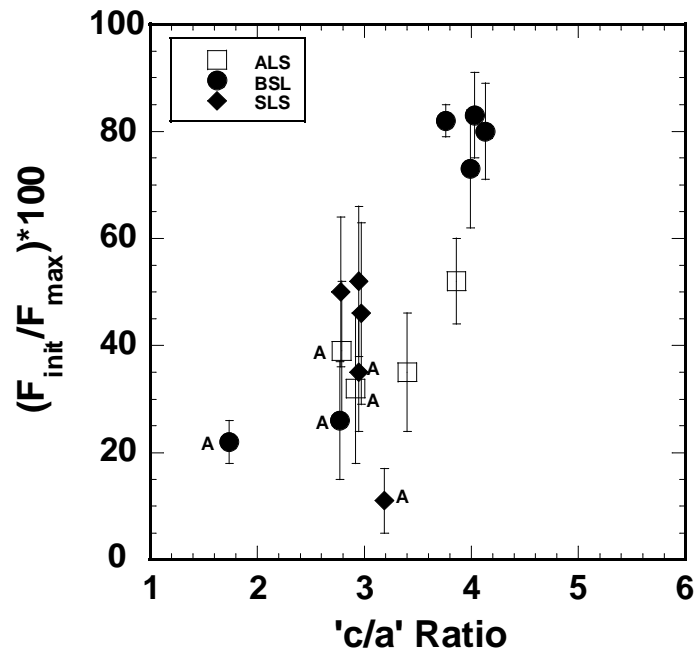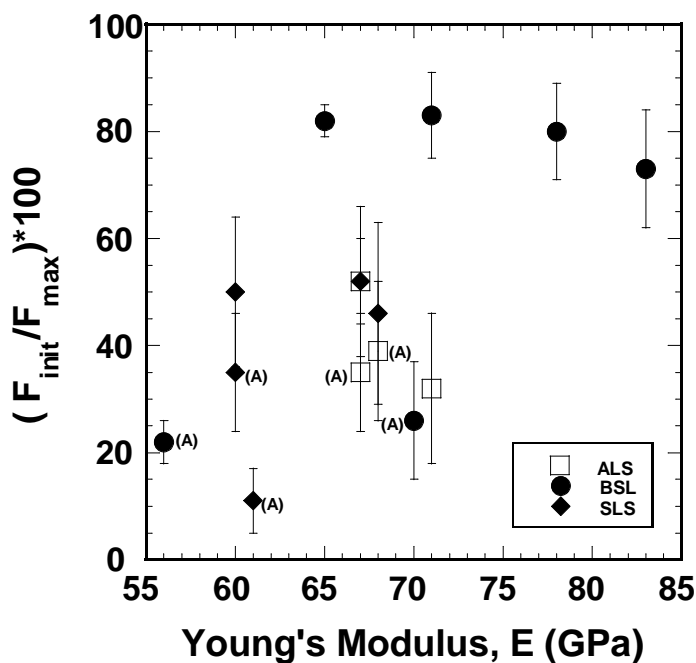***Figure 130.*** *The normalized initiation load for the first median-radial cracks to initiate on unloading as a function of Young's modulus for the Wagner glasses[9]. Data from Wagner[9].*

load for the Wagner glasses[9] are shown as a function of Young's modulus in Figure 130, and no correlation is seen.

4.6.6   E/H_V

The initiation load for the first median-radial cracks on loading and unloading is shown as a function of the ratio E/H_V in Figure 131. There is a trend of decreasing median-radial initiation load on loading with increasing E/H_V; however, glasses S1 and NS2 do not fit this trend. For median-radial initiation on unloading there is some indication that increased E/H_V corresponds to higher initiation loads, i.e., decreased initiation resistance. In addition, the 'anomalous' glasses, excluding S1, all have low E/H_V, and the lowest values of initiation load on unloading. However, in some sense, more correlation on unloading is expected on the basis that the complex stress-strain field generating the crack nuclei is completed on indenter loading, and thus the nuclei are just waiting to be activated on unloading. That is, more deviation with E/H_V would be expected on loading, rather than on unloading, because of the ill-defined and complex nature of the deformations occurring beneath the indenter on loading.

In Figure 132 the normalized initiation load for median-radial initiation is shown as a function of E/H_V, for the Wagner glasses[9]. No correlation is apparent for the sodium borosilicate (BSL) series of glasses.
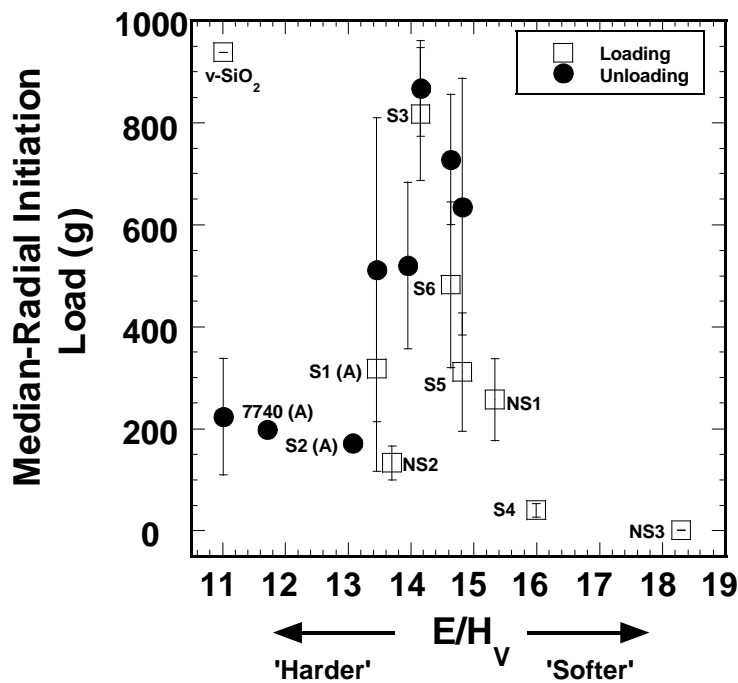
Figure 131. *The median-radial crack initiation load on unloading and loading for the 1 Kg (0.2 μm/s) tests, as a function of E/H$_V$ of the glasses.*
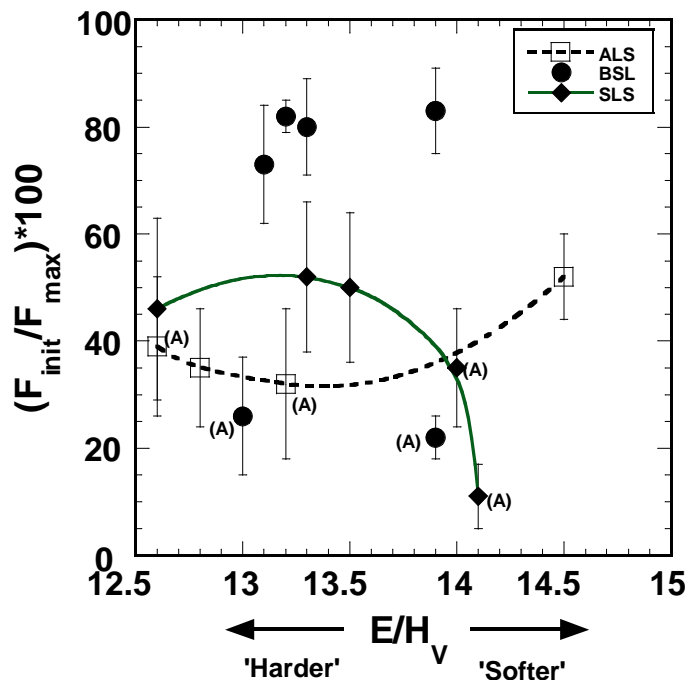
Figure 132. *The normalized initiation load for the first median-radial cracks to initiate on unloading as a function of E/H$_V$ for the Wagner glasses[9]. Curves are guides for the eye only. Data from Wagner[9].*

For the sodium aluminosilicate series (ALS) the normalized initiation load decreases slightly with E/H_V, and then increases. The initial decrease is not consistent with increased crack driving force, but the increase is.

For the soda-lime-silicate series (SLS), the normalized load remains nearly constant for E/H_V up to ~ 13.5, then decreases rapidly with increasing E/H_V. This trend does not agree with the increased crack driving force expected with increasing E/H_V. Rather, the increase in E/H_V correlated with a decrease in fracture toughness (increased crack length) for this glass series. That is, E/H_V had more influence with crack propagation than initiation in this glass series, which is in agreement with the original fracture mechanics interpretation of this quantity.

4.6.7 G/K

The median-radial crack initiation loads are shown as a function of the shear-to-bulk-moduli ratios in Figure 133. No overall trend is apparent; however, the glasses with values of G/K > 0.6 had all median-radial cracks initiate on unloading, with the exception of glass S1. In Figure 134 the normalized initiation load for the first median-radial cracks to initiate in the Wagner glasses[9] is shown as a function of the G/K ratio. No overall trend with initiation load is apparent.
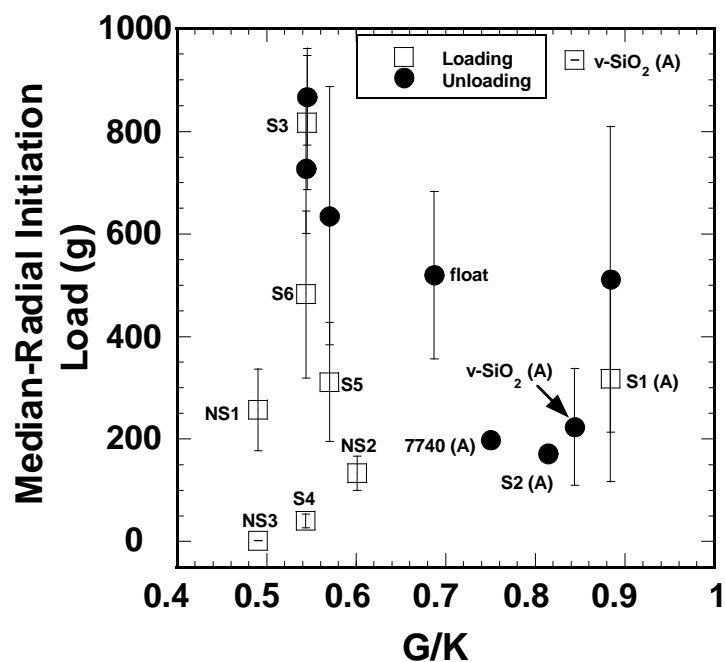
Figure 133. *The median-radial crack initiation force on unloading and loading for the 1 Kg (0.2 μm/s) tests, as a function of G/K of the glasses.*
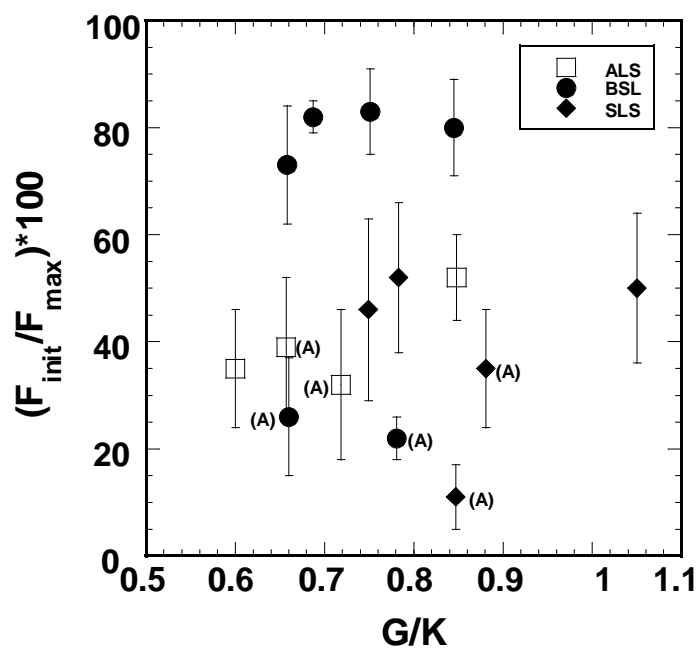
Figure 134. *The normalized initiation load for the first median-radial cracks to initiate on unloading as a function of E/H$_V$ for the Wagner glasses[9]. Data from Wagner[9].*

4.6.8 Density and Atomic Molar Volume

The median-radial initiation load is shown as a function of the glass density in Figure 135. No correlation is seen for initiation on loading. On unloading, it is apparent the glasses with the lowest densities (S2, 7740, v-SiO_2) had the lowest initiation loads for median-radial cracks. Low density is associated with the openness of the structures, and translates into lower residual stress around the indentation sites. This means the load must reach a lower level for the stress to become critical compared to glasses with higher densities.

In Figure 136 the median-radial initiation load is shown as a function of the atomic molar volume of the glasses. There is no correlation for either the median-radial initiation loads on loading or unloading. This is somewhat surprising given the slight correlation with density for the median-radial cracks that initiated on unloading.

4.6.9 Summary

In general, the median-radial crack initiation resistance increased with increasing fracture toughness and fracture surface energy for the glasses in the current work. In addition, increased resistance to median-radial initiation on unloading with decreasing brittleness indices H_V/K_{IC}, EH_V/K_{IC}, and c/a, was observed. The initiation load on loading also tended to increase
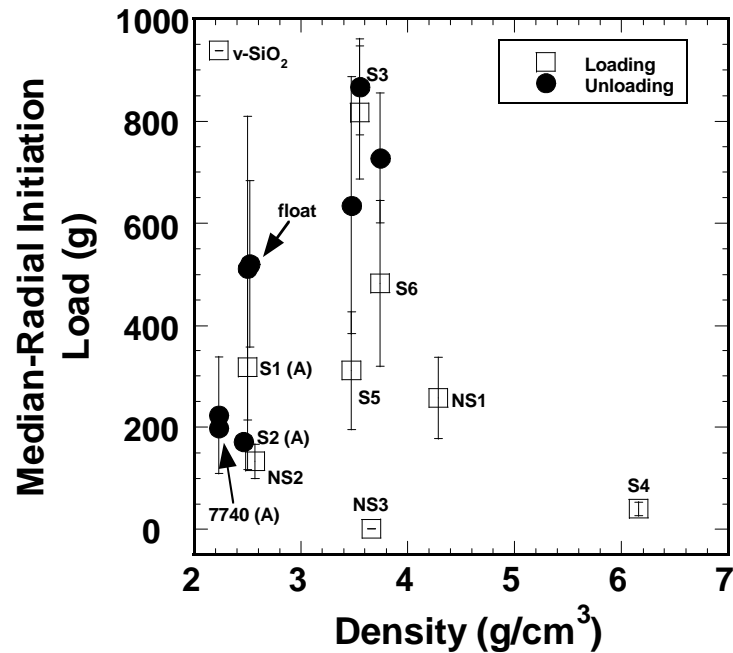
Figure 135. The median-radial crack initiation load on unloading and loading for the 1 Kg (0.2 μm/s) tests, as a function of glass density.
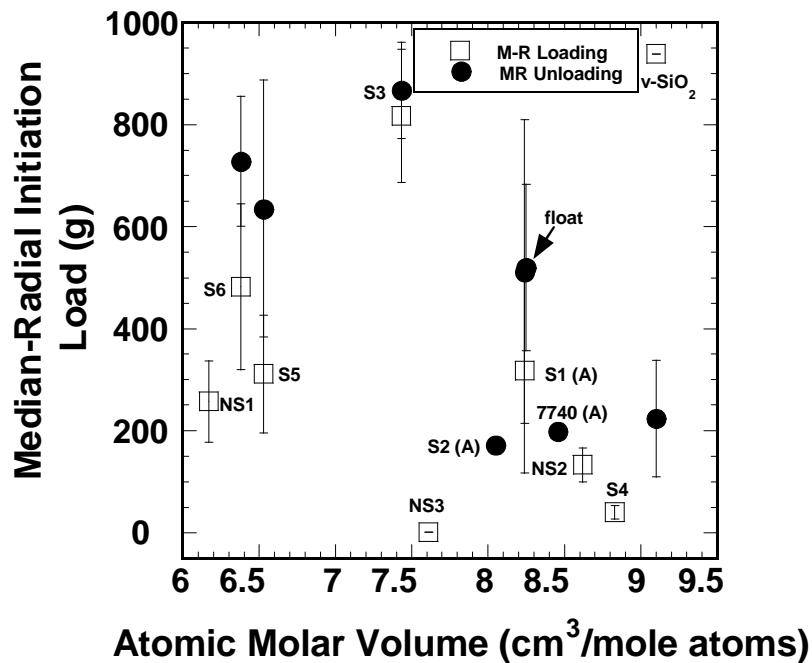
Figure 136. The median-radial crack initiation load on unloading and loading for the 1 Kg (0.2 μm/s) tests, as a function of the atomic molar volume.

with decreasing EH_V/K_{IC}. Also, in general, decreased resistance to median-radial crack initiation with increase of the quantity E/H_V was observed. The glasses with intermediate values of Vickers hardness and Young's modulus tended to have better resistance to median-radial cracking then glasses with higher and lower values of these properties. Glasses with relatively low density tended to have increased resistance to median-radial crack formation on unloading and also on loading to some extent. Glasses with $G/K > 0.6$, with the exception of S1 and possibly $v\text{-}SiO_2$, had median-radial cracks initiate only on loading for loads up to 1 Kg.

4.7   Load-Displacement Curve Results and Discussion

The load-displacement data for the recording microindentation tests performed at 1 Kg (0.2 μm/s) are shown in Table XXXV.

4.7.1 LVH_{max}

In Figure 137 the Vickers hardness under maximum load, (LVH_{max}), and the conventional Vickers hardness from the same tests (H_V), are shown as functions of the maximum penetration depth. It is useful to know that the conventional Vickers hardness shows a similar trend with LVH_{max}. This means the conventional hardness is also a good indicator of hardness under load. Of course, the trend of LVH_{max} is expected to vary directly with the

Table XXXV. Load-Displacement Data.

Glass	Max. Load (g)	p_{max} (μm)	p_0 (μm)	Elastic Depth Recovery (μm)	Percent Elastic Depth Recovery (%)	LVH (Kg/mm^2)
S1 (A)	1003 ± 3	17.6 ± 0.4	6.0 ± 0.1	11.6 ± 0.3	66.0 ± 0.6	123 ± 5
S2 (A)	1003 ± 2	17.2 ± 0.2	5.6 ± 0.1	11.6 ± 0.2	67.5 ± 0.5	128 ± 3
S3 (N)	1005 ± 2	15.9 ± 0.5	5.4 ± 0.4	10.5 ± 0.3	66.1 ± 1.7	150 ± 8
S4 (N)	1004 ± 2	20.0 ± 0.1	8.1 ± 0.2	11.9 ± 0.3	59.6 ± 1.3	95 ± 1
S5 (N)	1004 ± 3	14.8 ± 0.3	5.0 ± 0.1	9.8 ± 0.4	66.2 ± 1.1	175 ± 8
S6 (N)	1006 ± 2	16.0 ± 0.3	5.1 ± 0.1	11.0 ± 0.3	68.4 ± 0.8	148 ± 5
NS1 (N)	1006 ± 3	14.3 ± 0.1	5.0 ± 0.1	9.3 ± 0.2	65.0 ± 0.9	187 ± 4
NS2 (N)	1007 ± 3	19.2 ± 0.6	6.1 ± 0.1	13.1 ± 0.5	68.1 ± 1.0	104 ± 6
NS3 (N)	1004 ± 2	17.7 ± 0.2	6.9 ± 0.2	10.9 ± 0.3	61.3 ± 1.2	121 ± 2
Float (N-A)	1004 ± 2	17.9 ± 0.3	5.4 ± 0.1	12.5 ± 0.3	69.6 ± 0.6	119 ± 4
VITREOUS SILICA (A)	1004 ± 3	16.5 ± 0.5	3.7 ± 0.4	12.8 ± 0.7	77.6 ± 2.4	139 ± 8
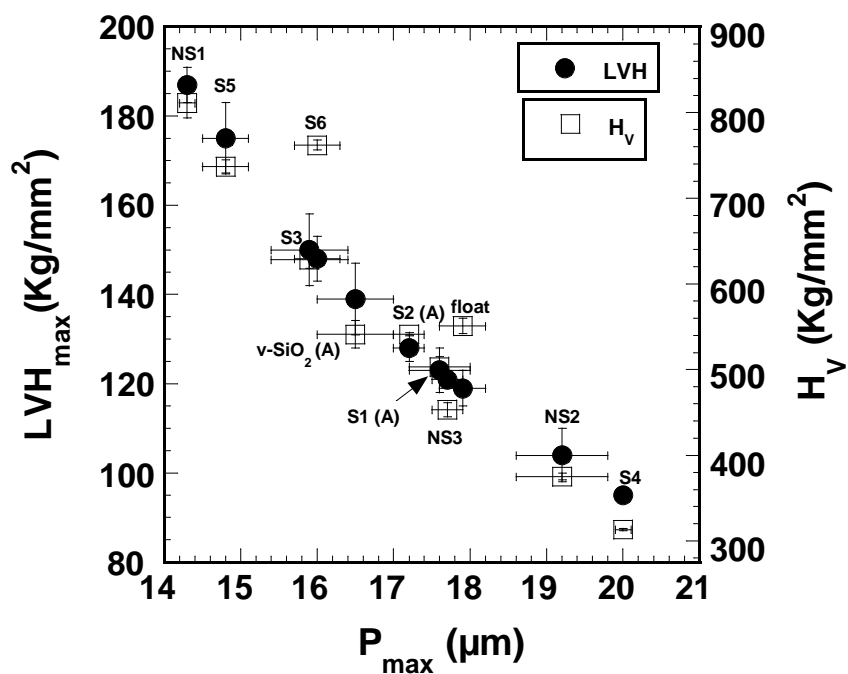
Figure 137. The Vickers hardness under maximum load (LVH$_{max}$) and conventional Vickers hardness (H$_V$) as function of the maximum penetration depth of the indenter. H$_V$ from 1 Kg recording microindentation data (see Table XXXII).

maximum penetration depth (see Eq. 12). One exception, however, is glass S6, in which the hardness under load is lower than expected based on its conventional hardness and the trend formed with the other glasses. Given the similarity of the conventional Vickers hardness of this glass with glass S5, this is unexpected. No plausible explanation for this behavior can be given.

4.7.2   Elastic Depth Recovery

Figure 138 shows that there is no correlation with the percent elastic depth recovery and the Young's modulus of the glasses. However, there is some correlation with the absolute values of depth recovery. For glasses NS1, S5, S3, NS3, S2, S1, and S4 there appears to be a strong trend of decreasing elastic depth recovery with increasing Young's modulus. Glasses S6, float, v-SiO$_2$, and NS2 do not fit this trend. Even for these latter four glasses, there is still a trend of decreasing elastic recovery with increasing Young's modulus. Lower Young's modulus implies more elastic (stretchable, less rigid) materials, which evidently show more elastic depth recovery.

In Figure 139 the depth recovery is shown as a function of the atomic molar volume of the glasses. No correlation is seen with the percent elastic depth recovery; however, the absolute elastic depth recovery is seen to generally increase with increasing atomic molar volume. There are a few exceptions. Glasses S6, float, and NS2 do not appear to fit the trend

243
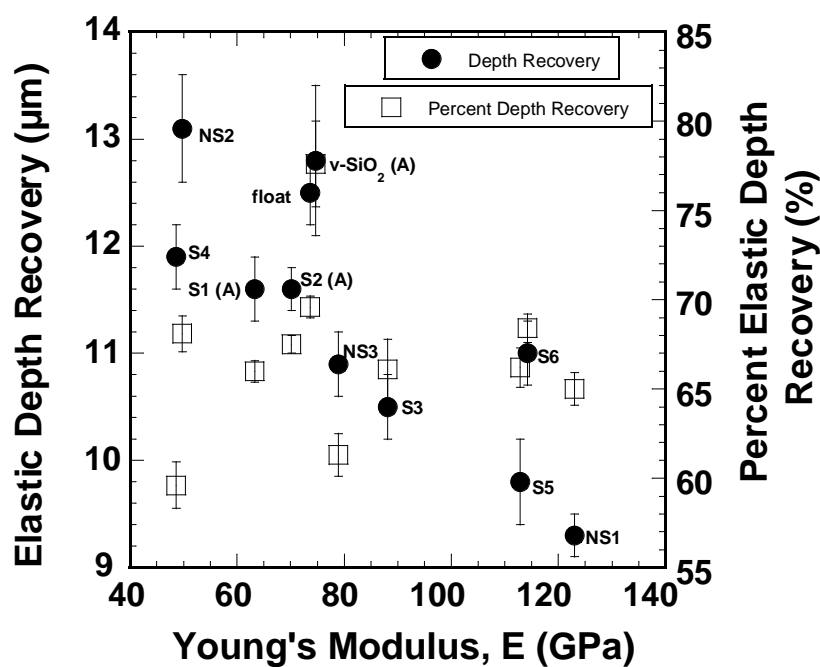
Figure 138. *The variation of elastic depth recovery and percent elastic depth recovery of the glasses as a function of Young's modulus.*
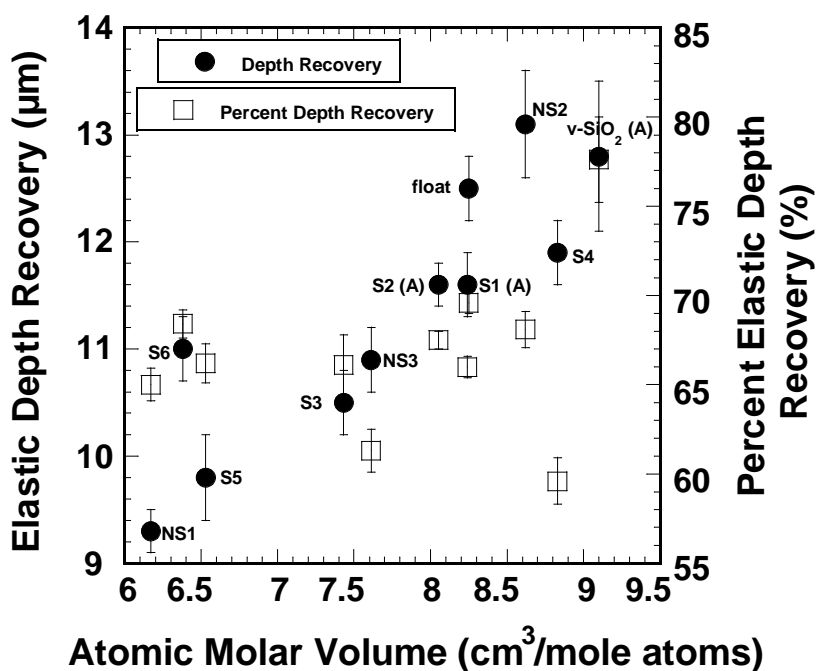
Figure 139. *The variation of elastic depth recovery and percent elastic depth recovery of the glasses as a function of the atomic molar volume of the glasses.*

244

established by the other glasses. Even for these latter three glasses, the recovery increases with atomic molar volume. These data suggest that open glass structures with relatively low Young's modulus are more capable of elastic recovery than more tightly packed, rigid structures. Open structures may allow compaction of material without breaking bonds, and this would be easier to achieve in lower-modulus materials because of decreased bond strength. The strained bonds then spring back on unloading. The very open structure and relatively low Young's modulus of vitreous silica supports this view.

Very little correlation was seen with either the densities of the glasses and the quantity E/H_V, and the elastic recovery of the glasses. The same was true of the Vickers hardness. The bulk modulus (K) showed little correlation with the elastic-recovery behavior of the glasses. The shear modulus showed a very similar, nearly identical, trend with the elastic depth recovery as for the Young's modulus. However, no correlation was seen with the shear modulus and percent elastic depth recovery. Little correlation was seen with the ratio G/K and the elastic recovery behavior.

4.7.3 Energy Data

The energy data extracted from the load-displacement curves are shown in Table XXXVI. In addition, the average volume of the unloaded indentations is shown. In the last column, the permanent deformation energy was divided

by the volume of the indentations to give a permanent deformation energy per unit volume for each glass, designated E_{UVPD}. The volume of the unloaded indentations was calculated using the following formula:

$$V = \frac{1}{3}a^2h \qquad (26)$$

where,

V = volume of the unloaded indentations

a = length of the side of indentation

h = residual indentation depth (p_o)

The formula is that for the volume of a square-based pyramid, which is the assumed shape for the indentations, i.e., the same shape as the Vickers diamond which created them.

The permanent deformation energy represents the area bounded by the loading and unloading load-displacement curves. It is the energy consumed in permanent volume deformation of the glass, i.e., in creating the indentation, and in creating/propagating any cracks. The energy associated with propagating median-radial and lateral cracks is assumed to be negligible compared to the energy associated with the volume deformation processes.

Table XXXVI. Energy Data from the Load-Displacement Curves.

Glass	Energy Loading (Total) (µJ)	Energy Unloading (Recovered) (µJ)	Permanent Deformation Energy (µJ)	Percent Permanent Deformation Energy (%)	Indentation Volume (µm^3)	Energy per Unit Volume Permanent Deformation (µJ/µm^3)x10^{-3}
S1 (A)	66.7 ± 1.0	44.6 ± 0.5	22.1 ± 0.6	33.1 ± 0.4	3684	5.99
S2 (A)	66.1 ± 1.1	46.3 ± 1.1	19.8 ± 0.5	30.0 ± 0.8	3216	6.16
S3* (N)	69.2 ± 2.5	48.4 ± 2.0	20.8 ± 0.8	30.0 ± 0.8	2330	8.93
S4 (N)	77.3 ± 0.4	45.3 ± 0.6	32.0 ± 0.5	41.4 ± 0.6	8026	3.99
S5 (N)	57.9 ± 1.5	38.3 ± 1.1	19.5 ± 0.4	33.7 ± 0.3	2109	9.25
S6 (N)	64.5 ± 1.5	43.0 ± 1.3	21.4 ± 0.3	33.3 ± 0.5	2074	10.32
NS1 (N)	56.9 ± 0.8	36.1 ± 0.5	20.7 ± 0.3	36.5 ± 0.3	1936	10.69
NS2 (N)	73.1 ± 2.1	48.9 ± 1.5	24.2 ± 0.7	33.1 ± 0.4	5039	4.80
NS3 (N)	69.0 ± 1.2	39.7 ± 1.1	29.2 ± 2.0	42.4 ± 2.2	4726	6.18
float (N-A)	69.4 ± 1.0	47.9 ± 1.1	21.5 ± 0.4	31.0 ± 0.7	3038	7.08
Vitreous Silica (A)	66.9 ± 2.1	53.7 ± 2.0	13.2 ± 1.1	19.7 ± 1.6	2104	6.27

The total energy represents the total energy put into the glass (and instrument) at the maximum load. The recovered energy represents the elastically stored strain energy recovered from the glasses (and instrument) on unloading. Since the elastic stored energy in the instrument was not accounted for in the curves, the total energy and recovered energies do not represent the energy going into and out of just the glass. However, the permanent deformation energy should be representative of the glasses, since all elastic deformations occurring on loading are recovered on unloading.

4.7.4 Energy and Hardness

In Figure 140 the conventional Vickers hardness (H_V) is shown as a function of the energy per unit volume permanent deformation (E_{UVPD}) of the glasses. As H_V increases so does E_{UVPD}. Thus, it can be concluded the conventional Vickers hardness of the current glasses, to a large extent, is a measure of the energy needed to create unit volume permanent deformation in them. The 'harder' glasses require more energy to create unit volume permanent deformation than less-hard glasses. This is significant, since it relates a material characteristic that has long since been regarded as somewhat elusive in terms of what it actually means, or is a measure of, to something more definitive.
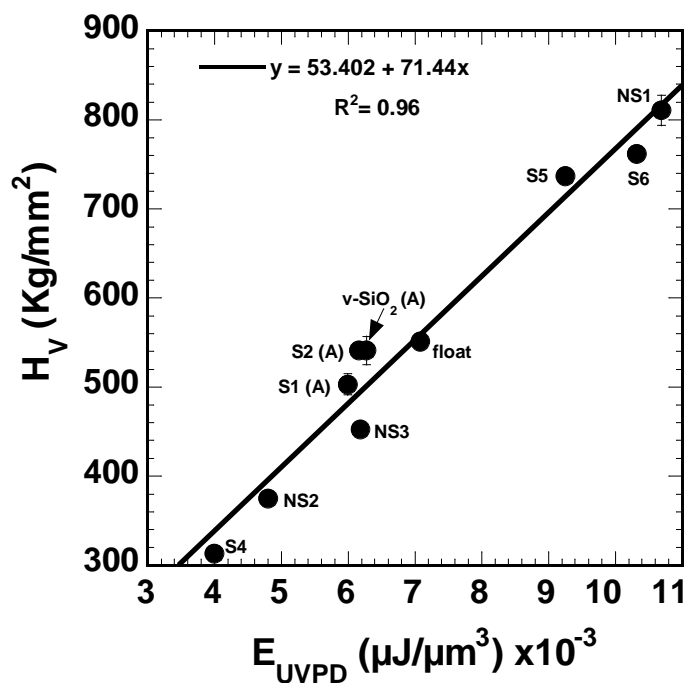
Figure 140. *Conventional Vickers hardness, H_V, as a function of the energy per unit volume permanent deformation, E_{UVPD}, of the glasses. H_V values are from 1 Kg recording microindentation data (see Table XXXII).*

4.7.5　Elastic-Plastic Deformation Character of Glasses

The percent elastic depth recovery of the glasses (Table XXXV) is one measure of the elastic-plastic deformation character of the glasses. A glass having 50% elastic recovery would have equal parts elastic and plastic deformation, i.e., ideally elastic-plastic. From the data, it is seen that all of the glasses have values greater than this, i.e., they are slightly more elastic than plastic. A convenient way to classify this behavior is shown in Figure 141, in which the percent permanent deformation energy is plotted as a function of the percent permanent deformation of the glasses. There is a strong linear correlation between the two. The glasses with high values of percent permanent deformation are also the same glasses that have the highest values of percent permanent deformation energy, and are considered more plastic. That is, the more 'plastic' glasses use a greater percentage of the indentation energy for plastic deformation than elastic recovery. However, it should also be noted that these are the same glasses that cracked readily on loading, i.e., glasses S4, NS3, NS1, NS2, S5, and S6. Figure 142 shows that the percent permanent deformation energy also increases nearly linearly with the quantity E/H_V of the glasses. Higher E/H_V are associated with 'softer' glasses, and increased percent permanent deformation energy. Relatively poor agreement was seen between the percent elastic depth
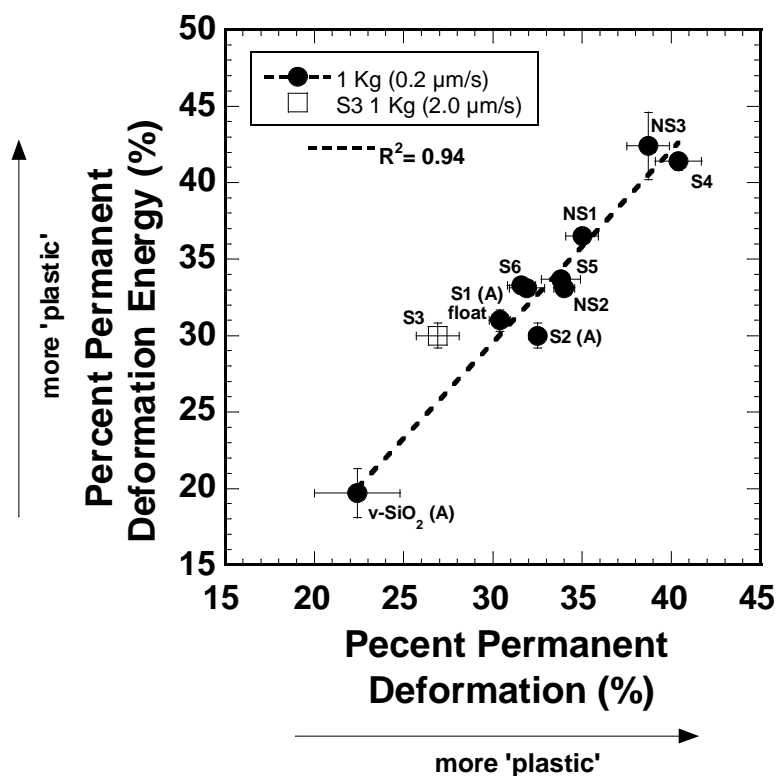
Figure 141. The percent permanent deformation energy as a function of the percent permanent deformation of the different glasses examined in the current work.
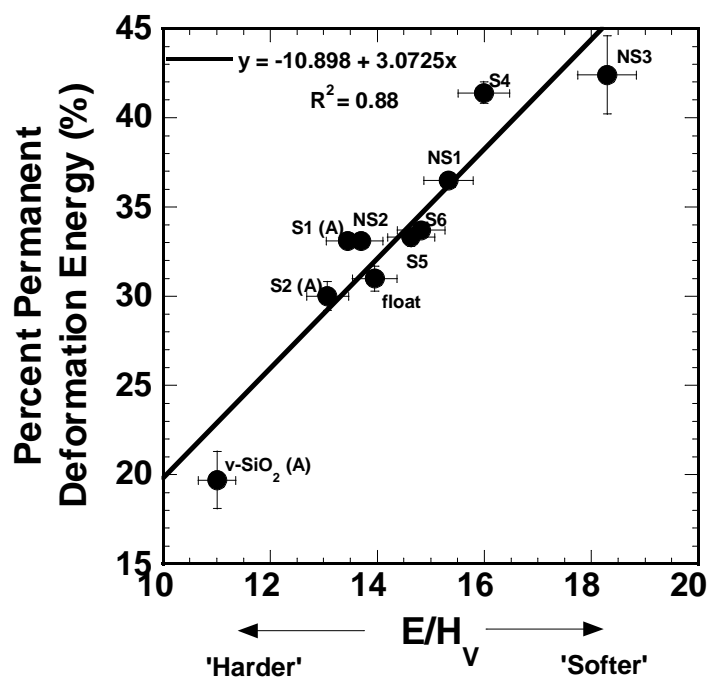
Figure 142. The percent permanent deformation energy as a function of the ratio E/H_V of the glasses.
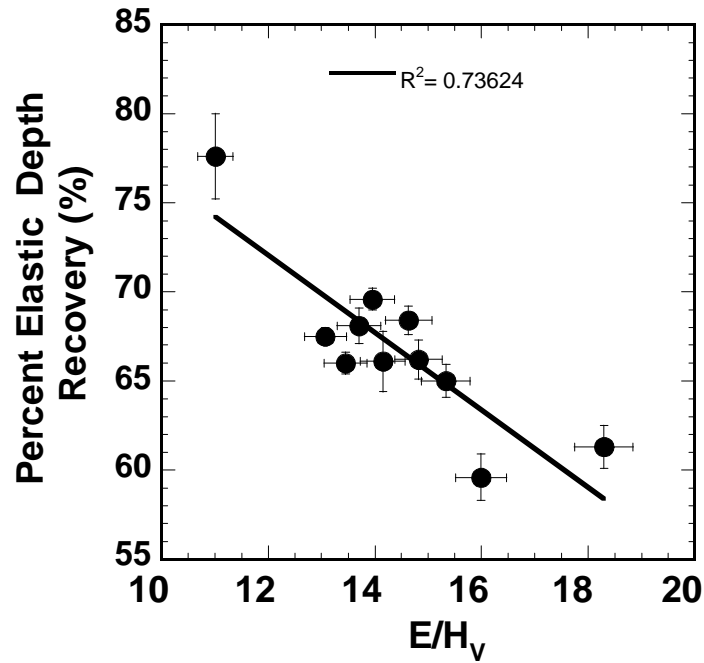
Figure 143. *The percent elastic depth recovery of the glasses as a function of the ratio E/H$_V$.*

recovery and the quantity E/H$_V$, as seen in Figure 143. It was expected that as this quantity increased, the percent elastic depth recovery would decrease with more predictability.

4.8   Surface Uplift Around Indentations

The surface uplift observed around the indentations in glasses S1, S2, S4, S5, S6, NS1, and float is shown as a function of the lateral crack length in Figure 144. The increased uplift is associated with longer lateral cracks, and the agreement is very good. Increased lateral crack size is associated with increased residual crack driving force (F_R) (and decreased fracture toughness), and hence the uplift is indicative of the 'plastic' zone trying to

push up and outward toward the surface. Because the surface of the glass is free of constraint, presumably the volume of the lateral crack is accommodated by this displacement. This supports the notion that glasses with significant uplift have increased residual crack driving force and overall decreased resistance to crack initiation. It is also possible that this upward displacement helps accommodate the volume of the indenter as well.
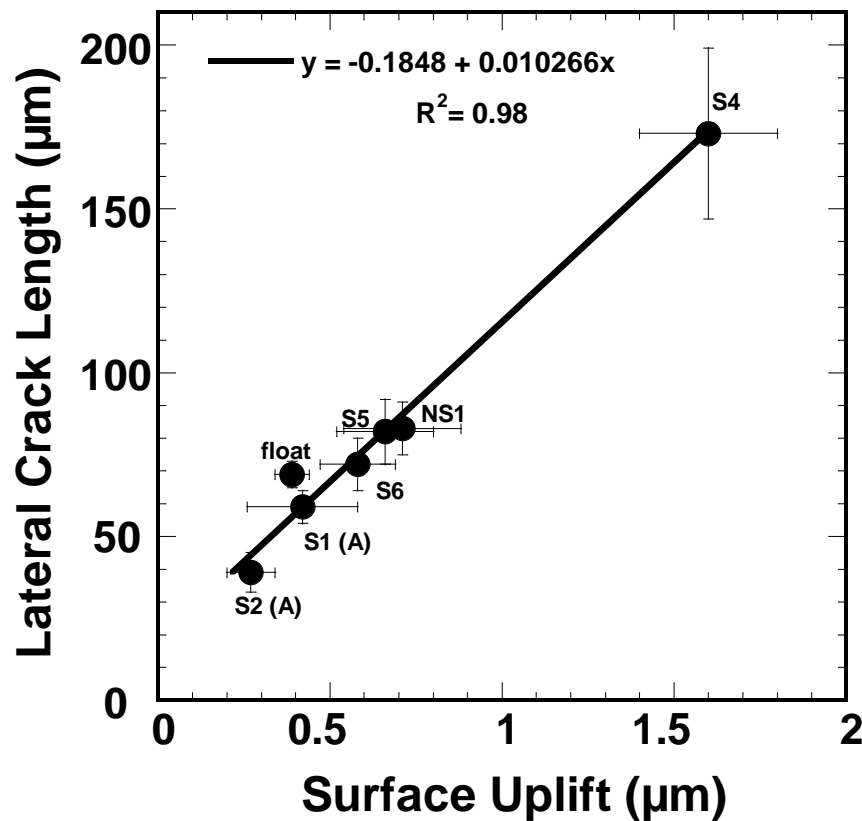
Figure 144. The variation of surface uplift around indentations as a function of lateral crack length. Increased uplift is associated with longer lateral cracks.

4.9   Acoustic Emission Data

4.9.1   AE Hit Data

The acoustic emission hit data collected from the crack initiation experiments is summarized in Table XXXVII. The total number of hits is listed, as are the partition of those hits occurring on the loading and unloading cycles. In addition, the number of hits on unloading due to lateral cracks is shown, and also expressed as a percentage of the total hits.

The anomalous glasses (S1, S2, 7740, Suprasil 312), the float glass, and glass S3, had the lowest percent lateral crack hits compared to the other glasses. This is consistent with an overall reduced crack driving force (lower E/H_V) in these glasses compared to the other glasses (one exception is glass NS2, which has a slightly lower value of E/H_V compared to glass S3). Since the initiation of lateral cracks on unloading is solely due to the residual stress field, a decreased number of lateral crack hits, and percentage of hits, is consistent with a more reduced residual-stress driving component in these glasses compared to glasses S4, S5, S6, NS1, and NS3.

The two most 'anomalous' glasses, v-SiO$_2$ and 7740 Pyrex™ borosilicate had the greatest number of hits on loading, due to the formation of numerous ring-cone cracks, which gave rise to many acoustic emissions. The detection of median-radial cracks on loading was most frequent in glass S1, and in

Table XXXVII. Summary of Acoustic Emission Hit Data.[*]

Glass	Hits Loading	Hits Unloading	Lateral Crack Hits Unloading	Total Hits	Percent Lateral Crack Hits (%)
S1 (A)	1.9 ± 1.7	0.8 ± 0.8	0.2 ± 0.4	2.7 ± 1.9	7
S2 (A)	0.6 ± 0.5	0.3 ± 0.7	0	0.9 ± 0.6	0
S3 (N)	0.6 ± 0.7	2.2 ± 0.9	0.1 ± 0.3	2.9 ± 0.7	3
S4 (N)	0.6 ± 0.7	3.7 ± 2.6	3.7 ± 2.6	4.3 ± 2.9	86
S5 (N)	0.4 ± 0.5	1.1 ± 1.0	0.5 ± 0.7	1.5 ± 1.4	33
S6 (N)	1.0 ± 0.7	1.2 ± 0.8	0.7 ± 0.8	2.2 ± 0.8	32
NS1 (N)	0.4 ± 0.7	2.6 ± 1.3	2.6 ± 1.3	3.1 ± 1.7	84
NS2 (N)	0.1 ± 0.3	0.7 ± 1.1	0.7 ± 1.1	0.8 ± 1.0	88
NS3 (N)	0 ± 0	3.4 ± 1.8	3.4 ± 1.8	3.4 ± 1.8	100
float (N-A)	0.1 ± 0.3	3.1 ± 0.3	0	3.2 ± 0.4	0
7740 Pyrex™ Borosilicate (A)	15.0 ± 5.0	4.7 ± 2.1	1.7 ± 1.5	19.7 ± 5.9	9
v-SiO₂ (Suprasil 312) (A)	17.9 ± 6.3	5.7 ± 1.9	3.5 ± 1.5	23.6 ± 6.8	15

[*] fraction of hits denotes frequency of occurrence

glass NS3, no median-radial cracks were detected on loading. A combination of acoustic emission hits from the formation of shear faults/bands on loading, and median-radial crack formation characterized the other glasses. In float glass and glass S2, no lateral-crack hits were detected. Figures 145 and 146 graphically compare the total number of acoustic emission hits detected, and the percent lateral cracks hits for each of the glasses, respectively.
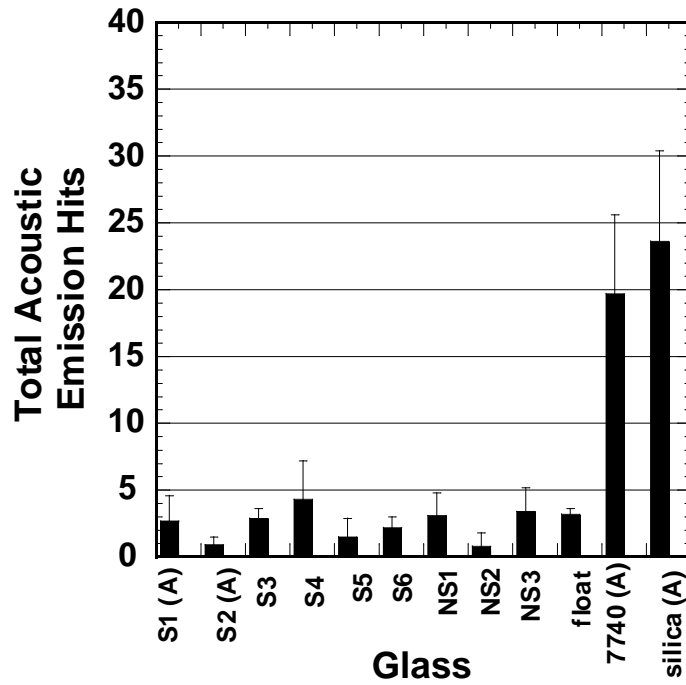
Figure 145. *The total acoustic emission hits for the different glasses from the crack initiation experiments, represented in a histogram.*
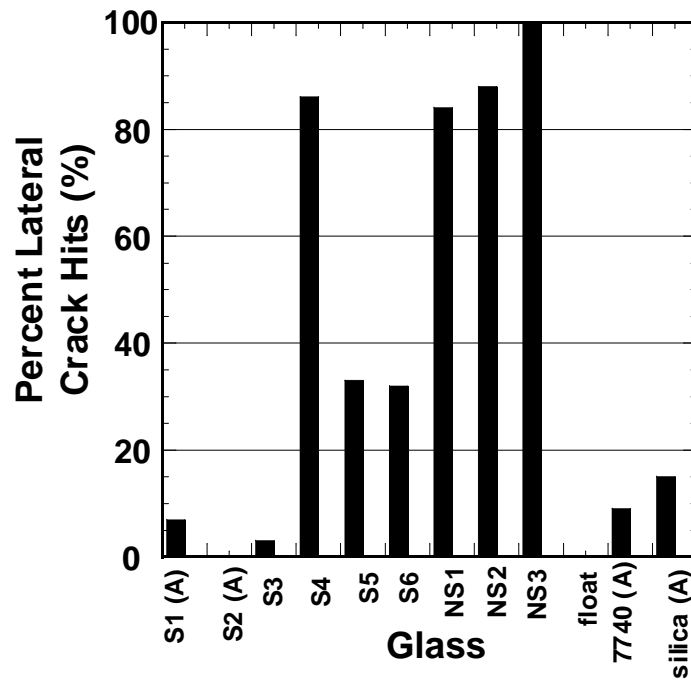
Figure 146. *The percent of the total acoustic emission hits that were lateral cracks, represented in a histogram. No lateral cracks were detected for glasses S2 and float.*

4.9.2 AE Energy Data

The accompanying acoustic emission energy data from the crack initiation tests is summarized in Table XXXVIII. The glasses that had a large percentage of lateral crack hits on unloading (S4, S5, S6, NS1, NS2, and NS3) are the same glasses in which the greatest fraction of energy was produced by lateral cracks. This points to a fundamental difference between the high-silica-containing glasses and those glasses containing little or no silica in terms of how the indentation energy is partitioned. In the latter glasses, it appears that most of the residual strain energy is used to propagate lateral cracks, consistent with the observation that median-radial cracks formed readily in these glasses on loading, in which case a large majority of the unused strain energy was available on unloading to propagate and form lateral cracks, leading to intense signals. In contrast, the 'anomalous' glasses, and the float glass, had median-radial cracking on unloading (S1 did have median-radials initiate on loading as well), in which case a majority of the strain energy was used to propagate these cracks, leaving less available for intense lateral-crack development compared to the other glasses. Glass S3 could also be put in this category, since a majority of the tests had some median-radial cracks initiate on unloading. The percent lateral crack energy is graphically illustrated in Figure 147 for the different glasses for comparison purposes.

Table XXXVIII. Summary of Acoustic Emission Energy Data.[*]

Glass	Energy Loading	Energy Unloading	Lateral Crack Energy Unloading	Total Energy	Percent Lateral Crack Energy (%)
S1 (A)	19.6 ± 24.2	11.9 ± 15.6	0.7 ± 1.6	31.5 ± 26.7	3
S2 (A)	0 ± 0	1.7 ± 3.9	0	1.7 ± 3.9	0
S3 (N)	6.7 ± 7.7	15.5 ± 12.1	0	22.2 ± 6.0	0
S4 (N)	0.2 ± 0.6	10 ± 16	10 ± 16	10 ± 16	100
S5 (N)	0.2 ± 0.4	1.3 ± 2.8	0.7 ± 2.2	1.5 ± 2.7	50
S6 (N)	1.8 ± 2.6	6.3 ± 7.1	5.4 ± 7.3	8.1 ± 8.0	62
NS1 (N)	0.3 ± 0.9	15.0 ± 16.0	15.0 ± 16.0	15.3 ± 15.7	98
NS2 (N)	0	1.8 ± 2.4	1.8 ± 2.4	1.8 ± 2.4	100
NS3 (N)	0	31.1 ± 41.7	31.1 ± 41.7	31.1 ± 41.7	100
float (N-A)	0	23.3 ± 3.3	0 ± 0	23.3 ± 3.3	0
7740 Pyrex™ Borosilicate (A)	n/a	n/a	n/a	66 ± 26	n/a
v-SiO$_2$ Suprasil 312 (A)	156 ± 98	89 ± 30	42 ± 31	245 ± 96	17

[*] The units are arbitrary, i.e., only relative comparisons between glasses is meaningful
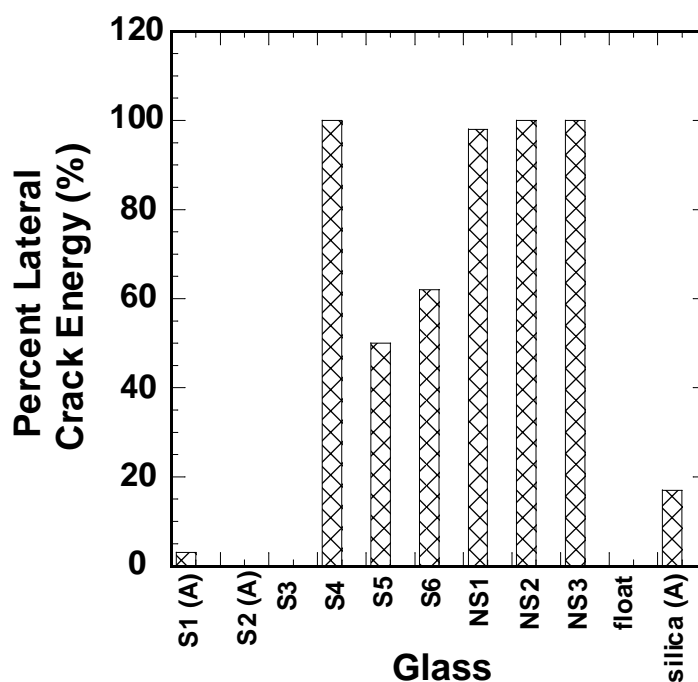
Figure 147. *The percent lateral crack energy for the different glasses represented in a histogram. Lateral crack hits were not produced in the float glass and glass S2; glass S3 had lateral crack hits detected, but no energy signal was produced from them.*

257

4.10 Considerations of Glass Composition and Structure

Descriptions of the most likely structural configurations of the examined glasses are presented below, based on available literature on similar compositions, and basic glass structural models in existence. In the section that follows, the overall crack initiation behavior is examined in light of these compositional (structural) considerations, and a model describing the overall behavior is presented.

4.10.1 Glass S1 (Lead-Alkali-Silicate Crown)

Approximate Composition (Mol %): 81 $SiO_2 \bullet 6Na_2O \bullet 5K_2O \bullet 5PbO \bullet 5Al_2O_3$

It can be seen this is primarily an alkali-silicate glass containing some lead and aluminum oxides. A three-dimensional network backbone is formed by the silica. The high percentage of silica is responsible for its 'anomalous' behavior. It is assumed the aluminum oxide is in network-forming positions, i.e., 4-fold coordinated, charged compensated by the Na^+ and K^+ ions. Since there are $\approx$ 10 moles Al^{3+}, $\approx$ 10 moles of R^+ are 'consumed.' This leaves $\approx$ 12 moles R^+ to create $\approx$ 12 moles of non-bridging oxygen's (NBO's). For such low Pb concentrations, the Pb^{2+} ions are most likely in network-modifying positions, randomly distributed within the Si-O-Si network, each mole of Pb^{2+} creating 2 moles NBO's.[70] The Pb^{2+} ions would be coordinated by two oxygen anions. Thus $\approx$ 10 moles NBO's are created from the lead ions.

Total molar oxygen content in glass S1 is $\approx$ 193. Thus, the molar NBO content is estimated to be (22/193), or about 11 mol % NBO.

There is a possibility this glass is phase-separated on a very small scale. Phase separation occurs for alkali-silicate glasses when total alkali is less than about 20 mol %.[60] The presence of Pb^{2+} and Al^{3+} would help prevent this. According to the manufacturer, this glass phase-separates when heated to $\approx$ 600 °C. The highly variable behavior with regards to median-radial crack initiation observed may be the result of slight inhomogeneity in the glass. Recall the other 'anomalous' glasses, i.e., S2, 7740 Pyrex™ borosilicate, did not form median-radials on loading. Glass S1 had 30% of tests form all median-radials on unloading; 20% of the remaining 70% of the tests had all median-radials on loading; the other 50% of the tests had some median-radials initiate on loading and some on unloading. This was the most variable behavior of all the glasses. Slight variations in composition (structure) with indentation location may be the reason for this.

4.10.2 Glass S2 (Zinc-Silicate Crown)

Approximate Composition (Mol %): $67SiO_2 \bullet 7Na_2O \bullet 10ZnO \bullet 11B_2O_3 \bullet 6Al_2O_3$

The majority component is silica, making up most of the three-dimensional network backbone. However, based on this glass's 'anomalous' behavior, this amount is not as high as expected. This suggests that other components act as network formers in 4-fold coordination in this glass. The boron and

aluminum oxides are likely candidates. The 14 moles of Na^+ can charge compensate a total of 14 moles of $(B^{3+}+Al^{3+})$ ions, i.e., convert B_3 to B_4 to form BO_4^- tetrahedra, and to form AlO_4^- tetrahedra by the same process, the remainder of B is assumed to be in 3-fold coordination, and any aluminum ions are assumed to act as modifiers in octahedral (6-fold) coordination with oxygen.[35] These extra Al^{3+} ions each create three NBO's.[35] For the sake of calculation, it will be assumed all Na^+ ions are associated with the boron ions. This means that 12 moles Al^{3+} create $\approx$ 36 moles NBO's. Zinc oxide can also act as a network former, though its usual role is that of a modifier.[71] In this sense, the zinc-oxide is expected to create NBO's. The possibility exists, however, that each Zn^{2+} can charge compensate additional BO_4^- and AlO_4^- tetrahedra, in a sense making the glass more 'anomalous' and increasing its 'openness.' However, the fact that large ring-cone cracks did not form as readily as in v-SiO_2 suggests there is some 'normal' character to this glass, provided by NBO's. Thus it will be assumed the 10 moles of Zn^{2+} create 20 moles NBO's. Total molar oxygen content is $\approx$ 202 moles. The total NBO content is $\approx$ 58 (36 + 20). This means the mol % NBO is $\approx$ (58/202)*100 is $\approx$ 29%. This is not a conservative value, and represents a high limit to the mol % NBO, since it assumes all ZnO acts as a network modifier. The mol % NBO should be higher than in glass S1, consistent with the decreased tendency to form well-developed ring-cone cracks at 3.5 Kg maximum load compared to glass S1.

4.10.3 Glass S3 (Barium-Borosilicate Dense Crown)

Approximate Composition (Mol %): $44SiO_2 \bullet 27BaO \bullet 25B_2O_3 \bullet 6Al_2O_3$

The single major constituent is still silica, but a significant amount of boron and barium oxides exist. Thus, this glass is a barium-borosilicate glass containing a minor amount of alumina. The network backbone structure is formed by both silica and boron oxide. The barium ions are seen as network modifiers. The aluminum may act as modifier or former, and helps prevent devitrification in this composition. Zhao et al.[72] studied the structure of barium-borosilicate glasses, concentrating on the distribution of NBO's, using ^{17}O magic-angle spinning (MAS) and triple-quantum (3QMAS) nuclear magnetic resonance (NMR) spectroscopy. Compositions studied ranged from, in mole %: (24-45 BaO)$\bullet$(30-60 B_2O_3) $\bullet$(24-55 SiO_2). Several key findings include:[72]

(i) Ba^{2+} forms NBO's on both Si and B sites, i.e., Ba-O-Si, and Ba-O-B.

(ii)   The silicon and boron networks are likely highly mixed together.

(iii)   Most of the Ba^{2+} goes to convert B_3 to B_4; however, some forms NBO's. The higher field strength of Ba^{2+} compared to Na^+ in sodium borosilicate glasses, promotes the formation of NBO at lower concentrations of modifier.

In principle, 27 moles of Ba^{2+} can (i) create either 54 moles NBO's, (ii) convert the 50 moles of B_3 to B_4 and create 4 moles NBO's randomly distributed on B

and Si sites, or (iii) any combination of the above. In this particular glass, the Ba/B ratio is ≈ 0.54. According to structural models for sodium borosilicate glasses, when the molar ratio Na/B is < 0.5, the sodium ions likely convert B_3 to B_4.[35,73] When Na/B is > 0.5, and depending on the ratio Si/B, some of the Na begins to create NBO's, and the B_4 decreases. This transition occurs at higher values of Na/B as the ratio Si/B increases. For glass S3 the Si/B ratio is ≈ 0.88, which is on the high side. It may thus be expected that most of the Ba^{2+} in this glass converts 3-fold boron (B_3) to 4-fold (B_4). This of course assumes the structural role of Ba and Na are similar. Zhao et al.[72] have shown that, to a first approximation, this is correct. However, they also found that the stronger field strength of the Ba^{2+} ion, compared to Na^+, distorts the structure around it more, which in addition to helping glass formation, may cause the Ba^{2+} to not follow the same 'rules' as Na^+ in borosilicate glass. Nevertheless, to a first approximation it will be assumed that 25 moles of Ba^{2+} converts all 50 moles of boron to BO_4. The remaining 2 moles of B^{2+} create 4 moles NBO's randomly distributed on the silicon sites. In principle, some could be used to charge compensate AlO_4; however, it is assumed that the 6 moles of Al^{3+} create ≈ 18 moles NBO. For this glass the total molar oxygen content is ~ 208 moles. The total NBO content is ≈ (4+18) 22 moles. Thus, the mole percent NBO content is ≈ (22/208)*100, or 11 mole %. The barium ions probably occupy interstices created by the SiO_4 and BO_4^- groupings. The relatively high density and low

atomic molar volume support this. The relatively high Vickers hardness, Young's modulus, and Tg of this glass support the notion that a majority of the boron is 4-fold coordinated, with charge compensation provided by the Ba^{2+} ions. If this were not so, it is likely the very low silica content of this glass ($\approx$ 44 mol %) combined with BO_3 groups, and formation of many NBO's on the silica sites (possibly boron sites as well) from the barium ions, would not yield a rigid glass. It is known that increasing the coordination of boron from 3- to 4-fold increases Vickers hardness and softening temperature in sodium borosilicate glasses.[74]

4.10.4 Glass S4 (Lead-Borosilicate Dense Flint)

Approximate Composition (Mol %): $13SiO_2 \bullet 58PbO \bullet 22B_2O_3 \bullet 6Al_2O_3$

This glass is a lead borosilicate containing a small amount of alumina. The alumina helps increase resistance to chemical attack, and devitrification, and it increases hardness. The major constituents accounting for $\approx$ 80 mol % are PbO and B_2O_3. Structural studies on lead-borate glasses have shown that for low Pb contents ($< \approx 20$ mol %), the Pb^{2+} acts as a network modifier converting boron into 4-fold coordination.[75] It also acts as a modifier in silica glasses for $< \approx 30$ mol % PbO, but can also be coordinated by two oxygen's as -Si-O-Pb-O-, for example, and not create NBO's.[75] At higher concentrations lead is a glass network former; this must certainly be so in the current glass, otherwise no solid glass could form with such low concentration of silica and

boron oxide. High-lead-oxide-containing glasses contain distorted PbO_4 pyramids, with the lead ion situated at the apex of the pyramid.[35,60,70] This is different from SiO_4 tetrahedra, where the cation (Si^{4+}) sits in the center.[60]

The SiO_4 tetrahedra are most likely dispersed among the PbO_4 network. It is also possible that some of the lead ions convert some boron to 4-fold coordination, in which case the PbO_4 would tend to associate with BO_3 more than BO_4.[70] Aluminum ions may act as network modifiers, forming NBO's. It is also possible they enter as network formers, with some of the Pb^{2+} providing charge compensation. The high polarizability and overall weak bonding of the lead ions creates a structure that is easily deformed. This is evident in the mechanical and thermal characteristics of this glass: Low Vickers hardness, low Young's modulus, high thermal expansion coefficient ($\approx$ 9.8 $x10^{-6}$/K) and low Tg. A two-dimensional chain-like structure most likely exists in this glass, with some cross-linking of chains by silica tetrahedra, boron tetrahedra, and van der Waals forces. Unlike the SiO_4 tetrahedra where each Si shares only one O with its neighbor, in PbO_4 units two O's are shared between each Pb^{4+} ion, which limits the dimensionality.

4.10.5 Glasses S5, S6; NS1 (Lanthanum-Borate Crown; Flint)

Approximate Compositions (Mol %):

S5: $8SiO_2 \bullet 6ZrO_2 \bullet 27CaO \bullet 51B_2O_3 \bullet 18La_2O_3$

S6: $6SiO_2 \bullet 6ZrO_2 \bullet 10CaO \bullet 7ZnO \bullet 60B_2O_3 \bullet 13La_2O_3$

NS1: $6ZrO_2 \bullet 5ZnO \bullet 60B_2O_3 \bullet 18\ La_2O_3 \bullet 7Y_2O_3 \bullet 5Nb_2O_5$

These glasses are similar in that they all contain significant amounts of boron oxide and lanthanum oxide, which together account for greater than 69 mol %. The glasses are thus modified versions of lanthanum-borate glasses. Glasses S5 and S6 contain some silica, whereas glass NS1 does not.

It is well known that homogeneous binary lanthanum borate glasses can be formed for lanthanum oxide concentrations greater than $\approx$ 20 mol %.[76] Although glasses S5, S6 and NS1 may contain less than this amount, they were clear and homogeneous after annealing, i.e., no phase separation was visibly apparent. The presence of the other cations most likely helps prevent phase separation by making mobility of ions more difficult.

The structure of lanthanum borate glasses in the metaborate (LaB_3O_6) compositional range is thought to consist of similar structural entities found in the crystalline metaborate (LaB_3O_6 -c).[76,77] These entities are a borate network consisting of infinite $(B_3O_6)_\infty$ chains which contain BO_4^- and BO_3 groups. Each BO_4^- group is thought to be bonded to four BO_3 groups. Randomness in the B-O bond angles generates the disorder characteristic of the amorphous state. Two oxygen atoms of the BO_3 groups link adjacent BO_4^- tetrahedra along a chain, while the third is believed to link adjacent chains in the third dimension by covalently bonding with other boron atoms, increasing the connectivity of the structure.[76] The lanthanum ions are seen as network modifiers helping connect the boron chains, having a coordination number of

around 10 with respect to oxygen.[76] Charge compensation of the BO_4^- units would be by the lanthanum ions as well. It is clear that because of the high T_g, Vickers hardness, and Young's modulus of the current glasses (S5, S6, NS1), the lanthanum ions cannot be creating many NBO's. In this sense, lanthanum may be better classified as an intermediate.

For glasses S5 and S6 the silica probably forms SiO_4 tetrahedra that are randomly dispersed in the borate network, which helps increase connectivity. The zirconia (ZrO_2) can also assume a network-former role. It has a relatively high field strength and can increase connectivity.[35] Again, it is not expected that the calcium ions in glasses S5 and S6 contribute to the formation of a large number of NBO's, from the evidence given earlier, i.e., high Vickers hardness, high T_g, and high Young's modulus. It seems more likely that the Ca^{2+} charge compensate BO_4^- tetrahedra, filling in the interstices and creating a more rigid, densely packed, and strong structure. The exact details are unknown, however. The ZnO may play a similar role as the CaO in glass S6.

The small amount of Y_2O_3 in glass NS1 likely assumes a similar role as does Al_2O_3 in Al_2O_3-La_2O_3-SiO_2 glasses, i.e., 4-fold coordination for relatively small amounts.[78] This structural role of aluminum would help increase the connectivity of the structure, and agrees with the high hardness, Young's modulus, and T_g of this glass. The similarity in glass transition temperature, Vickers hardness, Young's modulus, and fracture toughness of these three

glasses suggests their structures are similar, which is not surprising given the similarities in composition. All three glasses are relatively well-connected, densely-packed (low atomic molar volume), refractory glasses, possessing high elastic and deformation properties, but correspondingly low fracture resistance.

4.10.6 Glass NS2 (Potassium-Phosphate)

Approximate Composition (Mol %): $23K_2O \bullet 7Al_2O_3 \bullet 6La_2O_3 \bullet 64P_2O_5$

This glass is primarily a potassium phosphate glass (≈ 87 mol %) with some lanthanum and aluminum oxides. The structure of phosphate glasses is fairly well-known.[79,80,81,82] The molar ratio of oxygen to phosphorous in this glass is approximately 3:1, classifying this glass as an ultra phosphate.[79] Vitreous P_2O_5 contains three covalent bridging-oxygen bonds and one terminal- oxygen (TO) bond that is double bonded to the phosphorous and hence non-bridging. In theory the fraction of PO_4 tetrahedra having 3 BO's (Q_3) is 100% in v-P_2O_5. The TO bond is significantly shorter than the BO bond.[79] The basic building block is the PO_4 tetrahedron. The presence of the terminal-oxygen bond results in a structure that is much less rigid than if all oxygen's were bridging. It is believed that the structure of the pure glass former is a layered sheet-like structure, similar to that of v-B_2O_3, and hence is easily disruptable, resulting in low Tg and Vickers hardness, for example.[60,79] It may consist of 6-membered rings arranged in folded sheets.[79]

Initial additions of alkali, up to $\approx$ 20 mol %, are known to create NBO's on the PO_4 tetrahedra, depolymerizing the structure and lowering Tg.[79,80] However, further increases in alkali cause an increase in Tg up to about 50 mol %.[80] Reasons for this are not completely understood, but the alkali may serve as links between terminal oxygens of neighboring PO_4 tetrahedra, increasing the connectivity of the structure.[35,80] In the current glass, there is $\approx$ 23 mol % K_2O. It is likely most of the K^+ ions create just NBO's, i.e., only convert PO_4 Q_3 to PO_4 Q_2, but some may take part in cross-linking the structure as well. If there are some linear chains of PO_4 in this glass, the Al_2O_3 may form $AlPO_4$ units on these chains, in which case charge neutrality is satisfied, since the (8-) charge on the oxygens is balanced by the (8+) charge on the Al^{3+} + P^{5+} ions. Presumably, the La^{3+} ions may behave the same. The relatively low Tg of this glass ($\approx$ 520 °C), low Vickers hardness, low Young's modulus, high thermal expansion coefficient ($\approx$ 13.4 x10^{-6}/K), and low fracture toughness, suggest a glass that is loosely bonded, easily deformable, and having low resistance to fracture. The low density ($\approx$ 2.57 g/cc), very high molar volume ($\approx$ 48.4 cm^3/mol glass), and relatively high atomic molar volume ($\approx$ 8.62 cm^3/mol atoms) also suggests that this glass structure contains sizeable free interstitial volume. Assuming that 20 mol % of the K_2O creates NBO's, the molar percent NBO content for this glass is about (40/382)*100, or about 10 mol % NBO.

4.10.7 Glass NS3 (Fluoride Crown)

Approximate Composition(Mol%):

$6CaO \bullet 7P_2O_5 \bullet 9LiF \bullet 8CaF_2 \bullet 9MgF_2 \bullet 12BaF_2 \bullet 26SrF_2 \bullet 23AlF_3$

This glass is predominantly composed of fluoride components, with some, ≈ 13 mol %, additions from CaO and P_2O_5. It is considered a halide glass since the majority anion component is a halide element, i.e., fluorine. It could also be called a heavy-metal fluoride glass, though not a traditional type.[35]

The bonding in fluoride glasses is predominantly ionic due to the high electronegativity of the fluorine ion.[35,83] The structures of these glasses are not as well known as for some of the silicates, with perhaps the exception of the zirconium-fluoride glasses. In binary ZrF_4-BaF_2 glasses, the structure is composed of ZrF_7 and ZrF_8 polyhedra, in which the Zr^{4+} are coordinated by between 7 and 8 F^{2-} anions, in which edge sharing of polyhedra occurs.[83] A 3-D network based on these polyhedra is formed. The Ba^{2+} ions act as modifying cations, residing in the interstices between polyhedra, providing charge compensation on non-bridging fluorine's (NBF's), and helping hold the polyhedra together.

Glass NS3 consists of a wide array of components, the majority of which are AlF_3, SrF_2, and BaF_2. In AlF_3-based glasses, where the majority component is AlF_3, it is known that AlF_6 octahedra are the basic structural units. In glass NS3 no one single component is present in a large enough molar amount to have any such basic structural unit, as those presented

above for aluminum and zirconium, dominate the structure. Kawamoto and Horisaka[84] studied the structure of several barium, lead, and strontium metafluorozirconate glasses (50 mol % ZrF_4) and concluded that Zr ions are coordinated by eight fluorine ions, and Ba and Pb by ten. Chains of edge-shared ZrF_8 polyhedra were believed to have formed, and are ionically bonded together with the Ba, Pb, and Sr ions. It is most likely that glass NS3 consists of chains of fluoride molecules, randomly oriented and held together by ionic bonds. Since approximately 50 mol % of the glass is composed of AlF_3 and SrF_2, it is likely these components influence the structure the most. However, the nature of the structural units in the glass is unclear. Since no crystallization is apparent in this glass, the 'confusion' principle in which numerous cation components all compete for the same anion, so there is no strong anion arrangement by any one cation, possibly leads to glass formation.

4.10.8 Float Glass (Commercial Soda-Lime-Silicate)

Approximate Composition (Mol %):

$70.3SiO_2 \bullet 0.4Al_2O_3 \bullet 9.3CaO \bullet 6.1MgO \bullet 13.7 Na_2O \bullet 0.1K_2O$
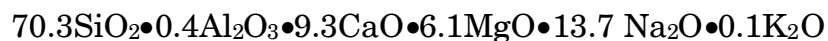
This glass is a commercially produced glass in the soda-lime-silicate family. The silica forms the 3-D network connectivity, modified by the alkali and alkaline-earth cations, which create NBO's.[35,85] The small amount of alumina helps prevent devitrification and increases chemical durability. The

molar percentage of NBO's can be estimated by noting that each mole of R^+ and R^{2+} yield one and two moles of NBO's, respectively. In addition, each mole of Al_2O_3 is expected to consume 2 moles of NBO's. Taking these factors into account, the approximate molar percentage of NBO is $\approx (57.6/171)*100 = \approx 34$ mol % NBO.

4.10.9 7740 Pyrex™ Borosilicate (Sodium-Borosilicate)

Approximate Composition (Mol %): $81SiO_2 \bullet 2Al_2O_3 \bullet 13B_2O_3 \bullet 4Na_2O$

This is a commercial sodium-borosilicate glass, produced by Corning Inc., with the trade-name Pyrex™. The primary constituent of this glass is silica, with over 80 mol %, hence this glass behaves 'anomalous.' This glass is known to be phase separated on a nano-scale, and so appears transparent to the naked eyed. A continuous silica-rich phase (≈ 96 %) with droplets of a sodium-borate-rich phase develops. The latter droplet phase is about 20 to 50 Å in size.[35] Any alkali present in the silica-rich phase presumably creates NBO's. Alkali in the borate-rich phase probably converts boron from 3- to 4-fold coordination.

4.10.10 Suprasil 312 (Synthetic Vitreous Silica)

Approximate Composition (Mol %): $100SiO_2$

Vitreous silica is the prototypical 'anomalous' glass. The structure is based on silica tetrahedra (SiO_4) connected at their corners. The randomness of structure results primarily from the variation in the Si-O-Si bond angles

between tetrahedra.[35] The openness of the structure is evident in its relatively high molar volume (~ 27 cm^3/mol) and low density (~ 2.2 g/cm^3).

The Suprasil 312 vitreous silica is prepared from a synthetic raw material which is subsequently fused in a flame. The raw material is prepared by flame hydrolyzation of silicon tetrachloride ($SiCl_4$) in an oxygen-hydrogen flame.[86] Impurities in the final glass are chlorine and OH ions. According to the manufacturer of this glass, the OH content is ~ 216 ppm, and the Cl content is about 2000 ppm. This means the glass contains roughly 216 μg of OH and 2000 μg of Cl per one gram of glass. The OH depolymerizes the silica network causing mechanical weakening and lowering of viscosity, for example.[86]

4.11 G/K Crack Initiation Diagram

The crack initiation behavior of the current glasses in terms of whether they exhibited median-radial crack initiation on loading is shown in Figure 148. The G/K ratio is plotted as a function of the normalized amount of RO_2 i.e., $\mathbf{RO_2}$ = RO_2/(RO+R_2O). Glasses S3, S4, S5, S6, NS1, NS2, and NS3 all have $\mathbf{RO_2}$ values of less than ≈ 1.8 and values of G/K less than ≈ 0.6. In this plot $\mathbf{RO_2}$ represents either SiO_2 or ZrO_2. For the Wagner glasses[9] $\mathbf{RO_2}$ represents only SiO_2. All of these glasses exhibited median-radial cracking early on the loading cycle for the 1 Kg tests. In particular, glasses S4, NS1,
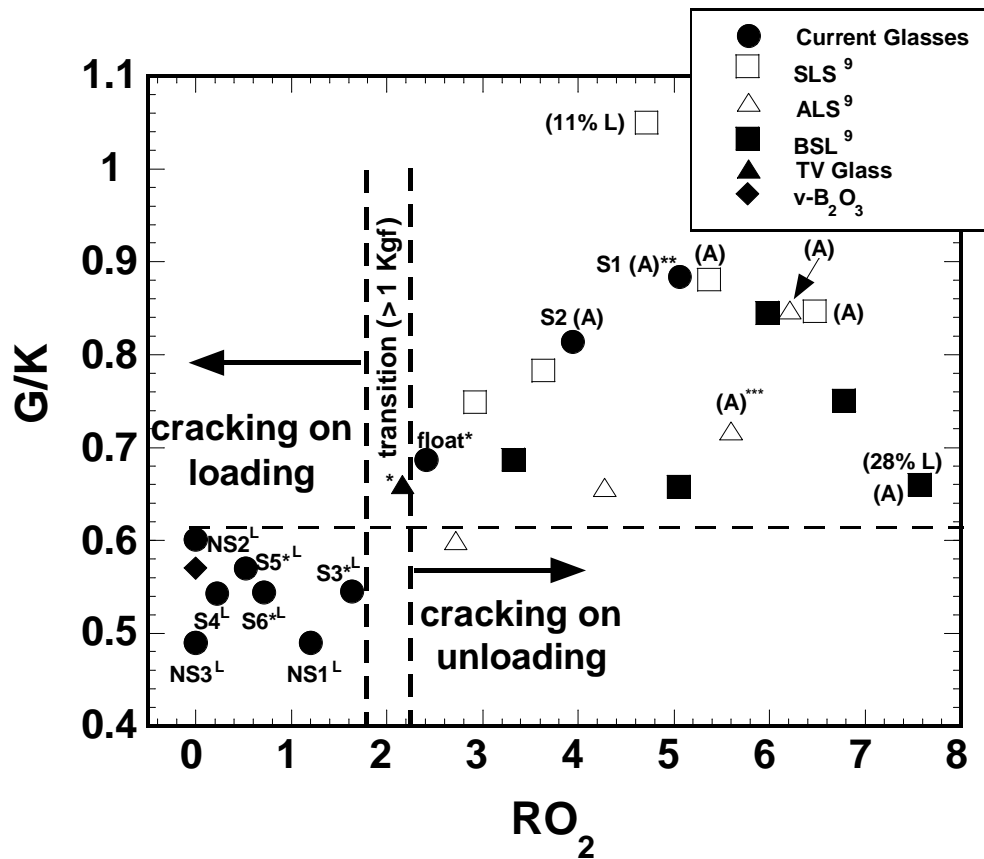
Figure 148. *G/K crack initiation diagram illustrating how, in general, the glasses with low **RO₂** and low G/K ratios have greater propensity for median-radial cracking on loading compared to glasses with higher values of these quantities, which have greater propensity for cracking on unloading. Glasses with superscript 'L' also had lateral crack formation on loading for loads up to 4 Kg. For complete description of graph and symbols see text.*

NS2, and NS3 had all median-radial cracks initiate on loading for all the 1

Kg tests. Glasses S3, S5, and S6 also had median-radial cracks initiate on

loading; however, not all of the median-radial cracks initiated for the 1 Kg

maximum load. For these three glasses, increasing the maximum load to 4

Kg resulted in the initiation of all median-radial cracks on loading, and thus

are indicated with an asterisk (*) because of this transition dependence on the maximum load. In addition, for glasses S5 and S6, 100 % of the tests had at least one median-radial crack initiate on loading, whereas for glass S3 only 50 % of the tests had median-radials initiate on loading. The higher RO_2 and G/K ratio of glass S3 suppressed the initiation of median-radial cracks relative to glasses S5 and S6. Glass NS1, although having a slightly higher RO_2 than glasses S5 and S6 had a lower G/K ratio, which is believed to increase the propensity for median-radial cracking, as will be discussed shortly. In addition glass S3 had the first median-radial cracks initiate at a substantially higher load ($\approx$ 817 g) relative to glasses S5 and S6 ($\approx$ 311 and 482 g, respectively).

Another important feature is that glasses S3, S4, S5, S6 (a few were observed for the 4 Kg tests, however none at 1 Kg), NS1, NS2, and NS3 all had lateral cracks form, to differing extents, for testing up to 4 Kg. In particular, glasses S4 and NS3 had the most well-developed lateral cracks for testing up to 1 Kg.

A TV funnel glass was tested with the recording microindenter up to a 4 Kg load. This glass was composed of mainly silica and lead oxide, with lesser additions of alkali and alkaline-earth oxides. The specimen was ground, polished, and annealed like the others. Testing conditions were 24°C and 41% RH. First median-radial cracks initiated in this glass at 1461 ± 807 g, for 90% of the tests. In one test all median-radials initiated on loading. This

glass is located in the 'transition (1 Kgf)' region on the diagram, indicating a transition took place from no cracking to cracking, but this occurred at > 1 Kgf. Recall the float glass also initiated median-radial cracks in 20% of the tests on loading, around 3500 grams load. Thus glasses having RO_2 within 1.8 to 2.4, are expected to have a transition to median-radial cracking on loading, but at higher loads compared to glasses with lower RO_2. In addition, no lateral cracks formed on loading for the TV glass, or float glass for that matter. It is apparent that as RO_2 increases from zero the propensity for median-radial cracking on loading, in general, decreases. Glass S2 in the current work was anomalous, but did not initiate median-radial cracks on loading for loads up to 3.5 Kg. Glass S1, although having median-radials initiate in 70% of the tests on loading, also had a significant number of tests initiate cracks on unloading, 50%. In addition, 30% of these latter tests had all median-radials initiate on unloading. This glass is indicated with a double asterisk (**) because of this behavior. This was not observed for any of the tests on glasses S4, S5, S6, NS1, NS2, or NS3. Two Wagner glasses[9], one a SLS and the other a BSL, had a low percentage of tests initiate median-radials on loading, 11% and 28% respectively, according to his data. The latter BSL glass was 'anomalous,' while the former SLS glass was 'normal.' From the diagram, it is seen that increasing the RO_2 to greater than ~ 4, in addition to making 'anomalous' behavior via ring-cone cracking more probable, can also make median-radial cracking on loading more likely.

However, it should be stressed that the frequency of median-radial cracking is still greatly reduced compared to the glasses below the transition region, and only a few glasses exhibited median-radials on loading. In addition, no median-radial cracks were seen on loading for the ALS series of glasses. Vitreous silica cannot be represented on this diagram because it would have a very high RO_2 value. Although median-radials were observed to form in a few tests up to 1400 g by Wagner[9] and at $\approx$ 983 g on loading by Cook and Pharr[11], these cracks are small, and in addition, more median-radials initiate on unloading. In this respect, the overall tendency to median-radial cracking in vitreous silica is still diminished compared to glasses below the transition region on the diagram. Also, the threshold for median-radial cracking observed after unloading was greatest for vitreous silica, glass S1, and glass S2 compared to the other glasses. All of this suggests that 'anomalous' glasses, in general, have reduced tendency for median-radial cracking compared to glasses with low RO_2, i.e., below about 1.8 or so. The triple asterisk (***) sign on 'anomalous' glass ALS designates this glass showed a transition to ring-cone cracking for 100% of the tests as the load was increased from 1.4 to 4 Kg, and was the only 'anomalous' Wagner glass[9] examined in the current work to do so. The 7740 Pyrex™ borosilicate glass is not represented on this diagram because it had a RO_2 value of 20.25, and would have significantly compressed the other data points. Recall this 'anomalous' glass initiated median-radials on unloading, and had G/K = 0.75.

Lastly, vitreous B_2O_3 is predicted to initiate median-radial cracks early on loading, based on its position on the diagram. In-situ observation was not possible on this glass to confirm this, however.

4.12 Crack Initiation Threshold Loads vs. RO_2

As shown in Figure 149 there was decent correlation between the median-radial crack initiation load on loading and the **RO_2** content for the 'normal' glasses. As the **RO_2** content increased, the initiation load generally increased for the 'normal' glasses. The 'anomalous' glass S1 does not fit this trend. In general, the glasses with higher **RO_2** content also had lower median-radial initiation loads on unloading, although the trend was not as convincing.

4.13 Explanation for Crack Initiation Behavior

4.13.1 The Role of G/K

It was discussed earlier that glasses with relatively high G/K ratio (G/K > 0.65) tended to exhibit a deformation response that was more compaction-controlled, while glasses with lower G/K ratios undergo more shear-'flow'-controlled deformation. All of the glasses that initiated median-radial cracks
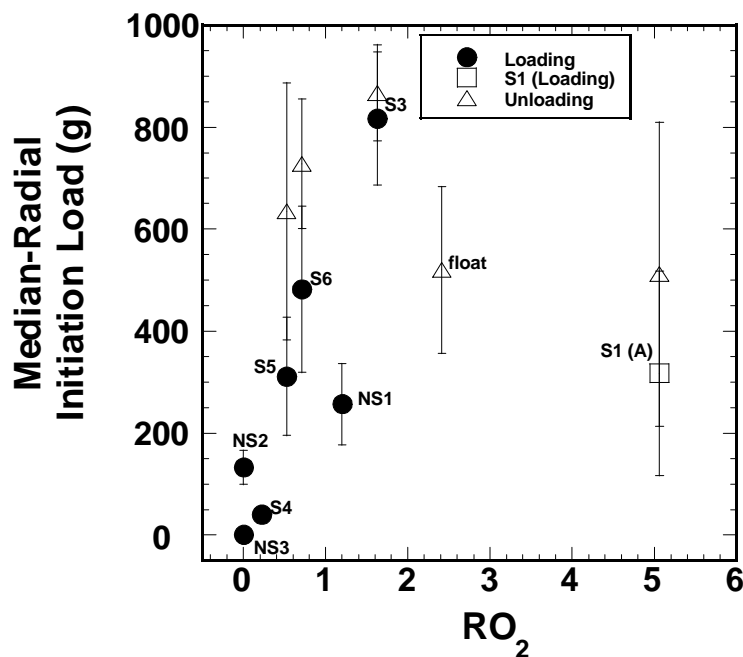
Figure 149. *The variation of initiation load, on loading and unloading, for the first median-radial cracks, as a function of RO₂.*

early on loading in the current work (S3, S4, S5, S6, NS1, NS2, NS3), with the exception of glass S1 and possibly vitreous silica, have low G/K ratios, i.e., G/K < 0.601. All of these glasses had low values of **RO₂**. The **RO₂** content, primarily in the form of SiO_2, but also ZrO_2, leads to open structures with rigid bonds. Glasses with low values of **RO₂** have structures that are more inclined to shear as opposed to hydrostatic compression. The structural descriptions and mechanical properties/characteristics of the different glasses put forth earlier is consistent with this viewpoint.

It is hypothesized that the tendency for those glasses with low **RO₂** to have wanted to shear, and hence change shape beneath the indenter on loading, caused extremely large strains and stresses, resulting in the observed

median-radial crack initiation at low loads. Lower values of fracture surface energy would possibly make it even easier for crack nuclei to form via material separation, and would also help account for the very low initiation loads observed in glasses S4, NS2, and NS3 in particular. For glass NS3, median-radial cracks were observed to initiate nearly instantaneously on loading, indicating the material at the corners of the Vickers diamond was immediately parted as soon as the indenter made contact. This glass had the second-lowest value of fracture surface energy, next to glass S4, which had the lowest, and which initiated median-radial cracks at the next lowest load on indenter loading, ~ 40 g. The indentation diagonals locally elevate the tensile stresses, and so cracks propagate more or less parallel to them.

4.13.2 The Role of E/H_V

According to Lawn et al.[20] the configurational strain (δ) varies as the volume of the plastic zone (V_p) to the volume of the indentation (V_i), which in turn varies as the ratio of plastic zone size (b) to indentation size (a), i.e., $\delta \approx V_p/V_i \approx$ (b/a). According to Hill's solution[87] for the expansion of an internal spherical cavity in an infinitely large elastic-plastic material, the quantities (b/a) and E/H_V are also related (Hill used the term 'c' to represent the extent of plastic deformation, not 'b', hence Hill used 'c/a' in his analysis). Hence, V_p/V_i and E/H_V should also be related. The following expressions can be used for the case of sharp indentation:[20,87]

$$\frac{V_p}{V_i} \approx \left(\frac{b}{a}\right)^3 \cot\Psi \tag{27}$$

$$\frac{b}{a} \approx \left(\frac{E}{H}\right)^{1/2} (\cot\Psi)^{1/3} \tag{28}$$

$$\frac{V_p}{V_i} \approx \left(\frac{E}{H}\right)^{3/2} (\cot\psi)^{1/3} \tag{29}$$

where,
V_p = volume of plastic zone beneath indentation
V_i = volume of indentation
b = plastic zone radius
a = indentation radius = d/2 (where d = diagonal length)
Ψ = indenter half angle (68°) for Vickers diamond

Equations 27 and 28 were combined to yield Eq. 29. To check the validity of Eq. 29, the volumes of the plastic zones beneath the indentations were calculated assuming the plastic zones were hemi-spherical in shape. The cross-sections of the indentations show that to some extent this is true, although some cross-sections appeared more cone-shaped than others. The depth of the plastic zones (see Table XXXIII) were taken as the radii of the spheres. The volumes of the plastic zones were then assumed to be one-half the volume of the sphere i.e.,

$$V_p = \frac{1}{2}\left(\frac{4}{3}\pi r^3\right) \tag{30}$$

where,

r = depth of plastic zone

The plastic zone volumes were then normalized to the indentation volumes. The latter were previously calculated from the depths and diagonal lengths of the indentations (see Table XXXVI). The data are shown in Table XXXIX (the indentation volumes are shown again in this table for easy reference). The normalized plastic zone volumes (V_p/V_i) range from 4.5 to 55.4. Although the actual values of relative plastic zone size may be brought into question, the relative ranking between the glasses is thought to be represented accurately. Figure 150 plots the normalized plastic zone volumes as a function of the ratio E/H_V (note that H in Eq. 28 and Eq. 29 is the Vickers hardness calculated using the *projected area* of contact i.e., $H = 2F/d^2$, and that H_V is the original (traditional) Vickers hardness number which uses the *actual area* of contact i.e., $H_V = 1.8544F/d^2$; however the difference between H and H_V is very small, the former being only about 8% higher). There is a clear indication that as the ratio E/H_V increases, the relative plastic zone volume increases. Recall E/H_V is related to the crack driving force in the fracture mechanics relation for indentation toughness (see Eq. 23 and Fig. 109).

Figure 151 is an E/H_V crack initiation diagram. As can be seen, glasses with $E/H_V > \approx 14$, in general, formed median-radial cracks readily on
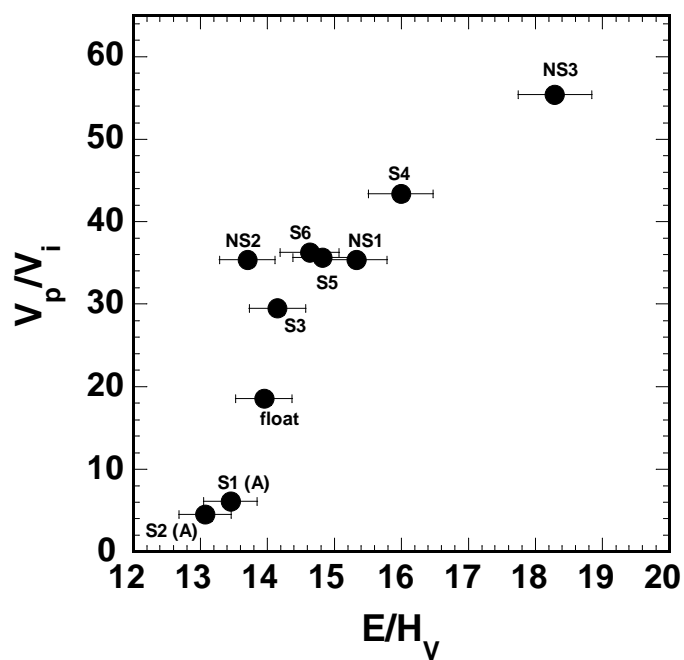
Figure 150. *The variation of the relative plastic zone volume (V_p/V_i) with the quantity E/H_V.*
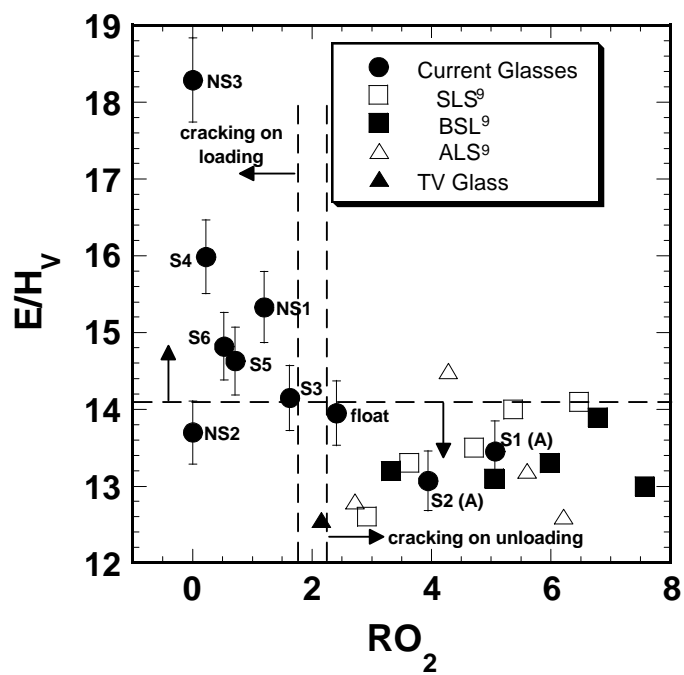
Figure 151. *E/H_V crack initiation diagram.*

Table XXXIX. Relative Plastic Zone Volume.

| Glass	Indentation Volume, V_i (μm^3)	'Plastic' Zone Volume, V_p (μm^3)	V_p/V_i
S1 (A)	3684	22,301	6.1
S2 (A)	3216	14,365	4.5
S3 (N)	2330	68,629	29.5
S4 (N)	8026	348,455	43.4
S5 (N)	2109	75,266	35.7
S6 (N)	2074	75,266	36.3
NS1 (N)	1936	68,629	35.4
NS2 (N)	5039	178,409	35.4
NS3 (N)	4726	261,799	55.4
float (N-A)	3038	56,549	18.6

loading. Note that the potassium phosphate glass (NS2) had slightly lower value of E/H_V than would be predicted based on its relative plastic zone size. These glasses also had low values of **RO$_2$**. Thus it appears that, in addition to providing driving force for *crack growth (propagation)*, the quantity E/H_V is also related to the tendency to *nucleate* median-radial cracks. Also, the glasses with highest values of E/H_V i.e., NS3 and S4, had significant lateral crack formation on loading. Recall that all the glasses with $E/H_V > \approx 14$ had some amount of lateral cracking on loading

As shown in Figure 152, there is also good correlation between V_p/V_i and the ratio G/K. This supports the notion that increased tendency to shear-'flow' should also give rise to greater relative plastic zone volumes.

However, as shown in Figure 153, there is no straightforward relationship between G/K and E/H_V, although in general, the glasses with the highest values of E/H_V tend to have the lowest values of G/K, and are the ones most susceptible to median-radial cracking under a sharp indenter.

4.13.3 Model of Crack Initiation Behavior

A model capable of qualitatively describing the general crack initiation behavior observed by the glasses in the current work is put forth. It is based on the concepts originally put forth by Lawn et al.[20] First, an elastic half-space is subjected to sharp indentation as shown in Figure 154. Here the material is under full-load. Now, suppose a half-space is removed in an un-indented portion of the same material (Fig. 150 (b)), of identical dimensions as that under full load. If this half-space is now indented while being supported underneath, under the same maximum load, as in Fig. 150 (c), it will undergo more lateral shape change because the elastic constraint of the surrounding matrix of glass is no longer present. This is shown in Figure 150 (c). Let the degree of lateral shape change be indicated by δ. In the next step, Figure 150 (d), a nearly hydrostatic stress is applied to the deformed half-space in order to return it to the dimensions in Figure 150 (b). This pressurized segment is then inserted into the removed half-space in Figure. 150 (b), and the 'hydrostatic' stresses removed. Some of the 'hydrostatic'
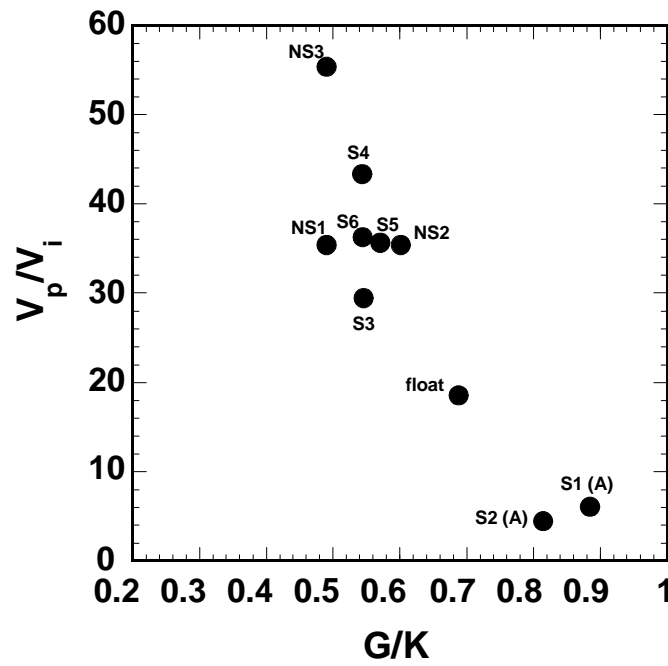
**Figure 152.** *The variation of the relative plastic zone volume with the quantity G/K.*
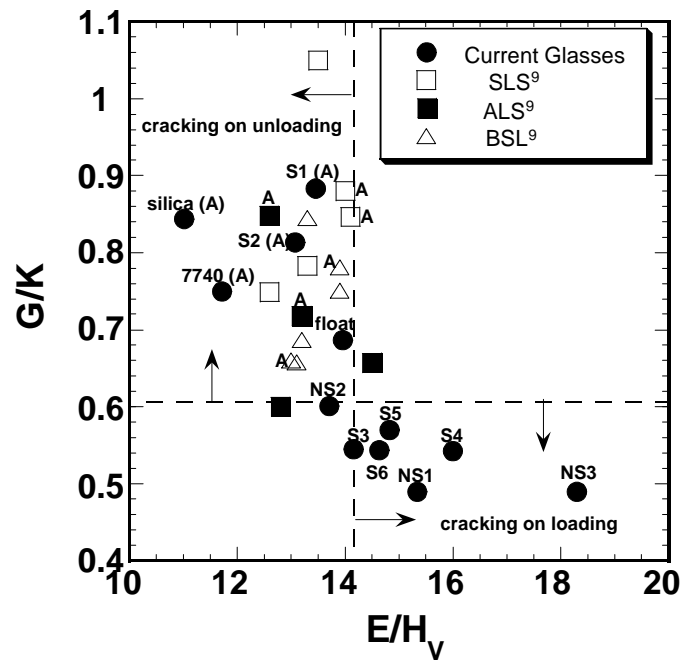
Figure 153. *The variation of G/K with E/H$_V$.*

stress will now relax from its maximum value, but not all of it. The 'plastic' zone will then be in a state of compression, but always wanting to expand outward to reach its equilibrium size. Along the interface between the 'plastic' and elastic zones the stresses will be highest because of strain incompatibility. Cracks are thus expected to initiate along the boundary.

It is hypothesized the glasses with low values of G/K, high values of E/H_V, and easily shearable structures, want to undergo greater shape change (larger δ), but are constrained from doing so by the surrounding elastic matrix. These glasses also tended to have the most densely packed structures, i.e., high density, low atomic molar volume, and low **RO₂**. This means these glasses have no choice, so to speak, but to change shape at more-or-less constant volume in order to accommodate the volume of the indenter, compared to more open structures which are capable of more densification (the one exception may be glass NS2 which probably has a rather open structure as indicated by its relatively high molar volume and low density, but because the structure shears easily due to its low shear modulus, intense strains (stresses) are generated nonetheless). This results in intense strains, and hence stresses, causing median-radial cracks to initiate early on loading. The numerous fine shear faults within the deformation zones of these glasses, and the 'core' of broken-apart material, attest to this. This behavior encompasses all the glasses shown in the bottom left portion of Figure 148. The structural descriptions of these glasses given earlier also support these

statements. The strains are postulated to be especially intense for glasses NS3 and S4, since these glasses initiated well-developed lateral cracks on the loading cycle. All the glasses in the bottom left portion initiated lateral cracks on loading to varying extents as the load was increased to 3.5 or 4 Kg. Glass S3 had only 10% of the tests initiate lateral cracks on loading, which agrees with its relatively higher RO_2 content, more open structure, and hence relatively lower crack nucleation tendency and residual crack driving force compared to the other more 'normal' glasses. For the glasses with higher RO_2 content (S1, S2, float, 7740 Pyrex ™, v-SiO_2, and Wagner's glasses[9]) the crack nucleation tendency and residual crack driving force are reduced because of the more open structures of these glasses, which allows them to undergo relatively more compaction; i.e., they have a reduced tendency to want to shear and change shape beneath the indenter. This reduces the nucleation and residual crack driving forces, hence these glasses in general tend to initiate median-radial cracks on unloading. One exception is glass S1. This glass may not be entirely homogeneous. If regions rich in alkali exist, they may allow more flow, causing large strains and hence stresses to build. Lateral cracking on loading also did not occur in these glasses, including glass S1, which is testament to the overall reduced crack nucleation and driving force in these glasses.
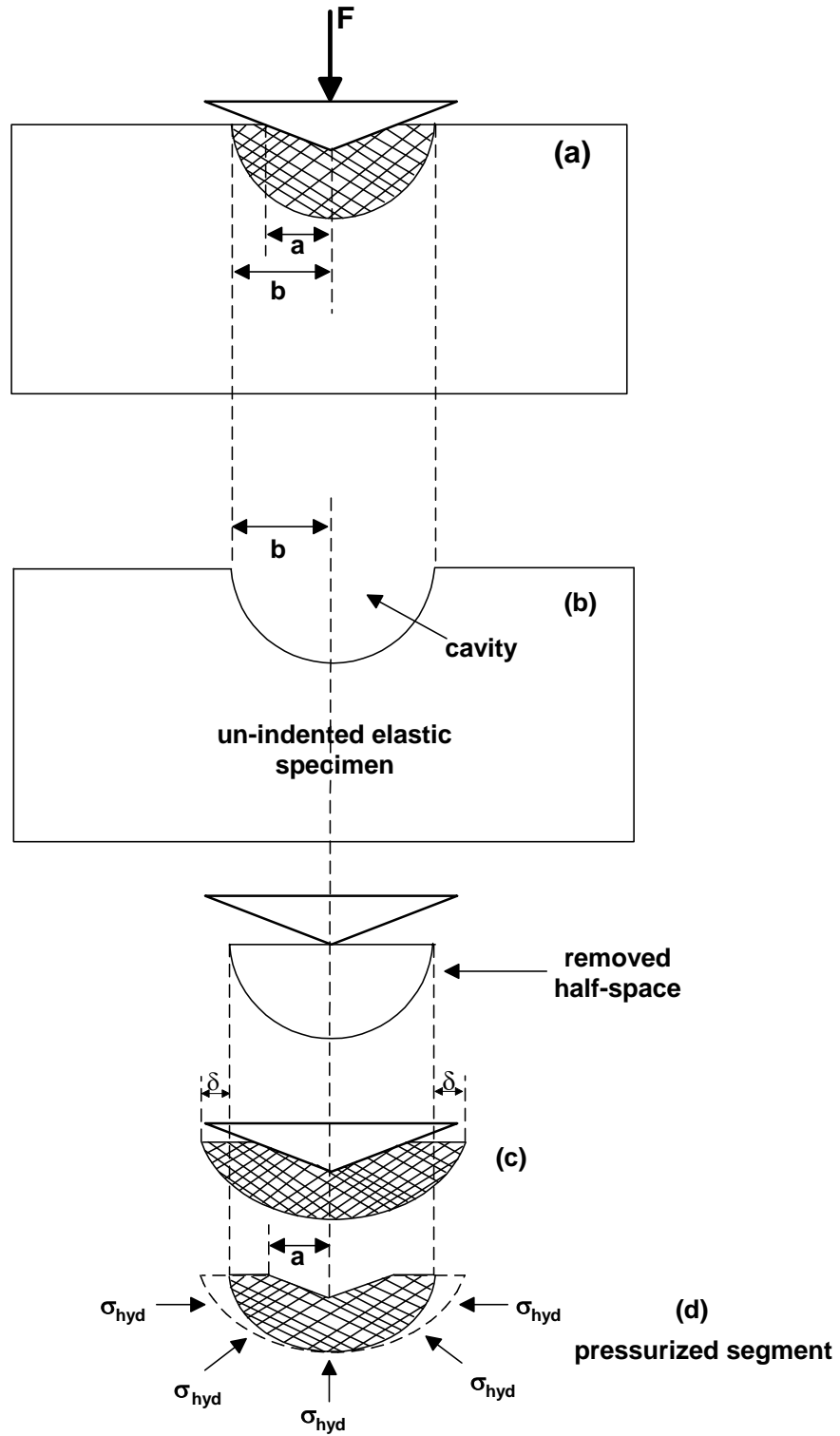
Figure 154. *Schematic illustrating the origin of the crack nucleation and crack driving forces caused by irreversible deformation. Based on concepts originally put forth by Lawn et al.[20]*

5.   SUMMARY

5.1   General Observations

The crack initiation behavior of nine optical glasses, float glass, 7740 Pyrex™ borosilicate, and Suprasil 312 vitreous silica glasses contacted with a Vickers diamond pyramid was investigated. It was found that the **RO₂**, which is the mol $RO_2/(RO+R_2O)$ ratio, had a large influence on the behavior of the glasses. This quantity, together with the G/K and E/H$_V$ ratios of the glasses, can account for the general behavior observed. For glasses S4 (lead-borosilicate dense flint), S5 (lanthanum-borate crown), S6 (lanthanum-borate crown), NS1 (lanthanum flint), NS2 (potassium phosphate) and NS3 (fluoride crown), median-radial cracks formed relatively early on the indentation loading cycle. These glasses are best classified as 'normal.' All of these glasses are characterized by low **RO₂**, low G/K, high E/H$_V$, and prefer to undergo shear rather than compaction. These glasses lack a well-connected three-dimensional network due to their limited amount of silica. Higher **RO₂** content was associated with higher median-radial crack initiation threshold on loading. The tendency for the plastic zone beneath these glasses to want to change shape, with consequent formation of shear fault lines, results in high strains and stresses, in turn causing easy median-radial crack initiation in these glasses. The barium-borosilicate dense crown glass, S3, had slightly

289

greater median-radial initiation resistance, presumably due to its higher RO_2 content provided by SiO_2. However, median-radials also initiated on loading for this glass at significantly higher loads compared to the other glasses. Glasses S4 (lead-borosilicate dense flint), NS2 (potassium phosphate), and NS3 (fluoride crown) had the least well-connected structures, and consequently the least resistance to median-radial crack initiation.

All the aforementioned glasses had lateral cracks initiate on loading, to differing extents. Glasses S4 and NS3 have the least well-connected structures, and underwent the most significant lateral cracking on loading. The strain (stress) mismatch at the elastic-plastic boundary is presumed to be so high in these glasses that significant lateral cracking can occur on loading.

Float glass could be classified as 'normal-anomalous,' since increasing the maximum load from 1 to 4 Kg resulted in some partial ring cracking, and also because a well-developed fault structure was not seen in the deformation zone. This was also observed in glass NS2 (potassium phosphate). Glass NS2 has a rather open structure (low density, high atomic molar volume). Presumably in both these glasses, increasing the maximum load resulted in increased elastic surface tensile stresses, causing the partial ring cracks to form. This may be explained by noting that, because of their relatively open structures (when compared to the other glasses), a portion of the deformation beneath the indenter is densification. When densification and shear flow can

no longer occur to a large extent, surface elastic tensile stresses start to build. Median-radial cracking occurred on unloading in float glass, consistent with its relatively high **RO₂** content, high G/K, and low E/H_V.

Glasses S1 (lead-alkali silicate crown), S2 (zinc silicate crown), 7740 Pyrex™ borosilicate, and Suprasil 312 are 'anomalous.' The deformation zones beneath glasses S1 and S2 lacked shear fault lines, consistent with the open network structures, low density, and high G/K values for these glasses. Whereas median-radial initiation was suppressed in glasses S2 and 7740 Pryex™ until the unloading cycles, median-radials initiated in glass S1 at relatively low forces. It is believed this glass may not be entirely homogeneous. Although the Suprasil 312 vitreous silica specimen underwent median-radial cracking on loading for loads > 1 Kg, the dominant crack system is the ring-cone, as it is for 7740 Pyrex™ as well. The slight amount of network modifier in the 7740 Pyrex™ suppresses median-radial initiation on loading compared to vitreous silica. The reduced crack driving stress in the 'anomalous' glasses is a result of their open structure. In addition, the median-radial cracks which did initiate on loading in Suprasil 312 did not extend much.

For the 'anomalous' glasses and float glass, the median-radial cracks appeared to be extensions of shear faults. The relatively open structures of these glasses results in severe (wide) shear faults forming. On unloading, these faults are the preferred sites for crack growth because of low constraint

at the surface. For glass S1, it was also shown that some median-radials appear to be extensions of shear faults, despite some of these cracks having initiated on loading. For the other 'normal' glasses, the median-radials appeared to extend from much closer to the corners of the indentations, and less likely from surface shear faults.

5.2 Effect of Loading Rate

Increased amounts of surface ring cracking were apparent for the 'anomalous' glasses S1 and S2 for tests with the faster loading rate of the conventional indenter. It is postulated the quicker loading rate allows less time for stress relief at the surface, causing elastic tensile stresses to be higher compared to slower rates.

For glass S2, the increased loading rate of the conventional indenter resulted in 100% of the indentations having median and lateral cracks initiate, compared to just 30% and 20%, respectively, with the recording microindenter. This was the most drastic effect of loading rate seen in the current work. The very fast rate of loading may cause more severe surface flaws and create increased driving force on unloading for crack extension, for both median-radial and lateral cracks. However, post-test optical microscopy of surface fault structure did not reveal any differences between the conventional and recording microindenter tests.

5.3 Effect of Maximum Load

Increasing the maximum load resulted in 'anomalous' crack initiation behavior for glasses S1 and S2, in which well-developed surface ring cracks formed. In addition, these ring-cracks were accompanied by well-developed cone cracks for a majority of the tests in glass S1, whereas for glass S2 only one test formed a well-developed cone crack. In addition, median-radial and lateral cracks initiated on unloading in all the tests for glass S2 at the higher load.

For glasses S3, S5, and S6, increasing the maximum load resulted in all median-radial cracks initiating on the loading cycle. In addition, lateral cracking on loading was more well developed for glasses S3, S5, S6, NS1, NS2, and NS3 at the higher loads. In addition, no evidence of 'anomalous' behavior was seen for all these glasses, except NS2, at the higher loads.

For the float glass, and glass NS2, evidence of partial ring cracking, i.e., 'anomalous' behavior, was seen at 4 Kg load. This suggests these glasses have some 'anomalous' character to them.

5.4 Median-Radial Crack Morphology

Based on the fractographic evidence of the cross-sections, and observations with the recording microindenter, what was believed to be two separate

median-radial cracks initiating on loading was in fact a single full-penny median-radial in glasses S3, S4, S5, S6, NS1, NS2, and NS3.

Following the initiation of this first crack, two other median-radials would initiate, but always at separate instances. The median-radials in glasses S4 and NS3 extended to the surface shortly after initiation on loading, whereas in glasses S3, S5, S6, NS1, and NS2 extension to the surface took place on unloading, due to slightly greater surface compression on loading. Depending on which side of the indentation is sectioned, either two in-plane median-radial cracks are observed, or a single full-penny median-radial. These conclusions are based on looking at numerous crack cross-sections, only a fraction of which were shown in the current work.

For all other glasses, the initiation of separate median-radial cracks appears to have occurred. One exception is the float glass. Some cross-sections showed a single full-penny median-radial crack to have initiated on unloading. Other cross-sections clearly showed two-separate cracks. Similar to the other glasses, the final crack geometry was half-penny.

6. CONCLUSIONS

1. The usual classification of 'normal' glasses as those undergoing median-radial cracking on unloading for relatively small loads does not hold for all glass compositions. All of the optical glass compositions that underwent significant shear-faulting behavior, i.e., 'normal,' volume conserving, initiated median-radial cracks early on indentation loading. These glasses also had a high tendency to form shallow lateral cracks.

2. If brittleness of glass is defined as the minimum load needed to cause median-radial cracking, then all of the optical glasses, with the exception of glass S2, are extremely brittle. The float glass and glass S2 are thus the least brittle, since these glasses only formed median-radial cracks on unloading for maximum loads up to 1 Kg.

3. Increased RO_2, in the form of silica, is seen as necessary to increase median-radial crack initiation resistance. However, too high a RO_2 will lead to ring-cone, and possibly median-radial, cracking. An optimum RO_2 of somewhere between 2.5 and 5 is seen as providing the best overall resistance to cracking. Sehgal and Ito's[14] low-brittleness glass, which did not form median-radial or ring-cone cracks for loads up to 3.5 Kg, had an RO_2 of ≈ 4.2. These glasses could best be described as 'normal-anomalous,' and include most of the Wagner glasses[9] originally coined as 'normal', as well as the float glass studied here.

4. Glasses with open structures and semi-rigid (strong) bonding have overall better resistance to crack initiation than either tightly packed, or loose, easily sheared structures. Tightly-packed structures have no choice but to change shape by shearing, and loosely-held structures prefer shear because this deformation mode offers the least resistance to deformation; both structures result in large strains and easy median-radial crack formation.

5. Overall, 'anomalous' glasses offer increased resistance to median-radial cracking both in terms of threshold load and crack extension (length) compared to 'normal' glasses. The reduced strain incompatibility between elastic and plastic zones in the 'anomalous' glasses is the prime reason for this, a direct result of their more open structure.

6. The median-radial cracks extending from the indentations in glasses with high RO_2, which includes float glass and all the 'anomalous' glasses, do so with more variability in location with respect to the indentation corners compared to the more 'normal' glasses (S3, S4, S5, S6, NS1, NS2, NS3). The median-radial cracks in these latter glasses extend from closer to the corners, and propagate more linearly with respect to the corners. It is believed the more open structures of the former (more anomalous) glasses creates more randomness in the direction of crack propagation. In addition, median-radial crack extension in the 'anomalous' glasses, and even float glass to some extent, appears to be from severe outer shear

faults that were punched into the material during indenter loading. That is, the shear faults are the precursors to the median-radial cracks in these glasses. In the *most* 'normal' glasses, however, the median-radial cracks did not appear to be directly connected with shear faults. Rather, the cracks seemed to be a result of direct material separation at the corners. While it is possible that shear faults were in someway involved, e.g., as crack nuclei, no good visible evidence was seen to support this. The more fine and uniform nature of the shear fault lines on the surfaces of the more 'normal' glasses (S3, S4, S5, S6, NS1, NS2, NS3) reflects the more uniform shear flow of these glasses compared to the 'anomalous' glasses and float glass, which had a wider, and more variable fault structure. This finer structure also resulted in fewer secondary radial cracks forming in these glasses, compared to float glass and the 'anomalous' glasses, where the numerous severe shear faults competed for the initiation of a dominant median-radial crack.

7. Overall, no one single mechanical property or characteristic alone can predict the initiation loads or overall behavior of any of the glasses examined in the current work. However, certain general observations can be made:

(i) The glasses with the lowest fracture toughness had the least resistance to median-radial cracking on loading. These glasses also had the lowest Vickers hardness (H_V) and Young's modulus (E). Glasses with the highest H_V and E were also prone to early cracking. Glasses with

intermediate values of H_V and E (S2, float, 7740 Pyrex borosilicate, v-SiO_2) had greater resistance to cracking, and had the highest values of fracture toughness.

(ii) Median-radial initiation resistance on unloading generally increased with increasing fracture toughness and fracture surface energy.

(iii) Some broad correlation exists between the brittleness indices H_V/K_{IC}, EH_V/K_{IC}, and the cracking behavior. In general, as both these indices increased (higher 'brittleness'), the initiation load for median-radial cracking on unloading increased. On loading, the latter index correlated slightly with the initiation results, i.e., in general, glasses with the highest values (more 'brittle') of EH_V/K_{IC}^2 had the least resistance to median-radial cracking, while no correlation was seen with H_V/K_{IC}.

(iv) In general, glasses with the lowest values of G/K and highest values of E/H_V had the least resistance to median-radial cracking. G/K is thought to be associated with the relative tendency of a glass to shear and change shape beneath an indenter. E/H_V may be related to the crack nucleation tendency and driving force that actually builds. Lower values of G/K are thought to be associated with increased tendency for a material to shear and change shape beneath an indenter, while higher values of E/H_V are thought to be associated with increased crack nucleation tendency and driving force around the plastic zone. Both quantities, and the **RO_2** amount, are thought to govern crack initiation behavior in glass.

7.   FUTURE WORK

It would be useful to computer model the strains (deformations) and stresses about the contact sites in these glasses to see how the results compare to the crack initiation behavior. This would provide some quantitative evidence of the concepts put forth in the current work.

Comparison of the indentation cracking behavior of the glasses to their strength and scratch-resistance behavior would help to more firmly establish the role and usefulness of crack initiation studies in glass. This is something that would be of prime importance to glass manufacturers.

A more rigorous structural analysis of the glasses based on spectroscopic results would help in correlating the cracking behavior with the glass structure. Such an in-depth study was not possible in the current work.

8. REFERENCES

1. A.A. Griffith, "The Phenomena of Rupture and Flow in Solids," *Philos. Trans. R. Soc. London,* **221** 163-198 (1920).

2. D.W. Mueller and G.D. Mylchreest, "Effect of Abrasion and Other Influences on Glass Surface Strength," American Ceramic Society Glass Division Autumn Meeting Presentation, 1947. Abstract in *Glass Ind.* **28** [10] 515 (1947).

3. E.B. Shand, "Experimental Study of Fracture of Glass: I, The Fracture Process," *J. Am. Ceram. Soc.,* **37** [2] 52-60 (1954).

4. R.E. Mould and R.D. Southwick, "Strength and Static Fatigue of Abraded Glass Under Controlled Ambient Conditions: II, Effect of Various Abrasions and the Universal Fatigue Curve," *J. Am. Ceram. Soc.,* **42** [11] 582-592 (1959).

5. J.C. Lambropoulos, "Presidential Young Investigator Award: Computational Micromechanics of Solids," Final Technical Report for Grant MSS-8857096, Department of Mechanical Engineering, University of Rochester, Rochester, NY, 1996.

6. M. Buijs and K. Van-Houten, "A Model for Lapping of Glass," *J. Mater. Sci.,* **28** [11] 3014-3020 (1993).

7. A. Arora, D.B. Marshall, and B.R. Lawn, "Indentation Deformation/Fracture of Normal and Anomalous Glasses," *J. Non-Cryst. Solids,* **31** [3] 415-428 (1979).

8. J.T. Hagan and S. Van Der Zwaag, "Plastic Processes in a Range of Soda-Lime Silica Glasses," *J. Non-Cryst. Solids,* **64** [1-2] 249-268 (1984).

9. C.J. Wagner, "Influence of Composition on Crack Initiation Behavior of Glasses"; M.S. Thesis. Alfred University, Alfred, NY, 1998.

10. N.L. Canfield, "Effects of Alkali and Alkaline Earth Additions on the Mechanical Properties of Silicate Glasses"; M.S. Thesis. Alfred University, Alfred, NY, 2000.

11. R.F. Cook and G.M. Pharr, "Direct Observation and Analysis of Indentation Cracking in Glasses and Ceramics," *J. Am. Ceram. Soc.,* **73** [4] 787-817 (1990).

12. K. W. Peter, "Densification and Flow Phenomena of Glass in Indentation Experiments," *J. Non-Cryst. Solids,* **5** [2] 103-115 (1970).

13. B.R. Lawn and D.B. Marshall, "Hardness, Toughness, and Brittleness: An Indentation Analysis," *J. Am. Ceram. Soc.,* **62** [7-8] 347-350 (1979).

14. J. Sehgal and S. Ito, "A New Low-Brittleness Glass in the Soda-Lime Silica Glass Family," *J. Am. Ceram. Soc.,* **81** [9] 2485-2488 (1998).

15. S.M. Wiederhorn and B.J. Hockey, "Hot Erosion of Glass," *J. Non-Cryst. Solids,* **38-39** [1] 433-438 (1980).

16. J.R. Varner, W. Hallwig, and A. Walter, "Impact Damage on Annealed and on Tempered Flat Glass," *J. Non-Cryst. Solids,* **38-39** [1] 413-418 (1980).

17. S.M. Wiederhorn, B.R. Lawn, and B.J. Hockey, "Effect of Particle Impact Angle on Strength Degradation of Glass," *J. Am. Ceram. Soc.,* **62** [11-12] 639-640 (1979).

18. Brian Lawn and Rodney Wilshaw, "Review Indentation Fracture: Principles and Applications," *J. Mater. Sci.,* **10** [6] 1049-1081 (1975).

19. K.L. Johnson, "The Correlation of Indentation Experiments," *J. Mech. Phys. Solids,* **18** [2] 115-126 (1970).

20. B.R. Lawn, A.G. Evans, and D.B. Marshall, "Elastic/Plastic Indentation Damage in Ceramics: The Median/Radial Crack System," *J. Am. Ceram. Soc.,* **63** [9-10] 574-581 (1980).

21. B.R. Lawn and A.G. Evans, "A Model for Crack Initiation in Elastic/Plastic Indentation Fields," *J. Mater. Sci.,* **12** [11] 2195-2199 (1977).

22. A.G. Evans, "Fracture Toughness: The Role of Indentation Techniques," pp. 112-135 in *Fracture Mechanics Applied to Brittle Materials*; ASTM STP 678. Edited by S.W. Freiman. American Society for Testing and Materials, Baltimore, MD, 1979.

23. C.M. Perrot, "Elastic-Plastic Indentation: Hardness and Fracture," *Wear,* **45** [3] 293-309 (1977).

24. S.S. Chiang, D.B. Marshall, and A.G. Evans, "The Response of Solids to Elastic/Plastic Indentation. I. Stresses and Residual Stresses," *J. Appl. Phys.,* **53** [1] 298-311 (1982).

25. E. H. Yoffe, "Elastic Stress Fields Caused by Indenting Brittle Materials," *Philos. Mag. A.,* **46** [4] 617-628 (1982).

26. G.R. Anstis, P. Chantikul, B.R. Lawn, and D.B. Marshall, "A Critical Evaluation of Indentation Techniques for Measuring Fracture Toughness: I, Direct Crack Measurements," *J. Am. Ceram. Soc.,* **64** [9] 533-538 (1981).

27. S.M. Wiederhorn, H. Johnson, A.M. Dines, and A.H. Heuer, "Fracture of Glass in Vacuum," *J. Am. Ceram. Soc.,* **57** [8] 336-341 (1974).

28. R.H. Doremus, *Glass Science*, 2nd ed.; pp. 163-164. John Wiley & Sons, New York, 1994.

29. J.T. Hagan, "Shear Deformation Under Pyramidal Indentations in Soda-Lime Glass," *J. Mater. Sci.,* **15** [6] 1417-1424 (1980).

30. T.P. Dabbs, C.J. Fairbanks, and B.R. Lawn, "Subthreshold Indentation Flaws in the Study of Fatigue Properties of Ultrahigh-Strength Glass," pp. 142-153 in *Methods for Assessing the Structural Reliability of Brittle Materials*; ASTM STP 844. Edited by S.W. Freiman and C.M. Hudson. American Society for Testing and Materials, Baltimore, MD (1984).

31. F.M. Ernsberger, "Role of Densification in Deformation of Glasses Under Point Loading," *J. Am. Ceram. Soc.,* **51** [10] 545-547 (1968).

32. J. Neely, "Hardness and High Pressure Deformation Mechanisms of Glass"; Ph.D. Thesis. Rensselaer Polytechnic Institute, Troy, NY, 1969.

33. P.W. Bridgman and I. Simon, "Effects of Very High Pressures on Glass," *J. Appl. Phys.,* **24** [4] 405-413 (1953).

34. J.D. Mackenzie, "High-Pressure Effects on Oxide Glasses: I, Densification in Rigid State," *J. Am. Ceram. Soc.,* **46** [10] 461-470 (1963).

35. A.K. Varshneya, *Fundamentals of Inorganic Glasses*. Academic Press, San Diego, CA, 1994.

36. D.K. Shetty, I.G. Wright, P.N. Mincer, and A.H. Clauer, "Indentation Fracture of WC-Co Cermets," *J. Mater. Sci.,* **20** [5] 1873-1882 (1985).

37. B.R. Lawn and M.V. Swain, "Microfracture Beneath Point Indentations in Brittle Solids," *J. Mater. Sci.,* **10** [1] 113-122 (1975).

38. B.R. Lawn, T.P. Dabbs, and C.J. Fairbanks, "Kinetics of Shear-Activated Indentation Crack Initiation in Soda-Lime Glass," *J. Mater. Sci.,* **18** [9] 2785-2797 (1983).

39. R. Tandon and R.F. Cook, "Cone Crack Nucleation at Sharp Contacts," *J. Am. Ceram. Soc.,* **75** [10] 2877-2880 (1992).

40. T.M. Cleary, "Effects of Surface Treatments on Crack Initiation in Glasses"; M.S. Thesis. Alfred University, Alfred, NY, 1995.

41. M. Wada, H. Furukawa, and K. Fujita, "Crack Resistance of Glass on Vickers Indentation," pp. 39-46 in *The Tenth International Congress on Glass*. Edited by M. Kunigi, M. Tashiro, and N. Saga. Ceramics Society of Japan, Kyoto, Japan, 1974.

42. J. Sehgal and J. Kase "Scratch-Resistant Glass," Asahi Glass Company Ltd., European Patent Application 96901989.2, February 5, 1997.

43. W.D. Kingery, R.R. Shaw, and D.R. Uhlmann, *Introduction To Ceramics*, 2nd ed.; pp. 109. John Wiley & Sons, New York, 1976.

44. M. Takata, M. Tomozowa, and E.B. Watson, "Effect of Water on Mechanical Properties of Na_2O-SiO_2 Glasses," *J. Am. Ceram. Soc.,* **69** [9] C156-C157 (1982).

45. F.M. Ernsberger, "Molecular Water in Glass," *J. Am. Ceram. Soc.,* **60** [1-2] 91-92 (1977).

46. C.K. Wu, "Stable Silicate Glasses Containing up to 10 Weight Percent of Water," *J. Non-Cryst. Solids,* **41** [3] 381-398 (1980).

47. R.F. Bartholomew, B.L. Butler, H.L. Hoover, and C.K. Wu, "Infrared Spectra of a Water Containing Glass, " *J. Am. Ceram. Soc.,* **63** [9-10] 481-485 (1980).

48. A.A. Pollock, "Acoustic Emission Inspection," pp. 278-294 in *ASM Metals Handbook*, 9th ed., Vol. 17. ASM International, Materials Park, OH, 1989.

49. R.A. Kline, "Acoustic Emission Signal Characterization," pp. 105-137 in *Acoustic Emission*. Edited by James R. Matthews. Gordon and Breach Science, New York, 1983.

50. J. Lankford and D.L. Davidson, "The Crack-Initiation Threshold in Ceramic Materials Subject to Elastic/Plastic Indentation," *J. Mater. Sci.,* **14** [7] 1662-1668 (1979).

51. B.V. Tanikella and R.O. Scattergood, "Acoustic Emission During Indentation Fracture," *J. Am. Ceram. Soc.,* **78** [6] 1698-702 (1995).

52. T.M. Cleary and J.R. Varner, "Crack Initiation During Hertzian Indentation of Normal and Anomalous Glasses-A Study Using Fractography and Acoustic Emission," pp. 491-500 in *Fractography of Glasses and Ceramics III*. Edited by J.R. Varner and V.D. Frechette. American Ceramic Society, Westerville, Ohio, 1995.

53. T.E. Wilantewicz, "The Effects of Lithium, Boron, and Magnesium Oxides on the Mechanical Properties of Silicate Glasses"; M.S. Thesis. Alfred University, Alfred, NY, 1998.

54. J. Krautkramer and H. Krautkramer, *Ultrasonic Testing of Materials*, 2nd ed. Springer-Verlag, Berlin, Germany, 1977.

55. W.D. Callister, Jr., *Materials Science and Engineering: An Introduction*. John Wiley & Sons, New York, 1994.

56. "Standard Test Method for Microhardness of Materials," ASTM Standard E 384 – 89. 1990 Annual book of ASTM Standards, Vol. 3.01. American Society for Testing and Materials, West Conshohocken, PA, 1990.

57. R.W. Hertzberg, *Deformation and Fracture Mechanics of Engineering Materials*, 2nd ed. John Wiley & Sons, New York, 1983.

58. D.B. Marshall, B.R. Lawn, and A.G. Evans, "Elastic/Plastic Indentation Damage in Ceramics: The Lateral Crack System," *J. Am. Ceram. Soc.,* **65** [11] 561-566 (1982).

59. CRC Handbook of Chemistry and Physics, 72nd ed. Edited by David R. Lide. CRC Press, Boston, 1991.

60. J.E. Shelby, *Introduction to Glass Science and Technology*. The Royal Society of Chemistry, Cambridge, UK, 1997.

61. G.H. Frischat, "Tabulation of Mechanical Property Data," pp. 609-620 in *Strength of Inorganic Glass*. Edited by C.R. Kurkjian. Plenum Press, New York, 1985.

62. Engineered Materials Handbook, Vol. 4, *Ceramics and Glasses*. Edited by Samuel J. Schneider. American Ceramic Society, Westerville, OH, 1991.

63. A. Makishima and J.D. Mackenzie, "Direct Calculation of Young's Modulus of Glass," *J. Non-Cryst. Solids,* **12** [1] 35-45 (1973).

64. M. Yamane and J.D. Mackenzie, "Vicker's Hardness of Glass," *J. Non-Cryst. Solids,* **15** [2] 153-164 (1974).

65. D.R. Tate, "A Comparison of Microhardness Indentation Tests," *Trans. Am. Soc. Met.,* **35** 374-389 (1945).

66. S.M. Wiederhorn, "Fracture Surface Energy of Glass," *J. Am. Ceram. Soc.,* **52** [2] 99-105 (1969).

67. N. Miyata and H. Jinno, "Strength and Fracture Surface Energy of Phase-Separated Glasses," *J. Mater. Sci.,* **16** [8] 2205-2217 (1981).

68. J.B. Quinn and G.D. Quinn, "Indentation Brittleness of Ceramics: A Fresh Approach," *J. Mater. Sci.,* **32** [16] 4331-4346 (1997).

69. J. Sehgal, Y. Nakao, H. Takahashi, and S. Ito, "Brittleness of Glasses by Indentation," *J. Mater. Sci. Lett.,* **14** [3] 167-169 (1995).

70. Eliezer M. Rabinovich, "Review: Lead in Glasses," *J. Mater. Sci.,* **11** [5] 925-948 (1976).

71. H. Doweidar, A. A. Megahed, S. Abd Al-Maksoud, M.S. El-Shahawi, and Y. El-Fol, "Properties and Structure of $ZnO-PbO-B_2O_3$ Glasses," *Phys. Chem. Glasses,* **35** [5] 187-192 (1994).

72.   P. Zhao, S. Kroeker, and J.F. Stebbins, "Non-Bridging Oxygen Sites in Barium Borosilicate Glasses: Results from 11B and 17O NMR," *J. Non-Cryst. Solids,* **276** [3] 122-131 (2000).

73.   Y.H. Yun and P.J. Bray, "Nuclear Magnetic Resonance Studies of the Glasses in the System Na_2O-B_2O_3-SiO_2," *J. Non-Cryst. Solids,* **27** [3] 363-380 (1978).

74.   N.A. Ghoneim and S.M. Salman, "Microhardness and Softening Point of Some Borosilicate Glasses in Relation to Their Structure," *Cent. Glass Ceram. Res. Inst. Bull.,* **31** [1-4] 9-12 (1984).

75.   A.M. Zahra, C.Y. Zahra, and B. Piriou, "DSC and Raman Studies of Lead Borate and Lead Silicate Glasses," *J. Non-Cryst. Solids,* **155** [1] 45-55 (1993).

76.   I.N. Chakraborty, J.E. Shelby, and R.A. Condrate Sr., "Properties and Structure of Lanthanum Borate Glasses," *J. Am. Ceram. Soc.,* **67** [12] 782-785 (1984).

77.   I.N. Chakraborty and D.E. Day, "Effect of R^{3+} Ions on the Structure and Properties of Lanthanum Borate Glasses," *J. Am. Ceram. Soc.,* **68** [12] 641-645 (1985).

78.   N.J. Clayden, S. Esposito, A. Aronne, and P. Pernice, "Solid State ^{27}Al NMR and FTIR Study of Lanthanum Aluminosilicate Glasses," *J. Non-Cryst. Solids,* **258** [1-3] 11-19 (1999).

79.   Richard K. Brow, "Review: The Structure of Simple Phosphate Glasses," *J. Non-Cryst. Solids,* **263&264** [1-3] 1-28 (2000).

80.   T. Uchino and T. Yoko, "Structure and Vibrational Properties of Alkali Phosphate Glasses from Ab Initio Molecular Orbital Calculations," *J. Non-Cryst. Solids,* **263&264** [1-3] 180-188 (2000).

81.   J.E. Shelby, "Properties of Alkali-Alkaline Earth Metaphosphate Glasses," *J. Non- Cryst. Solids,* **263&264** [1-3] 271-276 (2000).

82.   U. Hoppe, G. Walter, R. Kranold, and D. Stachel, "Structural Specifics of Phosphate Glasses Probed by Diffraction Methods: A Review," *J. Non-Cryst. Solids,* **263&264** [1-3] 29-47 (2000).

83. Jacques Lucas, "Halide Glasses-Recent Developments," pp. 3.1-3.26 in *Advances in the Fusion of Glass*. Edited by D.F. Bickford, W.E. Horsfall, F.E. Woolley, E.N. Boulos, J.N. Lingscheit, F. Harding, F. Olix, W.C. LaCourse, and L.D. Pye. American Ceramic Society, Westerville, OH, 1988.

84. Y. Kawamoto and T. Horisaka, "Short-Range Structures of Barium, Lead, and Strontium Meta-Fluorozirconate Glasses," *J. Non-Cryst. Solids,* **56** [1-3] 39-44 (1983).

85. T.I. Suratwala, R.A. Steele, G.D. Wilke, J.H. Campbell, and K. Takeuchi, "Effects of OH Content, Water Vapor Pressure, and Temperature on Sub-Critical Crack Growth in Phosphate Glass," *J. Non-Cryst. Solids,* **263&264** [1-3] 213-227 (2000).

86. R. Bruckner, "Properties and Structure of Vitreous Silica. I," *J. Non-Cryst. Solids,* **5** [2] 123-175 (1970).

87. R. Hill, *The Mathematical Theory of Plasticity*. Oxford University Press, Oxford, UK, 1950.

APPENDIX

Surface and Sub-Surface Damage for 5 Kg Indentation Sites
(Conventional Indenter, 5 s hold under load)

Surface   **Corresponding Sub-Surface**

S1 (A): Lead-Alkali-Silicate Crown
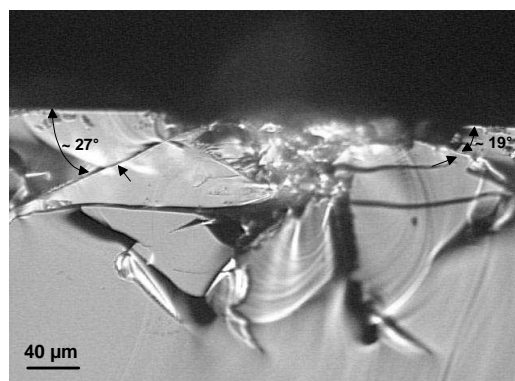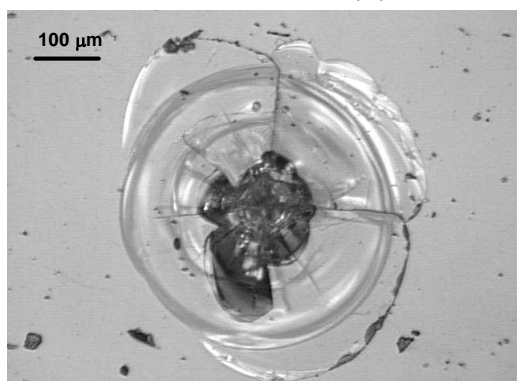
S2 (A): Zinc-Silicate Crown
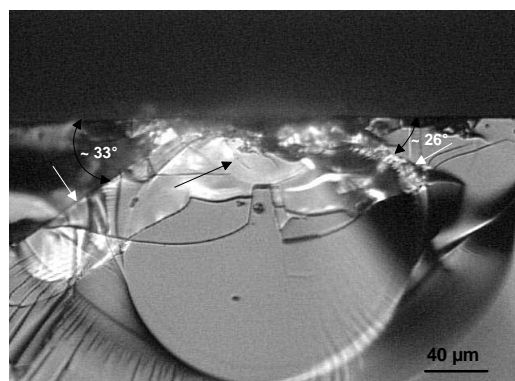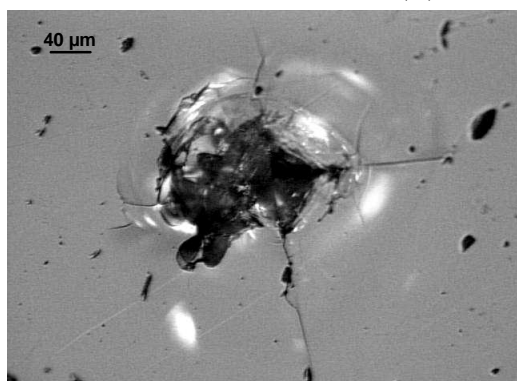
S3 (N): Barium-Borosilicate Dense Crown
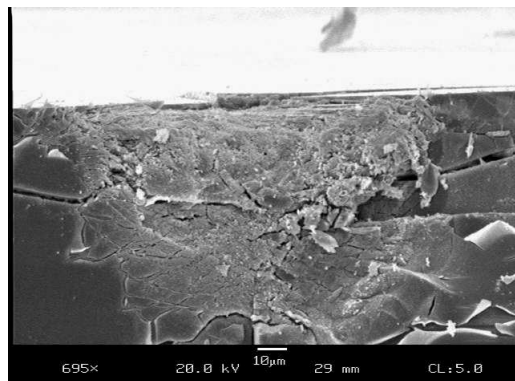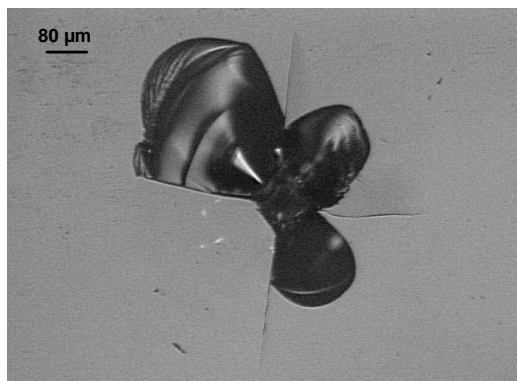
This cross-section for glass S3 does not correspond to same indentation site at left for glass S3.

308

S4 (N): Lead-Borosilicate Dense Flint
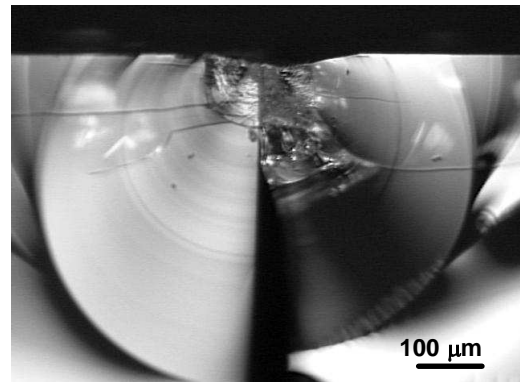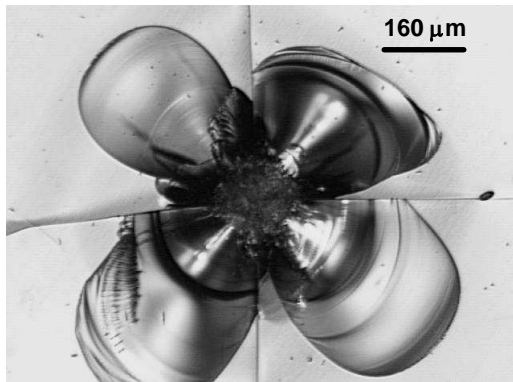
S4 (N): Higher-Magnification Image
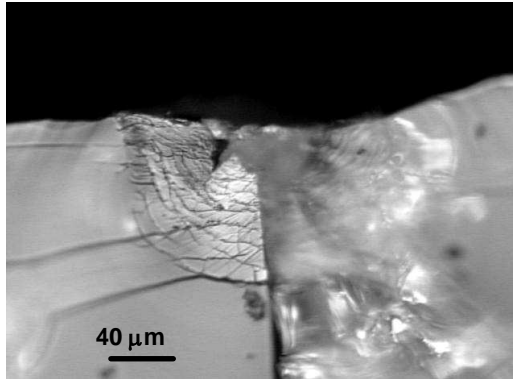
S4 (N): SEM Image
(different indent)
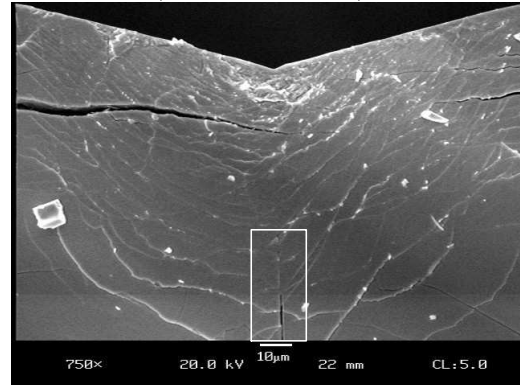
S4 (N): Additional Optical Image
(different indent)
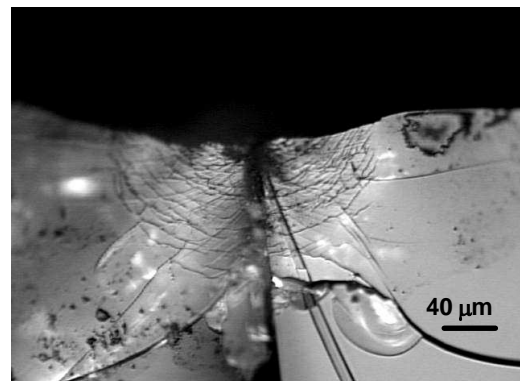
Surface	**Corresponding Sub-Surface**

S5 (N): Lanthanum-Borate Crown
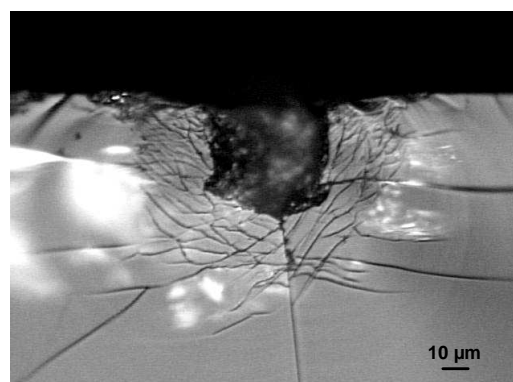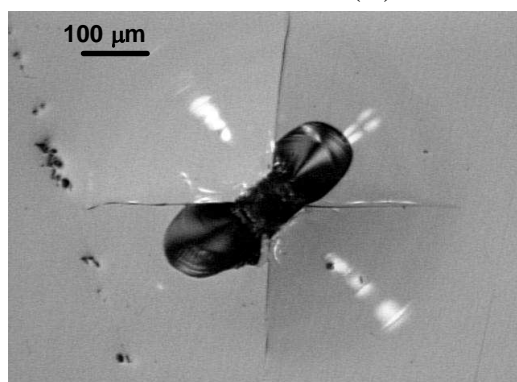
S6 (N): Lanthanum-Borate Crown
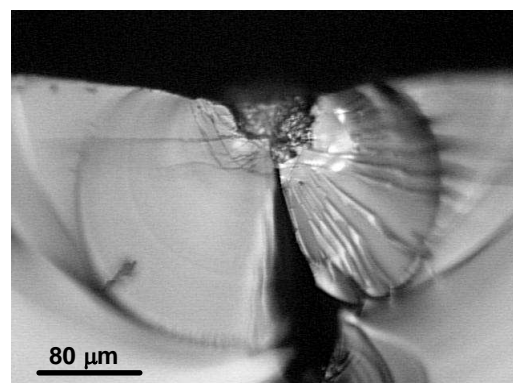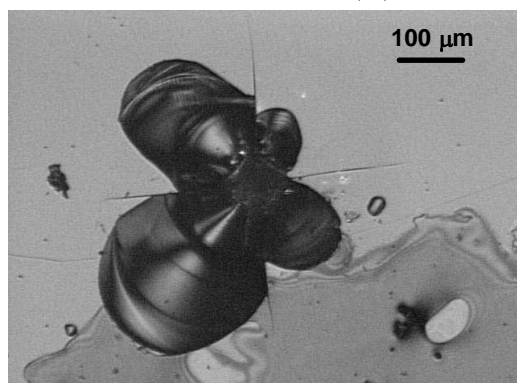
S6 (N): SEM Image
(different indent)
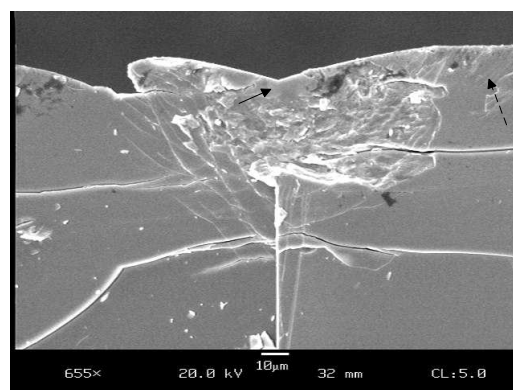
Surface　　　　　　　　**Corresponding Sub-Surface**

NS1 (N): Lanthanum-Borate Flint
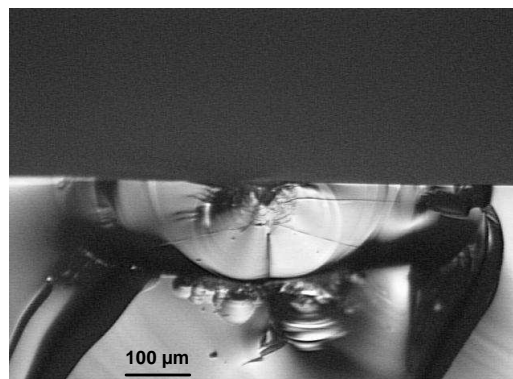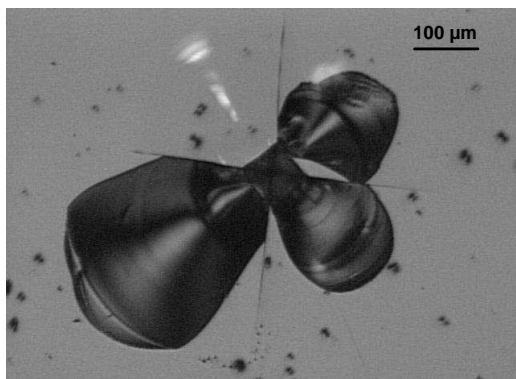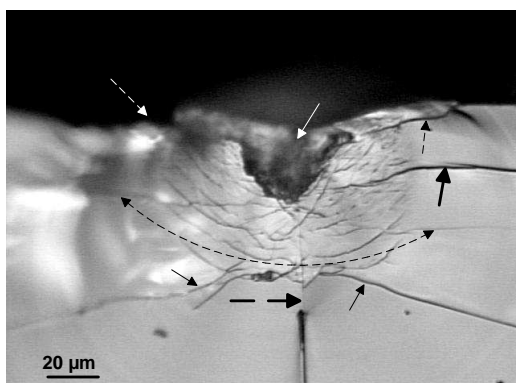
NS1 (N): Higher-Magnification Image　　　NS1 (N): SEM Image
(different indent)
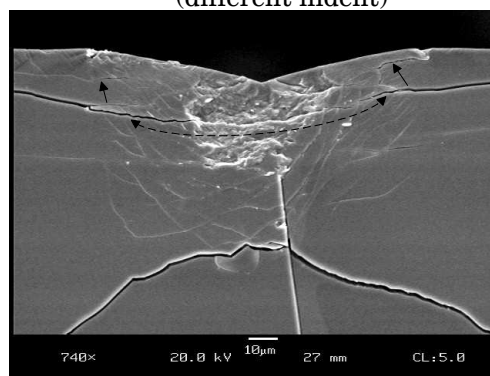
NS1 (N): Higher Magnification of above Image.

311
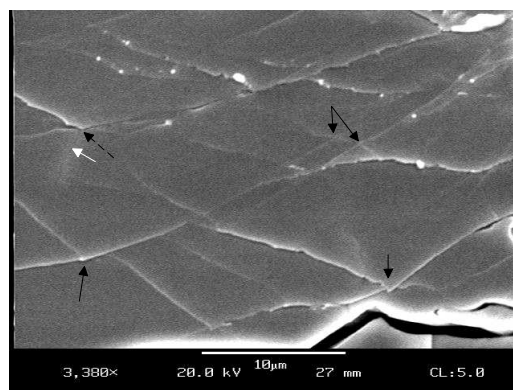
Surface

Corresponding Sub-Surface

NS2 (N): Potassium-Phosphate
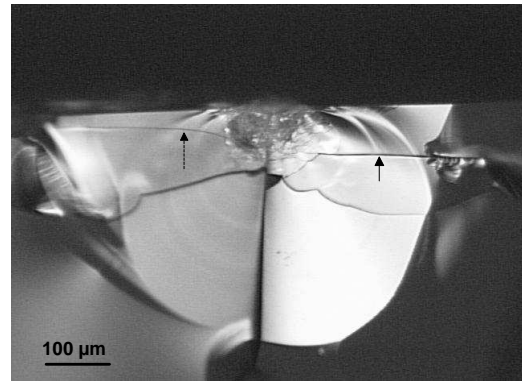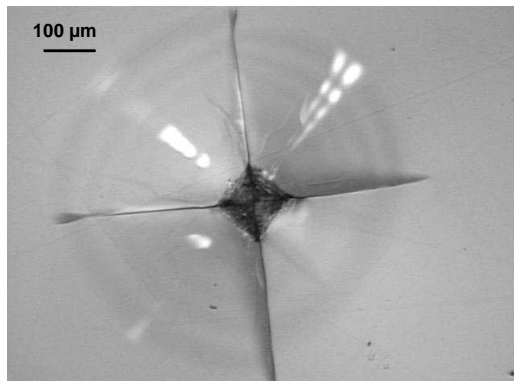
NS2 (N): Higher-Magnification Image
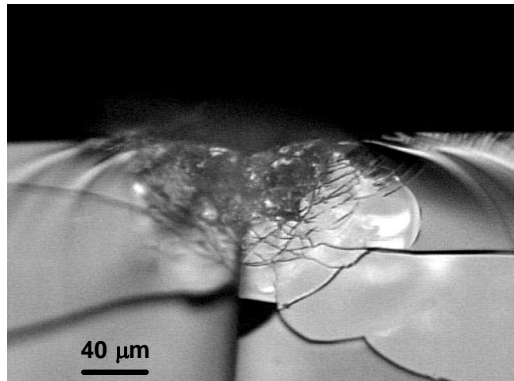
NS2 (N): SEM Image
(different indent)
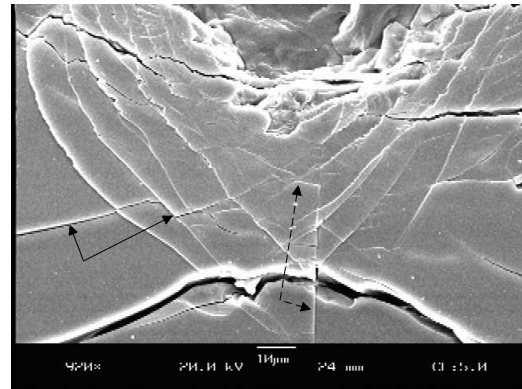
NS3 (N): Fluoride-Crown
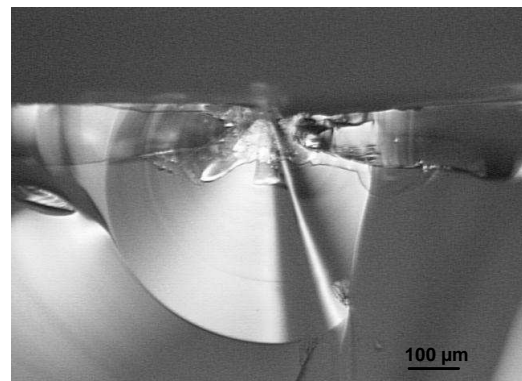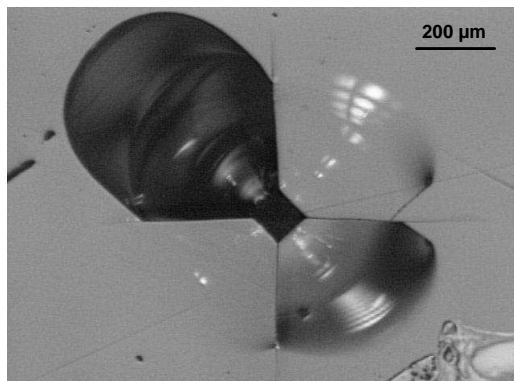
NS3 (N): SEM Image
(different indent)
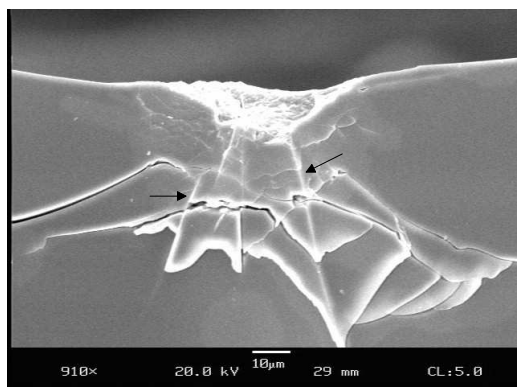
NS3 (N): SEM Image
(different indent)
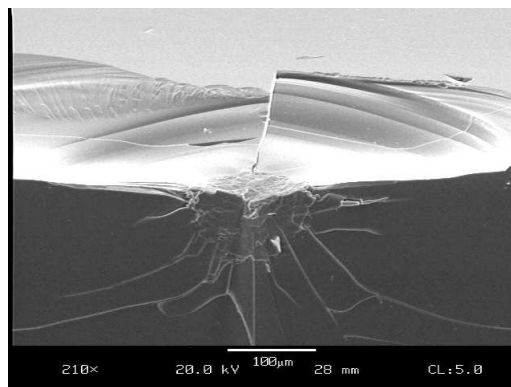
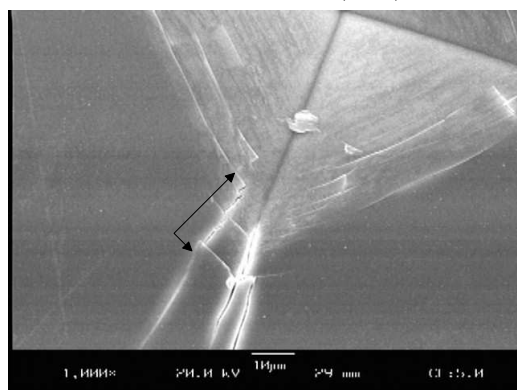NS3 (N): High-Magnification SEM Image of 'Plastic'-Zone at Upper-Right.
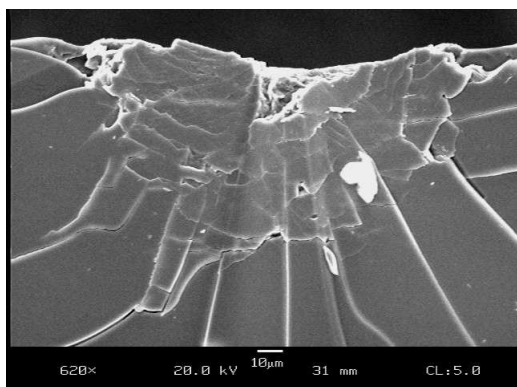
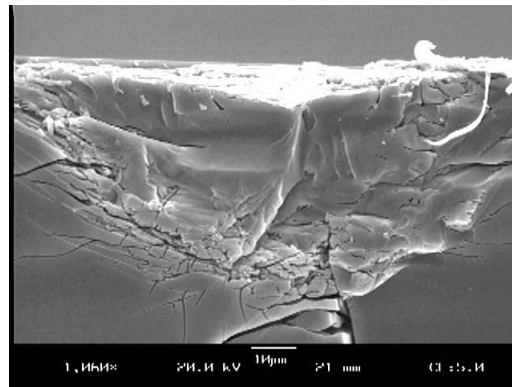NS3 (N): Higher Magnification SEM Image of 'Plastic'-Zone at Left.
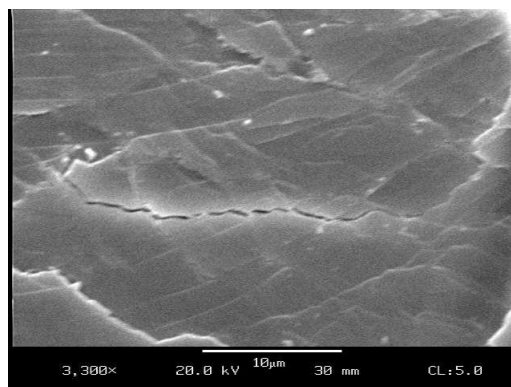
Surface

Corresponding Sub-Surface

Float (N-A): Alkali-Alkaline-Earth Silicate
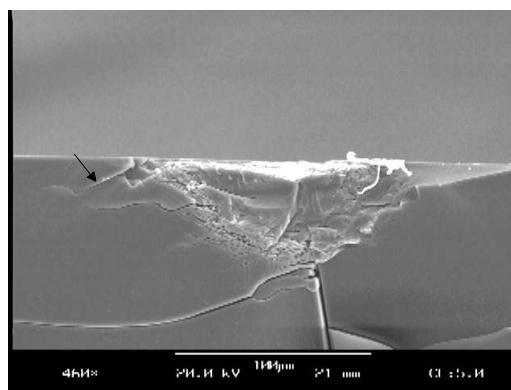
This cross-section for float glass does not correspond to same indentation site at left for float glass.
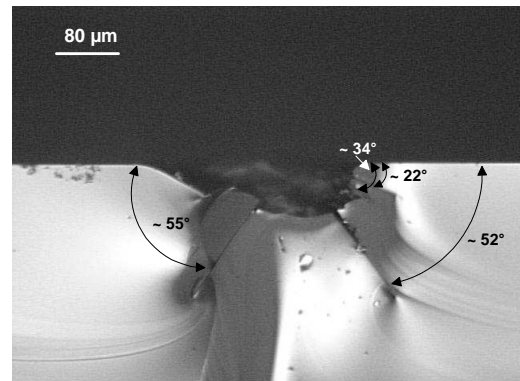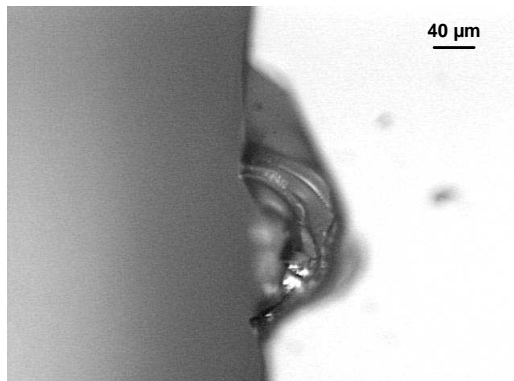
313

Float (N-A): High-Magnification SEM Image of
same 'Plastic'-Zone

Surface   **Corresponding Sub-Surface**

Vitreous Silica Microscope Slide Glass (A)

**4 Kg Indentation Site in Suprasil 312
(Recording Microindenter, 0.2 µm/s rate)**